

*Sustainable design and durability of  
domestic micro combined heat and  
power scroll expander systems*



*Thesis submitted in a partial fulfilment of the  
requirements of Bournemouth University for  
the degree of Doctor of Philosophy*

*by Iakovos Tzanakis*

*March 2010*

*Bournemouth University  
in collaboration with the  
Energetix Group Ltd.*



## **Abstract**

Research to understand the mechanisms of wear within the main components of three different micro-CHP scroll expander systems was conducted. This was performed in order to identify the possible tribo-mechanical effects (abrasion, adhesion, cavitation, fatigue) which occur on the substrate of these components during the operation of the scroll which can seriously affect the lifecycle of the micro-CHP unit.

Three-dimensional interferometer, surface scanning and scanning electron microscopy (SEM) were used for surface analyses. The critical components for durability were identified on the tip seal and the steel plate of the scroll expander. Abrasive wear derived from a two-body contact on the interface of the tip seal and the steel plate. Three-body wear was found across the steel plate of the scroll. Finally, cavitation pits were revealed. Interestingly, cavitation was generated by the increment of pressure. It was found that sufficiently high pressure can liquefy instantaneously part of the refrigerant close to the bottom boundary, creating conditions for the generation of cavitation bubbles within the liquefied refrigerant. This finding resolves the puzzle of how the refrigerant which enters the scroll in gas phase produces cavitation. The wear mechanisms identified can significantly reduce the performance of the scroll.

Specimens made from the steel plate (high carbon steel) and the tip seal (high performance reinforced fluoroelastomer) of the scroll expander were used for bench tests. The parts were used to perform sliding tribological tests using a special purpose-built modified micro-friction machine TE 57 in order to clearly identify the sliding wear and friction mechanisms. These tests were performed under a specific load and lubrication regime. The experimental conditions were adjusted to those of the industrial applications.

Furthermore an experimental study using an ultrasonic transducer (submerged into the fluids) was utilised to produce cavitation bubbles. Using high-speed camera techniques the bubbles were observed within the working fluids. A thorough investigation of the dynamic behaviour of the bubbles and their cavitation mechanisms was conducted using the two scroll fluids (lubricant/refrigerant). The experimental results were effectively correlated with the computational ones. Additionally, the impact of the scroll fluid cavities across the surface of various commercial steel grades, including the actual steel plate of the scroll, was determined. Finally, their cavitation performance and durability, over a prolonged period of time was investigated.

## **Publications Resulting From Thesis**

1. I. Tzanakis, M. Hadfield, Z. Khan. 2009. *Durability of domestic scroll compressor systems*. Surface effects and contact mechanics, 62 (229-240). ISBN: 978-1-84564-186-3
2. I. Tzanakis, M. Hadfield. *Observations of acoustically generated cavitation bubbles within typical fluids applied to a scroll expander lubrication system*. Journal of Hydrodynamics (submitted February 2010).
3. I. Tzanakis, M. Hadfield, A. Georgoulas, N. Kotsovinos. 2010. *Cavitation damage observations within scroll expander lubrication systems*. Tribology and design. ISBN: 978-1-84564-440-6
4. I. Tzanakis, M. Hadfield, Z. Khan, N. Garland. *Experimental sliding performance of the reinforced fluoroelastomer tip seal with high carbon steel applied to scroll expander systems*. Tribology Letters (submitted June 2010).
5. I. Tzanakis. “*Friction analysis and wear modes of the scroll expander*”. Internal Energetix document and presentation, Energetix Group Ltd (2009).
6. I. Tzanakis. “*Cavitation erosion failure mechanisms of the scroll expander*”. Internal Energetix document and presentation, Energetix Group Ltd (2009).

## **List of Contents**

Abstract.....	ii
Publications Resulting From Thesis.....	iii
Table of Contents .....	iv
List of Figures .....	viii
List of Tables .....	xix
List of Appendices .....	xx
Acknowledgments.....	xxi
Nomenclature.....	xxii
1 CHAPTER : INTRODUCTION .....	1
1.1 Background to Research.....	1
1.2 Aims of the Project.....	3
1.3 Objectives of the Project .....	4
1.4 Beneficiaries .....	5
1.5 Contribution to knowledge .....	5
1.6 Outline of the Project .....	6
2 CHAPTER : LITERATURE REVIEW.....	8
2.1 Refrigerants.....	8
2.1.1 Organic Rankine Cycle (ORC).....	9
2.1.2 Refrigeration Lubricants.....	11
2.2 Lubrication.....	11
2.2.1 Film Thickness.....	14
2.2.2 Lubrication of compressors .....	16
2.2.3 Viscosity .....	17
2.3 Polymers/Elastomers.....	18
2.3.1 Reinforced Polymers .....	19
2.4 Friction Theory .....	20
2.4.1 Friction Force.....	20
2.4.2 Friction Coefficient (Dry Contact).....	21
2.4.3 Friction Coefficient (Lubricated Contact).....	24
2.5 Tribological Considerations.....	25

2.5.1	Wear Theory .....	25
2.5.2	Wear of Polymers.....	27
2.5.3	Wear Parameters .....	28
2.6	Previous Studies.....	31
2.7	Cavitation.....	33
2.7.1	Cavitation Forms/Types .....	34
2.8	Bubble Dynamics.....	36
2.9	Cavitation Conditions.....	39
2.9.1	Effect of Viscosity .....	39
2.9.2	Effect of Surface Tension .....	40
2.9.3	Effect of Tensile Strength.....	40
2.9.4	Effect of Normalised Distance.....	41
2.9.5	Effect of Magnitude of Vibration .....	41
2.10	Cavitation Erosion Equations .....	42
2.11	Previous Studies.....	43
3	CHAPTER : SCROLL EXPANDER OPERATIONAL ANALYSIS .....	46
3.1	The CHP unit .....	46
3.1.1	ORC Process.....	48
3.1.2	Performance of the System.....	49
3.1.3	The Scroll Expander.....	50
3.1.4	Efficiency Drop.....	51
3.2	Case Study .....	53
3.2.1	Chemical Analysis .....	54
3.2.2	Surface Analysis .....	57
3.3	Cavitation Mechanism Analysis .....	68
3.4	Side Walls.....	84
3.5	Summary and discussion .....	87
3.5.1	Scroll's Surface Investigation.....	87
3.5.2	Analytical Results .....	87
4	CHAPTER : EXPERIMENTAL METHODOLOGY .....	89
4.1	Experimental Test Rigs .....	89
4.1.1	TE 57 micro-sliding wear/friction test rig.....	89

4.1.2	Cavitation Apparatus integrated to a High-Speed Camera Device.....	90
4.2	Surface Analysis .....	92
4.2.1	Optical Microscopy .....	92
4.2.2	Scanning Interferometer Microscopy.....	93
4.2.3	Scanning Electron Microscopy .....	94
4.3	Auxiliary devices .....	96
4.3.1	Hardness .....	96
4.3.2	Testometric Machine.....	97
4.3.3	Viscometer.....	97
4.3.4	Surface Tension .....	98
4.3.5	Optical Emission Spectrometry (OES) .....	99
4.3.6	Inductively Coupled Plasma Optical Emission Spectrometry.....	100
4.4	Sliding Wear Test Procedure .....	101
4.5	Cavitation Erosion Test Procedure .....	102
4.5.1	Incubation Period of Time.....	102
4.5.2	Prolonged Period of Time .....	103
4.6	Experimental Conditions .....	103
4.6.1	Sliding Wear/Friction.....	104
4.6.2	Cavitation Erosion.....	109
4.7	Testing Samples .....	112
4.7.1	Samples for the TE 57 .....	112
4.7.2	Samples for Cavitation .....	112
4.8	Samples Preparation.....	114
4.8.1	Samples Preparation for the TE 57 test rig.....	114
4.8.2	Samples Preparation for the Cavitation test rig .....	116
5	CHAPTER : FRICTION ANALYSIS AND WEAR MODES.....	117
5.1	Introduction.....	117
5.2	Test Methodology .....	117
5.3	Friction Results Analysis (Running-in time).....	118
5.4	Transfer films.....	121
5.5	Test results (prolonged period of time).....	124
5.5.1	Friction Data .....	124
5.5.2	Wear results analysis.....	130

5.5.3	Roughness Analysis .....	138
5.6	Lubrication analysis .....	141
5.7	Wear Mechanisms.....	144
5.8	Summary and discussion .....	161
5.8.1	Wear/Friction Modes.....	161
5.8.2	Wear Mechanisms.....	161
5.8.3	Friction/Wear Analysis.....	163
5.8.4	Lubrication Analysis .....	166
5.8.5	Surface Analysis .....	166
6	CHAPTER : CAVITATION EROSION FAILURE MECHANISMS .....	170
6.1	Introduction.....	170
6.2	Camera Results Analysis.....	170
6.2.1	Test Methodology .....	170
6.2.2	Results Analysis.....	182
6.3	Incubation Stage-Pits Analysis .....	187
6.3.1	Test Methodology .....	187
6.3.2	Experimental Results.....	188
6.4	Maximum Erosion Stage .....	200
6.4.1	Methodology.....	200
6.4.2	Experimental Results.....	201
6.5	Actual Scroll Steel Plate Erosion Damage .....	215
6.6	Summary and discussion .....	218
6.6.1	Photographic Results.....	218
6.6.2	Experimental Results.....	219
6.6.3	Comparison Results .....	221
7	CHAPTER : CONCLUSIONS & FUTURE WORK.....	223
7.1	Conclusions.....	223
7.2	Future Work.....	226
7.2.1	Sliding Wear .....	226
7.2.2	Cavitation .....	228
References	.....	254

## **List of Figures**

Figure 1: The progression of refrigerants from their advent through four generations	8
Figure 2: Cycle efficiency versus temperature @ 75% turbine isentropic efficiency ..	9
Figure 3: Different ORC A) Wet B) Isentropic C) Dry .....	10
Figure 4: Stribeck's curve determines the coefficient of friction to the product value $\mu V/W$ .....	13
Figure 5: Stribeck's curve for each type of machine .....	17
Figure 6: Schematic explanation of dynamic viscosity .....	17
Figure 7: The adhesion and the deformation mechanism generated during the sliding contact of an elastomer against a metallic surface. A) Initial position B,C) Deformation component D,E) Adhesion component .....	23
Figure 8: The illustration of the normalized distance of a cavitation bubble with radius $R$ and distance $s$ from the boundary wall .....	41
Figure 9: The experimental micro-CHP unit .....	46
Figure 10: Schematic presentation of Genlec micro-CHP unit .....	47
Figure 11: Scroll expander operation process .....	51
Figure 12: Two kinds of leakage, radial and flank, of the scroll expander .....	52
Figure 13: Main parts of the scroll expander used for tribological tests .....	53
Figure 14: Material structure of A) Steel plate B) Coating scroll .....	54
Figure 15: EPMA analysis a) of the scroll's base material b) of the anodic film .....	55
Figure 16: EPMA analysis of isolated fibres within the matrix of the fluoroelastomer tip seal .....	56
Figure 17: Circular wear marks on the high and low pressure regions of the scroll's steel plate .....	57
Figure 18: Different wear regions across the scroll's steel plate after 300 hours of continuous operation: A&B) Low pressure region, average depth of the wear marks 0.5-1 $\mu\text{m}$ . C&D) High pressure region average depth of the wear marks 2-4 $\mu\text{m}$ .....	59
Figure 19: The different wear modes formed by two-body abrasive wear on the 1000 working hours scroll expander A-C) Wedge forming mechanism B-D) Ploughing wear mode .....	59
Figure 20: A) Overview of the river marks formed across the steel plate B) A close up of an individual river mark C) Surface profile of the river marks .....	60

Figure 21: Two different groups A&B with accumulated three-body wear marks found across the high pressure regions of the scroll's steel plate. The wear marks initially detected with the optical microscope, analysed in detail with the SEM and finally their morphology is thoroughly investigated by ZYGO interferometer..... 61

Figure 22: Consecutive wear marks indicate three-body abrasive wear. Wedge-forming lines are also observed in vicinity areas..... 62

Figure 23: The interlayer delamination wear mechanism across the steel plate surface. Crack propagates parallel to the surface..... 62

Figure 24: Cavities across the surface of the steel plate of the SE<sub>300</sub>. A) Cluster of small size cavities B) SEM micrograph of the B1 cavity. B1-B2) Isolated cavities surface profile taken by ZYGO interferometer microscope..... 63

Figure 25: The high pressure area of the scroll expander SE<sub>1000</sub>. Cluster of cavities formed across the edges of the steel plate. Red arrows depict the most severe region damaged by cavitation impact. .... 64

Figure 26: Cluster of cavities across the high pressure region of the scroll expander SE<sub>1000</sub>. Close-up observation of the cavities with the use of the optical microscope and the ZYGO surface interferometer. .... 65

Figure 27: Characteristic detailed SEM micrographs of the cavities profile. Surface analysis of the specific cavities using ZYGO interferometer microscope. .... 66

Figure 28: Chemical composition of a cavity with accumulated oxygen. Chemical composition of a typical cavity. Oxygen traces are absent..... 66

Figure 29: Combination of wear mechanisms on the SE<sub>1000</sub> steel plate. Surface analysis of a random area in the high pressure region a) Three-body abrasive wear b) Cluster of cavities..... 67

Figure 30: Cluster of cavities in a random high pressure area of the SE<sub>1000</sub>. The depth of cavities is highlighted..... 67

Figure 31: The second step of the expansion process where the side walls of the scroll pushed by the working fluid. The critical area “A” is presented. .... 69

Figure 32: Schematic interpretation of the cavitation mechanism in the critical area “A” ..... 69

Figure 33: Schematic representation of the squeeze film between the tip seal and the steel plate ..... 70

Figure 34: The beginning of the expansion process is illustrated. The working fluid opens like a fan, rigorously striking the upper steel plate and simultaneously setting

the scroll into motion. The velocity profile, the vortex rings and the lubricant entrainment process are depicted. .... 73

Figure 35: Analytical simulation of the propagation mechanism of the jet stream of the working fluid as it is introduced through the inlet port of the scroll into the first expansion chamber. The 3D scroll model is representative of the SE<sub>300</sub> and SE<sub>100</sub>. .. 74

Figure 36: Detailed examination of the velocity profile and the vortex rings formed during the expansion process. Pressure distribution contours across the bottom of the scroll expander where cavitation was detected. Negative pressures are generated. ... 75

Figure 37: Geometry, computational mesh and boundary conditions of the first expansion pocket of the: SE<sub>300</sub> A) Initial position B) Final position and SE<sub>1000</sub> C) Initial position D) Final position..... 77

Figure 38: Velocity distribution of the jet stream in the final position of the moving wall for the SE<sub>100</sub>/SE<sub>300</sub> and SE<sub>1000</sub> respectively. Vortex rings and the entrainment mechanism are observed..... 78

Figure 39: Distribution of the static pressure in the initial and the final position of the moving part for SE<sub>100</sub>&SE<sub>300</sub>..... 79

Figure 40: Pressure distribution along bottom boundary for SE<sub>100</sub> and SE<sub>300</sub> (Initial position of the moving wall)..... 80

Figure 41: Pressure distribution along bottom boundary for SE<sub>100</sub> and SE<sub>300</sub> (Final position of moving wall)..... 80

Figure 42: Distribution of the static pressure in the initial and the final position of the moving part for SE<sub>1000</sub>..... 81

Figure 43: Pressure distribution along bottom boundary for SE<sub>1000</sub> (Initial position of the moving wall) ..... 82

Figure 44: Pressure distribution along bottom boundary for SE<sub>1000</sub> (Final position of the moving wall) ..... 82

Figure 45: Wear across the surface of the aluminium scroll A-B) Combination abrasive-adhesive wear C-D) Abrasive wear formed by the orbiting coating scroll.. 84

Figure 46: Adhesive wear on the coating scroll A) Original surface B) Adhesion appears as aluminium particles welded on the coating surface C) The quantity of the aluminium particles is increased D) A major part of the coating scroll is covered by aluminium particles..... 85

Figure 47: ZYGO micrographs show the features of the embedded aluminium particles onto the surface of the coating scroll A) Overview of the area with the

aluminium particles B) Close up investigation of the aluminium particles morphology .....	86
Figure 48: Cavities found across the tip of the aluminium scroll after 1000 hours of operation .....	87
Figure 49: Sliding friction/wear schematic bench test .....	90
Figure 50: An overview of the environmental chamber of the TE 57 micro-friction machine and of the ancillary equipment used for the sliding wear/friction experiments .....	90
Figure 51: Schematic of the cavitation experimental set up.....	91
Figure 52: Olympus BX 60 Optical microscope.....	93
Figure 53: ZYGO surface scanning interferometer .....	94
Figure 54: Scanning electronic microscope (SEM) .....	95
Figure 55: Hardness test machine .....	96
Figure 56: Testometric machine for performing tension and compression mechanical tests.....	97
Figure 57: DV-II+ PRO Digital Viscometer .....	98
Figure 58: The glass lab orifice tubes showing the curvature of the tested liquid. The schematic diagram explains the liquid lift.....	99
Figure 59: The experimental chamber of the optical emission spectrometry (OES). The interface of the OES shows the concentration percentage of the identified elements.....	100
Figure 60: Inductively Coupled Plasma Optical Emission Spectrometry (ICP-OES) for liquid analysis.....	101
Figure 61: The distribution of the sliding velocity according the sinusoidal movement of the TE 57 motor .....	105
Figure 62: Measuring the friction coefficient of the two involute scroll parts with the use of a sliding friction bench.....	106
Figure 63: Calculation of the tip seal surface area with the use of SolidWorks software .....	107
Figure 64: Material structure of A&B) Low carbon steel C) High carbon steel D) Chromium steel.....	113
Figure 65: The implementation of the testing samples used for sliding wear tests ...	115
Figure 66: Variation of friction coefficient with the applied load for different contact regimes .....	119

Figure 67: Variation of friction coefficient with the applied load for different velocity conditions.....	120
Figure 68: Variation of friction coefficient as a function of velocity/load for the high carbon steel/high performance reinforced fluoroelastomer contact under dry and lubricated conditions .....	121
Figure 69: A) Optical photograph of transfer films of the elastomer formed on the surface of the steel plate after 10 min test duration. B) SEM micrograph C) Optical micrograph D) ZYGO interferometer micrograph of the film deposition. (Load 40 N, sliding speed 0.5 m/sec) .....	122
Figure 70: Transfer films of the elastomer material detected on the surface of the steel plate after the completion of lubricated contact experiments. EPMA analysis graph reveals the presence of fluorine and sulphur, indicating the adhesive mechanism of the elastomer within a lubricant environment. Lubricant adhesion mechanism is highlighted. ....	123
Figure 71: Variation of friction force with sliding distance for various temperature regimes (V=0.25 m/sec, P=1.6 MPa, 20 hours).....	125
Figure 72: Variation of friction force with sliding distance for various temperature regimes (V=0.25 m/sec, P=0.8 MPa, 20 hours).....	125
Figure 73: Variation of friction force with sliding distance for various temperature regimes (V=0.5 m/sec, P=1.6 MPa, 20 hours).....	126
Figure 74: Variation of friction force with sliding distance for various temperature regimes (V=0.5 m/sec, P=0.8 MPa, 20 hours).....	126
Figure 75: Variation of friction force with sliding distance for various temperature regimes (V=0.5 m/sec, P=0.8 MPa, 60 hours).....	127
Figure 76: Variation of friction coefficient with sliding distance for various temperature regimes .....	128
Figure 77: Variation of friction coefficient with sliding distance for various temperature regimes .....	128
Figure 78: Variation of friction coefficient with sliding distance for various temperature regimes .....	129
Figure 79: Variation of friction coefficient with sliding distance for various temperature regimes .....	129
Figure 80: Variation of friction coefficient with sliding distance for various temperature regimes .....	129

Figure 81: Evaluation of the removed volume for various temperature regimes after 20 hours of running time. ....	131
Figure 82: Evaluation of the removed volume for various temperature regimes after 60 hours of running time. ....	131
Figure 83: The friction coefficient versus the applied load for different temperature regimes at a constant reciprocating velocity of 25 Hz (0.25 m/sec). ....	133
Figure 84: The specific wear rate versus the applied load for different temperature regimes at a constant reciprocating velocity of 25 Hz (0.25 m/sec). ....	133
Figure 85: The friction coefficient versus the applied load for different temperature regimes at a constant reciprocating velocity of 50 Hz (0.25 m/sec). ....	134
Figure 86: The specific wear rate versus the applied load for different temperature regimes at a constant reciprocating velocity of 25 Hz (0.25 m/sec). ....	134
Figure 87: Variation of the friction coefficient as a function of the PV factor for various temperature and time sliding regimes. ....	135
Figure 88: Variation of the time related depth wear as a function of the PV factor for various temperature and time sliding regimes. ....	135
Figure 89: Change in specific wear rate with friction coefficient.....	136
Figure 90: The wear resistance of the steel plate as a function of the PV factor for different temperature and time sliding regimes. ....	137
Figure 91: Surface profile of the worn regions across the steel and the elastomer surfaces. The experimental conditions were 0.5m/sec, 0.8MPa, 100C, 20hours. ....	139
Figure 92: Variation of the Ra roughness parameter as a function of the friction coefficient for all the 15 cases. ....	140
Figure 93: Variation of the Ra roughness parameter as a function of the specific wear rate for all the 15 cases. ....	140
Figure 94: Optical examination of the after test lubricant samples at 40 °C, 100 °C and 150 °C.....	143
Figure 95: An overview of the wear pattern formed due to sliding wear on the surface of the steel samples: A) Photo image of the steel samples for different applied loads, at 20N and 40N respectively. B) ZYGO interferometer image of the steel plate at 100 <sup>0</sup> C-20N-50Hz-20hours. Overview micrographs, of the reinforced elastomer tip seal sample after the completion of the test at 100 <sup>0</sup> C-20N-50Hz-20hours, taken with C) Optical microscope D) SEM E) ZYGO interferometer.....	145

Figure 96: Fluoroelastomer sample after the end of 20 hours sliding test (40N/0.5msec<sup>-1</sup>/100<sup>0</sup>C). The plastic deformation of the surface, overlapping layers due to thermal/melting effects, the deterioration of the substrate, the worn fibres disorientation, the detached particles, the embedded steel particles, the formation of peaks and lubricated valleys, is shown.....146

Figure 97: A typical pattern of the wear damage formed on the surface of the steel plate sample after the completion of the experimental process with the following conditions: 100<sup>0</sup>C-50Hz-60hours-20N. A) Optical microscope B) ZYGO interferometer.....148

Figure 98: Surface morphology of the wear lines distributed on the steel counterpart surface A) 0.8MPa, 0.5m/sec, 150<sup>0</sup>C, 20hours and B) 0.8MPa, 0.5m/sec, 100<sup>0</sup>C, 20hours .....149

Figure 99: A) Consecutive indentations across the linear wear lines of the steel plate, indicating the three-body abrasion mechanism B) A close up image reveals the indentations by the third-body particle.....150

Figure 100: Fluoroelastomer surface after A) 20h-100<sup>0</sup>C-20N-25Hz, B) 20h-100<sup>0</sup>C-20N-50Hz. Surface morphology for C) 25Hz reciprocating frequency, D) 50Hz reciprocating frequency. SEM micrograph of a E) detached particle, F) elastomer particles found on the steel plate/chemical analysis .....151

Figure 101: SEM micrograph of an after test elastomer surface: a) A pile of broken fibres b) High magnification of a broken fibre .....152

Figure 102: SEM micrograph of an elastomer surface after the completion of sliding test A-C) Broken fibres, fatigue cracks and detached particles are depicted D-E) Wear linear scratches found on the surface of a fibre are illustrated .....153

Figure 103: Optical micrograph of A) accumulated fibres within the elastomer matrix B) detailed representation of the damage surface of the fibres.....154

Figure 104: Optical microscope images of the fatigue crack developed by three-body abrasion particles. Zygo interferometer microscope reveals the size and the depth of this track.....155

Figure 105: High magnification SEM micrograph illustrates the degradation of the inside folds of the crack shows a ploughed crack developed across the surface of the elastomer material. ....155

Figure 106: ZYGO interferometer image shows the morphology of the inside folds of fatigue track. ....156

Figure 107: Fibre analysis on the surface of the fluoroelastomer. a) position of the fibre within the original surface (before test) b) fibre revealed on the surface (after test) c) fibre damaged “oblate shape” d) fibre between a micro-crack and a micro-ploughing wear mark.....	157
Figure 108: Typical steel plate wear damage. Test conditions were adjusted at 150 <sup>0</sup> C-60hours-20N-50Hz. A-B) Precise fine perpendicular cut across the edge of the steel surface by the reciprocating movement of the reinforced elastomer is observed. C-D) The main body of wear is governed by wear linear marks. E) A detailed representation of the steel edge ploughing mechanism is depicted .....	158
Figure 109: A representative wear track with the ridge formation on both sides. Experimental conditions were adjusted at 40 <sup>0</sup> C-60h-20N-50Hz.....	159
Figure 110: Three-body wear abrasion cracks formed at 100 <sup>0</sup> C on the surface of the steel plate a) average depth b) maximum depth.....	160
Figure 111: SEM micrographs of cluster of cracks generated by three-body wear mechanism. Test conditions: A) 20N-60 hours-50Hz-40 <sup>0</sup> C, B) 20N-60 hours-50Hz-100 <sup>0</sup> C .....	160
Figure 112: Classification of the sliding friction process leading to wear of the steel plate. ....	162
Figure 113: Classification of the sliding friction process leading to wear of the elastomer tip seal.....	163
Figure 114: Schematic diagram of the two competitive mechanisms generated during the steel/elastomer contact.....	164
Figure 115: Expansion mode of an acoustic cavitation water bubble at its incubation stage onto the lower surface of the horn. The frame size is 0.5×0.5 mm.....	171
Figure 116: Expansion mode of an acoustic cavitation lubricant bubble on the tip of the horn. The frame size is 1 x 0.5 mm. ....	172
Figure 117: Expansion mode of an acoustic cavitation refrigerant bubble on the tip of the horn. The “jelly” cloud shape is shown. The frame size is 1×0.5 mm. ....	173
Figure 118: The merging and splitting mechanisms of the water and the lubricant bubbles due to pressure variations. The frame size is 0.5×0.5 mm. ....	174
Figure 119: The merging mechanisms- the so called suck like effect- of the refrigerant bubble. The larger bubble absorbs the adjacent bubble. The frame size is 0.5×0.5 mm. ....	175

Figure 120: Behaviour of an acoustic cavitation water bubble in correlation to the normalized distance as it approaches the rigid boundary. The frame size is 0.5×0.5 mm.....	176
Figure 121: Characteristic collapse and rebound of an acoustic cavitation water bubble near the solid boundary. The frame size is 1×0.5 mm. ....	177
Figure 122: Collapse of an acoustic cavitation lubricant bubble near the solid boundary. A lubrication layer is formed. The frame size is 0.5×0.5 mm.....	178
Figure 123: Lubrication layer formed across the surface of the rigid boundary, prior to bubble's implosion. The frame size is 0.5×0.5 mm. ....	179
Figure 124: The extended lubrication layer across the surface of the rigid boundary. The frame size is 1×0.5 mm.....	179
Figure 125: The ceaselessly wobbling movement of an acoustic cavitation refrigerant bubble near the solid boundary. The frame size is 0.5×0.5 mm. ....	180
Figure 126: The different shapes the cavitation refrigerant bubble obtains in its maximum radius. The frame size is 0.5×0.5 mm.....	181
Figure 127: Variation of cavitation bubbles radius as a function of time .....	183
Figure 128: Variation of bubble velocity and the jet velocity versus time .....	183
Figure 129: Variation of the bubble distance approaching the boundary wall.....	183
Figure 130: Average jet velocity of the cavitation bubbles as a function of normalized distance. ....	185
Figure 131: Energy of the cavitation bubbles as a function of normalized distance. ....	185
Figure 132: Characteristic implosion of the lubricant bubble from point A to point B. Jet fluid velocity was calculated to be 150 m/sec. Frame size is 1.025×1.025 mm...	186
Figure 133: Cluster of cavities formation on steel plate surface after 10 minutes of testing. Optical micrographs showing the cavities formation: in lubricant and refrigerant environment. High magnification SEM micrographs showing the cavitation pits formed in these areas. ....	188
Figure 134: SEM and high magnification ZYGO micrographs showing a typical cavitation erosion pit formed in water, lubricant and refrigerant solution. ....	189
Figure 135: SEM micrographs showing the deformation of the tested steel types after 10 minutes of exposure to cavitation in a water solution. ....	190
Figure 136: Optical micrographs showing thermal pits formed on the surface of Chromium steel. ....	191

Figure 137: Optical microscope images showing the accumulation of cavities along the cracks of the High Carbon steel. SEM micrograph shows the morphology of the crack. High magnification ZYGO interferometer image shows the step of the crack. ....	192
Figure 138: Optical and SEM images of cavitation damage arisen on Low Carbon steel surface after 10 min of exposure to cavitation. A-C) Martensitic lathings and intergranular fracture revealed. ZYGO interferometer image shows a typical eroded area surface. D-G) Micro-tunnel and deformation pits are depicted.....	194
Figure 139: Comparison of the average typical and maximum depth of the cavitation pits in a) water b) lubricant c) refrigerant environments.....	196
Figure 140: Comparison of the average typical and maximum volume removed of the cavitation pits in a) water b) lubricant c) refrigerant environments.....	197
Figure 141: Comparison of the average typical and maximum eroded area of the cavitation pits in a) water b) lubricant c) refrigerant environments.....	198
Figure 142: SEM images of eroded areas at different stages: A) 1 h B) 3 h C) 5 h D) 8 h.....	201
Figure 143: A close up series of SEM micrographs showing the damage by cavitation erosion impact at different stages: A) 1 h B) 3 h C) 5 h D) 8 h.....	202
Figure 144: Morphologies of the steel samples after 8 hours exposure to cavitation erosion. ....	203
Figure 145: Cavitation erosion damage: in the low intensity area in between the crater and the outer annulus (A-D) and in the high intensity area in the centre of the ultrasonic source (E-H).....	205
Figure 146: Variation of volume loss with cavitation time for the steel samples overlay in water.....	207
Figure 147: Mean depth of erosion rate as a function of the tested time for the evaluated steels. ....	208
Figure 148: Mean depth of erosion as a function of tested time for the evaluated steels. ....	208
Figure 149: Correlation of cavitation erosion resistance as a function of time a) for five different time stages b) a detailed representation of the last two critical stages of the tests, 5 and 8 hours. ....	209
Figure 150: Evolution of the roughness parameters (Ra and RMS) in cavitation erosion tests.....	210

Figure 151: Correlation between the accumulated strain energy and the crater depth. ....	211
Figure 152: Correlation between the accumulated strain energy and the volume removed. ....	211
Figure 153: Representative section of cavitation damage for all the steel samples. The points where the hardness indentations were made are presented. ....	213
Figure 154: Hardness measurements after 3, 5 and 8 hours of exposure to cavitation. The number of areas is in accordance to figure 153. ....	213
Figure 155: Correlation of the mean erosion rate and the cavitation erosion resistance of the tested steels against the original steel plate of the scroll expander. The testing time was 1 hour for the steel samples overlying in a water liquid and 1000 hours for the actual steel plate of the scroll exposed to its extreme operational environment. ....	216
Figure 156: Schematic representation of the modified TE 57 test rig .....	227
Figure 157: The thermal imaging system FLIR ThermoCAM SC3000 integrated to the TE 57 sliding micro-friction machine. ....	228
Figure 158: Schematic representation of the viscosity test rig. ....	229
Figure 159: A) Mounting press B) Polishing wheels C) Cutting machine D) Ultrasonic bath .....	231
Figure 160: High carbon steel chemical analysis/Raw data .....	232
Figure 161: Chromium steel chemical analysis/Raw data .....	233
Figure 162: Two different regions of cavities A) Typical cavities B) Cavities with accumulated Oxygen. The cluster of cavities with O <sub>2</sub> is distinctive showing a corrosive pattern rather than a cluster of typical cavitation craters and cracks (the yellow lines indicating the analysis area). ....	235
Figure 163: The ISO 4406 standard. Classifies system cleanliness and determines particle counts in lubricants. ....	241

## **List of Tables**

Table 1: Chemical analysis of the scroll's steel plate .....	54
Table 2: Chemical analysis of the two scrolls .....	55
Table 3: Chemical analysis of the tip seal .....	55
Table 4: Description of the sliding experiments performed with the use of the TE 57 micro-friction machine .....	107
Table 5: Sliding wear tests/ Test conditions .....	108
Table 6: Physical Properties of the experimental liquids at $23\pm 2^{\circ}\text{C}$ .....	109
Table 7: Description of the cavitation tests performed with the use of the Cavitation ultrasonic experimental apparatus.....	110
Table 8: Cavitation erosion tests/ Test conditions .....	111
Table 9: Chemical analysis of the steel samples used for cavitation tests .....	112
Table 10: Mechanical properties of the steel samples used for cavitation tests .....	113
Table 11: Oil analysis of the lubricated samples, used for sliding wear tests. ....	142
Table 12: Calculated average micro-jet velocity and impact pressure of the experimental fluids.....	186
Table 13: Average erosion characteristics after the evaluation of 100 individual pits across the surface of the original steel plate. ....	215
Table 14: Measurements of the critical severe damaged area lie next to the inlet port. ....	215
Table 15: Dependence of saturation shear strength and friction of metals on the applied pressure.....	235

## **List of Appendices**

Appendix A: Auxiliary devices for experimental preparation.....	231
Appendix B: Chemical analysis-Characteristic analysis tables of the steel samples.	232
Appendix B: Chemical analysis-Characteristic analysis tables of the steel samples (continued).....	233
Appendix C: High carbon steel plate tensile test.....	234
Appendix D: Tables of $\tau_0$ and $\alpha$ in regards to the applied pressure .....	235
Appendix E: Evidence of corrosion within the cavities of the steel plate of the SE <sub>1000</sub> .....	235
Appendix F: Calculation of the contact load within the scroll expander .....	236
Appendix G: Friction/Wear results (A).....	237
Appendix G: Friction/Wear results (B) .....	238
Appendix G: Friction/Wear results (B continued).....	239
Appendix G: Friction/Wear results (B continued).....	240
Appendix H: Oil Analysis/ISO Cleanliness Codes.....	241
Appendix I: Surface Tension Measurements for various liquids.....	242
Appendix J: Cavitation-Erosion Test results (A).....	243
Appendix J: Cavitation-Erosion Test results (A continued).....	244
Appendix J: Cavitation-Erosion Test results (A continued).....	245
Appendix J: Cavitation-Erosion Test results (B).....	246
Appendix J: Cavitation-Erosion Test results (C).....	247
Appendix J: Cavitation-Erosion Test results (D).....	248
Appendix J: Cavitation-Erosion Test results (D continued).....	249
Appendix J: Cavitation-Erosion Test results (E) .....	250
Appendix J: Cavitation-Erosion Test results (E continued) .....	251
Appendix K: Characteristic measurements of various cavities found across the steel plate of the SE <sub>1000</sub> .....	252
Appendix L: Project Time-Plan .....	253

## **Acknowledgments**

This project constitutes an important part of my life as the last three years were devoted in assiduous research on the field of tribology and materials technology. Thesis wouldn't have been successfully completed within the time-plan without the motivation from inspirited people.

I would first like to express my sincere appreciation to Professor Mark Hadfield who effectively guided me as my mentor and provided a continuous support throughout my research. Every step in the progress of my work reflects his solid support and patient help. I would also like to thank Professor Nikolaos Kotsovinos for his useful suggestions and his valuable comments. Special thanks to Anastasios Georgoulas for his contribution on the evaluation of the CFX analytical results and to my former colleague Michalis Kapsetakis for his assistance in improving the graphic representation of the project drawings.

I would like to thank the Energetix Group Ltd for their co-sponsorship of this project. Sincere thanks to Russell Benstead and to Iain Henshaw for providing honest and informed feedback on real world scroll expander systems performance.

My appreciation also goes to Dr. Zulfiqar Khan and Dr. Nigel Garland for their sincere encouragement and useful advice. Many thanks to Professor Ioannis Berdaxas for providing essential information on the area of thermodynamics.

I also thank the technical staff at Bournemouth University, in particular Brian Wright and Kevin Smith, for their help in the workshop and Mrs Nita Verma at ETC in Brunel University for her assistance with surface analysis images.

Lastly, I offer my regards to my good friend and flatmate Dr. Dimitris Carayannopoulos who contributed time, skill and knowledge to this project. A special thanks also goes to my family who taught me the value of education and continued support me throughout my time in Bournemouth. Finally a heartfelt thanks goes to my partner Angeliki Kouvidi. Her patience and support over the last three years have been invaluable and greatly appreciated.

## Nomenclature

### Greek Letters

$\alpha$ : Pressure viscosity coefficient/Pressure coefficient/Angle of a conical asperity/Partition coefficient ( $\alpha \approx 1$ )  
 $\gamma$ : Heat capacity ratio/Normalized distance  
 $\Delta h$ : Height reduction of the sample/Water lift  
 $\Delta K$ : The range of stress intensity the crack is exposed to during each cycle  
 $\varepsilon$ : Poisson's ratio/Strain at yield point  
 $\varepsilon_s$ : Scroll isentropic effectiveness  
 $\theta$ : Contact angle  
 $\kappa$ : ratio of contact dimensions  
 $\lambda$ : Specific film thickness/Mean sliding distance  
 $\mu$ : Absolute or dynamic viscosity/Friction coefficient  
 $\nu$ : Kinematic viscosity  
 $\rho$ : Density  
 $\sigma$ : Surface tension  
 $\sigma'$ : Combined surface roughness  
 $\sigma^*$ : Standard deviation of asperity heights  
 $\tau$ : Shear stress/Shear yield stress  
 $\tau_0$ : Shear stress dependence of pressure  
 $\Phi_{meas}$ : Filling factor  
 $\varphi$ : Thermal density flow  
 $\phi_T$ : Thermal flow  
 $\psi$ : Plasticity index

### English Letters

A: Surface area/Real contact area/Eroded area  
C: Ultrasonic velocity  
d: Orifice diameter

$da/dN$ : The increase in crack with length  $a$  per cycle  $N$   
 $dh/dt$ : Squeezing term  
 $du/dy$ : Velocity gradient  
E: Elastic modulus  
 $E_d$ : Energy dissipated per asperity site  
F: Friction force  
 $F_{adh}$ : Adhesive force  
 $F_d$ : Drag force  
 $F_{def}$ : Deformation-Hysteresis force  
 $F_{pl}$ : Ploughing force  
G: Dimensionless material parameter  
g: Gravitational force  
H: Material hardness  
h: Film thickness/ Enthalpy of the working fluid  
 $h_{min}$ : Minimum film thickness  
k: Non-dimensional coefficient of  
 $k^*$ : Basic wear factor  
L: Contact width/Length area  
M: Number of asperities  
 $\dot{M}_{meas}$ : Measured mass flow rate  
 $\dot{m}$ : Working fluid mass flow rate  
 $N_{rot}$ : Rotational speed  
 $\eta_{cycle}$ : Efficiency of the ORC  
 $\eta_p$ : Isentropic efficiency of the pump  
P: Hydrostatic pressure/ Normal pressure  
p: Asperity pressure  
 $P_i$ : Impact pressure  
 $P_L$ : Pressure of the liquid outside the bubble wall  
 $P_s$ : Static pressure  
 $P_v$ : Vapour pressure

$P_0$ : Pressure on the bubble wall  
 $P_\infty$ : Liquid ambient pressure of the liquid far from the bubble  
 $Q_c$ : Condenser heat transfer rate  
 $Q_e$ : Evaporator heat transfer rate  
 $q$ : Flow rates  
 $R$ : Bubble radius/ Asperity radius  
 $R_q$ : Route mean square (RMS)  
 $R_x$ : Combined radius of contact solids  
 $R_0$ : Initial bubble radius  
 $r$ : Radius of eccentricity  
 $S$ : Sliding distance  
 $T$ : Temperature/ Torque  
 $T_c$ : Collapse time  
 $t$ : Test time  
 $U$ : Dimensionless speed parameter/Liquid sliding velocities  
 $U_c$ : Crack growth velocity  
 $U_{jet}$ : Jet velocity  
 $u$ : Sliding velocity/Average surface speed of the contact  
 $u_{su}$ : Supply specific volume  
 $V$ : Volume loss  
 $\dot{V}_s$ : Isentropic volume flow rate  
 $W$ : Applied load/Dimensionless load parameter  
 $W_{loss}$ : Frictional losses  
 $W_p$ : Power of the pump  
 $W_R$ : Wear resistance  
 $W_s$ : Specific wear rate  
 $W_{scroll}$ : Scroll expander power  
 $W_{sh}$ : Expander shaft power  
 $w$ : Total load between the mating surfaces  
 $w_h, w_0$ : Velocity of the moving column  
 $x$ : Stroke  
 $z$ : Average value of the asperities height

wear/Thermal diffusion factor

### **Empirical constants**

A, n, K,  $\pi$

### **Abbreviations**

CFC: Chlorofluorocarbon  
 CFD: Computational Fluid Dynamics  
 CHP: Combined Heat and Power  
 EHL: Elastohydrodynamic Lubrication  
 EPMA: Electron Probe Micro Analyzer  
 GWP: Global Warming Potential  
 HCFC: Hydro chlorofluorocarbon  
 HFC: Hydrofluorocarbon  
 HL: Hydrodynamic Lubrication  
 HP: High Pressure  
 ICP: Inductively Coupled Plasma  
 LP: Low Pressure  
 MDE: Mean Depth of Erosion  
 MDER: Mean Depth Erosion Rate  
 ODS: Ozone Depletion Substances  
 OES: Optical Emission Spectrometry  
 ORC: Organic Rankine Cycle  
 PEEK: Polyether ether ketone  
 PTFE: Polytetrafluoroethylene  
 RANS: Reynolds Average Navier Stokes  
 REC: Cavitation Erosion Resistance  
 SEM: Scanning Electronic Microscopy  
 SE<sub>100</sub>: Scroll expander 100 hours operational time  
 SE<sub>300</sub>: Scroll expander 300 hours operational time  
 SE<sub>1000</sub>: Scroll Expander 1000 hours operational time  
 TAN: Total Acidity Number

# 1 CHAPTER : INTRODUCTION

## 1.1 Background to Research

Micro-generation is the generation of electrical and thermal energy by small domestic appliances with very low or even zero carbon emissions. The micro-generation technology can deliver the most cost-effective energy savings and carbon savings. Micro-generation encompasses everything from Combined Heat and Power (CHP) units, to biomass stoves, roof mounted wind turbines and small solar panels which allow consumers to generate their own heat and electricity. The effective coverage of the domestic sector energy needs, the working efficiency, the energy savings and the potential prospects of these kinds of systems can be found in the recent work of Tzanakis [1]. Furthermore, the extensive use of micro-generation systems in an urban environment in combination with the world's first climate legislation (2009) by the UK government to reduce its emissions by 80 per cent by 2050 could constitute the framework for the successor to Kyoto which ends in 2012.

Combined Heat and Power (CHP) is an efficient way to generate electricity and heat simultaneously. CHP systems are a form of distributed generation that use internal or external combustion engines to generate electricity while recovering heat for other uses. The benefit of these technologies is their ability to utilize sustainable fuels which makes them environmentally friendly [2-4].

There are 5 main types of CHP technologies: reciprocating engines, micro-turbines, Stirling engines, fuel cells and the Organic Rankine Cycle (ORC). These efficient systems recover heat that normally would be wasted in an electricity generator, and save the fuel that would otherwise be used to produce heat or steam in a separate unit. The significant benefit of these systems is that the overall efficiency can be as much as 85-90%. Around 10-15% is converted into electricity while the rest is converted into thermal, except 5-10% which is released into the atmosphere by exhausts. By contrast, conventional generation of electric power throws away much of the heat generated in production, and conventional thermal energy generation often misses an easy opportunity to generate power. Thus CHP technology can be considered as the most efficient way to produce energy [2], [4-5].

For this research a specific type of CHP technology is used. The innovative micro-CHP system which was assessed in this project is called Genlec. This is a small domestic CHP unit which is assembled and distributed from the Energetix Micropower Group Ltd. The innovation is that the micro-CHP system's scroll actually functions as an expander, instead of

the classic compressor unit, producing electricity with simultaneous production of heat and hot water. In addition, the operation of the whole system is based on the Organic Rankine Cycle. In such a system the working fluid is an organic component, better adapted than water to lower heat source temperatures. It is friendly to the environment and thus contributes to the combat against the climate changes.

Since the scroll expander used in an ORC system was patented in 2003, by Energetix Micropower Limited, not a lot of work has been done regarding the design and the durability of the main components of the scroll during the last few years. Only a small number of papers have dealt with the operation of the scroll expander in an ORC system. The papers have mainly focused on the performance and the efficiency of the scroll expander rather than looking at the tribological aspects of the scroll's critical components during its operational period.

More specifically, Tzanakis et al [6] in a recent publication has thoroughly investigated the surface wear damage of a scroll expander system. Eventually the tribological wear mechanisms were revealed and the critical components for durability were identified. Furthermore, Kim et al [7] in a recent study showed that in a two-stage compression CO<sub>2</sub> trans-critical cycle by the application of a combined scroll expander-compressor unit, the efficiency of the scroll expander cannot be seriously affected by the pressure changes. The efficiency of the unit was calculated to be at 54.4%, with a radial and flank clearance around 8 µm. In addition he suggested that the efficiency of the expander could be increased by reducing the expansion chamber area. This can be achieved with the increase of the wrap height of the scroll. This outcome is in direct correlation with the nature of the project since scrolls with different heights were used and interesting tribological observations were drawn.

Moreover, Lemort et al [8] studied the performance of a scroll expander in an ORC. He tried to alter the design of the scroll expander in order to achieve better performances. The scroll achieved a maximum isentropic effectiveness of 68%. However the pressure drop in the suction area was the main drawback in the scroll's performance associated with two phenomena. Firstly, the suction port was blocked by the tip of the orbiting scroll. The effective suction port area was further reduced leading to attenuation of the overall pressure. Secondly, the tip seal was not extended to the end of the scrolls. Hence the fluid's velocity between the central and the adjacent chambers increased. Consequently, the supply pressure dropped. The drop in pressure caused by the abovementioned phenomena is in correlation with the outcomes of this study since it can enhance the generation of cavitation producing excessive wear damage in the suction area of the scroll expander.

Additionally, Quoilin et al [9] proposed a simulation model of an ORC system in order to optimize the operating conditions and the components of the cycle. A combination of the mass flow rate (at 0.9 kg/sec) and the rotational speed (at 2300 rev/min) optimizes the overall performance of the scroll expander. Initially, the maximum expander isentropic effectiveness was 68% corresponding to a maximum cycle efficiency of 7.4%. He managed to increase the efficiency to 9.9% by changing the working conditions (mass flow rate and rotational speed) of the system. The study was carried out with HCFC-123 refrigerant as a working fluid. In a similar study Kane et al reached a net efficiency of 12% [10]. Finally, Yanagisawa et al [11] carried out an experimental study on an oil-free air expander achieving a volumetric and isentropic effectiveness of 76% and 60% respectively. Aoun and Clodic [12] investigated the same expander operating with steam, improving its volumetric efficiency using a high performance fluoroelastomer tip seal (like in the actual scroll of this study). They managed to achieve a volumetric and isentropic effectiveness of 63% and 48% respectively.

Apart from these studies the majority of the researchers mainly focused on the operation of a scroll as a compressor [13-17]. Some of the outcomes of these studies, from a tribological point of view, can be applied in the operation of a scroll expander. The wear and friction mechanisms between the critical components of the scroll are similar for both systems. However, the determinant is that in the high pressure region of the expander, at the suction port, cavitation phenomena can be generated while the drop of pressure can seriously affect the performance of the scroll.

The aforementioned operational problems are caused by the reverse operation of the scroll compressor as an expander. However, this reverse motion has one particular advantage. If the scroll is rotated in the opposite direction by high pressure gas, the energy from the expansion process (high pressure to low pressure) is converted into electrical energy by turning a generator. Furthermore ORC is used, having a very low environmental impact in relation to the main parameters of the environmental policy, the ozone depletion potential (ODP) and the global warming potential (GWP).

## **1.2 Aims of the Project**

This research aims to investigate in depth, the implications of the main tribological mechanisms within the performance and the durability of a scroll expander system during its operational period. The critical components for durability were identified on the tip seal and on the steel plate of the scroll expander. The outcomes from this research could possibly improve the sustainable design of the scroll expander systems.

The tribological friction and wear mechanisms of the reinforced tip seal made of high performance fluoroelastomer against the steel plate made of high carbon steel under a specific lubrication regime, were examined. This included testing under dry and lubricated conditions using a novel micro-friction test rig. Furthermore an oil analysis of the testing lubricant was performed to investigate particle contamination and to evaluate the lubricant performance under various temperature regimes.

In addition, the cavitation mechanisms in the suction region of the scroll were revealed and assessed from a tribological point of view. This involved ultrasonic cavitation tests within refrigerant/lubricant fluids, hardness tests on the surface of the testing materials and photographic observations of the imposing mechanism of the cavitation bubbles near to a solid boundary (steel plate) with the use of a high speed camera.

### **1.3 Objectives of the Project**

The main objectives of this study are presented below:

- To identify the wear mechanisms of the main interacting parts of the scroll expander during its operation.
- To understand the tribological friction and wear mechanisms, of the high carbon steel plate against the high performance fluoroelastomer tip seal, in both dry and lubricated environment, under specific temperature, velocity and load conditions using the TE 57 micro-friction machine.
- To determine the friction force, the friction coefficient, the wear rate, the time related depth wear rate and the roughness of the steel plate over the tip seal under a specific lubrication regime.
- To evaluate the performance of the specific synthetic lubricant used in the experiments and to identify its chemical composition after completion of the tests.
- To design an appropriate experimental cavitation test rig capable of operating against a high speed camera and measure the size, the velocity and the pressure impact of lubricant, refrigerant and water bubbles during their implosion process.
- To measure the cavitation erosion rate, the volume loss, the strain energy and the hardness of different steel grades in order to compare their performances with the actual steel plate of the scroll expander.

## **1.4 Beneficiaries**

The project reveals the main damaging mechanisms of the scroll expander during its operation in a small combined heat and power system.

The specific study is focused on the durability of the main components of the scroll system over an extended period of time. The main operating target of the scroll expander is to reach the maximum service time limit. This is set by the Energetix Group Ltd to be 30,000 hours of continuous operation without changing or replacing the main parts of the micro-CHP system. The durability improvement of these systems can significantly reduce indirectly the level of greenhouse gases in the atmosphere, since the system's lifecycle will be increased and the amount of the after-system-usage wastes will be drastically reduced. Considering the fact that the scroll expander and compressor CHP systems, including the air conditioning scroll compressor and expander systems, have a mass-market appeal nowadays, their lifecycle extension is thought to be more essential than ever.

Additionally, the critical components of the studied scroll were subjected to friction, wear and cavitation tests while a comparison of their tribological behaviour with similar materials of a similar or a lower market cost was conducted. The project will enhance the product design of the scroll expander, investigating the durability and the performance of the micro-CHP system, providing beneficial outcomes and financial and future environmental prospects, to Energetix Group Ltd.

## **1.5 Contribution to knowledge**

The contribution of this project to knowledge is summarised within the following paragraphs.

The wear mechanisms which are seriously affecting the durability and the service life of the scroll expander were successfully interpreted. Two-body and three-body wear mechanisms were revealed, while cavitation is seen to play an important role by simultaneously increasing the wear rate and reducing the efficiency of the scroll.

Characteristically, in the suction area, where the expansion of the working fluid takes place, many clusters of cavitation pits were found and a hypothesis was made correlating the pits with the design and the operational environment of the scroll. The major source of cavity generation within the scroll was successfully revealed. Consequently, the cavitation erosion

mechanisms were determined. This was the first time research had focused on the generation and the interpretation of the cavitation phenomena in that specific area of a scroll expander.

Experiments close to the real operation conditions of the scroll have been carried out, revealing the excellent performance of reinforced fluoroelastomer against high carbon steel over a prolonged period of time. The pressure velocity graphs showed that the increment of the velocity or the reduction of the applied load can significantly increase the friction coefficient and the specific wear rate of the rubbing materials. Furthermore, with the increment of the applied load, the friction coefficient is proportionally reduced. Apparently, the sliding speed influence is much higher than that of the applied pressure.

In terms of cavitation, several tests were performed using the actual working fluids of the scroll expander. A remarkable performance of the refrigerant bubbles was observed during the cavitation process. The impact mechanism of the refrigerant bubble was considered to be very low. On the other hand lubrication bubbles were measured to have the highest impact mechanisms among the tested fluids. However a lubrication film thickness which was observed across the boundary wall can significantly reduce the actual damage by the lubricant bubbles' implosion.

Finally, the typical chromium steel, among various tested steel samples, was found to have the best performance against cavitation impact over different time steps. Even during the incubation period of the pits, chromium steel exhibited better performance compared to the other materials. Its excellent performance was also revealed when the actual working fluids of the scroll were used.

## **1.6 Outline of the Project**

This thesis is organised into seven chapters as follows:

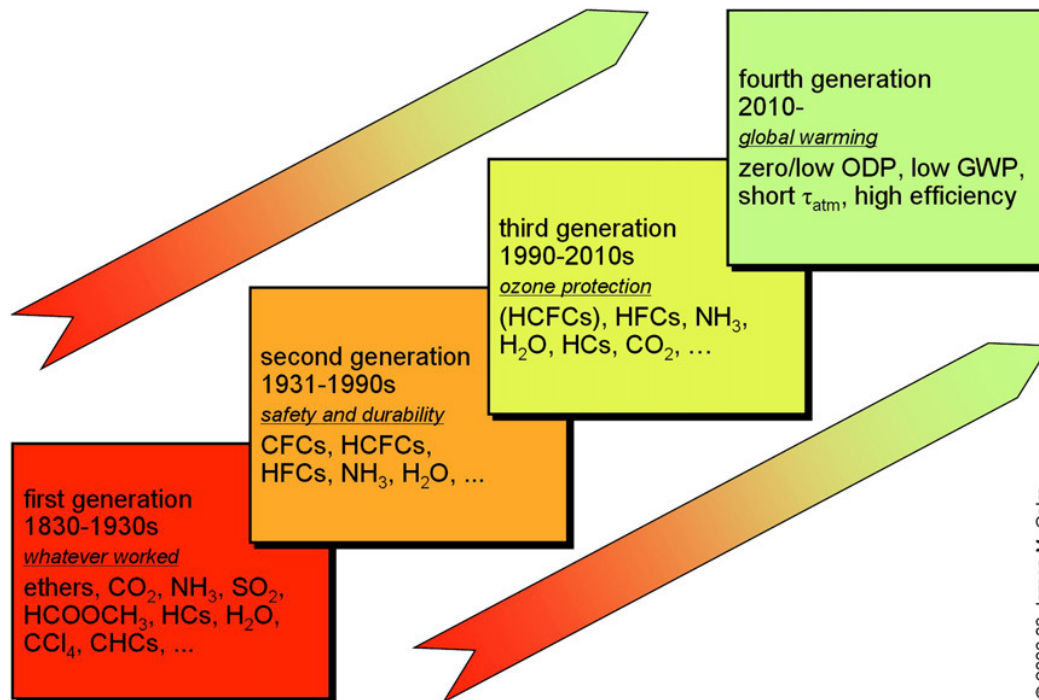
- Chapter 1 presents the general background of the research and the significance of the project. The contribution to knowledge is also briefly described.
- Chapter 2 is concerned with the literature review, emphasising similar work carried out by other researchers. Their outcomes were successfully associated with the ones of this project.

- Chapter 3 is devoted to the thorough surface investigation of the wear mechanisms of the scroll, after the end of its service period, as a main part of an experimental small domestic CHP system. The wear mechanisms were successfully interpreted while cavitation clusters were found in the suction port area. A simple finite element analysis (FEA) was conducted in order to indentify the primary cause which generates the cavitation phenomenon.
- Chapter 4 elaborates on the design of both test rigs including the analytical methodology and the samples preparation. Additionally, it describes the experimental equipment used in this study e.g the Optical Emission Spectrometry (OES), the Oil Analysis Spectrometer (OAS), the High Speed Camera, the Surface Analysis Microscopes (SEM, ZYGO, Optical) etc.
- Chapter 5 evaluates the experimental results of the wear and friction tests. The friction force, the friction coefficient, the wear volume rate and the wear volume loss were presented in correlation to other testing attributes like time, applied load and sliding velocity. Extensive discussion supports this chapter.
- Chapter 6 determines the erosion resistance of various steel types against cavitation erosion damage over a prolonged period of time. The volume loss, the roughness and the hardness were some of the parameters evaluated. In addition, cavitation pits were analysed during their incubation stage and compared in different fluid environments. Extensive discussion supports this chapter.
- Chapter 7 concludes the researcher's work and identifies new routes for further development and experimentation.

## 2 CHAPTER : LITERATURE REVIEW

### 2.1 Refrigerants

The use of refrigerants goes back to ancient times using stored ice, vapourization of water and other evaporative processes [18]. During the last two centuries extensive research was conducted on refrigerants and four distinctive generation eras can be defined, see figure 1. The first generation era made use of familiar solvents and other volatile fluids including whatever worked and was available. This method lasted for about a century. The second generation era was between 1931 to 1990 which was distinguished by a shift to fluorochemicals for safety and durability. Thomas Migley [19-20] with his extensive work was the forerunner for the commercial production of Chlorofluorocarbon (CFCs) and Hydrochlorofluorocarbon (HCFCs) refrigerants like R12 and R22.

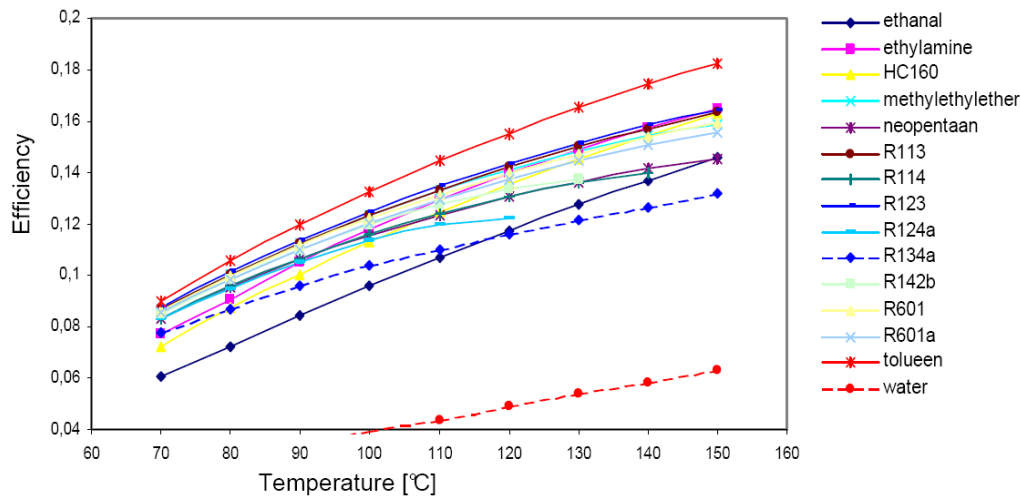


Source: page 1124, [21]

Figure 1: The progression of refrigerants from their advent through four generations

The third generation era started in the early 1990's and continues to the present day. Manufacturers commercialized the first alternative refrigerants in late 1989 and within 10 years the new generation of refrigerants, the Hydrofluorocarbon (HFCs), were introduced. HFCs eliminated the Ozone Depletion Substances (ODS) since they do not contain chlorine atoms. In addition HFCs comply with the provisions of the international regulations (i.e. The

Vienna Convention and the Montreal Protocol concerning ozone-depleting substances) and national laws and regulations on replacements for most ozone depleting refrigerants. Finally the fourth generation era of refrigerants starts from 2010 and focuses on the global warming potential (GWP). This era is driven by the scientific findings, regulatory requirements and market pressures of the last decades. The governing selection criteria for the new generation refrigerants must offer high efficiency to address low GWP [21-22].



Source: page 12, [23]

Figure 2: Cycle efficiency versus temperature @ 75% turbine isentropic efficiency

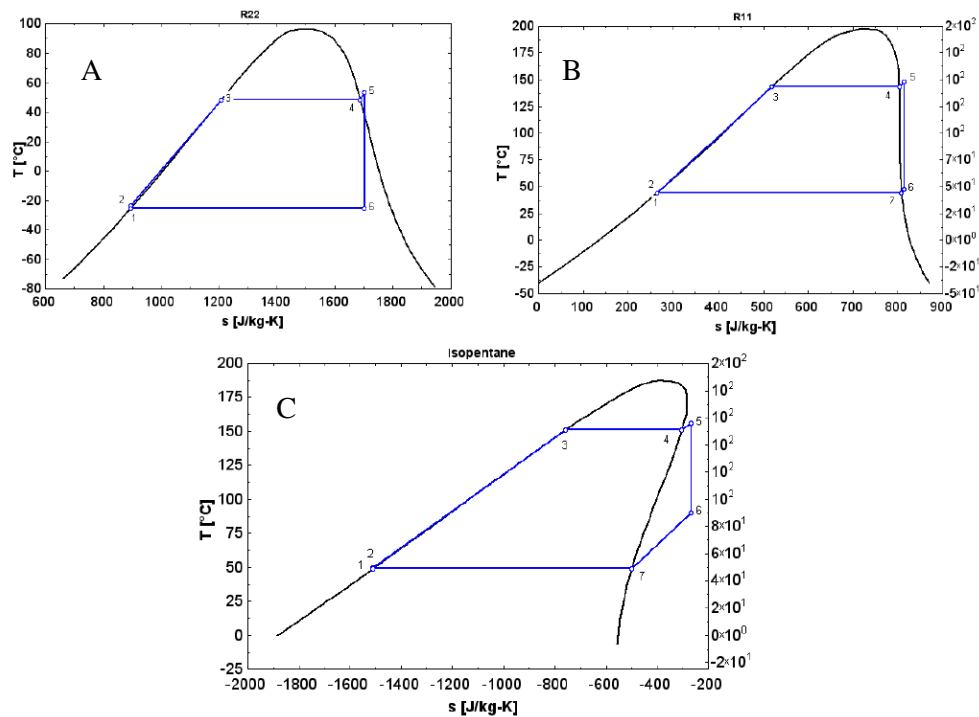
A refrigerant can be considered as an efficient organic working fluid like the one that is used for this project if it has a lower boiling temperature point and also if it is compatible with standard air conditioning and refrigeration equipment. Moreover organic fluids have more advantages than water and their energy efficiencies are superior (figure 2) in comparison to that of water. Nowadays, the majority of the scrolls are using organic working fluids for their operation. The reason is that the organic fluids operate at temperatures and pressures suitable for typical refrigeration equipment. They condense at central heating temperatures greater than atmospheric pressure while they are non-corrosive and compatible with suitable lubricants [24]. Thus the optimum selection of an environmentally-friendly and energy-efficient refrigerant can significantly enhance the performance and the lifecycle of many domestic appliances like the micro-CHP systems.

### 2.1.1 Organic Rankine Cycle (ORC)

The ORC is similar to the cycle of a conventional steam turbine, except for the fluid that drives the turbine, which is a high molecular mass organic fluid. The process should have a high thermal efficiency and allow a high utilization of the available heat resources. The

selected working fluids allow efficient low temperature heat sources to produce electricity in a wide range of power outputs (up to 3 MW electric power per unit) [25-27].

Moreover there are 3 basic types of an organic rankine cycle distinguished by the type of fluid which is employed (figure 3). The saturation curve in a T-s diagram can be a positive, negative or vertical slope. A dry fluid has a positive slope like an iso-pentane thermodynamic cycle, a wet fluid has a negative slope like R22, while an isentropic fluid has infinitely large slopes like R11 refrigerant. Dry and isentropic fluids show better thermal efficiencies because they do not condense after the fluid goes through the turbine as opposed to wet fluids that produce condensates within the turbine. The saturated fluid inside the scroll is not optimal because the condensate imposes a threat of damage to the expander by cavitation impact [26], [28-29].



Source: page 14 [29]

Figure 3: Different ORC A) Wet B) Isentropic C) Dry

In this project a high molecular organic working fluid was used as a refrigerant with a dry slope during the operation of the scroll expander due to its absolute compatibility with the ORC. Its large molecular mass and its high energy efficiency, enhance the performance of the micro-CHP unit.

### **2.1.2 Refrigeration Lubricants**

Refrigeration lubricants are very different from other industrial lubricants in terms of their required properties because they are usually used in scroll compressors or expanders for a very long time of period without any replacement or refilling [30].

Specifically, a refrigeration lubricant must perform several functions for effective and reliable operation of the refrigeration system. The lubricant must act effectively to protect the metal surfaces of the scroll expander with a suitable lubrication film thickness, preventing any excessive wear. The lubricant, apart from lubricating the mechanical system, cools the expander mechanism preventing any excessive heat generation, seals the expander's components and dampens the noise. In addition, an appropriate miscibility and mutual solubility with the refrigerant gas must be ensured, preventing oil starvation and potential breakdown in the scroll expander [31-32].

In a refrigeration cycle, some lubricant escapes from the expander discharge area and finds its way into the refrigeration cycle even with the efficient oil separator installed. If this oil is miscible with the refrigerant over the various temperatures and pressures in the refrigeration cycle it will return to the expander. Poor miscibility can result in a phase separation during the cycle which in turn can cause serious problems such as accumulation of oil on the inside of the heat exchanger tubes, reducing the heat transfer, the thermal conductivity and the overall performance of the CHP system [33].

On the topic of professional writing and referencing Sunami M (1999, p 991) states: 'The advantage of good solubility is that the refrigerant reduces the viscosity and surface tension of the oil in the heat exchangers and pipelines. The disadvantage is that the refrigerant reduces the viscosity of the oil in the compressor. Ideally the refrigerant should be less soluble with the oil at high temperature and more soluble at low temperature. In addition, the oil must exhibit good thermal and chemical stability over the range of conditions experienced in the application'.

## **2.2 Lubrication**

A lubricant is any substance that reduces friction, providing a smooth running and a satisfactory service life for the critical components of a lubricated system. Lubricating oils are mixtures usually derived from petroleum and additives. When the lubricant is required to provide quality lubrication these additives improve its performance. Parameters to be considered include: its viscosity under temperature, its density, its acidity level, its miscibility

with refrigerants, its vapour pressure and its lubrication performance altered by the contaminated particles. Some of these lubrication parameters, regarding the tested oil used in this study, will be analysed in a later paragraph (5.6) [34-37].

The lubrication regimes have been divided into the four following categories:

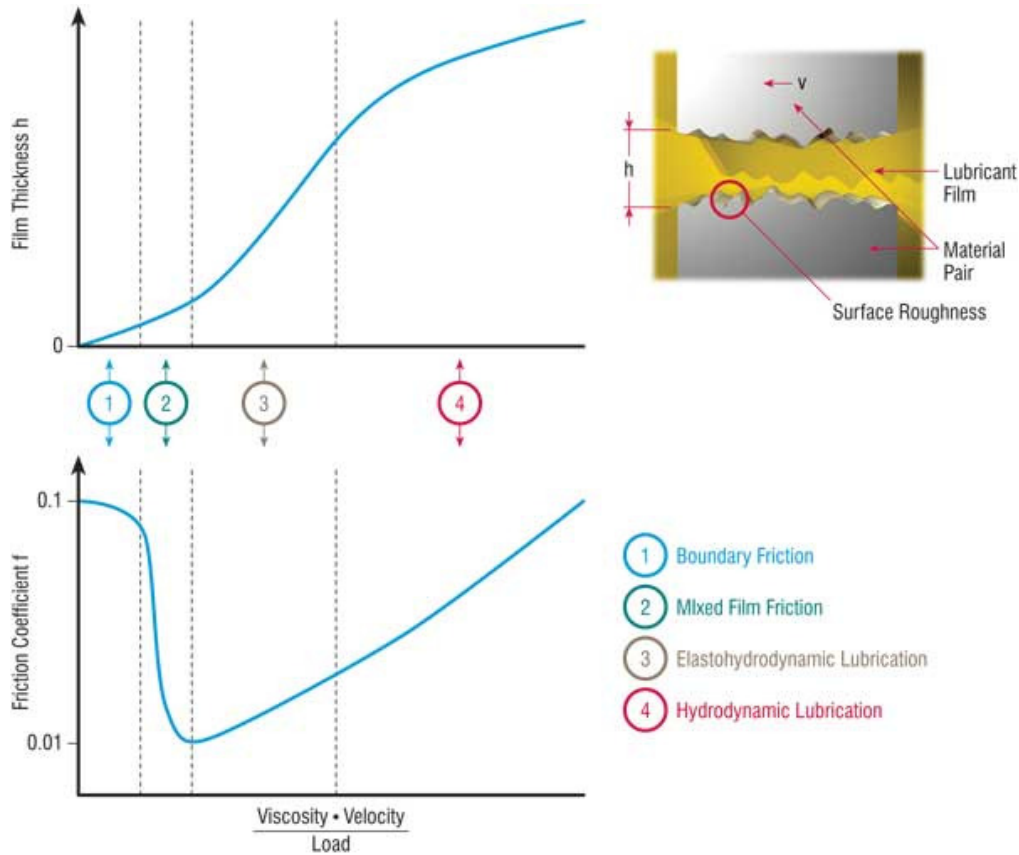
1. Hydrodynamic lubrication (HL): Hydrodynamic lubrication is characterised by conformal surfaces. When the elastic deformation of the solid bodies is similar in extent to the thickness of the lubricant film, HL occurs. The lubricating film is thick enough to prevent the opposing solids from coming into contact. Friction arises only from the shearing of the viscous lubricant. The pressures are low usually less than 5 MPa so the pressure-viscosity effects are small.
2. Elastohydrodynamic lubrication (EHL): Elastohydrodynamic lubrication can be defined as the study of lubricating films between elastically deformable solids and is usually characterised by non conformal surfaces. EHL occurs as pressure or load increases to a level where the viscosity of the lubricant provides higher shear strength than the surfaces can support. If the contact pressure exceeds the elastic limit of the surfaces, plastic deformation and increasing friction occurs. The EHL regime can be distinguished as having two different modes, the hard and the soft mode.

Hard EHL is characterised by metallic surfaces. Asperity contact occurs according to the prevailing loads. The pressures are quite high between 0.5 and 3 GPa. Under these pressures the viscosity of the lubricant is greatly increased and it will behave much more like a solid than a liquid within the contact zone.

Soft EHL is characterised by surfaces made of elastomeric materials, like fluoroelastomer, with large elastic distortions even for light loads. Moreover the viscosity within the conjunction varies little with pressure because the pressures are relatively low and the elastic effect predominates.

3. Boundary lubrication: Boundary lubrication is characterised by asperity contact. The fluid film effects are negligible and the contact lubrication mechanism is governed by the chemical and physical properties of thin surface films of molecular proportions. The surface films vary in thickness from 1 to 10 nm, depending on the molecular size. The frictional characteristics are determined by the properties of the solids and the lubricant film at the common interfaces.

4. Mixed lubrication: Mixed or partial lubrication is governed by a mixture of boundary and fluid film effects. Interaction takes place with one or more molecular layers of boundary-lubricated films. A partial fluid film lubrication action develops in the bulk of the space between solids. The film thickness is less than 1000 nm and greater than 10 nm.



Source: Magazine of machinery lubrication [38]

Figure 4: Stribeck's curve determines the coefficient of friction to the product value  $\mu V/W$

The aforementioned lubrication regimes can be distinguished by Stribeck's curve as figure 4 illustrates. Stribeck's curve has been widely used in the field of design and lubrication explaining various types of lubricant behaviour. Stribeck's curve illustrates the behaviour of friction coefficient as a function of the Sommerfeld number  $S = nV/W$ , where  $n$  is the dynamic viscosity of the lubricant,  $V$  is the relative velocity of the opposing surfaces and  $W$  is the applied load.

The first lubrication phase is the boundary lubrication where the film thickness is lower than the average roughness height of the rubbing surfaces. The second phase involves the mixed lubrication regime where a discontinuous film thickness is formed. When the lubrication film

thickness completely separates the surfaces the minimum friction coefficient value is observed. Beyond that minimum point in the curve, the friction coefficient starts rising again due to viscous friction within the lubricant and the elastohydrodynamic lubrication regime is observed. From then on the tribological parameters of the lubricant determine the tribological behaviour of the system and the hydrodynamic lubrication domain prevails.

### 2.2.1 Film Thickness

A very important parameter to evaluate the EHL regime between two contiguous surfaces which distort elastically under the hydrodynamic pressure is the minimum film thickness ( $h_{\min}$ ). Several useful empirical expressions have been presented over the years. Dowson and Higginson [39] were derived with an expression (equation 1) for line contacts for two rolling elements which can also be applied to the asperity contact of two sliding parallel blocks.

$$\frac{h_{\min}}{R_x} = 2.65 \frac{G^{0.54} U^{0.7}}{W^{0.13}} \quad (1)$$

However, the most famous equation for general elliptical contacts is the Hamrock and Dowson equation 2 which derived a few years later and is presented as follows [40]:

$$\frac{h_{\min}}{R_x} = 3.63 \frac{U^{0.68} G^{0.49}}{W^{0.073}} (1 - e^{-0.68\kappa}) \quad (2)$$

Where the symbols are defined as follows:

$\frac{h_{\min}}{R_x}$  is the dimensionless minimum oil film thickness

$G = \alpha E$  is the dimensionless material parameter

$U = \frac{\mu_0(u_1 - u_2)}{2ER}$  is the dimensionless speed parameter

$W = \frac{w}{ERL}$  is the dimensionless load parameter

Where  $h_{\min}$  is the minimum lubricant film thickness in mm,  $\alpha$  is the pressure viscosity coefficient in  $\text{GPa}^{-1}$ ,  $R_x$  is the combined or reduced radius of contact solids in mm,  $E$  is the reduced elastic modules in GPa,  $\mu_0$  is the lubricant viscosity at atmospheric pressure in Pa.s,  $u$  is the average surface speed of the contacting solids in mm/s,  $w$  is the total load between the

mating surfaces in N, L is the contact width in mm and  $\kappa$  is the ration of contact dimensions perpendicular to and parallel to the direction of motion [41].

The reduced elastic modulus is defined by the following equation 3:

$$\frac{1}{E} = \frac{1}{2} \left( \frac{1 - \varepsilon_1^2}{E_1} + \frac{1 - \varepsilon_2^2}{E_2} \right) \quad (3)$$

Where  $E_1$  and  $E_2$  are the elastic modulus of the two contacting solids respectively in MPa and  $\varepsilon_1$  and  $\varepsilon_2$  are the Poisson's ratio of the contacting solids.

The reduced radius  $R$  of the contacting solids is defined as (equation 4):

$$\frac{1}{R} = \frac{1}{R_1} + \frac{1}{R_2} \quad (4)$$

Where  $R_1$  and  $R_2$  are the radii of the contacting solids respectively.

In addition one parameter for portraying various lubrication regimes is called the specific film thickness or lamda ratio  $\lambda$ . The lamda ratio shows to which extent the asperity interactions will be in lubricated sliding. For  $\lambda > 3$  a full fluid film separates the two surfaces, the asperities of the surfaces do come into contact and the friction and wear are very low. If  $\lambda < 1$  then serious damage such as scuffing on the surface of the material occurs. This is applied in extremely high loads or low sliding speeds. Finally if  $\lambda$  is between 1 and 3,  $1 < \lambda < 3$ , contact between asperities occurs. The value of  $\lambda$  is determined by the minimum lubricant film thickness and the surface roughness of the material and it can be expressed by equation 5.

$$\lambda = \frac{h_{\min}}{\sigma'} \quad (5)$$

Where  $\sigma'$  which is the roughness of the two surfaces is defined by equation 6.

$$\sigma'^2 = R_{q1}^2 + R_{q2}^2 \quad (6)$$

Where  $R_{q1}$  and  $R_{q2}$  are the route mean square (RMS) roughness parameters for each surface respectively in  $\mu\text{m}$  [42].

The RMS is the average of the measured height distributions taken within the evaluation length or area and measured from the mean linear surface. The RMS is defined as follows (equation 7):

$$R_q = \sqrt{\frac{1}{L} \int_0^L z^2(x) dx} \quad (7)$$

In addition, Ra is the average roughness of all points from a plane fit to the test part surface for a given profile of length L. The Ra is the most common roughness parameter which is used to determine the morphology of a material's surface and is defined by equation 8:

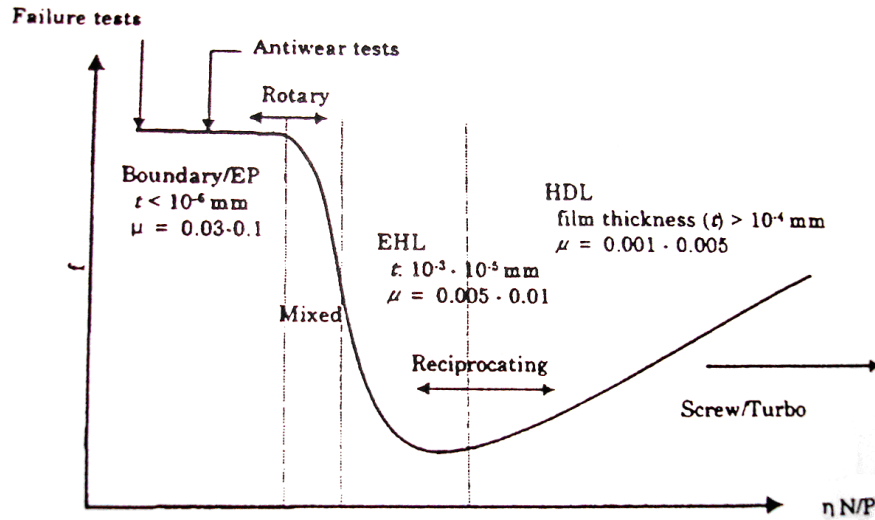
$$R_a = \frac{1}{L} \int_0^L |z(x)| dx \quad (8)$$

where L is the length area of the sample surface in  $\mu\text{m}$  and z is the is the average value of the asperities height in  $\mu\text{m}$ .

### 2.2.2 Lubrication of compressors

Refrigeration oils are lubricants for the compressors and their main purpose is lubrication. According to Jonson U (1998, p 12) 'The role of lubricants in refrigeration compressors is to reduce friction that prevents wear and also to act as a seal between high and low pressure sides of the compressor. In the rest of the system, however, the presence of lubricants acts as a contaminant which reduces the system efficiency'. Large heavy duty compressors and expanders are lubricated in the hydrodynamic lubrication range (HDL). A typical Stribeck curve shows the lubrication regime of various machine types, see figure 5 [43].

On the topic of professional writing and referencing Sunami M (1999, p 992) states: 'Small reciprocating compressors are operated in HDL and EHL areas. Lubricants with lower viscosities have lower friction coefficient numbers and provide lower energy consumption. Rotary compressors work under boundary and extreme pressure lubrication conditions. Moreover for scroll compressors with a lubricant performance in a pressurised refrigerant environment a reduction in film-forming capability was observed as the environment increases. The study of the wear performance also showed that combinations of lubricant and refrigerant with lower viscosities are subject to more severe conditions and even boundary lubrication'. Effects such as the reduction of lubricant viscosity with refrigerant solubility and the increase in solubility with pressure were confirmed [30], [44].

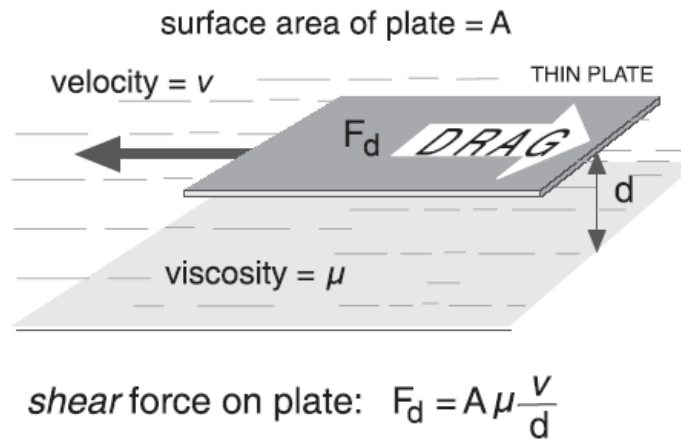


Source: [45]

Figure 5: Stribeck's curve for each type of machine

### 2.2.3 Viscosity

In fluid film lubrication the most important physical property of a lubricant is its viscosity. The viscosity of a fluid is associated with its resistance to flow. Particularly, at nano-scale viscosity is determined by the resistance arising from intermolecular forces and internal friction as the molecules move past each other. Figure 6 shows a thin plate travelling through a viscous fluid and the drag force (or shear force) resisting its motion.



Source: (XL170 user manual p 44)

Figure 6: Schematic explanation of dynamic viscosity

The resistance, or the drag force, can be described as a function of viscosity, surface area and the velocity divided by distance. The expression for velocity divided by distance is commonly used throughout viscosity measurement and is called the velocity gradient or shear rate. The expression for the drag force divided by surface area is called shear stress. Thus, the viscosity

of a liquid can be expressed with the help of the shear stress that is developed in a liquid when it is continuously moving at a specific velocity [46].

Thus the definitive expression relating shear stress and shear rate, which was first described by Newton in his famous book “Principia”, is defined by equation 9.

$$\tau = \mu\gamma \Leftrightarrow \frac{F_d}{A} = \mu \frac{du}{dy} \quad (9)$$

Where  $\tau$  is the shear which is applied on the molecules of the working fluid,  $F_d$  is the drag force opposed to the movement of the plate,  $A$  is the surface area of the thin plate,  $du/dy$  is the velocity gradient which is developed in the fluid and  $\mu$  is called absolute viscosity or dynamic viscosity.

The SI unit of viscosity is the Pascal second [Pa·s]

The ratio of absolute viscosity to the fluid density is called kinematic viscosity and is expressed by equation 10.

$$\nu = \frac{\mu}{\rho} \quad (10)$$

Where  $\nu$  is the kinematic viscosity in  $m^2/sec$  and  $\rho$  is the density of the fluid in  $kg/m^3$ .

### 2.3 Polymers/Elastomers

Polymer is derived from the Greek word *poly* (many) *mer-i* (parts). Polymer consists of long-chain organic molecules linked at various points by strong chemical bonds, mainly covalent bonds.

Elastomers are the most common type of polymers found in many everyday applications (tyres, seals, adhesives). Their main property is elasticity. The module of elasticity increases with the number of cross-linked bonds. The cross linked bonds are mainly within the bulk material. When the material is strained, the molecules untangle and align in the direction of strain. Visco-elasticity is caused by relative movement between the polymer molecules and the mechanism of strain accommodation which results in a very low elastic modulus while a comparatively high tensile strength is maintained. Visco-elasticity determines the important

sealing function whereas tribology governs the durability of the seal components. These principles are applied in the scroll expander system of this project [47].

Additionally, due to these mechanical properties, the mechanics of asperity contact for elastomers are radically different from the prevailing patterns of behaviour for most other materials. The elastomer surface consists of saturated hydrocarbon groups connected with weak Van der Waals bonds, enhancing ductility. The Van der Waals forces provide a significant component of frictional resistance for elastomers such as rubber and fluoroelastomer [47-48].

Fluoroelastomer is a visco-elastic material and its friction and wear behaviour are governed by visco-elastic properties. Fluoroelastomers can provide a unique combination of low friction coefficients and low wear rates. They are expensive compounds to produce and they have serious limitations in elevated temperatures because of their tendency to creep. Restrictions on wear resistance, strength and thermal conductivity, can be overcome efficiently adding suitable reinforcements and fillers in the appropriate amount and combination in the matrix of the elastomers [49].

### **2.3.1 Reinforced Polymers**

Reinforced polymers or polymer composites are a distinct category of polymer materials. They appear to have excellent resistance to adhesion and to abrasion wear mechanisms. Thus reinforced polymers are extensively used in demanding engineering applications like in aerospace and in chemical industries, where they are subjected to surface damage.

Reinforced polymers can alter their tribological properties using a variety of special fillers. The nature of the fillers determines the quality and the effectiveness of the polymers. The fillers are usually inorganic particles ( $\text{CaF}_2$ ,  $\text{ZnF}_2$ ) or ceramic particles ( $\text{Al}_2\text{O}_3$ ,  $\text{TiO}_2$ ,  $\text{SiC}$ ), the size of a few microns. They are introduced into different polymer matrices (PEEK, PTFE) incorporated with the bulk material. Many experiments have shown that reinforced polymers can provide substantially low frictional coefficient and wear rates. However, the poor thermal stability and the low melting points of the bulk material in correlation with high contact loads and friction velocities which the polymers are exposed to in various mechanical applications, can seriously affect their tribological performance [50].

## 2.4 Friction Theory

Friction is a force that resists sliding. It is described in terms of a coefficient, and is almost always assumed to be constant and specific to each material (using standard tests and is dependent on two surfaces in contact). According to the ASTM Standard G-40-93 friction force is the resisting force tangential to the interface between two bodies when, under the action of an external force, one body moves or tends to move relative to the other. Friction coefficient is the ratio of the force resisting tangential motion between two bodies to the normal force pressing those bodies together. These simple concepts obscure the causes of many problems in sliding systems.

In general friction force can be determined by the following equation 11.

$$F = W \times \mu \quad (11)$$

Where  $\mu$  is the coefficient of friction and  $W$  is the applied load. In other words friction force is proportional to the normal load. Moreover it is independent of the apparent area of contact and the sliding velocity [51-52].

### 2.4.1 Friction Force

When two surfaces are brought together the asperities will deform locally and frictional force arises. With metallic materials, the friction force is the sum of two other forces: the adhesive ( $F_{adh}$ ) and the ploughing ( $F_{pl}$ ), see equation 12. The adhesive derives from the shearing of the metallic junctions in the counterface of the rubbing materials. The ploughing is developed when the asperities of the harder material embedded across the surface of the softer material generate ploughing wear scars [53].

$$F = F_{adh} + F_{pl} \quad (12)$$

In the case of polymers, the sliding against a relatively smooth rigid counterface sufficiently changes the friction force. Elastic contact is much more likely to be formed than plastic since the value of  $E/H$  in equation 13 of the plasticity index  $\psi$ , drops down significantly. The value  $E/H$  of polymers is typically one tenth of that of metals. Generally, for values of the plasticity index  $\psi$  less than 0.6 or so, asperity deformation remains primarily in the elastic region. As the contact increases, the plasticity increases, with plastic deformation becoming dominant above 1.

$$\psi = \left( \frac{E}{H} \right) \left( \frac{\sigma^*}{r} \right)^{1/2} \quad (13)$$

Where E is the Young Modulus (MPa) of the material, H is its hardness (N/mm<sup>2</sup>), r is the asperity radius (mm) and  $\sigma^*$  is the standard deviation of asperity heights (mm). The term  $\sigma/r$  approximates to the mean asperity slope.

For polymer contact the term of ploughing is substituted by the hysteresis effect. Thus the frictional force F is the sum of two other forces, the adhesion and the deformation force or hysteresis, as presented by equation 14.

$$F = F_{adh} + F_{def} \quad (14)$$

For a reinforced polymer during its contact against a rigid material surface e.g. steel, the ploughing component has to be taken into consideration. Micro-ploughing wear marks can be found across the surface of both materials. Thus the frictional force can be determined as the sum of the adhesion, the deformation and the ploughing force (equation 15).

$$F = F_{adh} + F_{def} + F_{pl} \quad (15)$$

#### 2.4.2 Friction Coefficient (Dry Contact)

Contact between a polymer and a metal is mainly elastic while their friction coefficients commonly vary from 0.1 to 0.5. Moreover polymers are viscoelastic materials which significantly affects their stress-strain rate performance.

The coefficient of friction of a polymer surface against a hard surface in dry conditions can be expressed in terms of the contribution of adhesion and deformation (hysteresis) components. If the polymer consists of hard particle fillers (reinforced polymer), then in the overall coefficient of friction, the ploughing component has to be added (equation 16).

$$\mu_{overall} = \mu_{adh} + \mu_{def} + \mu_{pl} \quad (16)$$

The adhesion component of friction is produced due to the flow of the sliding polymer over the rigid asperities of the counterface material and conforms to its contours. The deformation

component which derives from such a flowing action is called hysteresis which increases with the decrease in Young's modulus of the polymer. The ploughing component depicts the plastic deformation in which a ridge of deformed material is pushed along ahead of the particle [54].

In polymers and especially in the elastomers, during dry sliding conditions the major component of friction is due to adhesion at the interface between two contact surfaces. Formation of polymer films is detectable on the hard counterface. Once the transfer film is formed, subsequent interaction between the film layer and a similar material is achieved, see figure 7 (D-E). Dividing the numerator and denominator in the definition for the friction coefficient by the true area of contact the adhesional component of friction according to Briscoe can be expressed with the following formula (equation 17) [55]:

$$\mu_{adh} = \frac{F}{W} = \frac{F/A}{W/A} = \frac{\tau}{P} = \frac{\tau_0 + \alpha P}{P} = \frac{\tau_0}{P} + \alpha \quad (17)$$

Where the shear yield stress  $\tau$  of the polymer is defined by equation 18 below:

$$\tau = \tau_0 + \alpha P \quad (18)$$

Where F is the friction force (N), W is the apply load (N), A is the real contact area ( $m^2$ )  $\tau$  is the shear yield stress of the polymer ( $N/m^2$ ), P is the hydrostatic pressure (Pa),  $\tau_0$  is the shear stress dependence of pressure ( $N/m^2$ ) and  $\alpha$  is the pressure coefficient which determines the change in the saturation shear yield stress with pressure [Appendix D, Table 15].

The adhesion mechanism is based on the layer shear model. The friction force is linearly related to the shear strength of the interfacial material. Moreover it is known from the pioneering work of Bridgman [56] that the yield stress of the polymer depends on the plastic flow stress of the material (hydrostatic pressure). Thus equation 17 shows that the coefficient of friction strongly depends on the applied load and the change of the hydrostatic pressure.

$$\mu_{def} = \left( \frac{ME_d}{A\lambda p} \right) \quad (19)$$

The deformation component is opposed to the sliding body and is not so significant, particularly for the elastomers. The accumulation of the viscoelastic body ahead of the slider

is a manifestation of the hysteresis effect figure 7 (B-C). Thus the deformational component according to Moore is defined with the following formula (equation 19):

Where  $M$  is the number of asperities,  $A$  the actual contact area ( $m^2$ ),  $E_d$  is the energy dissipated per asperity site (joules),  $\lambda$  is the mean sliding distance between sites (m) and  $p$  is the pressure on each asperity ( $N/m^2$ ). In general for viscoelastic materials due to hysteresis and deformation component the real contact area is not proportional to the applied load, but to two-thirds of the power of the load,  $W^{2/3}$ . [57].

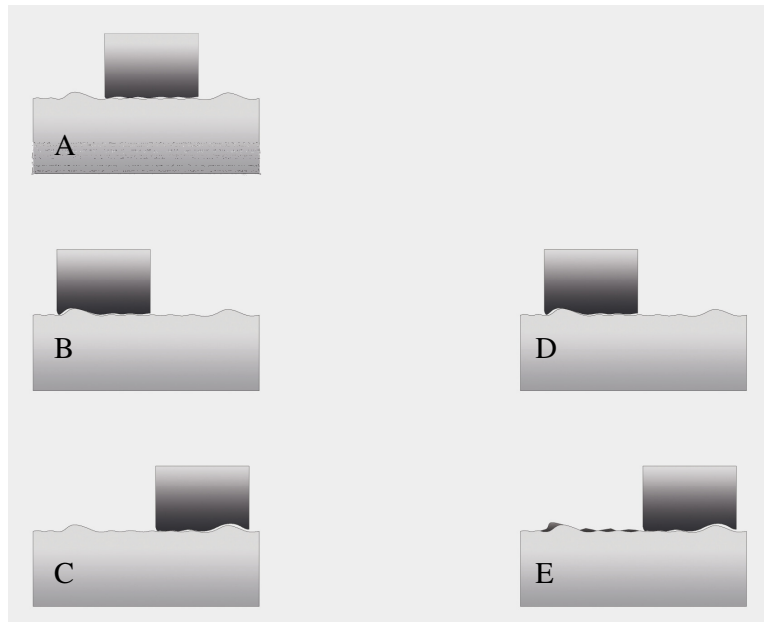


**Figure 7: The adhesion and the deformation mechanism generated during the sliding contact of an elastomer against a metallic surface. A) Initial position B,C) Deformation component D,E) Adhesion component**

Finally, the ploughing component in the case of the reinforced polymer contact, can significantly affect the overall friction coefficient during contact. The contribution of the ploughing component to the friction coefficient depends on the nature and the amount of the fillers in the bulk material of the polymer. Assuming that the ploughing scar is roughly conical in profile then the ploughing component can be defined with the following formula (equation 20) [58]:

$$\mu_{pl} = \left( \frac{2}{\pi} \right) \cot \alpha \quad (20)$$

Where  $\alpha$  is the semi-angle of a conical asperity.

### 2.4.3 Friction Coefficient (Lubricated Contact)

The concept of lubrication regimes is important, mainly for metal contact but also and for polymer contact. The lubricant decreases the frictional forces lowering the mechanical stresses and the wear mechanisms of the polymer surfaces. As will be discussed in a following paragraph (2.6), various comparisons of friction results have shown that the friction coefficient in a polymer contact can be reduced by 2 to 3 orders of magnitude with oil lubrication. In this study the difference was in the magnitude of approximately 2.

The lubrication regimes can be considerably affected by the change in the applied load or the sliding speed of the rubbing samples. At low sliding velocities less than 0.01m/sec the friction coefficient remains at a high level and the regime can be determined as a boundary. The friction force is still governed by the contribution of the dry area. As the velocity increases mixed lubrication appears. The contact spots are replaced by entrapment of liquid and the friction force decreases. Finally at higher velocities the friction force is hardly affected by the sliding speed and the hydrodynamic effect is generated [59].

With the increase of the applied load the contact temperature between the two tested surfaces increases due to frictional heat resulting in two contrary effects on the friction coefficient. On the one hand the shear strength of the polymer decrease and thus the friction coefficient decreases. On the other hand, the elastic modulus of the polymer decreases as the temperature rises resulting in an increase of the real contact area and thus of the friction coefficient. Generally, in an elastomer contact the first mechanism dominates, thus the friction coefficient is normally reduced [60]. Furthermore this can be better explained by the following formula presented by Z. Z. Zhang et al (equation 21) [61].

$$\mu \propto \frac{nu}{P} \quad (21)$$

Where  $\mu$  is the friction coefficient,  $n$  is the viscosity of the lubricating oil (Pa·s),  $u$  is the sliding velocity (m/sec) and  $P$  is the applied load (N/m<sup>2</sup>). Accordingly to that formula the friction coefficient of the metal/polymer contact decreases as the load increases in the case of oil lubrication.

## **2.5 Tribological Considerations**

Tribology is a compound word which derives from the Greek words 'tribos' and 'logos', meaning rubbing and word respectively. The word was first used in 1966 in Great Briain by H.P. Jost, chairman of a group of British lubrication engineers, to describe the scientific and technical domains focused on the study of friction, wear and lubrication phenomena. However the word tribology was foreign to many people even to some in science and engineering since the 1990's [53].

The concept of friction and wear has concerned great scientists since the time of Aristotle (384-322 BC). Leonardo Da Vinci later formulated two empirical laws of friction. Da Vinci found that the friction force is proportional to the normal load and independent of the contact area. To these a third law was added by Coulomb in 1785 stating that friction force is independent to sliding velocity. However the real understanding of wear and friction mechanisms was only achieved with the great developments that followed the industrial revolution in the early 18<sup>th</sup> century.

Nowadays tribology is a wide-ranging multi-disciplinary field of study and research investigating the lifecycle, the durability, the reliability and the efficiency, of every mechanical system which is manufactured around the globe. In addition, a recent review on the frontiers of fundamental tribological research emphasizes the concern over the environmental issues such as biodegradability in the development of tribo-materials in order that sustainability can be achieved [62].

### **2.5.1 Wear Theory**

When two surfaces come in contact they will suffer wear. Wear is defined as damage to a solid surface, generally involving progressive loss of material, due to relative motion between contacting surfaces. In general terms this is called sliding wear. Sliding wear can be lubricated when a type of lubricant interferes between these two surfaces or it can be dry when the surfaces of the materials that come in contact are sliding in air without lubricant.

Sliding wear can sometimes be described as adhesive wear. In sliding wear there are several physical and chemical processes that are involved apart from adhesive wear. For example the presence of debris in sliding wear causes further abrasive wear. As a conclusion the boundaries between different types of wear are not always clear.

Moreover wear under sliding conditions depends on the distance of sliding, the sliding velocity which affects the rate of frictional energy dissipation and the temperature of the interface, the nominal contact pressure between the sliding surfaces, the linear dimensions of the specimens and the duration of the test. These are the most important factors which affect sliding wear but there are several other factors, like testing temperature, atmospheric composition, and orientation of apparatus, which must also be considered and monitored in wear testing [47], [63-64]. The most common types of wear, which are involved in this project, are the abrasive and the adhesive wear.

### **2.5.1.1 Abrasive Wear**

Abrasive wear is a very common type of wear in materials. Abrasive wear is the most important among all the forms of wear because it contributes almost 63% of the total cost of wear [65]. The abrasive wear mechanism is basically the same as machining, grinding, polishing or lapping that is used for shaping materials. It arises when two interacting surfaces are in direct physical contact and one of them is significantly harder than the other. Under the action of a normal load, the asperities on the harder surface penetrate the softer surface thus producing plastic deformations. This type of wear can cause scratches, wear grooves and lead to material removal.

Abrasive wear can take place as plastic flow, brittle fracture or as a combination of both. The abrasive wear process is traditionally divided into two groups, the two-body and the three-body abrasive wear. In two-body abrasion the material is cut by fixed abrasive grains or protuberances sliding on its surface. Three-body abrasion is due to moving grains which are trapped between the two rubbing solid surfaces. If a trapped particle is significantly harder than the counter-face it will indent the surface causing plastic flow. If the particle is less than 1.2 times the hardness of the surface, it will itself be blunted and not indent the counter-face. Otherwise if the particle is greater than 1.2 times the hardness of the surface it will indent the surface. Finally abrasive particles during the abrasion process spend about 10% of the time in sliding, while they spend about 90% of time in rolling [66-68]. The rolling mechanism was proved to be critical for the attenuation of the friction coefficient and the wear rates in the studied contact.

### **2.5.1.2 Adhesive Wear**

It is widely accepted that adhesion at the interface between two contact surfaces plays a critical role in sliding resistance while it is also directly related with the visco-elastic properties of the polymers [69].

Adhesive wear is the result of localized welding between the sliding surfaces of contact. Adhesive wear can be characterised by high wear rates and large unstable friction coefficients. In addition adhesion mechanisms can be determined by the appearance of junctions or micro-welds between the surfaces that are subjected to friction. If these junctions are weak, shear occurs at the interface of the rubbing surface and wear is negligible. However, when junctions are strong, the softer material is subjected to shearing, transferred onto the harder material surface. This very common mechanism occurs in steel/polymer contact [70]. In this study the wear was significant since shearing prevailed on the wear mechanisms and substantial amounts of detached particles were detected.

For adhesive wear to occur it is necessary for the surfaces to be in intimate contact with each other. Surfaces which are held apart by lubricating films, oxide films etc. reduce the tendency for adhesion to occur. If the adhesive wear is the result of a breakdown of lubricated film separation the wear can be described as scuffing [42].

### **2.5.2 Wear of Polymers**

The wear of polymers is usually explained by the abrasive or adhesive mechanisms of wear. The resulting deformation in a polymer may be either plastic or elastic. In the first case the mechanism of wear can be termed abrasion or adhesion while in the second it is associated with fatigue.

In particular, the abrasive wear process can be distinguished by four different mechanisms: micro-ploughing, micro-cutting, micro-cracking and micro-fatigue [71]. Adhesive wear is associated with the softening and melting of polymer which occurs near the interface leading to an initial reduction in the friction coefficient. The interfacial temperature which has risen during the contact, results in a frictional heat dissipation which can seriously affect the mechanical properties of the rubbing materials. Thus, a smaller amount of energy is required to shear the softer layer of polymer than to overcome the initial adhesion and ploughing forces when the surfaces are harder. However, the wear mechanisms of polymers depend on the experimental conditions and upon the polymer type [72]. In elastomers for example with low elastic modulus the contact deformation will be almost totally elastic and fatigue mechanisms will dominate.

Elastomer and reinforced elastomer materials primarily fail due to two wear mechanisms, tearing and fatigue. Ultimately, these are not very distinct mechanisms because tearing or fracture is failure in the cycle of fatigue. In general, both forms of failure arise from high local

friction against the opposing surface (rough particles or smooth surfaces) relative to the strength of the elastomer.

Tearing mechanism is immediately visible. It occurs when elastomer slides on rough and hard surfaces. The fatigue mechanism occurs when elastomer slides on smoother surfaces. Generally, over a prolonged period of time, if the hard sliding specimen against the elastomer is sharp, abrasion wear results in a tensile failure (fractures) and if it is blunt, adhesion wear results in a fatigue failure. However, polymers have a superior durability in contrast to other materials and metals because of their very high resistance to abrasion by blunt grits, and their inability to fracture grits to produce fresh sharp edges [73-74]. In this study since the steel surface is very smooth, fatigue dominates on the matrix of the bulk elastomer material.

Finally, within the elastomer materials there is a further mechanism of wear occurring during abrasion which involves molecular degradation. Elastomers sustain very large strains during abrasion and this can cause chain-scission of the polymer molecules inside the rubber. The broken ends of the molecule are highly reactive since they have become chemical radicals. They rapidly combine with oxygen to form oxidation products. In addition, Chandrasekaran et al [75] has studied the friction and wear of rubber sliding on abrasive paper as a function of temperature and load. They conducted dry and lubricated unidirectional sliding tests and reported that the presence of lubricant reduced the coefficient of friction but accelerated wear due to chemical degradation of the rubber.

### **2.5.3 Wear Parameters**

In engineering design, the determination of wear parameters is crucial for the lifecycle and the durability of materials subjected to high load and velocity conditions.

The most common formula used for the calculation of the wear coefficient between two rubbing surfaces was developed by Archard and is defined with equation 22 [76].

$$k = \frac{VH_{soft}}{S_d F_n} \quad (22)$$

Where k is the non-dimensional coefficient of wear, V is the volume loss (mm<sup>3</sup>), H<sub>soft</sub> is the hardness of the softer material (Vickers), S<sub>d</sub> is the sliding distance (m) and F<sub>n</sub> is the normal load (N).

Landcaster using the equation 23 below proposed a simpler formula in terms of the specific wear rate [77].

$$W_s = \frac{V}{S_d F_n} \quad (23)$$

Where  $W_s$  is the specific wear rate ( $\text{mm}^3/\text{Nm}$ )

In order for the specific wear rate of a polymer to be determined, tensile strength and fatigue life have to be considered. Based on the concept of crack propagation, Lhymn developed equation 24 for the specific wear rate of a polymer including several mechanical properties [78].

$$W_{sp} = k \frac{S_d}{EH \epsilon \mu} U_c \frac{1}{F_n^6} \quad (24)$$

Where E is the modulus of elasticity (MPa), hardness of the polymer (Vickers),  $\epsilon$  is the critical strain at yield point (unitless),  $U_c$  is the crack growth velocity (mm/sec), k and  $\mu$  are the wear and the friction coefficients respectively.

The above equation 24 indicates that wear resistance  $W_R=1/W_{sp}$  increases with increasing load but decreases with increasing speed. Thus, this relation is totally compatible with the wear results from the experiments as will be evaluated in Chapter 5.

In addition fatigue wear can be correlated with the rate of fatigue crack growth and can be expressed with the Paris equation 25:

$$\frac{da}{dN} = A(\Delta K)^n \quad (25)$$

Where  $da/dN$  is the increase in crack with length  $a$  per cycle  $N$ ,  $\Delta K$  is the range of stress intensity to which the growing crack is exposed during each cycle and A and n are empirical constants. The value of the exponent n lies typically in the range from 1.5 to 3.5 for elastomers and 3 to 10 for rigid thermoplastics and thermosets [42].

Furthermore in order to evaluate the durability of materials under different wear conditions the time related depth wear  $W_t$  is frequently applied. Equation 26 presents the expression of the time related depth wear product.

$$W_t = k * Pu = W_s Pu = \frac{\Delta h}{t} \quad (26)$$

Where  $k^*$  is called the basic wear factor of the material and it is the same as the specific wear rate,  $P$  is the normal pressure ( $N/m^2$ ),  $u$  is the sliding velocity (m/sec),  $\Delta h$  is the height reduction of the specimen (m) during the test and  $t$  is the test time (sec).

Finally there are a couple of parameters which affect the wear behaviour, the frictional heating and the thermo-oxidation process.

During sliding contact, heat generation and energy dissipation associated with friction, appear as heat, flowing into the rubbing surfaces. In a steel/elastomer contact the heat will flux into the steel surface causing a rise in its bulk temperature. Thus the temperature augmentation can be described by the following expression (equation 27):

$$\Delta T = \frac{\mu Pu}{k} \quad (27)$$

Where  $k$  is the factor of thermal diffusion of the system,  $P$  is the contact pressure,  $\mu$  is the friction coefficient and  $u$  the sliding velocity. The factor  $k$  is determined by the properties of the steel such as thermal conductivity, specific heat, density etc. and the testing parameters like sliding speed, real contact area etc. [79].

Thermo-oxidation can cause ageing to a polymer surface modifying its physical and mechanical properties. The thermo-oxidation effect is determined by the amount of energy received by thermal dissipation on the surface of the polymer. The thermal dissipation in the contact area is defined as in equation 28.

$$\phi = \alpha \frac{\phi_r}{A} = \alpha \frac{\mu F_n u}{A} \quad (28)$$

Where  $\phi$  is the thermal density flow ( $\text{W}/\text{m}^2$ ),  $\phi_t$  is the thermal flow (W),  $\mu$  is the friction coefficient, A is the actual contact area ( $\text{m}^2$ ),  $\alpha$  is the partition coefficient ( $\alpha \approx 1$ ),  $F_n$  (N) and  $u$  (m/sec) the normal load and the sliding velocity respectively [80].

## 2.6 Previous Studies

A considerable number of papers dealing with the tribological behaviour and the performance of polymers and, to a lesser extent, with reinforced polymers, under dry and lubricated conditions, have been published. However, the wear behaviour of polymer materials is a multi-complex issue and it is widely recognised by even the latest studies, that the processes of wear in polymers are not well understood [81].

Effects on the applied load, sliding velocity and testing time were most commonly considered. Many studies have shown that the friction coefficient of polymers rubbing against metals increases with increasing the applied load [82]. Specifically, Guermazi et al [81] found that the friction coefficient of the high density polyethylene (HDPE) against steel increases with applied load but decreases with time. Similarly the observations of Unal et al [83] and Santner et al [84] showed that the friction coefficient increases with the applied load for various types of polymers.

Many other studies have shown different behaviours, typically that the friction coefficient of a polymer/steel contact significantly decreases with the applied load. In particular, Benabdallah [85] has found that the friction coefficient, decreases proportionally to the applied load from 5 N to 30 N while the wear rate increases with the load and decreases with the sliding speed (from 0.05 to 0.3 m/sec). In a recent study, Unal et al [86] found that for various polymers if the load increases the friction coefficient decreases while the augmentation of the sliding velocity from 0.5 to 2 m/sec increases the wear rates and the friction coefficient. Similarly Davim et al [87] in his latest study using reinforced PEEK/PEEK contact, verified the increment of friction coefficient and the specific wear rate with the increase of the sliding speed (from 0.25 to 0.75 m/sec) and the reduction of the contact stress (8 to 2.68 MPa) for a sliding distance of 15km.

Furthermore it is known that the friction coefficient and the wear behaviour of many polymers like elastomers, in fluid environments differ greatly from those in a dry condition. Lancaster [88] and Yamada and Tanaka [89] in an early study revealed that the wear rates of carbon reinforced polymers and PTFE respectively were greater than those obtained in dry

conditions. In a recent study Sumer et al [90] and Jia et al [91] have observed that the friction coefficient for PEEK/reinforced PEEK and for various carbon reinforced polymers respectively, can be considerably decreased in lubricated conditions as opposed to dry sliding conditions while the specific wear rate can be significantly increased. Finally, for different rubber types Karger-Kocsis et al [92] in his recent study found that the specific wear rate is reduced with increasing load and the hardness of the material. In addition the friction coefficient was proportional to the reduction of the surface roughness and to the increment of hardness.

The augmentation of the wear rates of the polymers under lubrication conditions can be explained in two ways. On one hand the polymers tend to absorb water molecules and weaken the intermolecular bonds between the polymer chains. This results in the shear strength and the Young's modulus being decreased. On the other hand the liquid environment disturbs the formation of closed transfer film on the counterpart. In other words the lubricants "*wash the surface*" avoiding debris adhering to the steel surface [91-93].

The attenuation of the friction coefficient values of the polymers under lubrication conditions is due to substrate smoothening by the lubricant due to viscoelastic deformations on the polymer surface. The presence of fluid between the polymer and the hard substrate reduces not only the adhesion but also the hysteresis component of friction. On a lubricated substrate the valleys turn into fluid pools which are sealed off and effectively they create a smoother substrate surface. Smoothening reduces viscoelastic deformation from the surface asperities and thus reduces the overall friction [47], [94]. In addition the viscoelastic deformation of polymers due to load follows the equation  $\mu = KN^{(n-1)}$  where  $\mu$  is the friction coefficient,  $N$  is the apply load,  $K$  is a constant and  $n$  is also a constant its value between  $2/3$  and  $1$ . According to this equation the friction coefficient decreases with the increment of the load. However, when the load increases to the limit load value of the polymer the wear and friction effects will be increased due to the critical surface energy of the polymer. Thus, the frictional heat increases the sliding temperature of the friction surfaces, which leads to relaxation of the polymer molecule chain, resulting in the chemical degradation of the polymer matrix [81], [83], [90]. Finally, according to a most recent study by Deleau et al in high velocity of a few tens of metres per second, the hydrodynamic effect can be introduced reducing the wear and the friction rates [59].

In addition the rise of temperature can accelerate the polymer transfer film process onto the steel surface. The transfer film is usually very thin, a few microns, containing molecular chains orientated parallel to the sliding direction. Benabdallah in its latest work [95] has

shown how surface temperature can affect the transfer film formation and the wear behaviour of various polymer types (POM, HDPE, PA66, PP, PVC, Torlon, PTFE). Especially in dry contact, with the absence of the *washing effect*, the transfer film tends to increase the real contact between the two bodies due to increased thermal expansion, leading to a higher adhesion force and friction coefficient [79]. On the other hand, a thicker film can sustain more loads, providing protection to the rubbing materials and decreasing the wear rates. Furthermore, in a lubricated contact, according to Zhang et al [96] and Degradge et al [80], mechanochemical reactions lead to a thermo-oxidation process and a chemical reaction film is formed across the steel surface. Hence, the wear resistance of the sliding contact is improved.

The tribological behaviour of reinforced polymers against rigid surfaces has gained the interest of many researchers. Recent research studies have shown that fillers, fibbers and nano-particles can improve drastically the performance of polymers [62], [97-98]. The type the orientation and the length are the critical parameters of the polymers for the evaluation of their performance under sliding conditions. For example, a recent investigation by El-Tayeb et al [99] has shown that the wear rate of a carbon glass reinforced polymer (CGRP) under dry sliding conditions against a steel counterface, is affected by the orientation of the fibres. The anti-parallel orientation of the fibres to the sliding movement at speeds above 2.2 m/sec was chosen to give the most significant drop in the wear rate. In another study Bijwe [49] has observed that wear rate is lower in a normal orientation and higher in the anti-parallel for various polymers with sliding velocity 0.87 m/sec while a 30 wt% of short glass fibre was the optimum percentage for highest wear resistance [100]. In addition, accordingly to Chang et al [101] the wear performances of carbon fibre reinforced composites were strongly related to the procedure of the fibre peeling-off. Moreover, large fibre debris can easily flake and fracture, decreasing the wear resistance of the polymers [102] owing to a three-body abrasive wear effect [47] whereas the smaller fibre debris can be helpful for the formation of the transfer film leading to a friction coefficient reduction [103-104]. Finally, the peeled-off and fractured fillers can play a crucial role in reducing the friction coefficient on introduction of the *rolling effect*. This *rolling effect* helps to reduce the shear stress and contact temperature between the rubbing surfaces [105].

## **2.7 Cavitation**

Cavitation is a dynamic phenomenon, characterised by bubble generation. Cavitation is known as a repeated formation and violent collapse of gas bubbles in a liquid caused by the instantaneous transition of liquid phase to gas phase due to instantaneous fluctuation of local pressure. These fluctuations nucleate bubbles, which instantly implode, producing shock

waves and liquid-jets. In particular, when the local pressure in the liquid is lower than the saturated vapour pressure at ambient temperature, there will be cavities nucleating and growing. The cavities collapse when they are transported to a higher pressure region within the liquid, generating huge hydrodynamic pressures. When the collapse of bubbles occurs close to solid surfaces, the interaction of the large amplitude shock waves and the micro-jets has the potential to generate highly localized and transient surface stresses, resulting in severe material damage [106-107].

Cavitation can be generated by creation of new bubbles due to pressure variations or by the expansion of tiny pre-existing bubbles called nuclei. Moreover in many applications where pressure variations are at a critical level, cavitation can be easily initiated by small quantities of gas which are trapped in the bulk liquid by solid impurities and particles within the liquid or by tiny micro-cracks or voids on the material's surface.

Cavitation can be differentiated into inertial and stable [108]. Inertial cavitation involves the rapid growth and collapse of the bubbles while stable cavitation involves the conservation of a continuous oscillatory motion of bubbles [109]. In this project inertial cavitation was mainly observed in the water and lubricant environment. Oscillatory cavitation was observed in the refrigerant environment as preventing bubble implosion.

### **2.7.1 Cavitation Forms/Types**

There are two forms of cavitation which induce the growth of a bubble inside a liquid environment: vaporous cavitation and gaseous cavitation.

Vaporous cavitation is when the bubbles which are filled by vapour of the liquid are generated by pressure reduction. Gaseous cavitation is when microscopic gas bubbles found in a liquid, are forced to oscillate by pressure differential or temperature augmentation, grow in size and then rapidly collapse. In reality the situation is more complicated since the cavitation bubbles usually contain a mixture of vapour and gas. Additionally cavitation can be distinguished in four different types according to the way the bubbles are generated.

Hydrodynamic cavitation produced by pressure variations due to geometry of the hydraulic structure. Examples are the ship propellers and the hydro turbines.

Acoustic cavitation produced by pressure variations due to acoustic waves into the liquid. An example is the ultrasound on a liquid environment.

Optic cavitation produced by rupturing the liquid when it is exposed to photons of a high intensity light source. Examples are the laser beams.

Particle cavitation produced by elementary particles like protons rupturing the liquid and producing rapid superheating to the liquid moleculars increasing their tendency to evaporate. An example is the bubble chamber [110].

According to Lauterborn hydrodynamic and ultrasonic cavitation are produced by tension in the liquid while the cavitation process in the optic and in the particle type can be achieved by depositing energy into the liquid [111].

### **2.7.1.1 Acoustic Cavitation**

The principle of acoustic cavitation is based on the high intensity ultrasound which is applied to liquid and thus creates cavitation bubbles. The pressure varies according to the applied sound waves. When a liquid is subjected to a sufficiently low pressure, it ruptures while the liquid's pressure falls below its vapour pressure resulting in the formation of cavitation bubbles.

When a cavitation bubble is subjected to a higher pressure the collapse mechanism of the bubble begins. At the point where the static pressure tends to increase more than the vapour pressure of the liquid/mixture, the mass of the vapour/gas should be re-liquefied. The transition process from the vapour/gas phase to the liquid one is not instantaneous and both phases coexist for a minimal period of time. For the reason that there is a big difference in the density between the liquid phase and the vapour/gas phase, (for example an air cavitation bubble has  $\rho=1 \text{ kg/m}^3$  and the water liquid  $\rho=1000 \text{ kg/m}^3$ ) the re-liquefied phenomenon of the cavitation bubble is followed by a substantial increase in the static pressure. The volume of the water which corresponds to the mass of the vapour/gas is very low. Thus, during the re-liquefied mechanism of the bubble a vacuum space is formed which tends to be filled by the surrounding liquid. Thus, a high momentum micro-jet is formed, projected towards the solid boundaries, damaging the surface [112].

In the acoustic cavitation, as the process is generally non-linear, the radius of the bubbles does not proportionally change to the sound pressure. In addition because of the high compressibility the bubbles are subjected to by the sound waves, much potential energy is obtained during the expansion while huge kinetic energy is released when they collapse [110].

## 2.8 Bubble Dynamics

The equations of bubble dynamics, describing the bubble growth and collapse in various liquid environments, were first studied by Lord Rayleigh in the early 19<sup>th</sup> century. The equation which applies for an empty spherical bubble, assuming that the surface tension is negligible, since no gas is contained is (equation 29):

$$\frac{P_L - P_\infty}{\rho} = R\ddot{R} + \frac{3}{2}\dot{R}^2 \quad (29)$$

This is the *fundamental equation* of bubble dynamics. Where R is the bubble radius,  $\dot{R}$  and  $\ddot{R}$  are Newton's notations, the first and the second derivative of R with respect to time t,  $P_L$  is the pressure of the liquid just outside on the bubble wall,  $P_\infty$  is the liquid ambient pressure of the liquid far from the bubble and  $\rho$  is the density of the liquid.

Assuming an adiabatic process ( $PV^\gamma = \text{constant}$ ) when the cavitation bubble radius changes from R to  $R_0$ , then the equation which applies for a bubble containing a gas quantity can be expressed with equation 30.

$$R\ddot{R} + \frac{3}{2}\dot{R}^2 + \frac{2\sigma}{R} = \frac{P_v - P_\infty}{\rho} \quad (30)$$

Thus the analytical expression can be written as:

$$R \frac{d^2R}{dt^2} + \frac{3}{2} \left( \frac{dR}{dt} \right)^2 + \frac{2\sigma}{R} = \frac{1}{\rho} \left[ \left( P_0 + \frac{2\sigma}{R} \right) \left( \frac{R_0}{R} \right)^{3\gamma} - P_\infty \right] \quad (31)$$

The equation 31 was first derived and explored by Noltingk and Neppiras [113] where  $\sigma$  is the surface tension of the liquid,  $P_0$  is the pressure on the wall of the bubble,  $\gamma$  is the ratio of the specific heat of the gas and  $R_0$  is the initial radius of the bubble before it expands to a radius R at a constant temperature.

In order to render equation 31 more coherent in later years the viscosity parameter was added. Now the equation can be written as:

$$R\ddot{R} + \frac{3}{2}\dot{R}^2 + \frac{2\sigma}{R} + \frac{4\mu\dot{R}}{R} = \frac{P_v - P_\infty}{\rho} \quad (32)$$

Thus the analytical expression is defined by the equation 33.

$$R \frac{d^2R}{dt^2} + \frac{3}{2} \left( \frac{dR}{dt} \right)^2 + \frac{2\sigma}{R} + \frac{4\mu}{R} \frac{dR}{dt} = \frac{1}{\rho} \left[ \left( P_0 + \frac{2\sigma}{R} \right) \left( \frac{R_0}{R} \right)^{3\gamma} - P_\infty \right] \quad (33)$$

Where  $\mu$  is the viscosity of the liquid

Finally, a large number of additional important parameters can affect the dynamic behaviour of the bubbles like mass and heat transfer, the compressibility of the fluid and most importantly the geometry of the cavitation bubbles. Frequently bubbles do not keep their spherical shape and during growth change to different weird shapes. However the equations presented above, afford a practical and quite realistic approach to the study of various liquids [114].

Furthermore Rayleigh in 1917 developed a theoretical formula which correlates the time collapse with the maximum radius of the bubble (equation 34) [115].

$$R_{\max} = \frac{T_c}{0.915 \sqrt{\rho / (P_\infty - P_v)}} \quad (34)$$

Where  $R_{\max}$  is the maximum radius of the spherical bubble,  $T_c$  is the collapsing time,  $\rho$  is the density of the liquid,  $P_\infty$  is the liquid pressure taken far from the bubble pressure and  $P_v$  is the vapour pressure.

As it is further described in a following paragraph (2.9.4), the bubbles which collapse near a rigid boundary do not maintain their spherical shape but elongate across the surface of the boundary into a toroidal shape. Therefore, the Rayleigh formula is not applicable for a cavity collapse near the boundary [116].

The formation of the micro-jet is strongly dependent on the normalized distance (paragraph 2.9.4). For higher values of the normalized distance the micro-jet impact becomes higher as Phillip et al. adduced in their study [117]. In some cases this principle may not apply. The reason is that a layer of the fluid is formed across the surface of the rigid boundary,

resembling a cushion which reduces the impact effect of the jet. On the other hand, if the cavity is close to the boundary, despite the velocity being lower, there is no fluid layer cushion, thus the impact is higher. Therefore it is difficult to adopt an accurate theoretical approach for the micro-jet velocity and its impact pressure.

The above phenomenon was also observed in this study and it will be discussed later. The micro-jet which is formed in the lubrication bubble had a higher velocity compared to the other liquids. In this case a protective layer was formed during the cavitation process absorbing the impact and protecting the material surface.

The general expressions which determine the micro-jet velocity for a water bubble and the impact pressure (water-hammer) for various liquids were developed by Plesset and Chapmann and presented by the equation 35 and 36 [118].

$$u_{jet} = 8.97\gamma^2 \sqrt{\frac{P_s - P_v}{\rho}} \quad (35)$$

and

$$P_i = \rho C u_{jet} \quad (36)$$

where  $\rho$  is the density of the liquid and  $C$  the ultrasonic velocity in the liquid. Moreover the average jet velocity can be estimated, as Claus-Dieter Ohl suggests in his study using equation 37 [119].

$$u_{jet(ave)} = \frac{2R_{max}}{T_c} \quad (37)$$

Finally the potential energy of a bubble at its maximum radius can determine the jet deformation during the bubble implosion. Thus the bubble energy can be specified when all kinetic energy is turned into potential energy. For a spherical bubble this quantity can be estimated by using equation 38 [120-121].

$$E_p = \left( \frac{4\pi R_{max}}{3} \right) (P_s - P_v) \quad (38)$$

The above equation states that the bubble energy is determined by its maximum volume and the corresponding pressure gradient, where  $P_s$  is the static pressure of the liquid around the bubble and  $P_v$  is vapour pressure of the bubble.

## **2.9 Cavitation Conditions**

Cavitation conditions determine the level of the cavitation damage and the erosion rate during an experimental or an application process. Extensive research has been carried out by many researchers in order to find a comprehensive correlation between the cavitation mechanism and cavitation conditions. The most important parameters affecting cavitation damage are presented in the following sections (2.9.1-2.9.5).

### **2.9.1 Effect of Viscosity**

It is well known that viscosity affects the cavitation process. The issue of the effect of viscosity on cavitation threshold has led to some debate within published literature, with claims of increased or decreased cavitation activity arising from different studies of similar environments.

Brujan [122] has shown that higher levels of viscosity can substantially mitigate the tendency of cavitation activity to damage. Popinet et al [123] in his study has found that the amplitude of the oscillations decreases due to viscous damping while the jet impact velocity decreases as viscosity increases. Williams et al [124] and Berker et al [125], reported a mitigating effect of viscosity in the jet propulsion by the bubbles collapse of various fluids. Karunamurthy [126] in his thesis presents the viscosity influence on the rate of erosion showing that as viscosity increases erosion decreases. However, Meged et al [127] has found that there is no direct correlation between the viscosity of a liquid and the cavitation erosion mechanism after a series of experiments using 20 different liquid lubricants.

In this study the effect of viscosity within the tested fluids is highlighted. In the water and lubricant environment, the viscous forces reduce the amplitude of the radial oscillation of the spherical shaped bubbles. In the refrigerant environment where the viscosity is the lowest, the oscillations of the cavitation bubbles are regular and rigorous. Interestingly, the oscillations are restricted in random small areas across the bubble's body creating a wobbling effect. However, the results are in agreement with Meged's study [127] since no correlation between the viscosity and the impact potential of the bubbles was drawn.

### **2.9.2 Effect of Surface Tension**

In regards to surface tension in a micro-scale level the bubble growth and the elongation is continuously influenced by the surface tension forces which are dominant at this scale [128]. According to Iwai et al [129], experiments which were conducted in various water solutions with different surface tensions showed that surface tension increases the liquid-jet impact and the bubble size. By contrast in a cavitation environment Liu et al [130] in a recent study has shown that higher surface tension values lead to smaller sized bubbles reducing the collapse duration.

In the present study even if the surface tension is lowest in the refrigerant environment, the wobbling behaviour of refrigerant bubbles, as discussed in Chapter 6, reduces the risk of collapsing to a minimum revealing a very interesting mechanism. However, the combination of surface tension and viscosity forces is critical for a precise interpretation of the bubble's cavitation performance.

### **2.9.3 Effect of Tensile Strength**

Another very important liquid property affecting the cavitation process is the liquid's tensile strength. According to Megel et al [127] as cavitation is caused mainly by the application of tensile stress in liquids, tensile strength can be considered as a dominant property of controlling their cavitation.

The tensile strength of a liquid is defined as the maximum negative pressure that a liquid in an isothermal metastable state can withstand before it ruptures (cavitates). Generally, in all liquids the tensile decreases as the temperature increases leading to a more rapid formation of cavitation bubbles.

At ambient temperature the minimum of isotherm curves correspond to extremely high negative absolute pressure in the order of -1000 bar for water while for the actual refrigerant of the project it can reach the -1250 bar as Utz et al [131] presents in his study. However, these values corresponded to a molecular level of analysis of the two liquids and cannot be matched with the behaviour of the tested liquids of this project. A more coherent explanation of the peculiar performance of the refrigerant bubble is needed.

### 2.9.4 Effect of Normalised Distance

In the case of a bubble collapsing near the boundary wall, the oscillation frequency of the bubble is reduced, thus the prolongation factor of the collapse time has to be considered [132]. This factor is the normalized distance  $\gamma = s/R_{\max}$  where  $s$  is the distance of the boundary from the bubble centre and  $R_{\max}$  is the maximum bubble radius (figure 8). Normalized distance is the main parameter for classifying the bubble dynamics near a rigid boundary [116]. For  $\gamma > 3$  the micro-jet reaches higher velocities leading to a liquid-liquid impact reducing the possibility of a counter-jet. For values between  $3 \geq \gamma \geq 1$ , a counter-jet is formed. Finally for  $\gamma < 1$  the bubble will touch the boundary wall and will then deform to obtain a toroidal shape. In this case no counter-jet is developed [133].

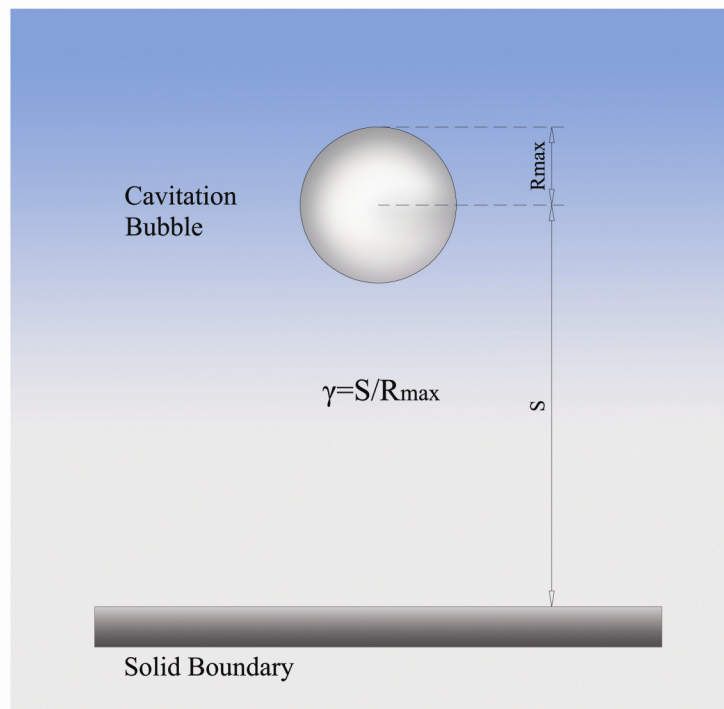


**Figure 8: The illustration of the normalized distance of a cavitation bubble with radius  $R$  and distance  $s$  from the boundary wall**

### 2.9.5 Effect of Magnitude of Vibration

It has been shown using water as a cavitating medium that the vibratory cavitation erosion rate of steel materials increases in a linear fashion with vibration amplitude and, therefore, applied power [134-135]. In an ultrasonic device the maximum bubble radius, bubble energy, liquid-jet impact pressure and velocity are directly proportional to the acoustic power [121].

It has also been indicated that the damage of material due to cavitation phenomena is related to the cavitation intensity. In very low amplitudes of the specific ultrasonic system used in this project, less than 3 microns peak to peak, the bubbles are keeping a bubbly morphology without collapsing near the solid surface. However, over a 10 micron peak to peak amplitude the erosion rate is significantly increased up to the maximum available amplitude of 60 microns. In this study amplitude of 50 microns was used according to the ASTM G32-03 standard method. More details can be found in the thesis of Karunamurthy which used exactly the same experimental system [126].

## 2.10 Cavitation Erosion Equations

Following the completion of the experimental procedures, some basic equations were utilised in order to enable the volume loss and the surface erosion damage of the steel materials to be thoroughly evaluated.

The erosion loss was expressed in terms of the mean depth of erosion (MDE) and the mean erosion rate (MDER) and is calculated according to equations 39 and 40 respectively.

$$MDE(\mu m) = 10 \frac{\Delta W}{\rho A} \quad (39)$$

and

$$MDER(\mu m / h) = 10 \frac{\Delta W}{\rho A \Delta t} \quad (40)$$

where  $\Delta W$  is the weight loss in mg,  $\Delta t$  is the test time in hours,  $A$  is the cavitated area of the specimen in  $\text{cm}^2$ , and  $\rho$  is the density of the specimen in  $\text{g/cm}^3$ .

The cavitation erosion resistance (REC) is defined as the reciprocal of the mean erosion rate and expressed by equation 41.

$$REC(h / \mu m) = \frac{1}{MDER} \quad (41)$$

Since cavitation erosion damage has a fatigue character, the accumulated strain energy estimates the rate of the erosion and the resistance of the samples against cavitation. The accumulated strain energy is expressed by the following equation 42.

$$\Sigma En = V\Sigma\left(\frac{\sigma^2}{2E}\right) \quad (42)$$

where V is the volume loss in mg,  $\sigma$  is the yield strength in MPa and E is the Young modulus in GPa.

## 2.11 Previous Studies

Cavitation is a chain series of interaction mechanisms the result of which is the erosion of material surfaces. Thus, most cavitation phenomena are associated with serious damage near to boundary walls.

Cavitation erosion damage is caused by removal of material or plastic deformation of a solid surface when it undergoes high pressure impacts during a cavity collapse. In particular, the solid boundaries absorb the impact energy deriving from the implosion of the bubbles. This leads to elastic deformation, plastic deformation or fracture [139]. Their destructive consequences can be found in many different fields like hydraulic machinery, material science and medicine and turbomachinery [136-140].

Turbomachinery has long been recognised as one of the major fields of cavitation. Turbomachinery involves machines that transfer energy between the rotor and the working fluid, including both expanders (turbines) and compressors. The expander transfers energy from the fluid to the rotor while the compressor works in the opposite way by transferring energy from the rotor to the fluid [141]

In this project only the scroll expander with the maximum service hours (1000 hours) experienced severe damage in its main components, which is without any doubt identified as cavitation damage. The fluid environment consists of two scroll fluids: the high molecular organic fluid (refrigerant) which is mainly in a gas form and drives the scroll and the synthetic oil (lubricant) which protects the parts of the scroll from excessive wear. Limited experimental information concerning lubricant and refrigerant bubble formation and their dynamic performance is available within published literature [142-143].

On the other hand, ultrasonic cavitation was extensively investigated in the last century and a substantial number of papers dealing with the erosion-rate, hardness and durability of various materials have been published. Hattori et al [144] in his latest study summarised the cavitation

erosion of various stainless steel types over the last 32 years after a thorough review of the literature. He has presented the mean depth erosion rate (MDER) of various steel types to cavitation impact. The rates were varied from 3 to 5  $\mu\text{m}/\text{h}$  for durations of 5 and 8 hours respectively. In addition, he showed that the resistance of the steel can be significantly increased according to the carbon content. Haosheng et al [145] in his study distinguished the typical stages of cavitation erosion of a typical Chromium steel (40Cr) sample according to the mass loss curves. It is found after 5 hours of exposure to cavitation the mean depth erosion (MDE) was 25  $\mu\text{m}$ . Zhang et al [146] in his recent work has effectively calculated the MDER of CrNiMo stainless steel to be around 25  $\mu\text{m}$  after 5 hours running cavitation test. Dojicinovic et al [147] calculated the MDE of a medium carbon steel to be around 9  $\mu\text{m}$  after 4 hours of testing time. Steller [148] in his study presented the MDER of two different steel types: a medium carbon 45 steel and a stainless steel 1H18N9T. He found that after 8 hours of exposure to cavitation, the MDER was around 25  $\mu\text{m}/\text{h}$  for the carbon steel and 35  $\mu\text{m}/\text{h}$  for the stainless steel. Chiu et al [149] has shown the different MDER of the AISI 316L stainless steel surface modified with NiTi powder. The steel with the highest hardness (700 HV) after coating treatment, achieved the lowest MDE of about 0.5  $\mu\text{m}$  after an 8 hours test. Chiu et al [150] has also investigated the cavitation behaviour of the AISI 316L stainless steel finding that the MDE after 5 hours of test is about 12  $\mu\text{m}$ . Finally Hattori et al [151] defined the MDE and MDER of a low carbon steel S15C exposed to cavitation for a prolonged period of time. The MDE was found to be around 40  $\mu\text{m}$  and the MDER was estimated at around 8  $\mu\text{m}/\text{h}$ .

For many steel grades, the phase formation and the dislocation structure cause alterations in their properties changing their cavitation erosion resistance [152]. Many pits have been observed on the material's surface after cavitation impact and the damage was found to depend on the hardness of the sample [153]. Hardness is strongly related with the dislocations of the crystal structure. The strain fields of adjacent dislocations increases as the dislocation density of a material increases. The formation of new dislocation networks causes dislocation blockade and motion is restricted [154]. The density of the dislocation networks is increased especially along the grain boundaries and around the surface of the cavitation pits [155]. In consequence, high increase of micro-hardness is observed [156-157]. In contrast, the heat influence, the repeated impact pressure and the interactions between the dislocations and the grain structure cause the material flow [158]. This in turn causes decrease of micro-hardness [159-160].

In addition, the phase transformation process is related to the cavitation erosion behaviour of various steel grades. A matrix with high work hardenability, low stacking fault energy and high martensitic transformability can absorb more impact energy during bubble implosion

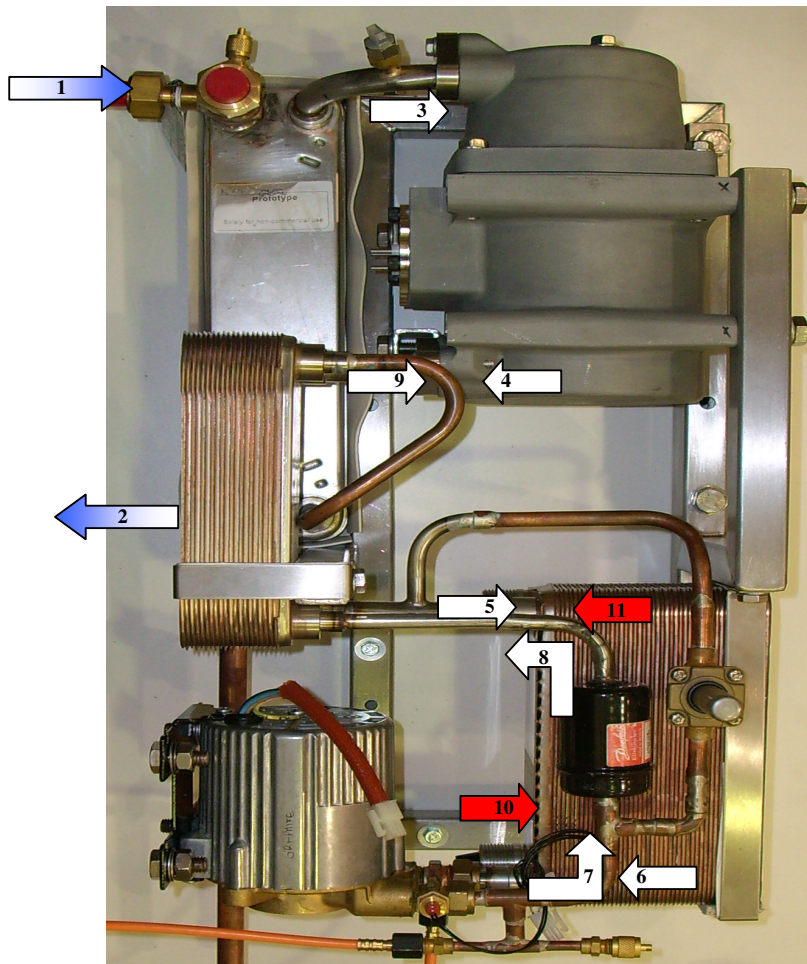
resulting in higher cavitation resistance [161]. Heathcock and Protheroe [162] comparing the cavitation resistance of two austenitic stainless steels found that the  $Fe\gamma$  (FCC cell structure) to  $Fe\alpha$  (BCC or BCT, depending on carbon content, cell structure) phase transformation improves the cavitation resistance of the steels. They showed that low martensitic transformability, high stacking fault energy and low hardness significantly decrease the cavitation erosion resistance of steels. Furthermore, Wang and Zhu [163] have found that martensite is formed during the cavitation mechanism and that the phase transformation process is related to the work-hardening ability, the energy absorption and the elasticity of the materials. Krella et al. [164] has found that the best cavitation erosion resistance of austenitic steel is linked with the ability of the impact energy absorption by the phase transformation  $Fe\gamma \rightarrow Fe\alpha$  causing a change to the material properties. Liu et al [157] adduce that the work-hardening ability and the “forming and transferring” mechanism are attributed to high cavitation resistance of the steels. According to his study hardness cannot be considered as a dominant factor for cavitation erosion resistance.

Finally, cavitation erosion damage can be strongly correlated with the fatigue process which Richman and Mc Naughton found and later G. Wang numerically studied [165-166]. Furthermore, as Matevz Dular has found, cavitation erosion can also be generated by the accumulation of the pits during the incubation time showing the tendency of cavitation damage to cluster formation [167]. However, no simple relations between them have yet been found while there is still debate about the sequence of events that leads to material loss. Despite all these experimental techniques and analytical methods over the last few decades which were used to assess material resistance to cavitation, a quantitative and qualitative analysis of material behaviour against cavitation effects still remains an open subject for further investigation [166-167].

### 3 CHAPTER : SCROLL EXPANDER OPERATIONAL ANALYSIS

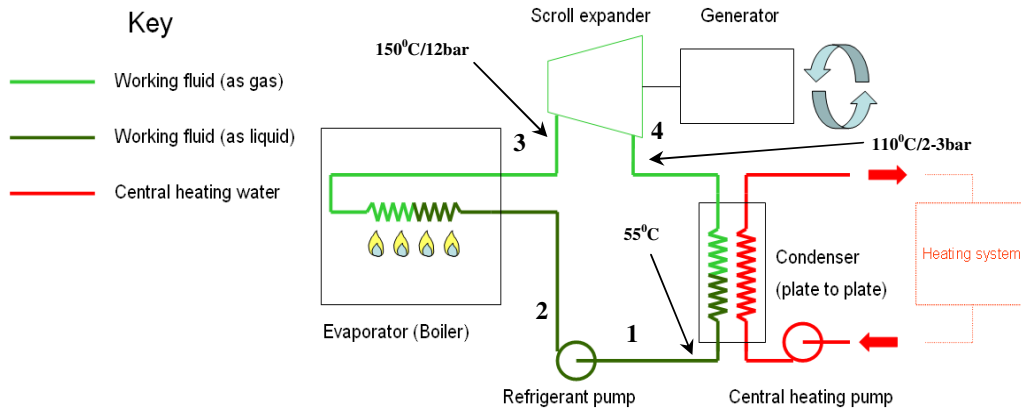
#### 3.1 The CHP unit

The experimental domestic micro-CHP system used for this project is illustrated in figure 9. The micro-CHP system consists of a small fluid pump, a scroll expander unit, a pressure relief valve, a filter drier, two heat exchangers and an evaporator. The first heat exchanger is directly connected to the boiler unit and heats up the working fluid as it passes through tubes before entering the scroll. The second heat exchanger plays the role of the condenser, condensing the working fluid transferring the heat to the central heating circuit of the house which provides space heating and hot water. Finally, the scroll expander turns a generator to produce electricity.



Source: (Energetix Group Ltd)  
Figure 9: The experimental micro-CHP unit

Refrigerant and lubricant scroll fluids were used during the operational time period. The refrigerant was the driving force of the scroll while the lubricant was protecting the scroll from severe wear.



Source: (Energetix Group Ltd)

Figure 10: Schematic presentation of Genlec micro-CHP unit

The route the working fluid follows in this micro-CHP system is analytically described by the arrows in figure 9. The heated steam from the primary heat exchanger in the boiler enters the evaporator (1). Then the condensed steam returns to the primary heat exchanger (pipe not shown) (2). The working fluid as it enters the evaporator, instantly evaporates, raises in pressure and temperature at around 12 bar and 150 °C respectively, and feeds into the inlet of the scroll (3). The expanded working fluid exits the scroll, in an approximate temperature of 110 °C and pressure of around 2-3 bar. Simultaneously, electricity is produced. Then the working fluid enters the first heat exchanger where part of the heat is transferred to the liquid working fluid prior to entering the evaporator (4). The slightly cooled working fluid exits the first heat exchanger and enters the condenser (5). The gaseous working fluid, releases its thermal energy and condenses as it heats the hot water system of the house (arrows 10 and 11 show the flow of the hot water circuit in and out of the condenser - pipework is not visible). Then the condensed working fluid exits the condenser and enters the pump (6). The liquid working fluid is lifted in pressure by the pump (which also provides circulation around the system) and then enters the filter-drier which removes any traces of moisture and particulates in the system (7). The liquid working fluid then exits the filter-drier (8) and enters the first heat exchanger where it is exiting the scroll (4). Thus the liquid working fluid is preheated, exits the first heat exchanger (9) and finally enters the evaporator and the cycle repeats.

The micro-CHP system as an integrated domestic boiler has an efficiency of about 88-90% overall which approximates to a 10% electrical efficiency and an overall heat to power ratio of about 9:1. The ORC in isolation has about 12% net efficiency. The system produces 9 kWt (kilowatt of Thermal Power) and 1.1 kWe (kilowatt of Electric Power) per hour consuming 1.2 m<sup>3</sup>/h of natural gas in the boiler unit. The system's mass flow rate is measured by a flowmeter at 0.028 kg/s. The system's working fluid is a high molecular organic fluid while the whole process is based on the Organic Rankine Cycle (ORC).

### 3.1.1 ORC Process

The thermodynamic behaviour of the above micro-CHP system is explained with the schematic diagram of the ORC for dry working fluids like the one used in this micro-CHP system (figure 10).

Each process in the cycle can be described with the following equations assuming that the mass flow rate leakage and the heat losses (adiabatic process) are negligible.

Process 1→2 (Pump): Includes the lifting of pressure by a refrigerant pump; this process can be ideally considered as isentropic. The pump power can be expressed by the equation 43.

$$W_p = \frac{W_{p,ideal}}{n_p} = \frac{\dot{m}(h_2 - h_1)}{n_p} \quad (43)$$

Where  $W_{p,ideal}$  is the ideal power of the pump in Watt,  $\dot{m}$  is the working fluid mass flow rate in kg/s,  $n_p$  is the % isentropic efficiency of the pump, and  $h_1$  and  $h_2$  are the enthalpies of the working fluid in Joules at the inlet and outlet of the refrigerant pump for the ideal case.

Process 2→3 (Evapourator): This is a constant-pressure transfer of heat. The evapourator heats the working fluid at the pump outlet to the turbine inlet condition. The heat transfer rate from the evapourator into the working fluid is given by equation 44.

$$Q_e = \dot{m}(h_3 - h_2) \quad (44)$$

Where,  $h_3$  and  $h_2$  are the enthalpies of the working fluid at the exit and the inlet of the evapourator, respectively.

Process 3→4 (Expander): The scroll expander converts heat energy into electrical power. Ideally, this is an isentropic process for dry working fluids. However, in fact, the efficiency of the energy transformation in the turbine is generally low. The scroll expander power is given by equation 45.

$$W_{scroll} = W_{scroll,ideal} n_{scroll} = \dot{m}(h_3 - h_4) n_{scroll} \quad (45)$$

Where  $W_{scroll,ideal}$  is the ideal power of the scroll,  $n_{scroll}$  is the scroll's isentropic efficiency, and  $h_3$  and  $h_4$  are the enthalpies of the working fluid at the inlet and outlet of the scroll.

Process 4→1 (Condenser): This is a condensation process in the condenser and the working pipes. In this process the working fluid is cooling down and the condenser heat rate can be expressed by equation 46 as follows.

$$Q_c = \dot{m}(h_1 - h_4) \quad (46)$$

Where,  $h_1$  and  $h_4$  are the enthalpies of the working fluid at the outlet and the inlet of the condenser, respectively.

### 3.1.2 Performance of the System

The performance of the system is evaluated in terms of the overall organic cycle efficiency, the isentropic effectiveness and the filling factor of the scroll expander.

The total cycle (thermal) efficiency of the ORC is defined as the ratio between the net power of the cycle and the evaporator heat rate (equation 47).

$$n_{cycle} = \frac{W_{scroll} - W_p}{Q_e} = \frac{(h_3 - h_4)n_{scroll} - (h_2 - h_1)n_p^{-1}}{(h_3 - h_2)} \quad (47)$$

The scroll expander's overall isentropic effectiveness (%) is defined by the ratio of the measured shaft (electrical) power and the isentropic expansion power (equation 48).

$$\mathcal{E}_s = \frac{W_{sh}}{\dot{M}_{meas}(h_3 - h_4)} = \frac{W_{scroll} - W_{loss}}{\dot{M}_{meas}(h_3 - h_4)} = \frac{W_{scroll} - 2\pi N_{rot} T}{\dot{M}_{meas}(h_3 - h_4)} \quad (48)$$

Where,  $\dot{M}_{meas}$  is the measured mass flow rate (kg/sec),  $W_{sh}$  (Watt) is the expander shaft power which is split into the internal expansion power  $W_{scroll}$  and the mechanical losses  $W_{loss}$  due to friction between the involute scrolls and losses in the bearings. These losses can be expressed as a function of the mechanical losses by the torque  $T$  (Nm) and by the rotational speed  $N_{rot}$  ( $sec^{-1}$ ) of the expander.

The filling factor  $\Phi_{meas}$  represents the volumetric performance of the scroll expander (equation 49). It is defined as the ratio between the measured mass flow rate and the mass flow rate theoretically displaced by the expander. It increases with internal leakage and supply cooling down, but decreases with the supply pressure drop [8].

$$\Phi_{meas} = \frac{\dot{M}_{meas} \cdot u_{su}}{\dot{V}_s} \quad (49)$$

Where  $u_{su}$  is the supply specific volume ( $m^3/kg$ ) and  $\dot{V}_s$  is the isentropic volume flow rate of the scroll ( $m^3/sec$ ).

### 3.1.3 The Scroll Expander

A scroll is a device that uses two interleaved spiral shaped scrolls to compress or to expand mainly refrigerants which are used as the working fluid for these systems. In this case it is used as an expander. One of the scrolls is fixed whilst the other orbits eccentrically without rotating, thereby the working fluid is trapped and simultaneously expands into the gas pockets between the scrolls. Crescent shaped gas pockets are formed bounded by the two involute scrolls and the base of each involute. As one scroll is orbited with respect to the other, the gas pockets move from the centre towards the outer periphery and increase in size causing expansion. In addition no valves are needed in the scroll expander unit. Eventually, the noise and vibrations are restricted while the durability of the unit is improved. Finally only a small number of moving parts are required and the rotary motion can be completely balanced.

The operation of the specific scroll used in this study consists of three distinctive phases figure 11. In the first phase, the working fluid enters the central chamber of the scroll where it expands instantly setting the scroll into operation (Blue Colour). In the second phase, the working fluid travels inside the formed closed chambers along the fixed scroll, dropping in pressure and temperature (Purple Colour). In the third phase, the chamber is not closed and the working fluid leaves the scroll (White Colour), eventually discharging into the rest of the system continuing the ORC.

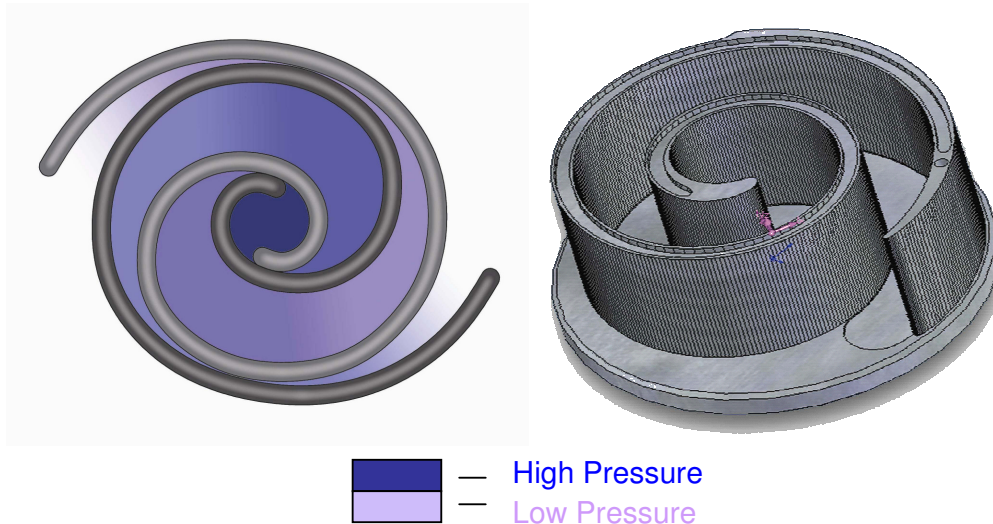


**Figure 11: Scroll expander operation process**

The scroll which was used for this report is a small volumetric negative displacement device driven by the working fluid. It operates in a high pressure ratio 5:1 between the suction and the discharge valve. The particular scroll expander has an inlet volume of  $13.75 \text{ cm}^3$  and an outlet volume of  $31.625 \text{ cm}^3$ , giving a volumetric expansion ratio of 2.3. The rotational velocity of the scroll is 2800 to 3300 rev/min with an eccentricity diameter of 10 mm.

### 3.1.4 Efficiency Drop

Heat transfer, leakage and scroll geometry are the main aspects for the efficiency drop of the scroll expander. The first two parameters are responsible for the reduction of the volumetric efficiency of the working fluid. The scroll geometry can generate severe wear problems like cavitation and further abrasion [168-169].

Leakage is one of the main concerns for the performance improvement of the scroll expander since it is directly related to the surface damage and the excessive wear of its main components. There are two main paths of leakage inside the scroll (figure 12). One path derives from the gap which is created between the bottom or the top plate and the scrolls while the second path is formed by a gap between the flanks of the two scrolls. The first kind of leakage is called radial leakage while the second one is called flank or tangential leakage. This study is concerned with the radial leakage as the critical damage extends to the bottom and the top regions of the scroll expander.

The design requirements of the scrolls are very strict. The manufacturing requires a very high degree on assembly in order to minimize any undesirable machining tolerances. The working

surfaces of the scrolls are inner surfaces and are very difficult to be perfectly machined. In the case of large components the larger the machine tolerances the greater will be the quantity of the scroll's leakage [170].

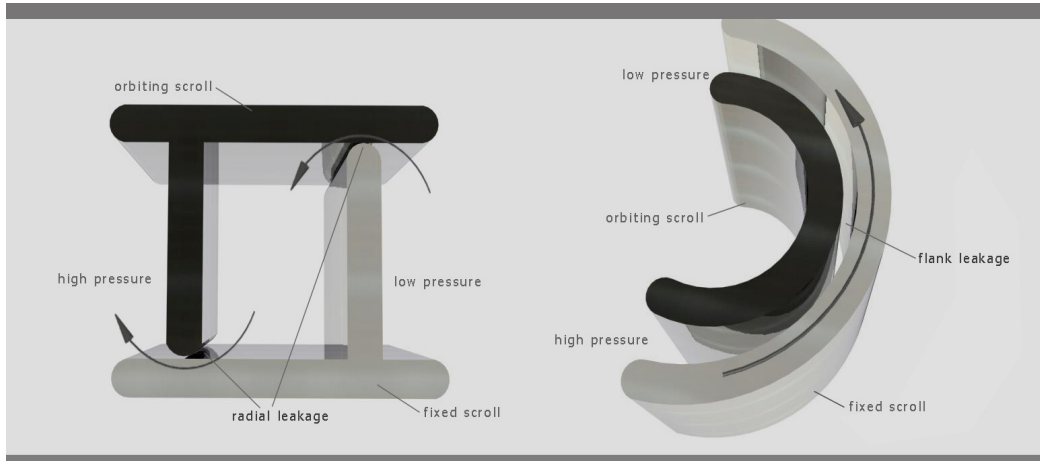


**Figure 12: Two kinds of leakage, radial and flank, of the scroll expander**

Furthermore, some scrolls vary in design. Some of them have thickened lobes on the inner most wraps of the labyrinths which seal off the scroll chambers from the entrance port and provide higher resistance to axial and shear stresses produced by the expansion impact from the working fluid. Some others maintain a minimum opening chamber presented to the inlet port, like the actual ones used in this project. Either way the scroll's first chamber fills with gas at a constant pressure. The inlet port is therefore blocked by the labyrinths of the scroll and the chamber is hermetically sealed off. From that point onwards the central pocket drops in pressure as it expands.

There are thus many complications regarding the scroll's performance and durability. As reviewed by C. Cuevas et al [171] higher rotation speeds or pressure ratio can steeply increase the refrigerant exhaust temperature which can chemically degrade the lubricant and the refrigerant, leading the scroll system to a thermal mechanical failure. Moreover, L. Paramonov [172] has found that a high pressure ratio results in a high start up friction torque while the high pressures will introduce more efficiency losses. Apparently, the biggest problem is the leakage of the gas which is responsible for the reduction of the volumetric efficiency of the working fluid. According to P. Howell [173], typically the gap is around 1 micron ( $\mu\text{m}$ ) across. However, this may be increased by wear or poor machining, and it is known that if it reaches around 8 microns ( $\mu\text{m}$ ), the scroll can become useless.

### 3.2 Case Study

Three different scroll expanders connected in a micro-CHP experimental system were tested under the same operational conditions for three different periods of time 100, 300 and 1000 hours respectively. Thereafter, a thorough surface investigation was conducted on those scroll expander systems (SE<sub>100</sub>-SE<sub>300</sub>-SE<sub>1000</sub>). The SE<sub>100</sub> and SE<sub>300</sub> had the same design with an inlet port of 8 mm diameter and a wall height of 3 cm. The SE<sub>1000</sub> had a slightly different design with 6 mm inlet diameter and a 1.5 cm wrap height. The inlet velocity of the working fluid (refrigerant) was accurately measured to be 16 m/sec for the higher scrolls (SE<sub>100</sub>-SE<sub>300</sub>) and 31 m/sec for the shorter scroll (SE<sub>1000</sub>).



**Figure 13: Main parts of the scroll expander used for tribological tests**

The distinction of the above scroll types regarding their design is proven to be a critical parameter for the generation of the cavitation phenomenon and for the interpretation of the cavitation mechanisms. In theory, the smaller the expansion area is, the higher is the efficiency that can be achieved by the scroll expander. However, in a prolonged period of

time, e.g. during the operational period of a domestic micro-CHP system, cavitation can be considered as a critical issue as far as the lifecycle of the system is concerned. Thus, design implications, from a tribological point of view, can play a crucial role in improving the service life of the system.

The critical components for durability were identified on the tip seal, the steel plate and the side walls of the scroll expander (figure 13). The experimental tests of this study were focused on the radial leakage points between the bottom plate and the tip seal of the scrolls. Thus, sliding friction/wear tests were conducted using the actual materials of those components, in order that their tribological performance could be evaluated and their wear/friction attributes thoroughly interpreted.

### 3.2.1 Chemical Analysis

The surface analysis initially focused on the surface of the steel plate and on the side walls of the scroll (figure 13). Initially the steel sample was etched in a solution of 2% Nital in order for its grain structure to be determined. Then with the help of an Optical Emission Spectrometer (OES) the steel sample was effectively distinguished in its chemical elements (table 1). The analysis showed that the steel plate's structure comprises of isolated spheroidal carbides (light dots) in a matrix of tempered martensite (figure 14 A). The scrolls' chemical analysis showed that the base material structure comprises of a fine silicon eutectic in a matrix of an aluminium solution with isolated intermetallic compounds (table 2).

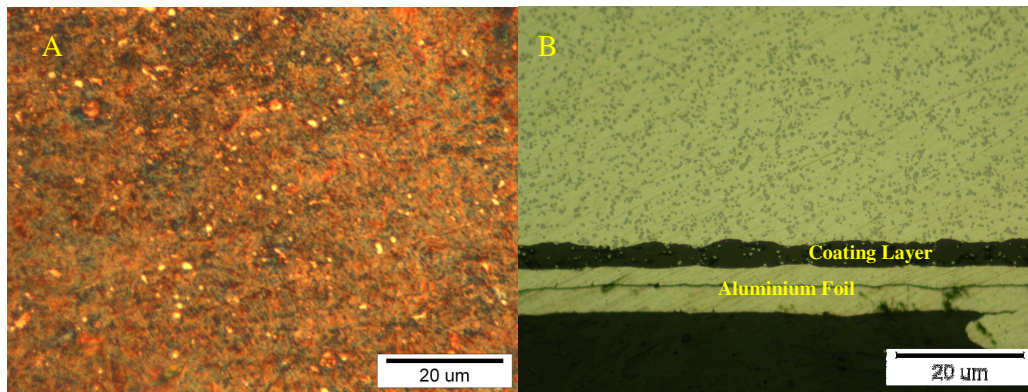


Figure 14: Material structure of A) Steel plate B) Coating scroll

Steel Plate	%C	%Mn	%Si	%S	%P	%Cu	%Ni	%Cr	%Fe
Wt%	0.96	0.53	0.27	0.003	0.021	0.01	0.02	0.18	REM

Table 1: Chemical analysis of the scroll's steel plate

Scrolls	%Si	%Fe	%Cu	%Mg	%Cr	%Ti	%Ni	%Mn	%Al
Wt%	11.32	0.22	3.58	0.45	0.01	0.03	0.01	0.01	REM

**Table 2: Chemical analysis of the two scrolls**

Tip Seal Bulk Material	%F	%Si	%Ca
Wt%	96.39	2.54	1.07

**Table 3: Chemical analysis of the tip seal**

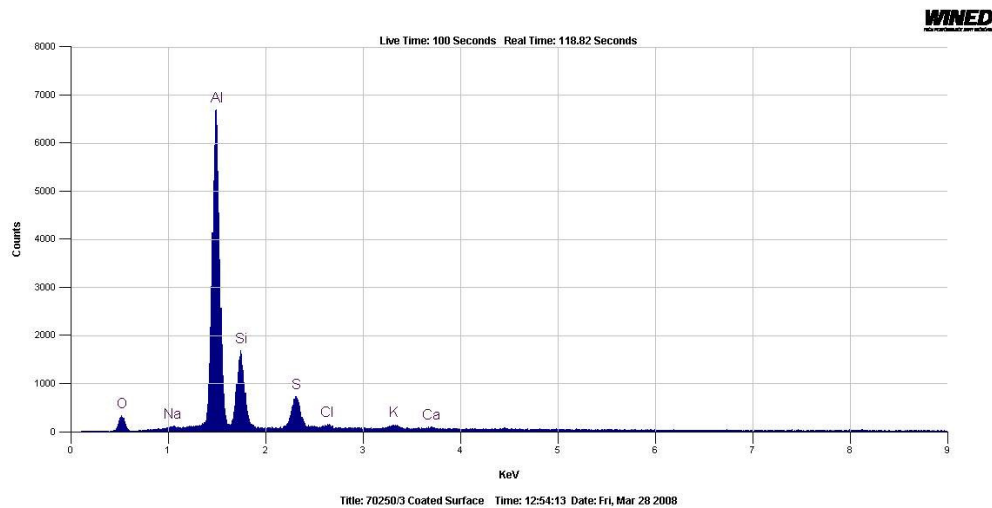
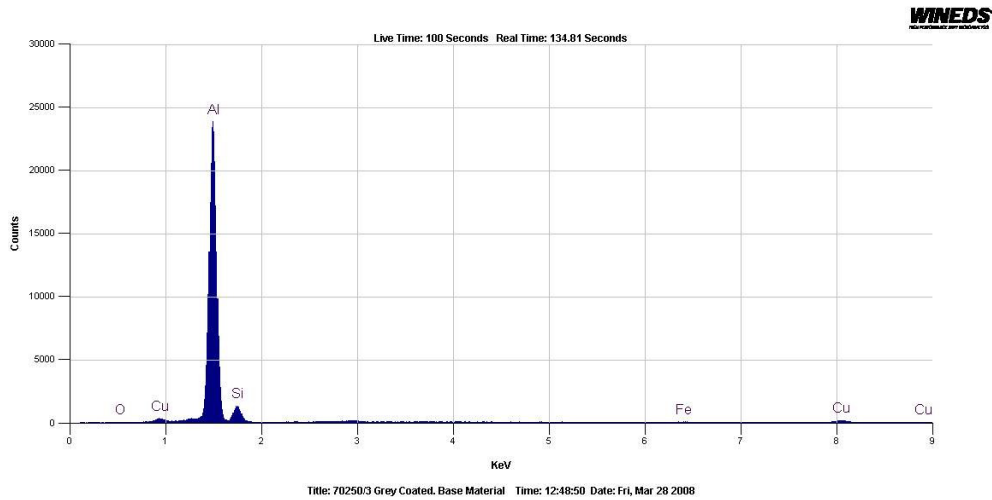


**Figure 15: EPMA analysis a) of the scroll's base material b) of the anodic film**

The anodic film/layer is the black layer between the silicon containing base material and the outer aluminium foil (figure 14 B). This foil wrap is only used to help resolve the anodic film. The anodic film is hard and non-conductive and increases the wear resistance of the scroll.

The type of the layer coating across the orbiting scroll is developed using an anodizing process, immersing the scroll in a bath of sulphuric acid.

With the use of an optical microscope the thickness of the coating was measured. It was found to be 20 microns. Silicone particles appear as translucent black dots across the surface of the aluminium base material. The presence of these dots implies the high concentration of silicon in the composition of the aluminium. This can also be observed on the EPMA graphs (figure 15). The method used for the construction of the scroll was probably high pressure die casting, and so the addition of silicon and copper particles increases the performance of the aluminium base material. Silicon increases melt fluidity accommodating the manufacturing process of the scroll while copper increases hardness reducing the ductility of the material.

The tip seal is a reinforced fluoroelastomer material in a matrix of a fluorine mixture reinforced with short fibres of inorganic particles like  $\text{CaF}_2$  or ceramic particles like  $\text{SiO}_2$  and  $\text{SiC}$  in the size of a few microns (maximum  $100\ \mu\text{m}$ ).

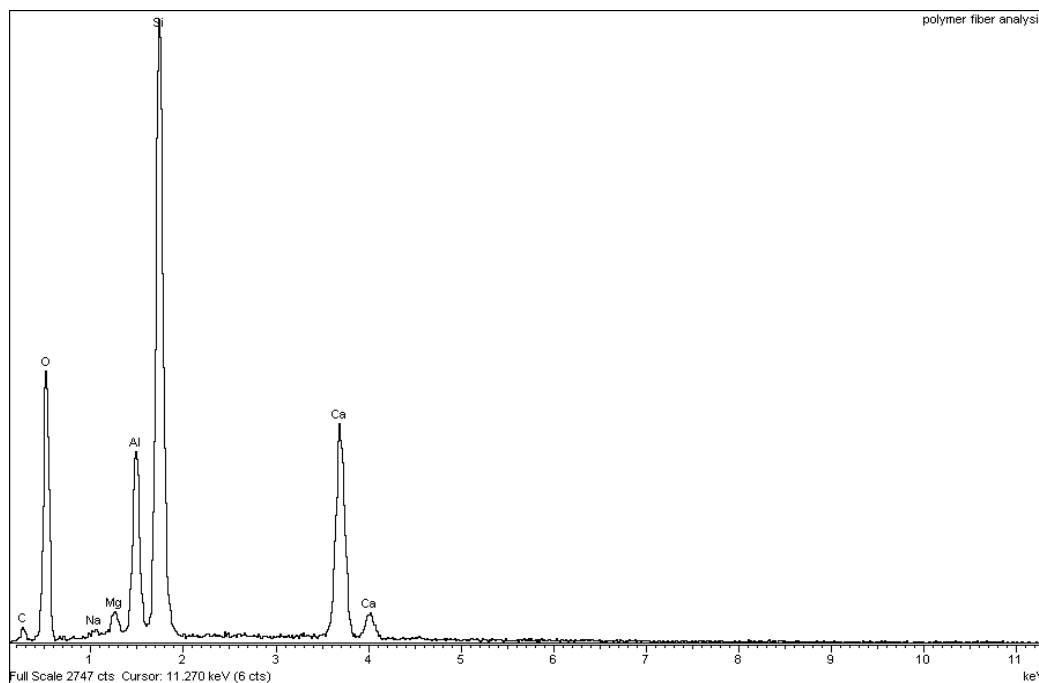


**Figure 16: EPMA analysis of isolated fibres within the matrix of the fluoroelastomer tip seal**

As the analysis of reinforced polymers is complicated, the specific chemical analysis of the fluoroelastomer tip seal was done in two steps. In the first step the bulk material was analysed with the use of a Scanning Electronic Microscope (SEM) and the results of its chemical

analysis are illustrated in table 3. In the second step isolated fibres were analysed with the use of the Electron Probe Micro Analyzer (EPMA) and the results are depicted in figure 16.

### 3.2.2 Surface Analysis

A thorough surface examination of the main components for all of the scrolls (SE<sub>100</sub>-SE<sub>300</sub>-SE<sub>1000</sub>) was conducted. The interpretation of the wear and cavitation mechanisms for the high carbon steel plate was successfully completed. For the side scrolls the examination of their damaged surfaces proved to be complicated because of their circular geometry and their size. The scrolls could only be fitted under the optical microscope. Hence, observations and measurements were performed only with this type of microscope. For the tip seal not many conclusions were drawn from the initial surface investigation. The black colour, the high level of elasticity and the good wear behaviour of the tip seal, made the tribological investigation extremely difficult. The deformation of the surface shape and roughness was minimal and impossible to be identified. Thus, only the experiments with the use of the TE 57 (Chapter 5) interpreted the wear mechanisms of that highly efficient material against the steel plate.

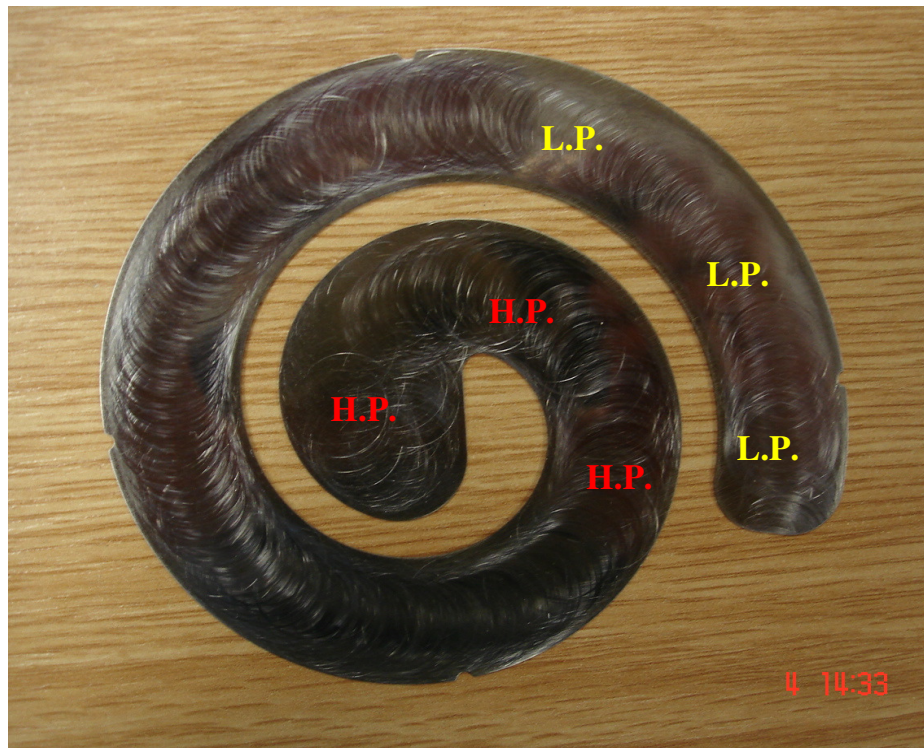


**Figure 17: Circular wear marks on the high and low pressure regions of the scroll's steel plate**

The surface analysis of the steel plate showed the wear mechanisms which are dominative during the operation of the scroll. The process which was followed to enable the surface of

the steel plate to be thoroughly analysed, consisted of the use of three different microscopes, an optical, an electronic (SEM) and an interferometer (ZYGO) microscope. Moreover the investigation focused on two different regions of the scroll (figure 17). These were the high pressure region (H.P.) and the low pressure region (L.P.).

### **3.2.2.1 Two- and Three-Body Abrasion**

The first interesting observation that was extracted examining all the scroll steel plates was the different nature of the wear marks between the high and the low pressure region figure 18. Characteristically, on the low pressure region of the SE<sub>300</sub> the linear grooves are more superficial and not so deep with an average depth of 0.5-1 micron. In contrast to that, on the high pressure region the marks are about 3 times wider and around 4 times deeper with an average depth of 2-4 microns. Interestingly, in the high pressure region linear wear marks with a maximum depth of 7-8 microns were also identified. This is rough evidence of what was expected to be seen in the experiments with higher condition temperatures.

Moreover, the wear which is even obvious to the naked eye and prevails not only on those two regions but across the whole surface of the scroll's plate can be determined as a two-body abrasive wear. Two-body abrasive wear derives from the sliding contact of the steel plate and the hard particles of the reinforced polymer.

On the SE<sub>1000</sub> wear marks was slightly denser especially in the high pressure region, although they had a similar size and depth with linear grooves found on the SE<sub>300</sub>. Thus, through out an extended period of time the wear rate of the high carbon steel plate against the tip seal seems to have stabilized or even reduced, preventing any excessive wear which could seriously affect the life cycle of the scroll. This performance was also observed in the TE 57 experiments as it will be analysed in Chapter 5.

In figure 19 the two distinctive wear modes found in the majority of the wear areas of the steel plate, are illustrated. In figure 19 (A-C) the linear pattern is disrupted and aggressive damage across the sides of the track is evident. It appears that a wedge-forming mechanism by a sharp wedge-like wear particle has been generated across the edges of the linear groove. The sharp wedge-like wear particle has built up a continuing wedge grooving. Sliding takes place at the bottom of the wedge where adhesive transfer of a thin layer from the underlying counterface continues to increase the size of the wedge slowly. This wear mode appears as a combined effect of adhesion at the interface contact and shear fracture at the bottom of the wedge.

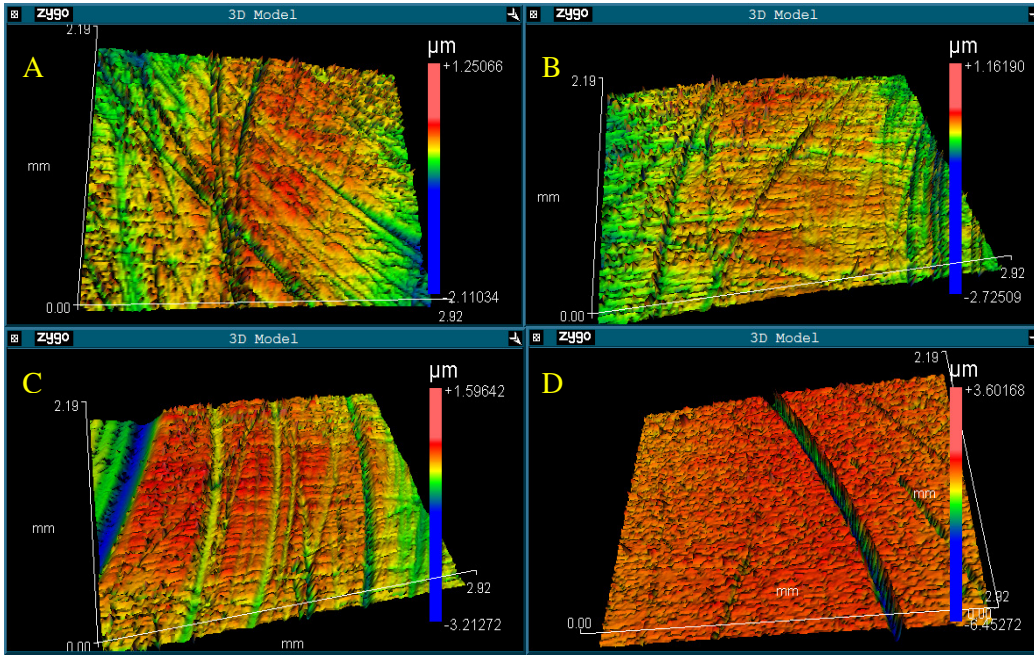


**Figure 18: Different wear regions across the scroll's steel plate after 300 hours of continuous operation: A&B) Low pressure region, average depth of the wear marks 0.5-1  $\mu\text{m}$ . C&D) High pressure region average depth of the wear marks 2-4  $\mu\text{m}$**

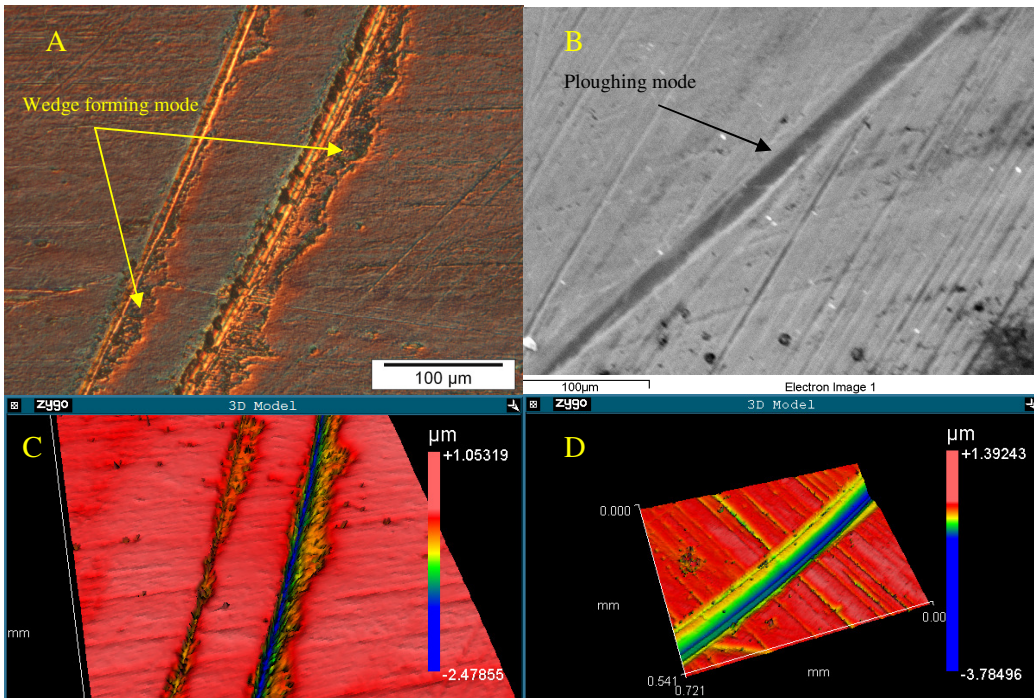


**Figure 19: The different wear modes formed by two-body abrasive wear on the 1000 working hours scroll expander A-C) Wedge forming mechanism B-D) Ploughing wear mode**

In contrast, a ploughing wear mode is observed in figure 19 (B-D). The consequence of ploughing is that a certain volume of surface material is removed and a smoother abrasive

groove is formed. However, in ploughing mode, the wear particle is not generated. Thus by looking at these two distinctive wear modes it can be said with certainty, that wedge-forming wear is responsible for the generation of third-body wear damage.

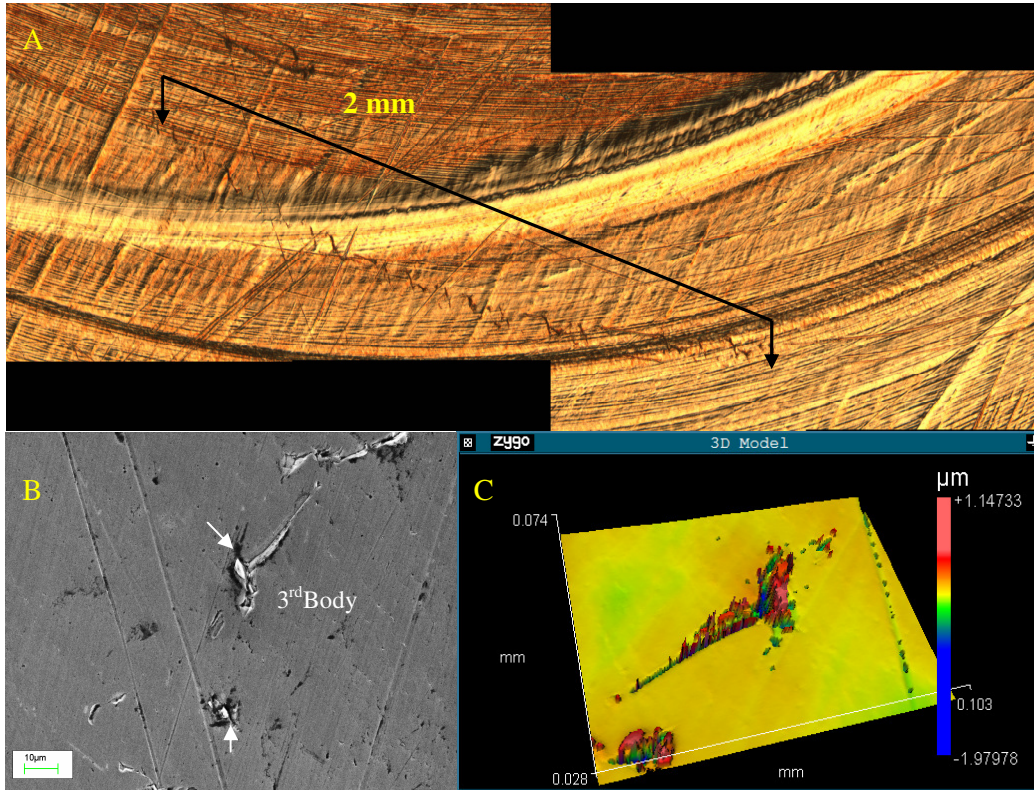


**Figure 20: A) Overview of the river marks formed across the steel plate B) A close up of an individual river mark C) Surface profile of the river marks**

Three-body abrasion wear was identified in many areas of the scroll's steel plate. On the low pressure region detailed river marks (figure 20) were detected. What is more interesting is that they do not follow the path of the wear circular marks but have a totally different direction figure 20 (A). The SEM showed (figure 20 B) that the three-body abrasion is the clue to these long rivers, with many cavities have being formed around these areas, something which will be discussed in detail in Chapter 3 and 6. The figure 20 (C) also highlights the formation of a possible fatigue crack developing along the steel plate surface.

In addition, at the high pressure region many long river marks were also observed although having a slightly different nature from the previous one. On these marks the effect of the three-body abrasion wear is more obvious. The material which was removed created deep cracks into the material surface. The depth of these cracks was around 7-10 microns. These cracks can result in a more severe wear regime, see figure 21.

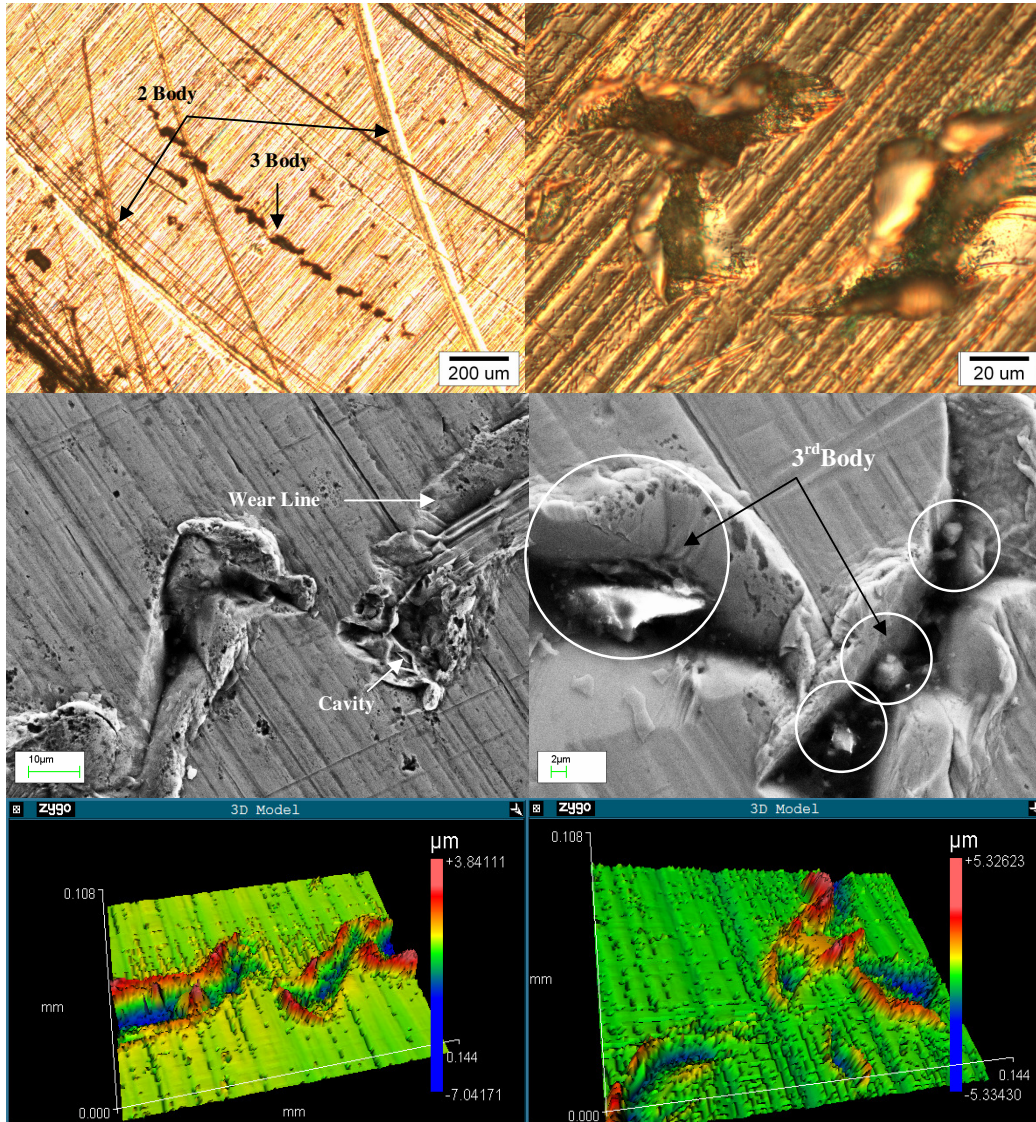


**Figure 21: Two different groups A&B with accumulated three-body wear marks found across the high pressure regions of the scroll's steel plate. The wear marks initially detected with the optical microscope, analysed in detail with the SEM and finally their morphology is thoroughly investigated by ZYGO interferometer.**

In figure 22 the cluster of abrasion cracks and the wedge-forming wear mechanism, co-exist. The length of the cracks is very significant, with consecutive similar shaped cracks indicating the presence of third-particles. Wedge-forming abrasion lines were generated during the wear process. The wear of the steel plate occurs by subsurface deformation which induces crack nucleation. Subsequently, the cracks propagate parallel to the surface. Eventually, thin wear sheets are produced along the surface.

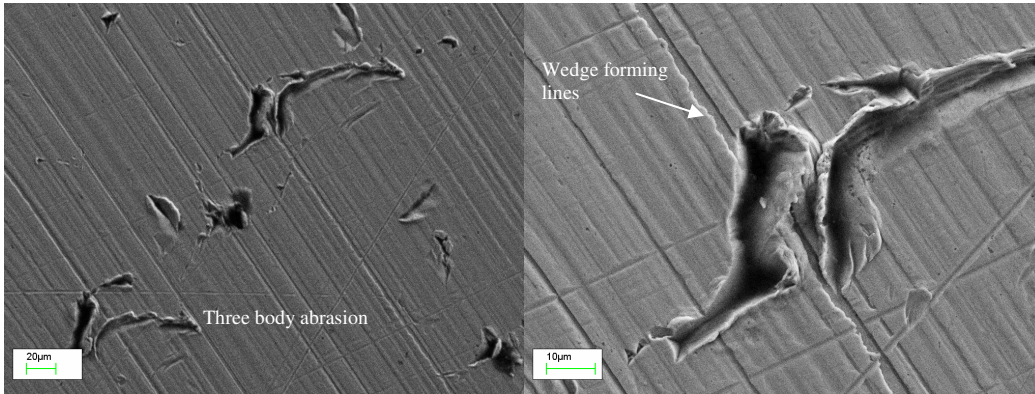


**Figure 22: Consecutive wear marks indicate three-body abrasive wear. Wedge-forming lines are also observed in vicinity areas.**

In figure 23 a step interlayer delamination wear mechanism is observed as a result of the three-body abrasion contact. The steel surface through which the cracks propagate is plastically deformed as a result of the accumulated contact stresses during the sliding contact. Crack growth does not proceed very near the surface because of the large plastic zone around its tip, but is confined to a narrow range of depth where the shear stresses lead to the growth of a crack parallel to the steel surface [174]. The crack turns upwards to the surface and long thin laminar subsurface planar cracks are formed.

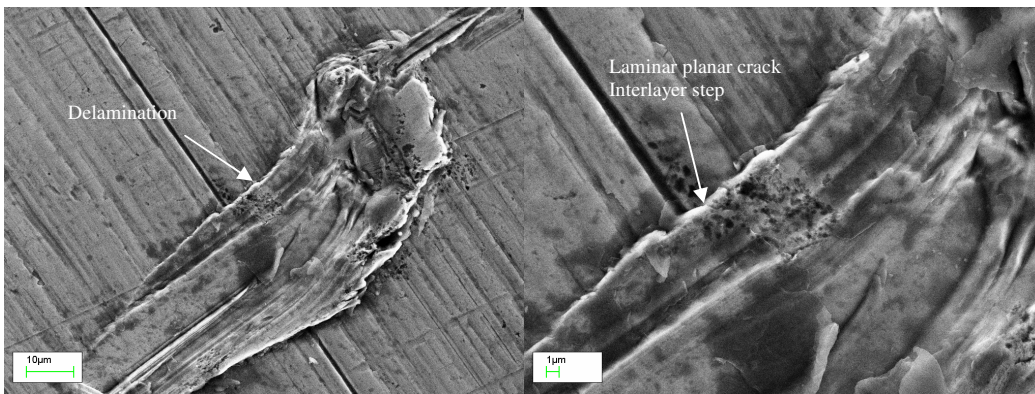


**Figure 23: The interlayer delamination wear mechanism across the steel plate surface. Crack propagates parallel to the surface.**

### 3.2.2.2 Cavitation Erosion

During the investigation of all the scroll plates for any traces of cavitation pits or cavitation clusters, interesting observations were made. Initially, in the SE<sub>100</sub> with the minimum running time, only 100 hours, a total absence of cavities was observed.

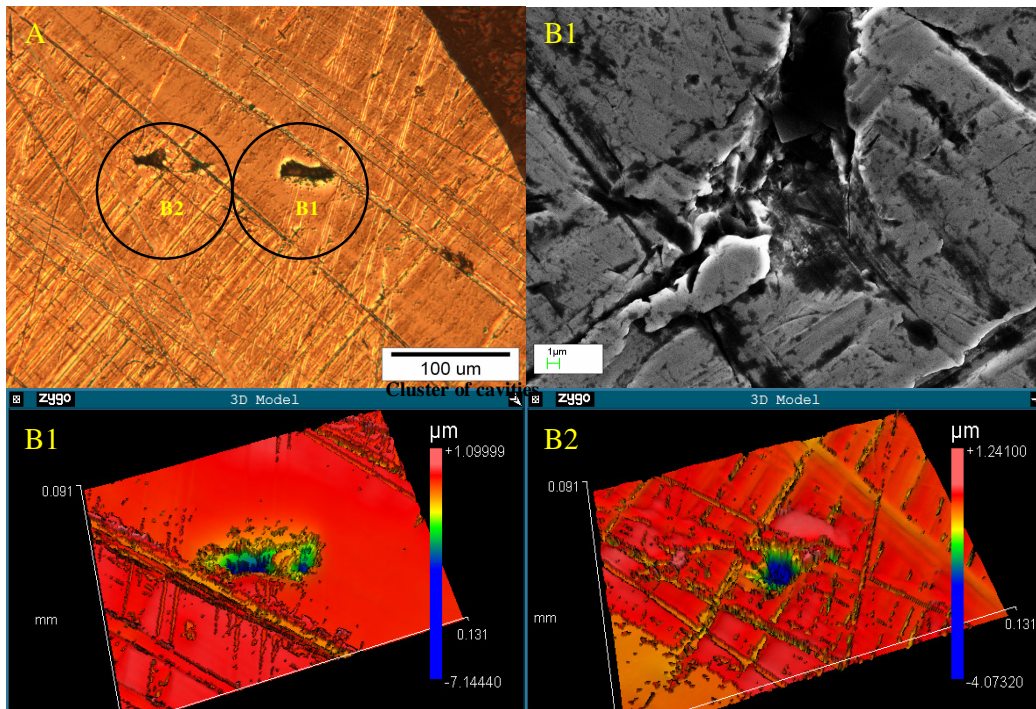


**Figure 24: Cavities across the surface of the steel plate of the SE<sub>300</sub>. A) Cluster of small size cavities B) SEM micrograph of the B1 cavity. B1-B2) Isolated cavities surface profile taken by ZYGO interferometer microscope**

In the SE<sub>300</sub> many cavities were found on different spots across the surface of the steel plate, implying the presence of random cavitation effects. A few random points were identified with a cluster of cavities in a very small size, a couple of microns, across many different areas of the scroll. Also evidence of isolated round-shaped and bigger size cavities were spotted at many different points, especially in the high pressure region (figure 24 A). SEM image (figure 24 B1) shows how destructive the cavitation impact can be while their characteristic geometries were defined with the interferometer microscope (figure 24 B1-B2).

Finally, during the surface analysis of the scroll's steel plate with the most operating hours SE<sub>1000</sub>, the cavitation phenomena were even more severe and were easily identified under the microscope. The domestic micro-CHP system was continuously run for a thousand hours. After the end of the process, the scroll expander of the micro-CHP unit was disassembled and its high carbon steel plates were isolated and sent for surface investigation. This procedure was followed in order to analyse thoroughly the surface of the steel plate. Three different types of microscopes, an optical, an electronic (SEM) and an interferometer (ZYGO) microscope were deployed.

Interestingly, during the surface analysis of the scroll's steel plate, cavitation erosion was easily identified under the optical microscope. Many cavitation pit clusters were spotted across the high pressure regions of the steel plate at the beginning of the expansion process. The cavities were mainly accumulated along the edges of the steel plate, creating a continuous layer of cavities of about 1.5 mm wide on the upper edge (red arrows). Surprisingly, on the low pressure regions of the steel plate, at the end of the expansion cycle, no trace of cavities was found. The part of the steel plate where cavities are developed is illustrated by the arrows in figure 25. The red arrows show the most severe part of the plate governed by consistent cavity clusters. That severe area will be further analysed in Chapter 6. Across the black arrows cavity clusters are more isolated but evenly deep and destructive.

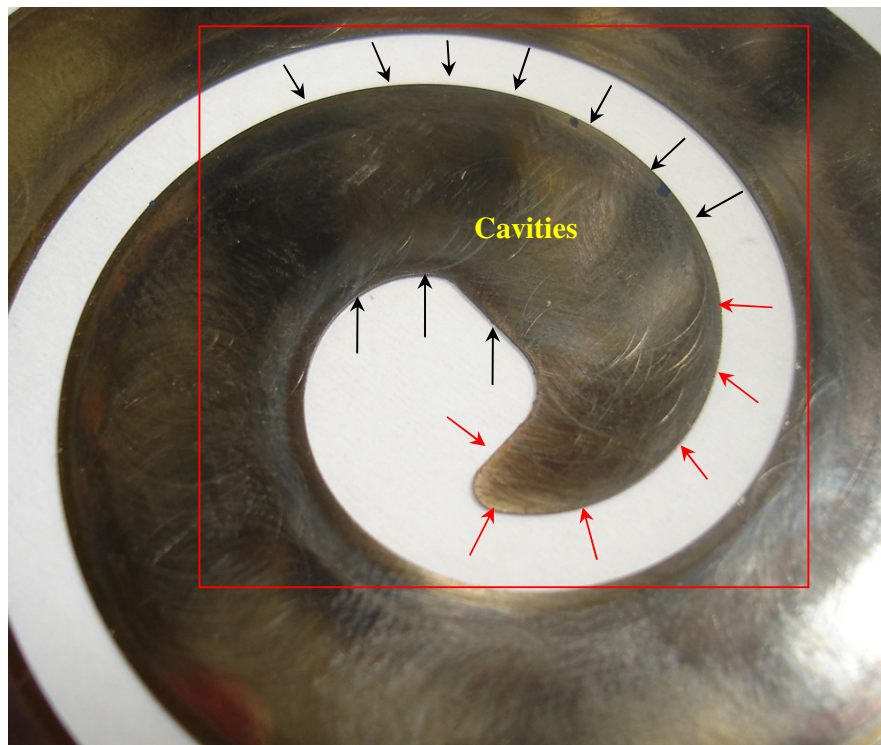


**Figure 25: The high pressure area of the scroll expander  $SE_{1000}$ . Cluster of cavities formed across the edges of the steel plate. Red arrows depict the most severe region damaged by cavitation impact.**

The average width of the steel plate is around 12.5 mm. However, in the areas where cavitation was revealed the width is less, due to the geometrical profile of the plate. Thus, the 1.5 mm width range of the cavities across the edges of the steel plate can be considered as severe damage (figure 26). The existence of cavities can rapidly increase the cavitation process creating deeper holes hence increasing the leakage and reducing the efficiency of the scroll.

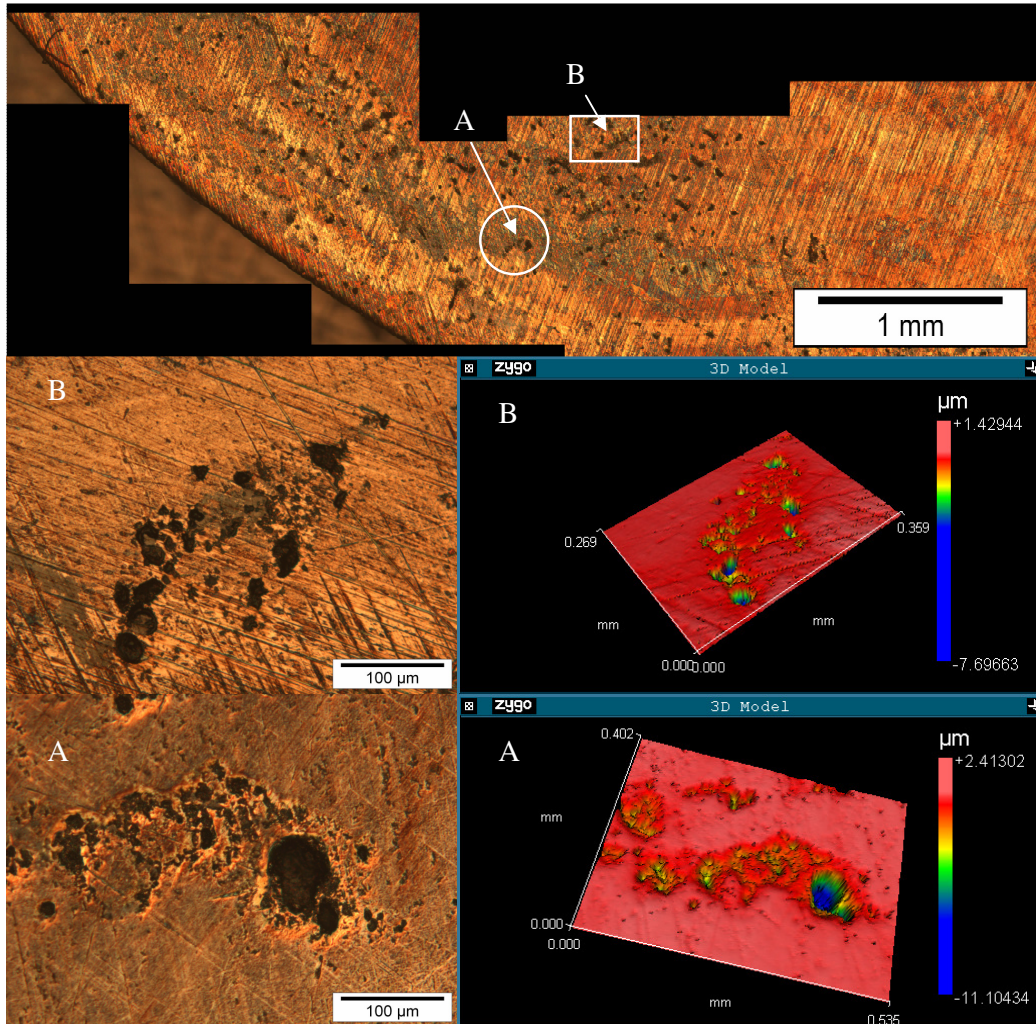


**Figure 26: Cluster of cavities across the high pressure region of the scroll expander SE<sub>1000</sub>. Close-up observation of the cavities with the use of the optical microscope and the ZYGO surface interferometer.**

In the series of pictures in figures 26 and 27, the cavities can be clearly seen and analysed. The average depth of the individual cavities was estimated around 6-8 microns. In some cases the depth of the cavities was up to 10 microns. In addition, the size of their crater and especially their depth was big enough for individual cavities. This can be interpreted by the fact that small cavities, cracks or grooves are attracting bubble implosion, rapidly increasing in their size and transforming their shape under a prolonged period of time into craters. These big cavities were formed due to a consistent and rigorous impact from the bubble implosion inside a single cavity. The growth of cavitation pits is caused largely by the linking up of nearby pits. The process of their enlargement into craters is dependent on time and history.

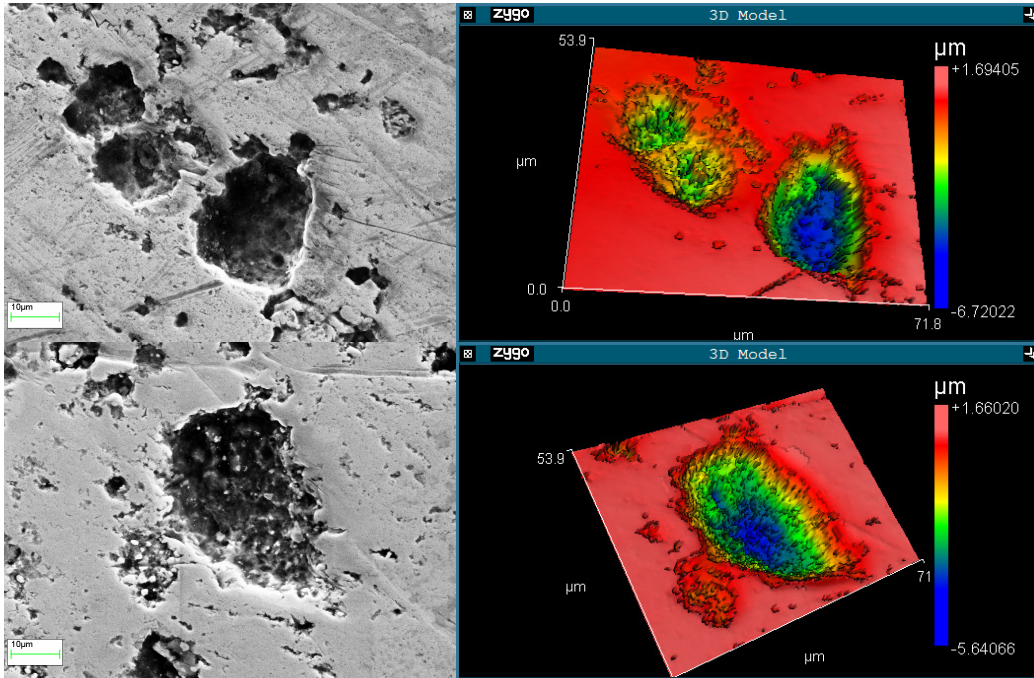


**Figure 27: Characteristic detailed SEM micrographs of the cavities profile. Surface analysis of the specific cavities using ZYGO interferometer microscope.**

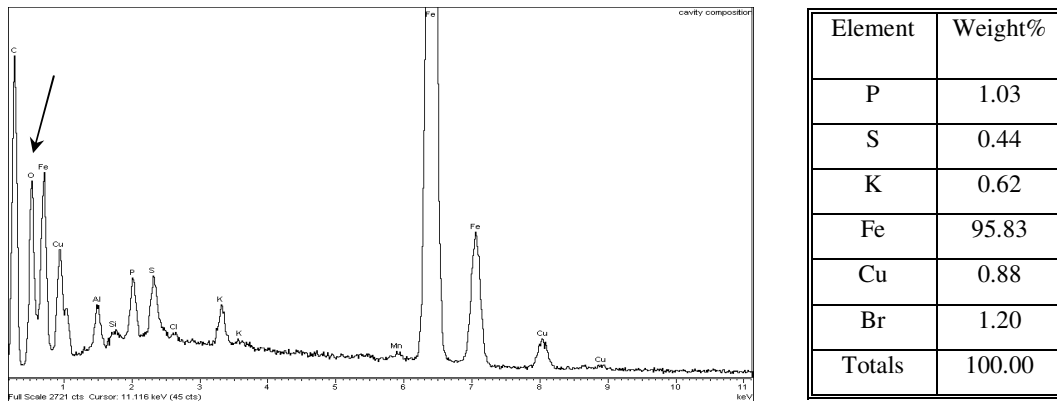


**Figure 28: Chemical composition of a cavity with accumulated oxygen. Chemical composition of a typical cavity. Oxygen traces are absent.**

Furthermore, an alternative scenario for the production of these cavities by the synergetic effect of the possibly corrosive environment is considered. An extensive chemical analysis within the craters of the pits has shown that a small quantity of oxygen ( $O_2$ ) is accumulated in some of the pits while in some others there was a complete absence of  $O_2$  (figure 28). Oxygen is considered as the main element for generating corrosion on a material's surface. On the steel plate the cavities with accumulated  $O_2$  were probably oxidized during the disassembly process prior to being sent for analysis in the laboratory facilities of Bournemouth University.

Thus, there was some time for oxidation/corrosion to be developed and to degradate the samples superficially (Appendix E).

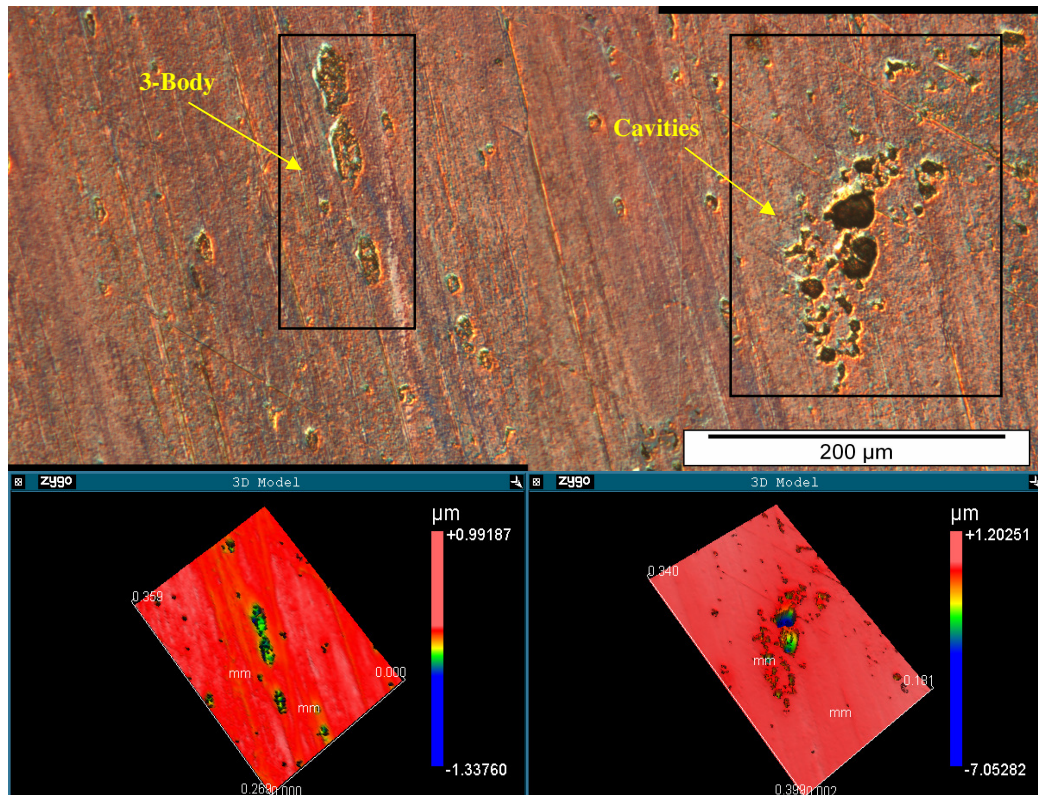


**Figure 29:** Combination of wear mechanisms on the SE<sub>1000</sub> steel plate. Surface analysis of a random area in the high pressure region a) Three-body abrasive wear b) Cluster of cavities

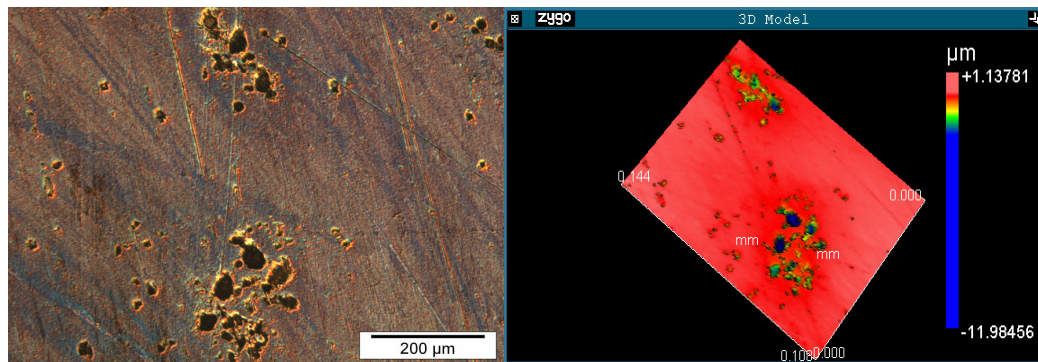


**Figure 30:** Cluster of cavities in a random high pressure area of the SE<sub>1000</sub>. The depth of cavities is highlighted.

In addition, as three-body wear was also identified near to these cavitation areas, it was possible the third-body (particle) was generated by the cavitation phenomena across these areas. The cavities, which are possibly developed by cavitation impact, erode the surface of the steel plate while steel particles are released into the lubricant solution. These particles can

in turn produce three-body abrasion wear during the contact of the two opposite surfaces. This mechanism can be interpreted by the fact that the size of the holes created by three-body abrasion, are similar to the ones created by cavitation impact.

Characteristically, figure 29 reveals the formation of three consecutive wear spots generated by a third-body contact. Nearby, a cluster of cavities has been formed. Apparently, the shape and the morphology of that cluster of pits implies that the pits were generated because of the cavitation impact and not because of third-body wear mechanism. Since the size of the third-body print is similar to the size of the bigger holes in the vicinity cluster, the conclusion which can be drawn is that the third-body is derived as a fragment particle during the destructive damage of those areas by cavitation impact. Additionally, a depth comparison also reveals the distinction of these wear mechanisms. The pit depth derived by the third-body wear mechanism, is five times less than that obtained by the cavitation mechanism. Eventually, cavitation erosion is incorporated with the third-body wear mechanism to produce severe damage. Finally, in figure 30 the depth of another bunch of cavities, in a random area of the high pressure region of the SE<sub>1000</sub>, is highlighted. It can be clearly seen that the cavities propagate into the substrate to a significant depth of more than 10 µm.

### **3.3 Cavitation Mechanism Analysis**

The environmental conditions inside the scroll during its operation, are not adequate enough (having checked the thermodynamic properties of both working fluids) to produce a physical augmentation of the vapour pressure, of the liquid mixture (refrigerant/lubricant) in order to accelerate the formation of the bubbles. Thus, the question is to ascertain which of the two scroll fluids produce the cavitation damage and by which mechanism. At first glance the pressure and temperature conditions inside the scroll expander are such that the lubricant liquid has no chance to change from liquid to gas phase (to produce bubbles). The refrigerant which enters the scroll as gas at high temperature (around 150 °C) is supposed always to remain in a gas state. Thus, the means of generating cavitation by instantaneous transformation of phases from liquid to gas is complex.

The interpretation of the generation of cavities along the steel plate surface was a complicated issue. Two different hypotheses were made aiming to explain to a certain extent the cavitation erosion mechanisms. Since the cavitation pits were found only across the high pressure region of the scroll, where the first stage of the expansion process is taking place, a correlation was developed between the pressure conditions and the jet velocity of the stream, the design aspects of the scroll and the performance of the working fluids (refrigerant/lubricant).

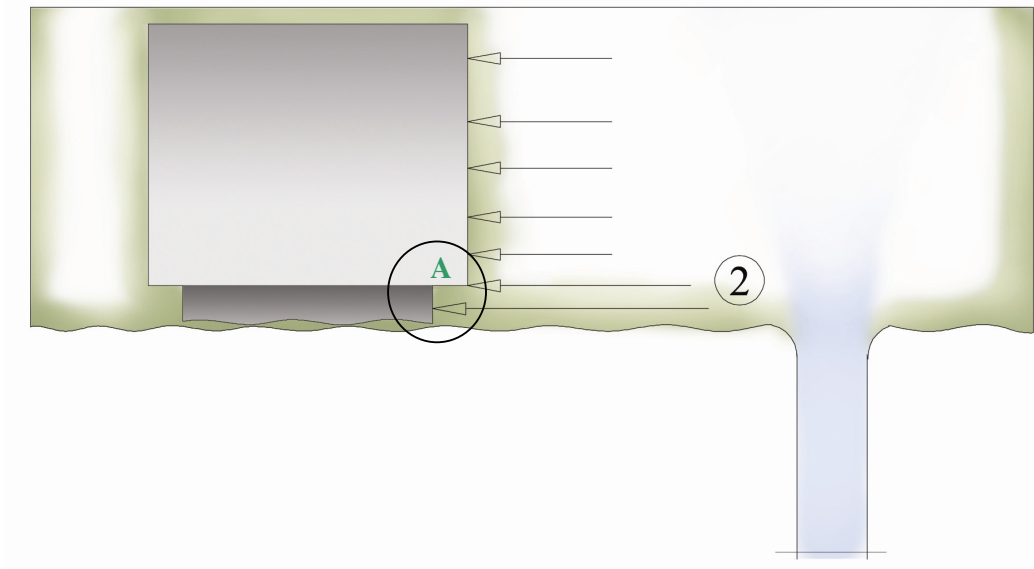


**Figure 31: The second step of the expansion process where the side walls of the scroll pushed by the working fluid. The critical area “A” is presented.**

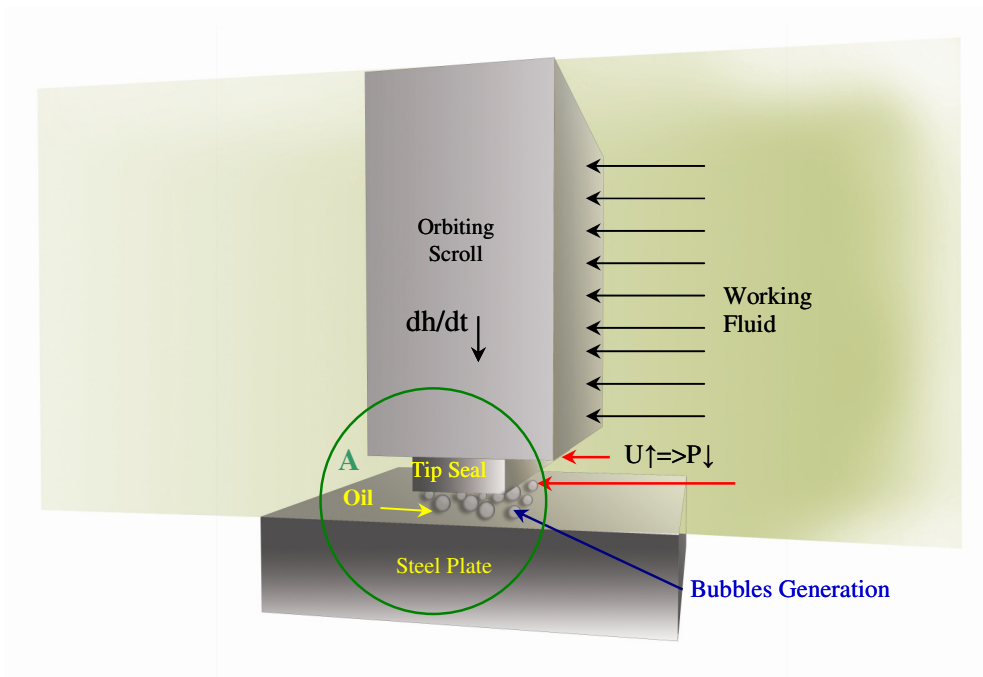


**Figure 32: Schematic interpretation of the cavitation mechanism in the critical area “A”**

The first hypothesis relates to the theory of the squeezed films within parallel surfaces. The concept of the squeezed films involves two parallel sliding surfaces with their relative normal velocity squeezing the lubricant out of the contact area. When the surfaces move towards each other, positive pressures are developed. However, when the surfaces move apart, negative pressures dominate leading to cavitation bubbles in the fluid film. Thus, in a system where

positive and negative squeeze occurs in the presence of a liquid working fluid, cavitation is almost inevitable.

This mechanism can be applied in the scroll expander system during its operation. After the first expansion pocket the working fluid aggressively pushes the scroll side wall to instantly move as figure 31 illustrates. Hence, the second step of the expansion process which sets the scroll into operation occurs. As the working fluid pushes the orbiting scroll the protection lubricant film is simultaneously pushed. The tip seal and the steel plate trap and squeeze the moving lubricant in the critical area “A”. This process is further enhanced by the vibration effects during the operation of the scroll. Apparently, negative and positive pressure areas are developed. The cavitation incubation mechanism is generated (figure 32).

The cavitation mechanism generated by the squeezed opposed surfaces of the tip seal against the steel plate, is explained in detail in figure 33. A close up of the critical area “A” reveals the generation of the cavitation mechanism. To illustrate the principles involved in this cavitation mechanism, the existing two sliding surfaces, the polymer tip seal and the high carbon steel plate of the scroll expander, are considered to be parallel with very smooth roughness surfaces. Using the Reynolds equation for the equilibrium of an element and the continuity of the flow in a column, with the squeeze term of velocity  $dh/dt$  included, the pressure distribution, the applied load and the squeeze time were defined.

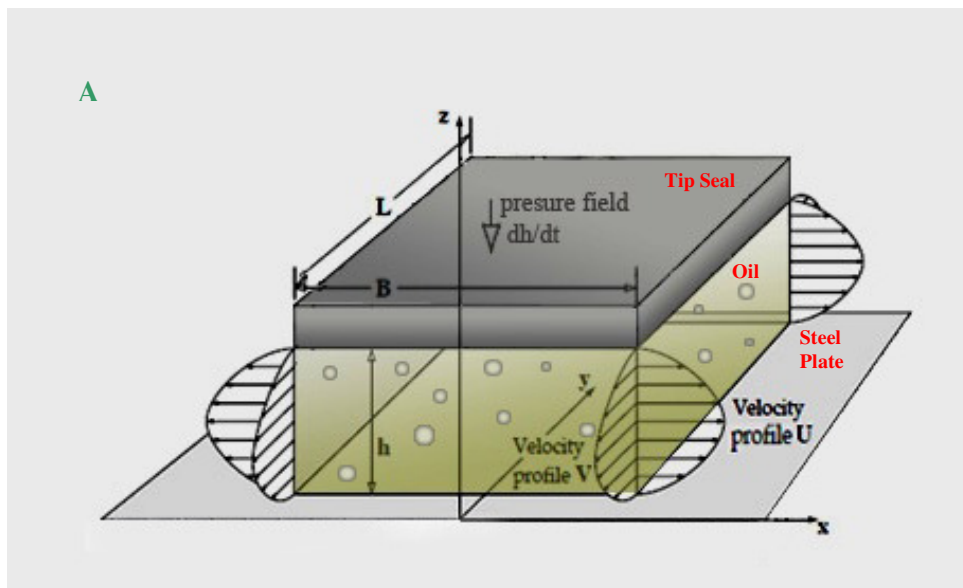


Figure 33: Schematic representation of the squeeze film between the tip seal and the steel plate

From the equilibrium of an element in a lubricated environment the fluid velocities can be obtained (equation 50). Hence, in the equilibrium the following expression is applied.

$$\frac{d\tau_x}{dz} = \frac{dp}{dx} \text{ and } \frac{d\tau_y}{dz} = \frac{dp}{dy} \quad (50)$$

Thus the velocities for the x and y axis respectively can be expressed from the following equation 51.

$$u = \left( \frac{z^2 - zh}{2\mu} \right) \frac{dp}{dx} + (U_1 - U_2) \frac{z}{h} + U_2 \text{ and } v = \left( \frac{z^2 - zh}{2\mu} \right) \frac{dp}{dy} + (V_1 - V_2) \frac{z}{h} + V_2 \quad (51)$$

Where  $\tau_x$  and  $\tau_y$  are the shear stress (Pa) acting in the x and y axis respectively, p is the pressure (Pa), u and v are the surface velocities (m/sec) in x and y axis respectively,  $U_1$  and  $U_2$  are the velocities (m/sec) in the upper and the lower boundary of the x axis and  $V_1$  and  $V_2$  are the velocities (m/sec) in the upper and the lower boundary of the y axis, h is the film thickness (m) and  $\mu$  is the absolute viscosity (Pa·s)

From the continuity of flow in a column of lubricant the equation 52 is derived. Flow rates ( $\text{m}^3/\text{sec}$ ) per unit length,  $q_x$  and  $q_y$ , expressed by equation 53, can be found from integrating the lubricant velocity profile (equation 51) over the film thickness.

$$\frac{dq_x}{dx} + \frac{dq_y}{dx} + (w_h - w_0) = 0 \quad (52)$$

Where:

$$q_x = -\frac{h^3}{12\mu} \frac{dp}{dx} + (U_1 + U_2) \frac{h}{2} \text{ and } q_y = -\frac{h^3}{12\mu} \frac{dp}{dy} + (V_1 + V_2) \frac{h}{2} \quad (53)$$

The term  $(w_h - w_0)$  is the vertical flow across the film which describes the rate of change in the film thickness, where  $w_h, w_0$  is the velocity at which the column moves up and down respectively (*the squeezing term dh/dt*). Assuming that surface velocity in y axis is zero  $V=0$  then:

$$\frac{d}{dx} \left( \frac{h^3}{\mu} \frac{dp}{dx} \right) + \frac{d}{dy} \left( \frac{h^3}{\mu} \frac{dp}{dy} \right) = 6U \frac{dh}{dx} + 12 \frac{dh}{dt} \quad (54)$$

Where, U is the surface velocity (m/sec) in x axis defined by the sum of the apportioned velocities  $U=U_1+U_2$  in the lowest  $z=0$  and in the highest point  $z=h$  of the film thickness respectively (figure 33). In addition assuming an isoviscous lubricant and zero entraining velocity, equation 54 can be simplified even more and becomes:

$$\frac{d}{dx} \left( h^3 \frac{dp}{dx} \right) + \frac{d}{dy} \left( h^3 \frac{dp}{dy} \right) = 12\mu \frac{dh}{dt} \quad (55)$$

Equation 55 defines the hydrodynamic pressure field when the wedge-effect is absent ( $dh/dx$  constant).

Thus the pressure distribution as a function of the squeezing velocity  $dh/dt$  is expressed with equation 56.

$$p = \frac{6\mu}{h^3} \frac{dh}{dt} \left( x^2 - \frac{B^2}{4} \right) \quad (56)$$

The load that the plates can support, or more exactly the force separating the plates, can be obtained by the following formula (equation 57).

$$\frac{W}{L} = - \frac{\mu B^3}{h^3} \frac{dh}{dt} \quad (57)$$

The time necessary for the film thickness between parallel plates to change between specified limits, the squeeze time, is expressed with equation 58:

$$\Delta t = \frac{\mu B^3 L}{2W} \left( \frac{1}{h_2^2} - \frac{1}{h_1^2} \right) \quad (58)$$

Where B is the width of the plate (m), L is the length of the plate (m), W is the applied load (N)

This first hypothesis has a weak point which is that cavitation was found only in the high pressure region of the scroll and not across the whole surface of the steel plate. The above theory applies to every region of the scroll where the two parallel surfaces of the tip seal and the steel plate squeeze the lubricant. Since cavitation is not observed everywhere the

hypothesis is possibly misleading. Furthermore the applied pressure between the surfaces (Chapter 4) is quite low reducing the chances for locally generating high pressure differences within the liquid lubricant during the running time of the scroll system. Additionally, the fact that the driving fluid has the maximum velocity in the inlet port it can possibly give an extra squeeze boost to the lubricant which is accumulated between the gaps of the steel plate (figure 32). These geometrical gaps, which are formed because of the design philosophy of the scroll, look like step bearings, accumulate the lubricant mixture between the tip seal, the scroll wall and the steel plate, squeezing and increasing its velocity. Consequently, according to the Venturi effect fundamentals ( $U \uparrow \Leftrightarrow P \downarrow$ ) a drop of pressure in the liquid lubricant in these constricted sections can possibly occur.

The second hypothesis relates to the entrainment of the ambient fluid inside the jet stream during the inlet of the working fluid inside the scroll as the schematic representation illustrates in figure 34. This mechanism has stronger points in interpretation of the cavitation mechanism since it can only be applied in that specific high pressure region where the cavitation pits were found. The theory behind the mechanisms of fluid entrainment inside a developed jet stream can be found in the pioneering work of N. Kotsovinos [175].

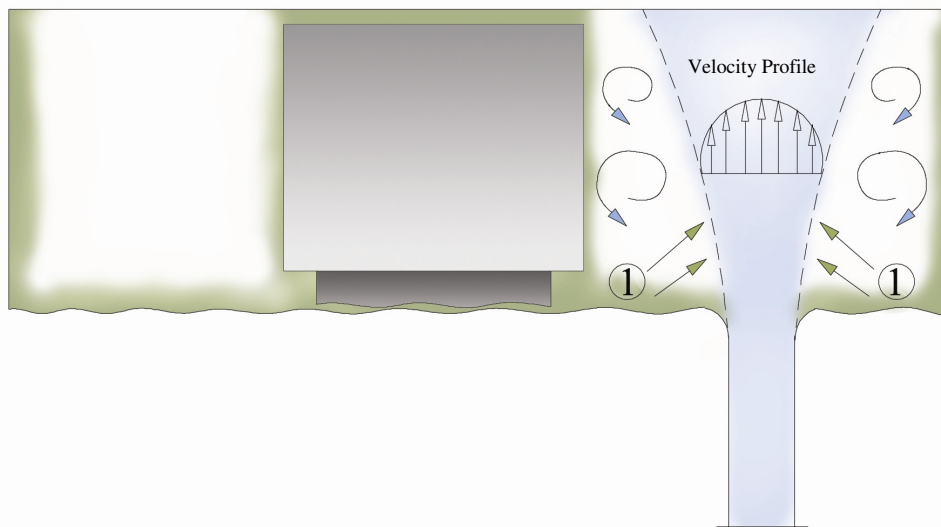


**Figure 34: The beginning of the expansion process is illustrated. The working fluid opens like a fan, rigorously striking the upper steel plate and simultaneously setting the scroll into motion. The velocity profile, the vortex rings and the lubricant entrainment process are depicted.**

Specifically, when the working fluid is injected by the inlet port to the expansion high pressure chamber, the turbulent jet stream, rolls up into toroidal spiral shapes. These shapes are well-known as vortex rings. During the formation process of the vortex rings, in each of the sides of the jet stream respectively, some of the ambient fluid entrains into the main body of the stream and into those spiral rings, lowering the ambient pressure of the liquid mixture.

Thus, negative pressures can be generated across the surface of the steel plate especially at the points where initially the liquid mixture was laid down and then was entrained into the jet stream (number 1 in figure 34). In this case cavitation is possible to be developed.

Using computational fluid mechanics (CFD), a finite element mesh was conducted in order to allow the cavitation mechanism of the scroll expander to be revealed. Initially, the numerical results produced with (CFD) methods, offered by the commercial CFD software FLUENT, explain the generation of cavitation bubbles inside the scroll expander. The experimental results reveal the performance of the working fluids and their impact mechanisms on the actual steel plate of the scroll. The initial aim was to successfully identify the entrainment of the fluid into the jet stream and the ambient pressure drop in a simulated water environment under standard operating conditions (25<sup>0</sup> C temperature and 1 bar pressure). A 3D model of a tank was used for this preliminary investigation. Then, the exact operational conditions of both of the scroll types were applied within a 2D experimental model and the actual properties of the working fluid were utilized from the FEA software for a new simulation. Consequently a more coherent, real-world, analysis was conducted.

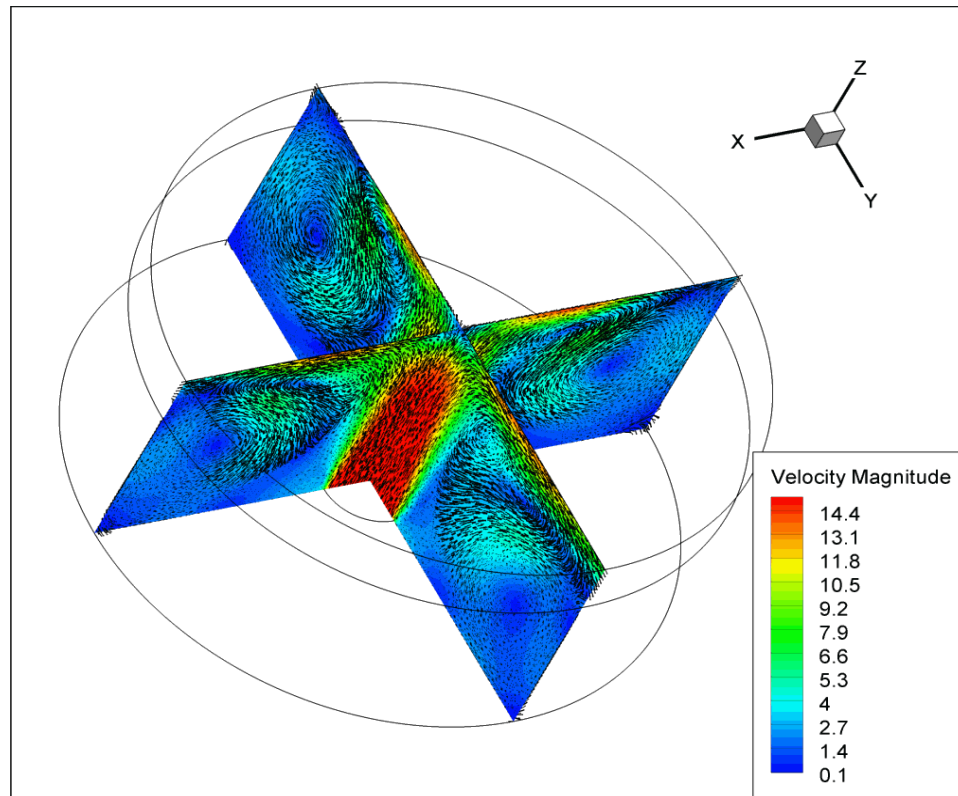


**Figure 35: Analytical simulation of the propagation mechanism of the jet stream of the working fluid as it is introduced through the inlet port of the scroll into the first expansion chamber. The 3D scroll model is representative of the SE<sub>300</sub> and SE<sub>100</sub>.**



investigation was focused on the jet stream's expansion mode and on the bottom surface of the steel plate. A complete 3D analytical simulation of the expansion mechanism of the scroll expander, involving the design and the interaction of the two scrolls, is a very complicated issue and is beyond the scope of this research.

This preliminary analysis of the performance of the working fluid as it enters the scroll expander is an approximation of the distribution of the pressure drop across the steel plate surface (figure 36). Interestingly, entrainment was observed across every side of the refrigerant jet stream as it was entering the scroll. With a quick glance it can be seen that in many areas negative pressures were developed. Especially, near to the inlet port where cavitation was mainly observed, negative pressures reach their peak values (around 0.13 bars). The results from this primary analysis were adequate enough to confirm that the negative pressures can be created by fluid entrainment. The next step was to test if these pressure drops can be achieved within the scroll expander, utilizing its actual operating conditions with FLUENT software.

With the use of CFD methods, a finite volume numerical approach was applied in order to reveal the cavitation mechanism of the scroll expander. A representative 2D analysis of the scroll was performed. The numerical model that was used in the simulations solves the Reynolds Averaged Navier Stokes equations (RANS). Closure of the turbulent stress terms is achieved with the application of the standard  $k$ - $\epsilon$  turbulence model. In more detail the equations solved are the continuity equation, the momentum equation, the energy equation and the transport equations for the turbulent kinetic energy ( $k$ ) and its dissipation rate ( $\epsilon$ ), respectively. At the solid boundaries of the geometry a wall boundary was applied, with enhanced wall treatment for the prediction of the turbulent quantities at the near-wall regions. A velocity-inlet boundary condition was used for the inlets and a pressure-outlet boundary condition for the outlets.

The aim was to investigate the behaviour of the jet stream and the fluid entrainment mechanism as it develops inside the first expansion chamber for both scroll types. The initial conditions were adjusted to those of the real case scenario. Thus for the SE<sub>100</sub> and SE<sub>300</sub> hours scroll type the velocity was adjusted to 15.9 m/sec while for the SE<sub>1000</sub> hours scroll the velocity was 31 m/sec. The temperature and pressure ambient conditions were kept the same in both scrolls (150 °C and 12 bar pressure). The outlet pressure was assumed to be 8 bars after the first expansion pocket. The outlet pressure was not important since we were interested in examining the incubation period of the expansion mode of the refrigerant stream and the entrainment mechanism.

Two critical areas were chosen for the analysis of both scrolls. The first area is the moving wall (right side-outflow) at its minimum distance from the inlet port (inflow) in the very first stage of the expansion process. The second area is at the maximum operating distance of the moving wall (outflow) from the inlet port. In the first scroll type with height 3 cm a total number of 22572 quadrilateral cells were used in the initial position (figure 37 A), while the final position consists of a total number of 27489 quadrilateral cells (figure 37 B). In the second scroll type with height 1.5 cm a total number of 20493 quadrilateral cells were used in the initial position (figure 37 C), while the final position consists of a total number of 22050 quadrilateral cells (figure 37 D). In both cases, grid clustering was used near the boundaries.

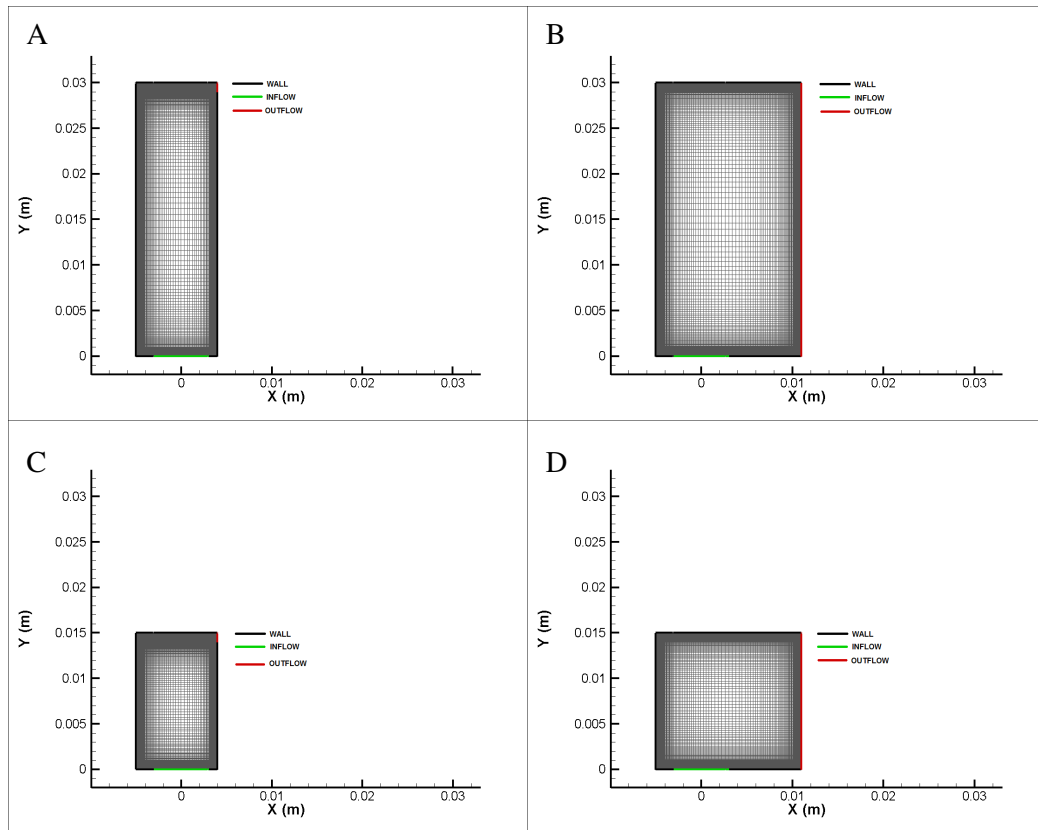
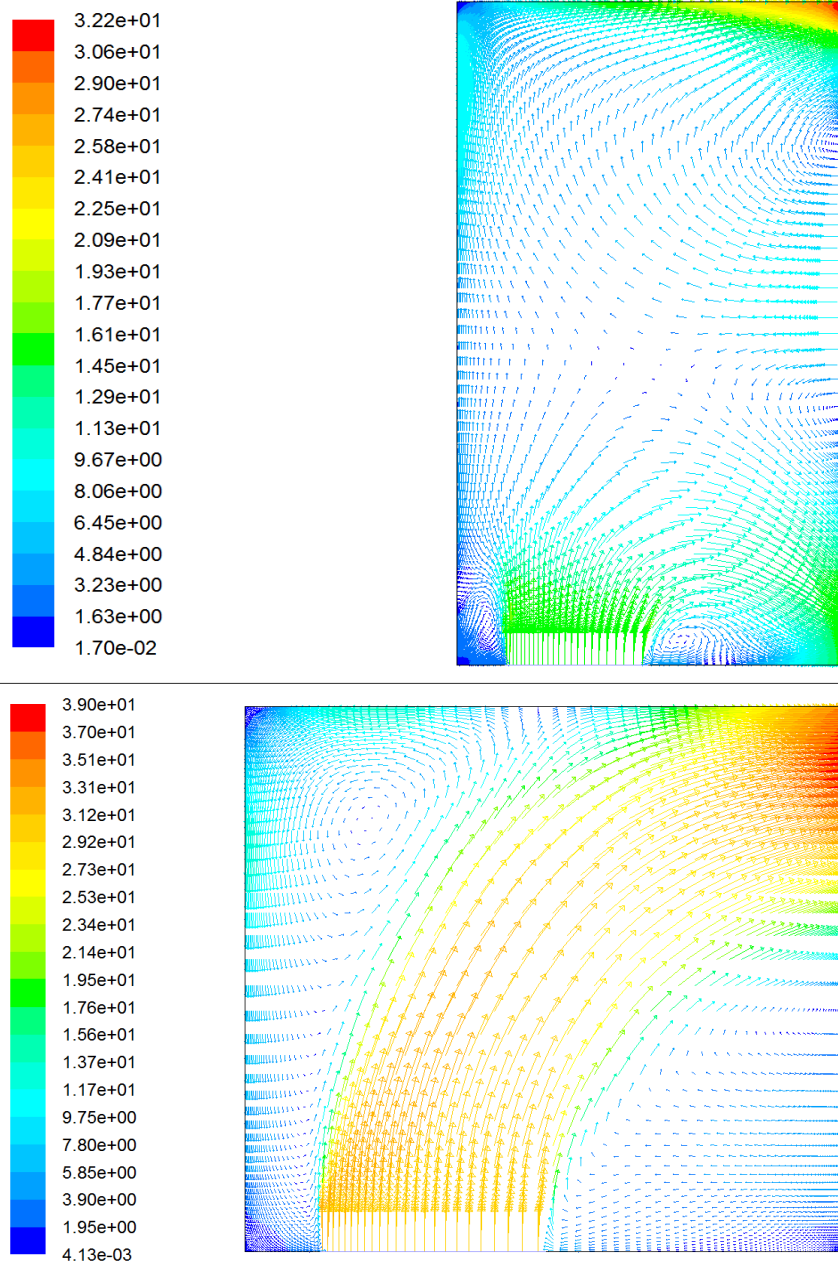


**Figure 37: Geometry, computational mesh and boundary conditions of the first expansion pocket of the: SE<sub>300</sub> A) Initial position B) Final position and SE<sub>1000</sub> C) Initial position D) Final position**

At the early stage of the scroll operational mode there are no gaps created. Therefore refrigerant is prevented from passing to the next pressurised chamber as it is introduced to the scroll. The refrigerant thrust pushes the scroll wall creating a gap. Thus, in the first case of the numerical analysis, a small gap was used for the equation of continuity to be solved. This was the worst scenario for generating entrainment mechanisms and high pressure fluctuations inside the scroll. In the second case, where the optimum scenario for avoiding cavitation due

to pressure fluctuations or the entrainment mechanisms is used, the gap is assumed to be across the whole side of the scroll wall, when the moving wall (outflow) is at its maximum possible operating distance from the inlet port. In both scenarios the shape and the operational conditions of the scroll expander were adjusted to the real-world case, for representative results. Each pressure cycle according the operational mechanism of the scroll lasts 20 msec.



Velocity Vectors Colored By Velocity Magnitude (m/s)

**Figure 38: Velocity distribution of the jet stream in the final position of the moving wall for the SE<sub>100</sub>/SE<sub>300</sub> and SE<sub>1000</sub> respectively. Vortex rings and the entrainment mechanism are observed.**

It was believed that the cavitation mechanism was derived from the low pressure at the lower scroll boundary induced by the refrigerant. Thus, a drop of pressure by the entrainment was thought to be sufficient enough to make the lubricant volatile. Surprisingly, only a small pressure drop was observed in the entrainment points while a tremendous increment of pressure was spotted in both of the scroll types.

In the first case for both the scroll types, where the moving wall was near to the inlet port, there was an absence of entrainment fluid and a rapid increment of the ambient pressure. In figure 38, the entrainment mechanism which was developed during the second case, where the moving wall was in the maximum possible distance from the inlet port, is presented.

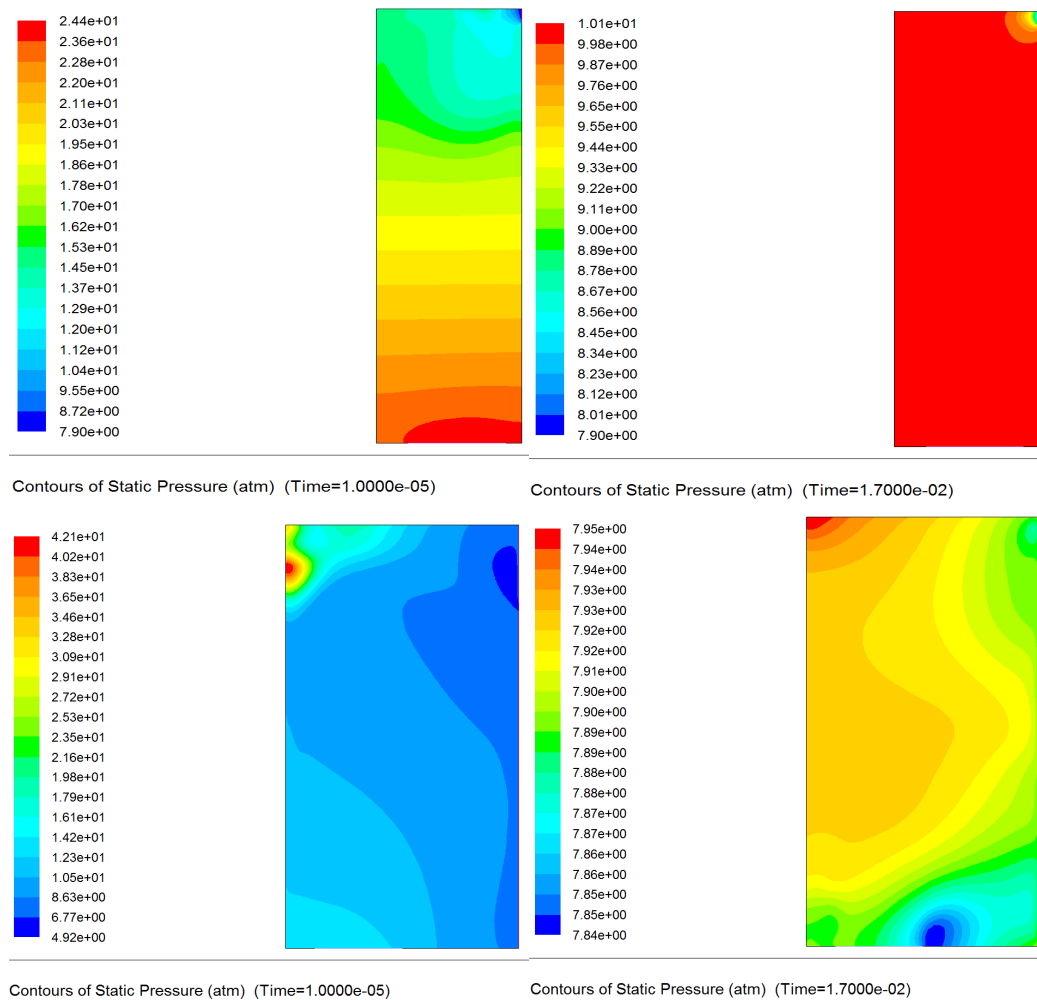


**Figure 39: Distribution of the static pressure in the initial and the final position of the moving part for SE<sub>100</sub>&SE<sub>300</sub>**

In figure 39 the pressure distribution inside the SE<sub>100</sub> and SE<sub>300</sub> is depicted for the initial and the final position of the moving wall. Interestingly, comparing the velocity vector and the

static pressure images it can be observed that the entrainment of the liquid, found in vortex ring areas, does not affect the static pressure by dropping its magnitude. On the contrary, the static pressure has an enormous increasing effect on generating conditions for the refrigerant gas to instantly liquefy. This phenomenon is more intense across the bottom of the scroll, where cavitation was found, as the contours illustrate.

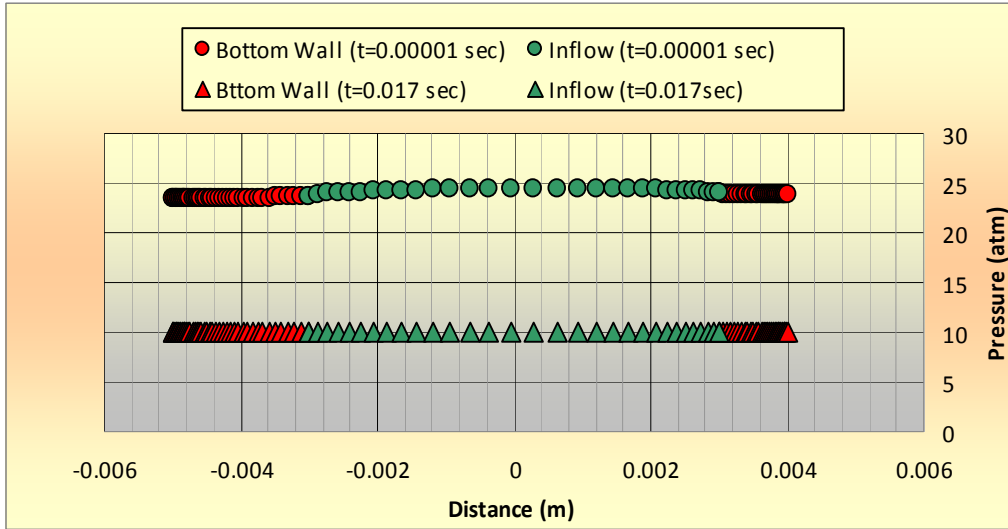


**Figure 40: Pressure distribution along bottom boundary for  $SE_{100}$  and  $SE_{300}$  (Initial position of the moving wall)**

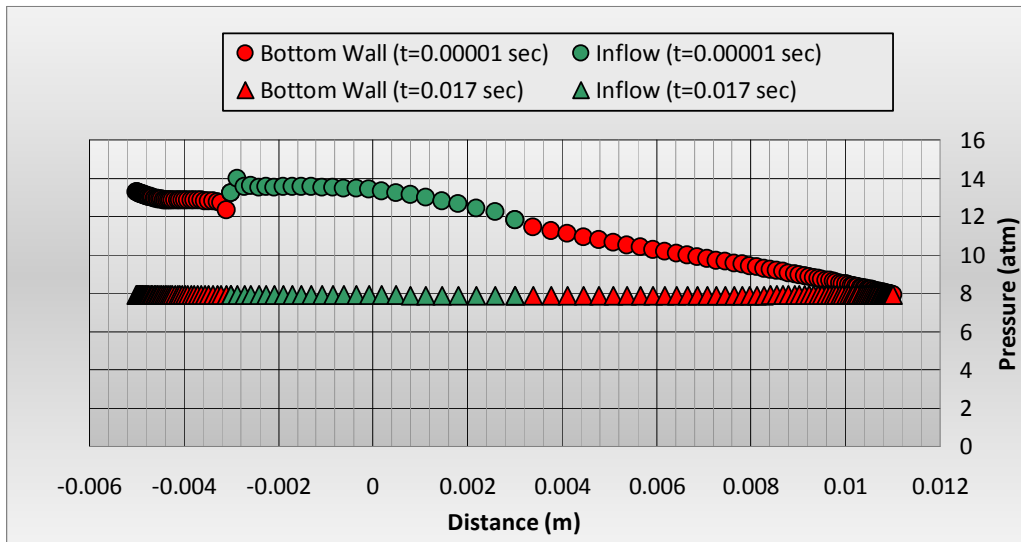


**Figure 41: Pressure distribution along bottom boundary for  $SE_{100}$  and  $SE_{300}$  (Final position of moving wall)**

Specifically, in figures 40 and 41 the instantaneous pressure distribution for  $t=1 \mu\text{sec}$  and  $t=17 \text{ msec}$  for the case of  $SE_{300}$  and  $SE_{100}$ , is presented. The graphs are focused on the bottom steel plate. In figure 40, for  $t=1 \mu\text{sec}$ , when the jet stream from the refrigerant is developed, there is a steep increment of the ambient pressure. The pressure rapidly increases from 12 atm to 25 atm. This high pressure lasts for approximately  $30 \mu\text{s}$  and then it gradually decreases until it stabilises at the end of the pressure cycle at 17 msec. The time of  $30 \mu\text{s}$  is enough for a bubble to be generated and to be developed in a round shaped cavity as the high speed photographic observation revealed (paragraph 6.2). Thus a huge production of bubbles is expected. In figure 41 there is a slight increase of pressure reaching the maximum value of 14 atm. In this case the liquefaction process of the refrigerant is close to its transformation limit, according to its thermodynamic properties, thus a substantial production of bubbles is possibly restricted.

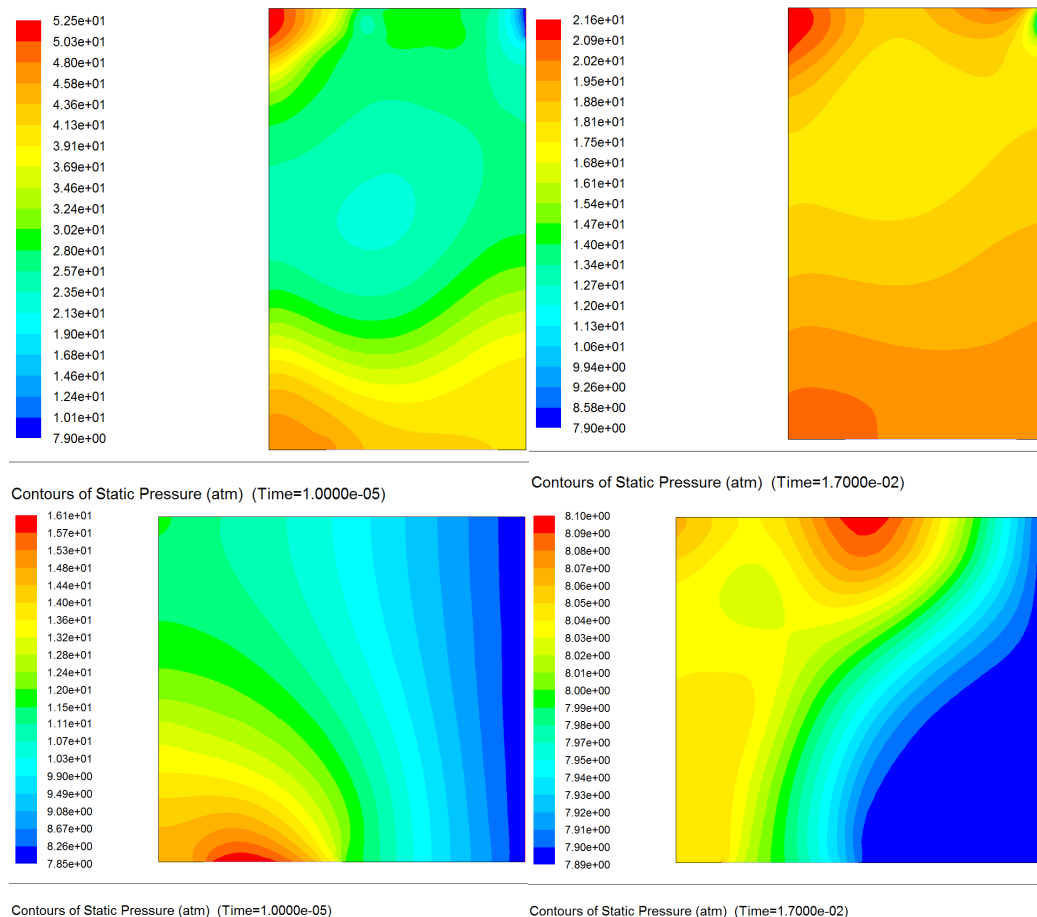


**Figure 42: Distribution of the static pressure in the initial and the final position of the moving part for  $SE_{1000}$**

In figure 42 the pressure distribution inside the  $SE_{1000}$  is depicted for the initial and the final position of the moving wall. Interestingly, it can be seen that as the working fluid enters into

the first expansion chamber the static pressure, is enormously increased, reaching a significant value of 53 atm in certain areas. Comparing the results from the previous scroll systems it is obvious that the inlet velocity of the working fluid plays a major role in that steep increment of the pressure. Apparently, this incredibly high pressure can possibly affect the side walls of the scroll as well as other critical components within the scroll. The shear stresses produced by the expansion impact of the working fluid can seriously damage these components, leading to a catastrophic failure of the scroll unit over a prolonged period of operation time.

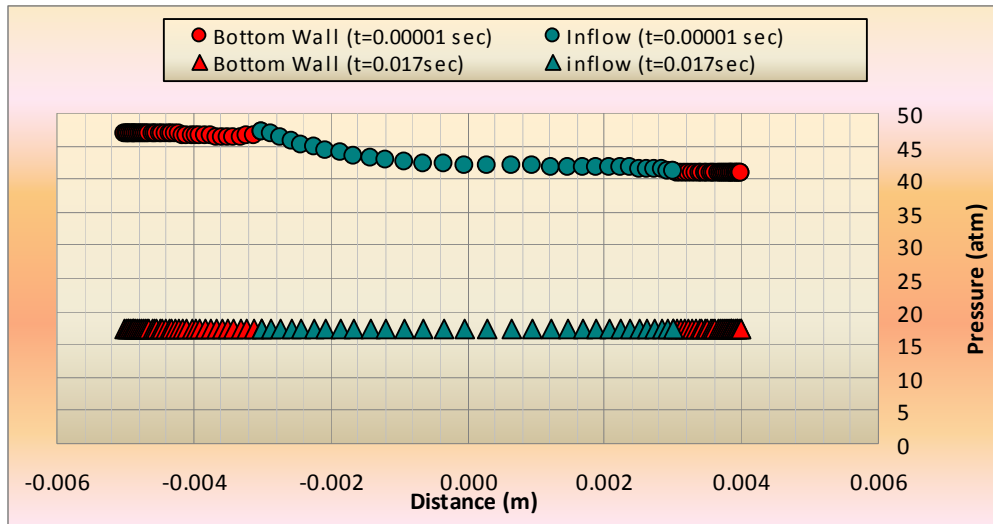


Figure 43: Pressure distribution along bottom boundary for  $SE_{1000}$  (Initial position of the moving wall)

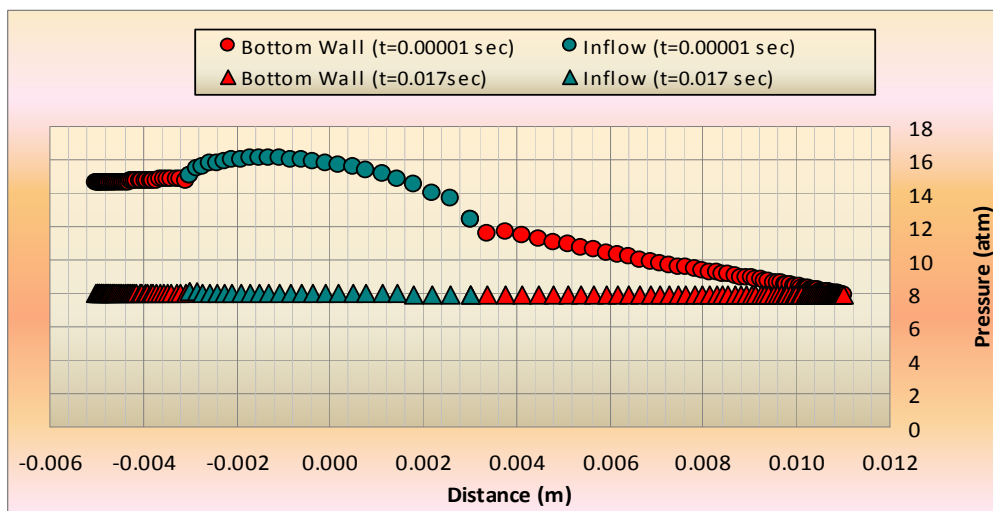


Figure 44: Pressure distribution along bottom boundary for  $SE_{1000}$  (Final position of the moving wall)

Additionally, in the equilibrium condition where the momentum of the working fluid falls, the static pressure is still high enough to produce cavitation bubbles by liquefying part of the refrigerant even after the end of the expansion cycle at  $t=17$  msec. In the case where the wall is in the maximum possible position during the operation of the scroll the pressure in a few areas is still sufficiently high to liquefy part of the refrigerant. However, in the time where equilibrium is achieved the pressure is quite low avoiding refrigerant liquefying.

Figures 43 and 44 present the instantaneous pressure distribution for the case of the  $SE_{1000}$ , across the bottom plate where cavitation was found, for  $t=1$   $\mu$ sec and  $t=17$  msec. The resulting pressure curves resemble the previous analysis. From both figures 43-44, for  $t=1$   $\mu$ sec, when the jet stream from the refrigerant is developed, there is a steep increment in the ambient pressure. In figure 43 the refrigerant pressure reaches for  $t=1$   $\mu$ sec an extremely elevated level of around 45 atm across the bottom surface. Then, for  $t>30$   $\mu$ sec the pressure decreases and is stabilized at around 17 atm until the end of the pressure cycle.

The same mechanism applies when the moving wall is at the maximum operating distance from the inlet port. As figure 44 shows, the ambient pressure across the bottom wall increases to 16 atm and then drops down to 8 atm. In both cases the pressure is high enough and the transformation of the lubricant from liquid to gas phase is restricted. Therefore it seems that the lubricant fluid is not responsible for cavitation. However, in both cases within the  $SE_{1000}$  the pressure is high enough to liquefy instantaneously part of the refrigerant close to the bottom boundary, creating conditions for the generation of cavitation bubbles within the liquefied refrigerant. This finding resolves the puzzle of how the cavitation erosion mechanism on the steel plate is produced.

On the basis of numerical simulation results, it is advocated that the cavitation mechanism is related to the initial instantaneous high pressure at the lower scroll boundary induced by the refrigerant inflow gas jet. Instantaneously part of the refrigerant gas phase is transformed to a liquid phase due to high pressure, which subsequently due to turbulent environment and high pressure fluctuations produces cavitation bubbles within the refrigerant in liquid phase.

The increment of pressure is massive, accelerating the formation of refrigerant bubbles. In the case of the  $SE_{100}$  and  $SE_{300}$  the pressure did not show any extreme augmentation except the initial position where pressure was high enough to liquefy the refrigerant. Additionally the operational period was substantially lower to the  $SE_{1000}$ . Thus, the formation of cavities on the steel plate surface was negligible. In the  $SE_{1000}$  the pressure fluctuation ration is enormously high, for both of the moving wall positions, leading to a rapid formation of refrigerant

cavitation bubbles. Thus, the steel plate of the SE<sub>1000</sub> in the critical region next to the inlet port, experiences consistent erosion damage due to formation of numerous cavitation clusters. Finally, the lubricant layer which avoids severe contact between the steel plate and the tip seal can be seriously affected by the presence of the cavitation bubbles. The bubbles can significantly reduce the thickness of the lubricant layer leading to a more severe contact of the opposing surfaces. Thus, the contact between the steel plate and the tip seal becomes rougher while the friction coefficient and the wear rate could possibly be increased.

### 3.4 Side Walls

On the side walls of the scrolls there is surface contact between the stationary aluminium scroll and the orbiting coating aluminium scroll. The hardness of the aluminium scroll was measured to be around 170 HV, while the hardness of the coating scroll on the coating surface was measured to be around 350 HV. This might suggest that the anodised film hardness is not as hard as it was expected to be but is still much harder than the base material. This hardness difference can theoretically imply that the orbiting scroll will probably damage the stationary scroll during their contact.

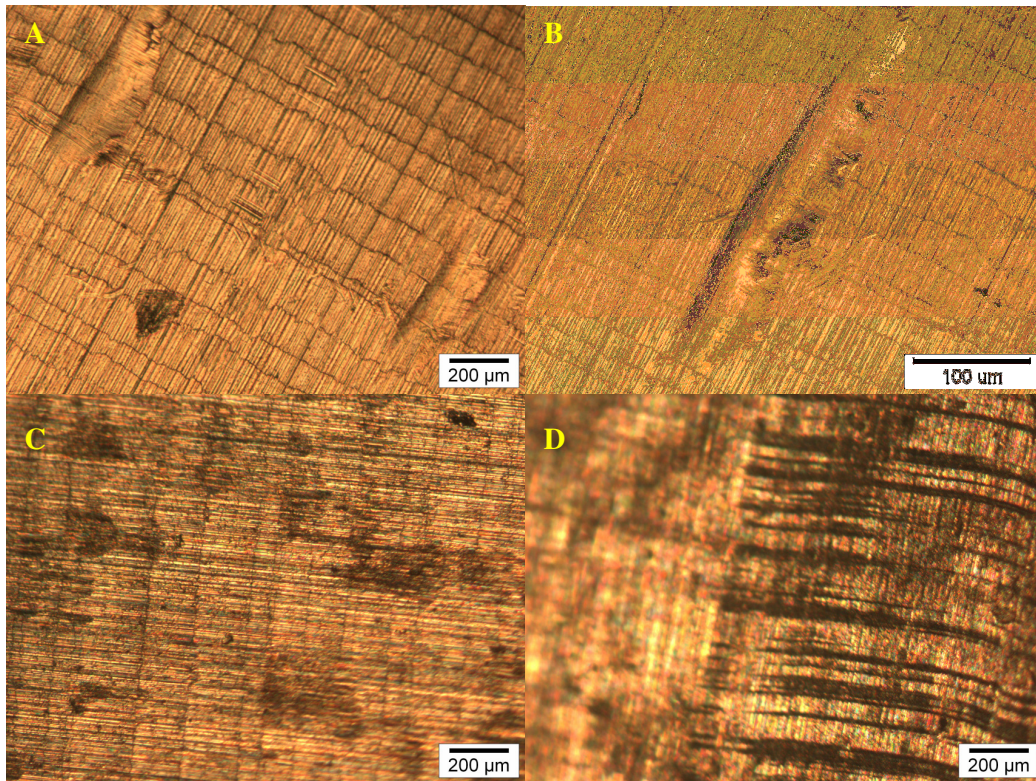


**Figure 45: Wear across the surface of the aluminium scroll A-B) Combination abrasive-adhesive wear C-D) Abrasive wear formed by the orbiting coating scroll**

Under the optical microscope the above was confirmed. On the surface of the stationary aluminium scroll many wear valleys and a lot of random linear wear scars, which are probably generated by two-body abrasive wear, were observed (figure 45). Moreover many aluminium particles which derived from abrasion and mainly by adhesion wear were clearly identified on the surface of the coating scroll (figure 46). They were welded or embedded across the anodic film. Thus the black coating surface is gradually increasing in height with the addition of the aluminium particles and the contact between the side walls of the scroll is becoming more severe. The wear damage and the flank leakage can be steeply increased.

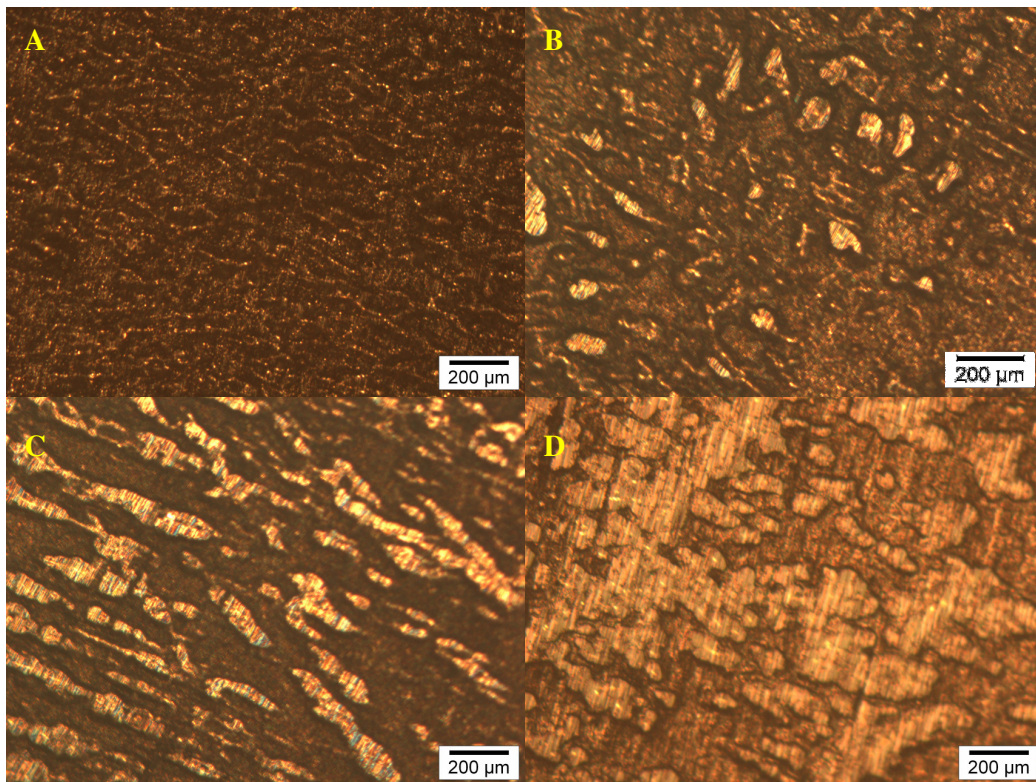


**Figure 46: Adhesive wear on the coating scroll A) Original surface B) Adhesion appears as aluminium particles welded on the coating surface C) The quantity of the aluminium particles is increased D) A major part of the coating scroll is covered by aluminium particles**

In the above case the wear regime on the surface of the orbiting scroll can be considered mainly as adhesive. Adhesive wear is the result of localized welding between the sliding contact surfaces. For adhesive wear to occur it is necessary for the surfaces to be in intimate contact with each other. Surfaces which are held apart by lubricating films or oxide films reduce the tendency for adhesion to occur. This is why the one scroll is coated and is separated from the other using lubrication film. Apparently during the operation of the scroll even those protection films cannot effectively prevent the wear damage.

With the use of ZYGO interferometer microscope the adhesive mechanism was revealed. The coating surface of the scroll was effectively scanned and the attached parts of the aluminium scroll were detected (figure 47). The intensity map images clearly show the aluminium particles (white colour) distributed across the scroll's coating surface. The height of the embedded aluminium particles onto the coating surface of the scroll is up to 10  $\mu\text{m}$ . The maximum size of the aluminium particles is up to 500  $\mu\text{m}$  while their average roughness is about 0.250  $\mu\text{m}$ . The mild roughness profile, indicates that a consistently intimate contact with the asperities of the aluminium scroll is achieved, leading to a less severe wear regime. Additionally, the large amount of the attached aluminium particles reveal that a smoother contact between the aluminium particles and the asperities of the aluminium scroll is achieved. However, the flank leakage could be steeply increased while the efficiency of the scroll can be significantly reduced.

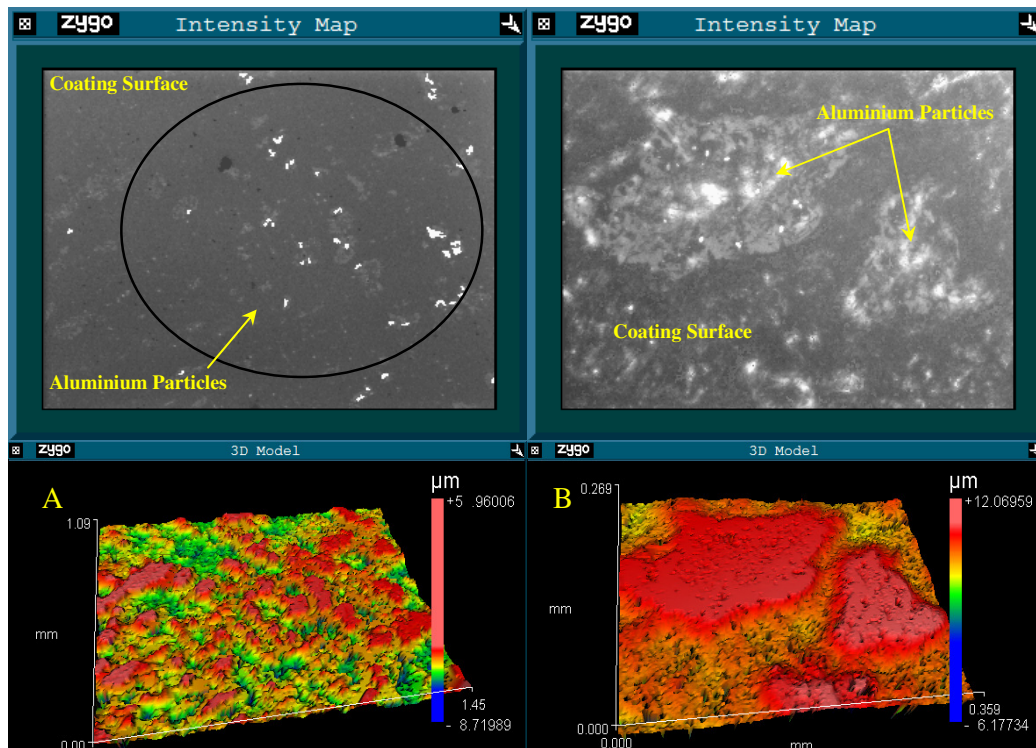


**Figure 47: ZYGO micrographs show the features of the embedded aluminium particles onto the surface of the coating scroll A) Overview of the area with the aluminium particles B) Close up investigation of the aluminium particles morphology**

In addition, cavities found across the tip of the aluminium scroll indicate consecutive cavitation impacts in that specific region. This was expected to be revealed according to the interesting results of the analytical simulation process. Moreover, the presence of cavities on the bottom tip of the aluminium scroll confirms the theory of the squeezed films.

Interestingly, the depth of these cavities was wider and slightly deeper compared to the ones found across the steel plate. This is reasonable since the aluminium scroll is much softer than the high carbon steel plate and more prone to surface damage. Notable material loss is observed. The function of the aluminium tip in sealing the inlet port after in every expansion cycle and the vicinity leakage points, can be significantly reduced.

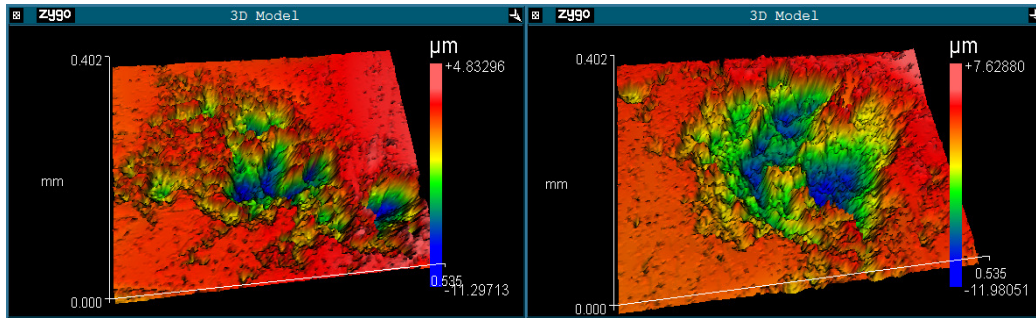


**Figure 48: Cavities found across the tip of the aluminium scroll after 1000 hours of operation**

In figure 48, a typical cluster of cavities can be found on the tip of the aluminium scroll. Additionally, more investigation is needed in order to analyse and interpret the level of impact by the cavitation mechanism and the extent of the critical damage. However, this issue is beyond the scope of this research and has to be considered in future projects.

### **3.5 Summary and discussion**

#### **3.5.1 Scroll's Surface Investigation**

The surface analysis of the three different scroll expander systems was mainly focused on two different regions of the steel plate: the high and low pressure regions. Within the low pressure region the wear marks were superficial. Within the high pressure region the marks were on average 3 times wider and around 4 times deeper. The two-body abrasive wear prevails across the plate surface of the whole scroll. In addition, cavitation and three-body abrasion wear were identified in many areas of the scroll's plate. Characteristically many cavities were found across the edges of the steel plate in the first expansion chamber. Cavitation was generated due to elevated pressure fluctuations. This was interpreted by the analytical results produced with the use of computational fluid mechanics.

#### **3.5.2 Analytical Results**

It is reasonable to conclude from the analytical results of this study the mechanism responsible for cavitation leading to the erosion of the scroll's steel plate was determined.

Refrigerant is the fluid medium which generates cavitation bubbles due to elevated pressure fluctuations inside the high pressure gas pockets of the scroll expander. This finding resolves the question of how the refrigerant which enters the scroll in a gas phase produces cavitation. This is really an exceptional situation. Usually cavitation occurs in an environment where basically the fluid in motion is in liquid phase, which at low pressure is transformed into gas, producing cavitation bubbles. In this situation the fluid in motion is in gas phase, which is locally liquefied under very high pressure, producing cavitation bubbles within the high pressure region. It has not been possible to discover a similar finding in any published literature.

Additionally, it was shown that with an increment of the inlet velocity, huge amounts of pressure are generated within the first expansion chamber of the scroll. On one hand this can probably increase the performance and the efficiency of the scroll. On the other hand vast shear stresses can be accumulated between the main components of the scroll leading to a plastic deformation and a fatigue failure of the scroll unit, in due course. Thus, a balance between the geometry, the inlet velocity of the working fluid and the efficiency of the scroll expander has to be precisely achieved in order to restrict the failure mechanisms.

## **4 CHAPTER : EXPERIMENTAL METHODOLOGY**

In this chapter the experimental methodology used for the completion of this research is described. Several sets of laboratory tests were conducted to study the friction, wear and cavitation mechanisms of the main parts of the scroll expander. The critical components for durability were identified on the tip seal and the plate of the scroll expander. Subsequently, these components were used to perform sliding tribological tests using a special purpose-built modified micro-friction machine and a cavitation test apparatus. The experimental conditions were adjusted to those of the industrial applications. The tests were performed in a coherent sequence involving systematic monitoring of their crucial parameters.

The main difficulty which was revealed throughout this stage was the formation of the samples. The main components were inappropriate for bench tests due to their large size. Eventually, an optimum formation was the key factor to overcome this problem. Thus, suitable preparation resulted in samples which fitted inside the experimental machines for further tests.

### **4.1 Experimental Test Rigs**

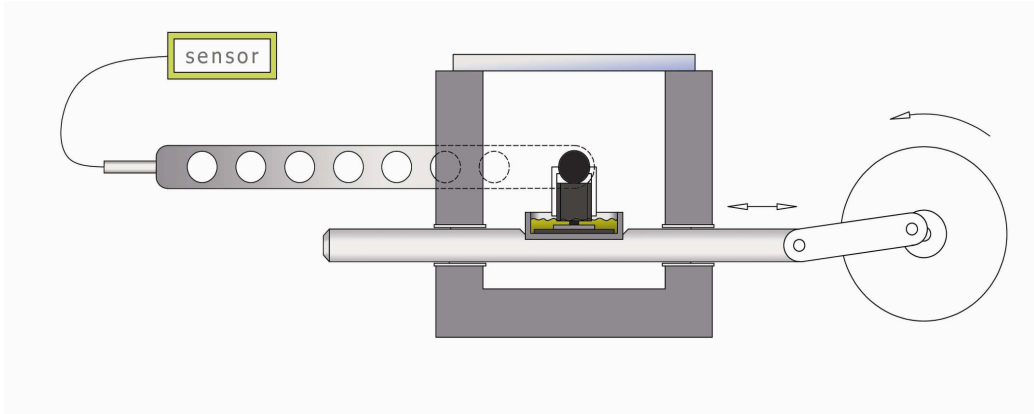
Two different experimental test rigs were used in this project. In the first part of this study, sliding wear/friction tests were performed with the use of the TE 57 micro-friction machine. In the second part cavitation erosion tests were conducted with the use of a cavitation apparatus integrated with a high speed camera device.

#### **4.1.1 TE 57 micro-sliding wear/friction test rig**

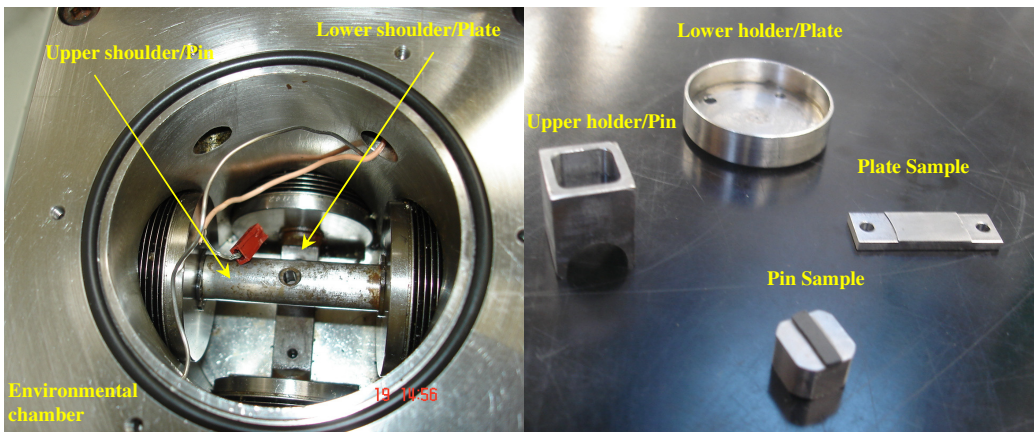
The TE 57 micro-friction machine is designed to provide an accelerated method for assessing friction and wear between pin and plate materials under various tribological conditions [176]. In the TE 57 bench test system, the sample follows a sinusoidal movement as it is produced by an electric rotary motor. This reciprocating tribometer was thought to approach the scroll's movement. The movement of the involute scrolls of the expander is an eccentric continuous movement with a 10 mm diameter at a frequency of 50 Hz. Both movements caused sliding wear. Thus an effective evaluation of the wear effects inside the scroll during its operation can be estimated.

Figure 49 shows a schematic of the wear bench-test machine. The equipment is based upon a standard set-up from Phoenix Ltd model TE 77 micro-friction machine. A modification allows for control of the environmental conditions surrounding the contact to simulate those

found within the scroll expander. The resultant micro-friction machine operates by sliding a lower-plate sample in a reciprocating motion against a fixed sample pin or ball.



**Figure 49: Sliding friction/wear schematic bench test**



**Figure 50: An overview of the environmental chamber of the TE 57 micro-friction machine and of the ancillary equipment used for the sliding wear/friction experiments**

In figure 50 the environmental chamber, the slider plate and the pin are illustrated. The slider (plate) is mounted on a support lubrication bath (lower holder) connected to the actuator (lower shoulder). The pin sample sits inside the upper holder. The upper holder is fixed in the upper shoulder of the system. The pin is connected via a feedback mechanism to a transducer to provide friction force feedback and hence friction co-efficient [177]. A controller permitted the generation of the reciprocating movement at a desired constant speed. Finally, a contact force of up to 50N is applied using a spring loaded lever arrangement.

#### **4.1.2 Cavitation Apparatus integrated to a High-Speed Camera Device**

Cavitation erosion tests were utilized in the present study to analyse and evaluate the performance of the cavitation bubbles generated within the two scroll working fluids. The experimental apparatus is described in figure 51. The experiments were performed according

to the ASTM G32-03 standard method. The ASTM method proposes a standard probe of 15.9 mm diameter to be generally used for cavitation tests. However, in this study a probe of 5 mm was deployed to produce cavitation bubbles for more definitive images. In addition, the rate of the erosion damage developed on the tested sample by the 5 mm probe is significantly lower compare to the standard probe. Thus, it would be easier for the researcher to identify the pits formed across the steel sample surface during the incubation period of time.

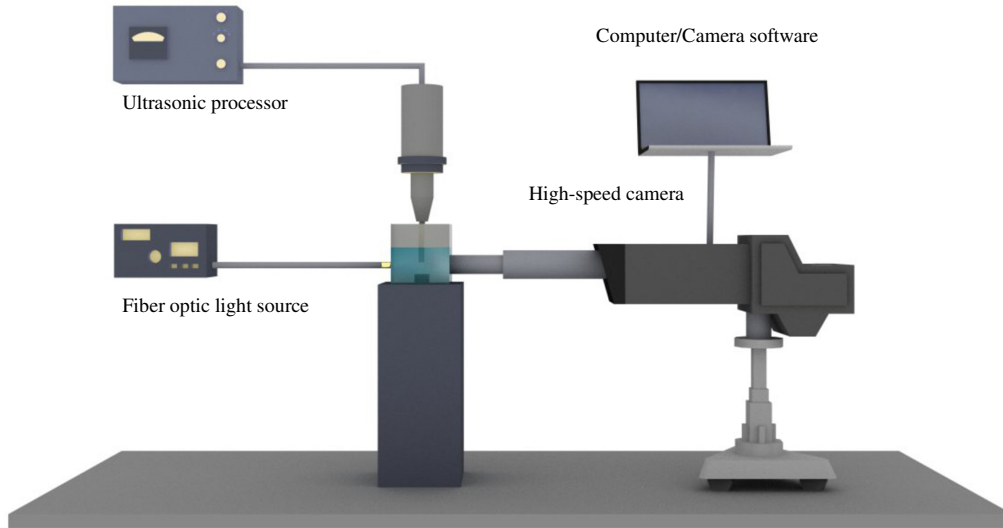


**Figure 51: Schematic of the cavitation experimental set up**

Experiments were carried out by using a piezoelectric transducer at a fixed frequency of 20 kHz. The transducer was connected to the ultrasonic generator. The ultrasonic horn had a plane surface oscillating in a simple harmonic motion [178]. Peak to peak amplitude of the horn tip was adjusted to be at 50  $\mu\text{m}$ . All tests were timed and were run for the required time interval. This was achieved by a timer connected to the ultrasonic generator which automatically turns the power supply to the transducer on and off. Furthermore, the steel samples were machined accurately by a cutting machine. Then the steel samples were placed on a Bakelite base. All the test samples were polished to a few microns accuracy and went through a surface analysis to ensure that they were free from any surface defects prior to testing.

The samples were mounted on the bottom of a small transparent tank with a maximum capacity of 0.5 L and in a large transparent tank (5 L) respectively. The small tank was used for cavitation tests dealing with the incubation stage of the pits while the large one was used for tests which take a prolonged period of time. The implemented steel samples on the

Bakelite base were immersed in the liquid and mounted on the bottom of the tank during the experimental period. The ultrasonic horn was submerged into the liquid environment of the tank and was strictly adjusted to a distance of 0.5 mm from the sample's surface. The distance between the horn tip and the sample is critical as it can influence the erosion rate.

A high speed camera (Phantom v7.3) was installed at one side of the tank. At the opposite side of the tank a high intensity fibre optic light source (2 kW) was installed to provide enough light to the critical areas for investigation. The Phantom v7.3 supplies a full frame (800x600 pixels) recording rate, with a maximum shutter speed of up to 500,000 frames per second with 1  $\mu$ second exposure time. In this study the speed modes of the camera used for the photography varied between 30,000 fps and 220,000 fps with a 10  $\mu$ sec exposure time. During the tests a Leica mono zoom amplifier was used in front of the camera achieving a resolution of approximately 8  $\mu$ m/pixel.

## **4.2 Surface Analysis**

After the end of the tests a comprehensive examination on sample surfaces was conducted. Advanced surface analysis techniques like optical microscopy, scanning electron microscopy and scanning interferometry were used in order to indentify the nature of the wear and cavitation mechanisms. These techniques were also used during the micro-structure examination of the samples (3.2.1 and 4.1.2).

### **4.2.1 Optical Microscopy**

The optical microscope utilised for this project was the Olympus BX 60 figure 52. This microscope was the first tool used for inspection. The optical microscope is simple to use and provides quick and representative results. It uses visible light and a collection of microscope lenses of 5, 10, 20, 50 and 100x magnification for intensive surface observations. Apart from the traditional system of eyepiece, the microscope is fitted with a digital camera to monitor and capture images. These images are then displayed on a monitor via a computer link.

A quality analysis of an image requires the use of various combinations of polarizing filters in order that the mountain (peaks) and the valleys (troughs) can be revealed. In addition, the effective measurements of the size and the depth of the wear mark, found in this image, using appropriate commands of the software and further microscopy techniques can be well estimated. Finally, in some cases stitching of an image is essential. With stitching a broader image of the sample in the desirable magnification is available for a thorough optical investigation.



**Figure 52: Olympus BX 60 Optical microscope**

#### **4.2.2 Scanning Interferometer Microscopy**

The ZYGO surface interferometer is a very powerful tool in the field of materials surface analysis figure 53. Its operating principle is based on the white light scanning interferometry and is capable of mapping an area of a few millimetres wide in a single measurement with sub-nanometres resolution, providing instantaneous information about surface roughness, shape and waviness. The surface finish of the original surface can be measured and compared with the surface morphology after the test. The three-dimensional surface mapping profilometer can accurately measure the surface roughness, the depth of cavitation pits and wear grooves, the size and periphery of the cracks, the step heights and the volume loss.

Initially the sample was carefully set onto the moving platform of this advanced equipment. Then light focus is adjusted on the sample surface by moving the instrument head. The fringes have to be revealed in the monitor and extended as wide as possible across the screen for a superior analysis. After setting the height and the focus point, light intensity is the next parameter to be adjusted. Thereafter measurements take place using the appropriate

parameters of the MetroPro software. In some cases, calibration of the machine was needed in order to avoid any undesirable fluctuations.



**Figure 53: ZYGO surface scanning interferometer**

Finally stitching is another parameter of the software which can be proved useful in many measurements. After a number of detailed scans across the surface with specific magnification, the generated images can be stitched together to create a full 3D profile of the surface and the wear scars. This technique was enabled the author to accurately determine the size parameters, the roughness, the wear erosion rate and the volume loss from all the tested samples.

#### **4.2.3 Scanning Electron Microscopy**

Scanning electron microscopy is widely used for providing high quality micro-structure images and obtaining chemical composition of the material samples. Its advanced technology is making it one of the most versatile instruments for surface investigations. In this project two different SEM systems were used: a typical SEM found at Bournemouth University (figure 54) and a technologically superior model, the Zeiss Supra 35 VP, used by the author at Brunel University.

The sample was entered into the vacuum chamber and was placed in position. The chamber is vacuumed in order to avoid any electron dispersal or scatter due to collisions with other molecules. The electron gun was adjusted to a desirable working distance (WD) for the highest possible definition images. The system generates an illuminating beam of electrons (kV) controlled by the SEM operating console. The higher the voltage the better the image resolution but the greater the heat that is generated on the specimen. Thus, lower voltages (10 kV) may have to be used for delicate samples like the elastomer tip seal. Higher voltages (20 kV) can be used for non biological specimens like metals [179].



**Figure 54: Scanning electronic microscope (SEM)**

The SEM proved to be extremely useful for the interpretation of the wear mechanisms on the elastomer surface because the black surface colour of the tip seal did not allow ZYGO to create proper 3D images or the optical microscope to generate fine images. Moreover SEM was used for element analysis in order that the debris found on the surface of both samples after test could be indentified to show the nature of the wear regime.

### 4.3 Auxiliary devices

A few extra devices were used in order to enhance the experimental data and to improve the quality level of the research. All the auxiliary systems used for this project are briefly described in the following sections (4.3.1-4.3.6).

#### 4.3.1 Hardness

With the hardness test, the mechanical hardness of all the tested samples was effectively measured (figure 55). With the micro-hardness test, the transition of the mechanical hardness across the cavitation samples was calculated. Specifically, the fluctuation of hardness values across the main crater, formed by cavitation impact, and its outside periphery were evaluated and plotted into graphs.



Figure 55: Hardness test machine

Prior to cavitation tests, the sample was positioned on the base of the hardness machine. Then the applied load and the downward speed were adjusted. The load used varied from 50 to 100 N. The speed was adjusted according to the hardness standards. The hardness values of the samples were successfully interpreted. After the completion of the cavitation tests, micro-hardness tests were performed using 8.825 N applied load. Subsequently, the tested samples

were moved to the optical microscope for precise measurements of their size indentations. The actual size of the indentations in combination with the hardness Vickers textbook will reveal the appropriate micro-hardness values of the materials.

#### 4.3.2 Testometric Machine

With the help of the Testometric machine (figure 56) the material properties of the scroll's steel plate were successfully determined. The sample was properly modified to obtain the bone shape required for this test and was gripped by the edges within the machine jaws. Then the software parameters were entered in the interface console and the tension process was started. The data was obtained in plotted graphs (Appendix C).



Figure 56: Testometric machine for performing tension and compression mechanical tests

#### 4.3.3 Viscometer

With the use of the DV-II+ PRO Digital Viscometer (figure 57) the viscosity of the lubricant used in the cavitation tests was properly measured. Then, a correlation of the viscosity values with other parameters from the cavitation tests was conducted.



**Figure 57: DV-II+ PRO Digital Viscometer**

Initially a calibration of the system was made using water liquid. The operation of the viscometer is based on the fluid resistance the spindle experiences as it rotates. A minimum quantity of 300 ml of lubricant was poured into a glass beaker and the appropriate spindle attached to the viscometer was immersed into the liquid. The deeper the spindle was immersed into the fluid the higher the measurement accuracy was achieved. Special stainless steel low viscosity spindles can measure a wide range of viscosities from 15 to 6,000,000 mPa·s with 1% of full scale range torque measurements accuracy. The speed can be varied from 0.01 to 200 rev/min. Temperature measurements and data outputs are gathered by the Rheocalc software and are automatically displayed on a PC monitor.

#### **4.3.4 Surface Tension**

Surface tension was another critical parameter to the cavitation experiments. The surface tension under the same temperature conditions was estimated for all the three liquids. Three different dried and thoroughly cleaned orifice tubes were deployed for each of the three liquids respectively. Ten millilitres of each liquid was poured into the tubes and the liquid lift was calculated. The measurements of the liquid lift were precisely indicated with the use of the optical microscope. The lens of the microscope was focused on the critical points of the

lifted part of the liquid across the side wall of the tubes and the height different was found and successfully calculated, see figure 58.

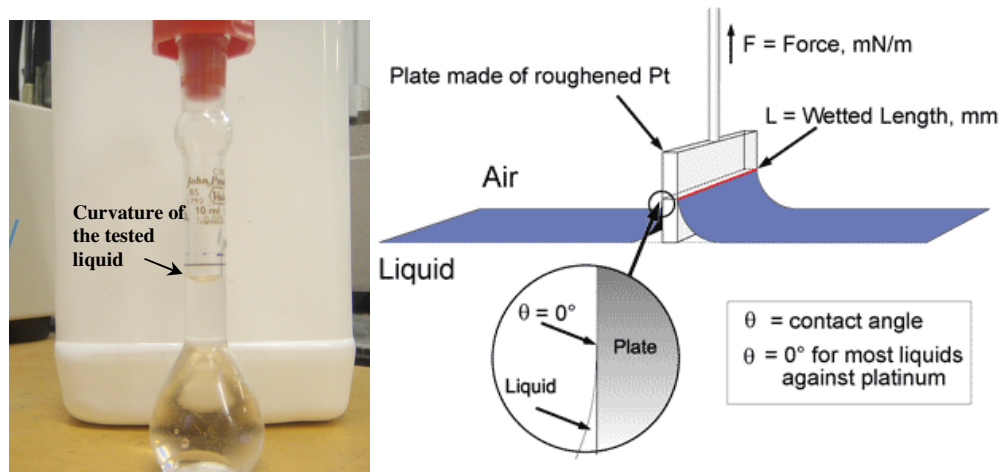


**Figure 58:** The glass lab orifice tubes showing the curvature of the tested liquid. The schematic diagram explains the liquid lift.

The surface tension calculations were conducted according to the following equation 62 and are presented in Appendix I.

$$\Delta h = \frac{4\sigma \cos \vartheta}{\rho g d} \quad (59)$$

Where  $\Delta h$  is the water lift (mm),  $\sigma$  is the surface tension in (mN/m),  $\theta$  is the contact angle between the liquid and the wall of the tube which in all the measurements was assumed to be zero,  $\rho$  is the density of the liquid (kg/m<sup>3</sup>),  $g$  is the gravitational force (m/sec<sup>2</sup>) and  $d$  is the orifice diameter (mm).

#### 4.3.5 Optical Emission Spectrometry (OES)

The Optical Emission Spectrometry was used for a thorough chemical examination of the studied steel samples (figure 59). The operational principles of the OES are based on the electrode which creates a high intensity sparkle on the surface of the testing sample. The sample sits on the top of the electrode and is hermetically sealed in a metallic box. The air is totally removed from the tested area with the use of argon gas. In that way, during the operation process, the light from the reflection on the surface of the sample after the electrode sparkle travels without any loss.

The light then reaches the photomultiplier which distinguishes the elements which the tested material consists of. Each element has a specific wavelength and so reflects at a specific angle. Thus, the photomultiplier which corresponds to the 10 basic elements can effectively distinguish the composition of the sample into its elements.

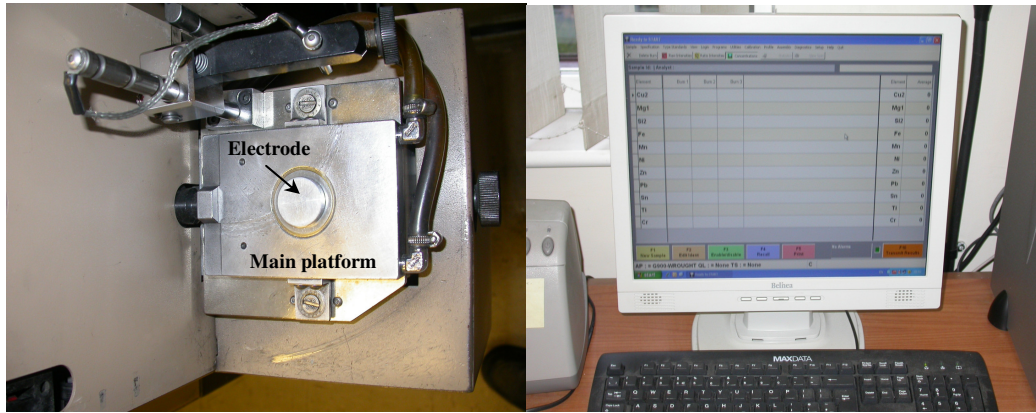


**Figure 59: The experimental chamber of the optical emission spectrometry (OES). The interface of the OES shows the concentration percentage of the identified elements.**

With the help of the appropriate software the results from the photomultiplier can be reproduced into a percentage. Thus, after the end of the analysis, the concentration percentage of the individual elements of the tested samples was successfully identified. The OES was used for the chemical analysis of all of the steel samples (Appendix B).

#### **4.3.6 Inductively Coupled Plasma Optical Emission Spectrometry (ICP-OES)**

A comprehensive oil analysis was also conducted with the use of an optical emission spectrometry system (figure 60). The oil samples after the end of the sliding tests were drawn off and placed into plastic bottles. The plastic bottles with four different types of oil at 40 °C, 100 °C and 150 °C and a bottle with fresh oil were sent for analysis to the Inductively Coupled Plasma Optical Emission Spectrometry (ICP-OES).

The IES-OES is a major technique for elemental analysis. A thoroughly homogenized used oil is dissolved with suitable solvents and then mixed with water, prior to being fed into the plasma. Plasma consists of a hot, partially ionized gas, containing an abundant concentration of cations and electrons that make the plasma a conductor.

The first step in the procedure is the conversion of the molecules in the sample to individual atoms and ions using a high temperature radio frequency induced by ionized (typically argon)

plasma. Then, the sample solution is introduced to the ICP instrument by free aspiration or an optional peristaltic pump. Finally, ICP-OES utilizes ultraviolet light (UV) and visible spectrometry to image the plasma at the exact wavelength of ionic excitation of the element of interest. In other words by comparing emission intensities of elements in the test sample with emissions intensities measured with the standards, the concentrations of elements in the test sample are calculated [180].



**Figure 60: Inductively Coupled Plasma Optical Emission Spectrometry (ICP-OES) for liquid analysis**

#### **4.4 Sliding Wear Test Procedure**

Initially testing was distinguished in batches, grouped according to the lubricant type. This was performed for two reasons. Firstly in order to avoid any impurities of a severe lubricant regime (e.g 150 °C) to be contaminated within the fresh oil introduced for the lower temperature regimes (e.g 40 °C). Secondly to collect the lubricant after each single test in plastic bottles in order to send it for chemical analysis in the OES.

The contamination or the degradation rate for all three lubricant regimes was checked for consistency after each experiment. Therefore, a full disassembly and cleaning regime was

only required if the lubricant type had totally changed affecting the nature of the tests. This action was taken twice before the completion of the sliding tests. The chamber, the bellows and the components exposed to the dirty lubricant required cleaning. This was carried out using an ultrasonic bath with acetone cleaning fluid.

At the beginning of the experiments the samples were appropriately mounted inside the environmental chamber. The load then had to be applied manually. To obtain reliable and comparable results, the contact loading of all tests needed to be identical. In order for this to be achieved, a dentist's mirror and a torch were used. The mirror provided a real-time image of the contact state between the pin and the plate. Thus with this method, all the pre-loading contacts were eliminated and the operating height was calibrated to the same value for all the tests.

Thereinafter 3 ml of lubricant were introduced into the bath using a clean syringe. Then the lid was placed into position and sealed the top of the chamber. The temperature was raised to the desired level and controlled by a pair of thermocouples. The sliding tests provided information on friction force and coefficient over time. Data represented the charge temperature, the reciprocation frequency, the friction force and the friction coefficient generated during the tests and was recorded using the machine's control software. Any wear results at the contact points were observed during post-test analysis. After the end of the experiments the lid was removed, the tested lubricants were drawn off using a syringe and stored in the appropriate analysis bottles. Then the samples were removed, cleaned with acetone using an ultrasonic bath cleaner and finally sent for post-test analysis.

#### **4.5 Cavitation Erosion Test Procedure**

The cavitation erosion test procedure was divided into two parts. In the first part the test procedure during the incubation time of the cavities will be described. The second part involved the use of samples under a prolonged period of time. The ultrasonic system was fully calibrated before being used for the experiments.

##### **4.5.1 Incubation Period of Time**

The experiments performed regarding the incubation cavities could be affected by several factors. The presence of any debris or any remain liquid in the 0.5 L experimental tank from previous tests could possibly affect the rationalism cavitation mechanism. Thus, before and after every test the square container was cleaned and dried to avoid the presence of any impurities. Then, the samples were mounted on the bottom of the tank.

According to the nature of the test, the appropriate liquid was poured in a sufficient level for generating cavitation. The horn was immersed into the liquid and its distance from the sample was adjusted. The appropriate adjustment was made with the use of a 0.5 mm thickness feeler gauge and kept constant for all the tests. The perpendicularity of the horn in regards to the surface of the sample ensured the maximum performance of the ultrasonic transducer. The high speed camera was focused on the upper area of the sample while a fibre optic was providing adequate light. All the tests were run strictly for 10 minutes ensuring only the generation of cavitation pits and that the temperature levels remained steady. The tested temperature, after being adjusted to the desired level, was controlled at regular time intervals by a digital thermometer.

Once the test was over the system was turned off and the test specimens were carefully removed from the bottom of the tank. Thereafter, the samples were cleaned in an ultrasonic bath with cleaning liquid acetone and dried with a blower before being sent for surface analysis.

#### **4.5.2 Prolonged Period of Time**

For the experiments to study the durability performance of various steel grades under a prolonged period of time, a simpler procedure was followed. Instead of a small tank a large 5 L tank was used in order that the temperature remained constant for all the tests. The sample was mounted on a small vice press which was submerged onto the bottom of the 5 L container. In these experiments only distilled water was used. Furthermore, after every test the tip of the horn was thoroughly checked. If it was found to be damaged, it was properly machined with a lathe in order to achieve the desirable flatness and enable it to be re-used for further cavitation tests. Apart from the above changes everything else was strictly followed according to the process described previously for the incubation period.

#### **4.6 Experimental Conditions**

The experimental conditions were adjusted as close as possible to those of the scroll expander for both test rigs. On one hand, the operational contact environment of the TE 57 within the test chamber approaches the conditions found in the critical areas of the scroll expander. On the other hand, the physical properties of the liquid environments used in the cavitation tests, were kept in close proximity to the actual operation environment of the working fluids within the scroll.

#### 4.6.1 Sliding Wear/Friction

For the micro-friction machine to provide meaningful results, the test parameters should have followed those of the scroll expander as closely as possible. Hence, the temperature, the speed and the contact load of the scroll expander, during its operational period, were initially estimated prior to being applied for sliding wear experiments.

The tested temperatures were adjusted to three different critical values, at 40 °C, 100 °C and 150 °C. The selection was made according to the start-up conditions of the scroll where the temperature is about 35-40 °C, the outlet temperature of the working fluid from the scroll around 100°C and the inlet temperature of the working fluid to the scroll approximately 150 °C.

The tested velocities in the TE 57 machine were adjusted to two different values at 25 Hz and 50 Hz with an equivalent radius (stroke) of 5 mm. This gave a reciprocated average sliding (surface) velocity of 0.5 m/sec and 0.25 m/sec respectively. The rotational speed of the scroll was approximately 3000 rev/min with a diameter eccentricity of 10 mm. This gave a continuously sliding velocity of 1.57 m/sec.

$$x = x_0 \sin(2\pi ft) \quad (60)$$

$$u = \frac{dx}{dt} = x_0 2\pi f \cos(t) \quad (61)$$

In the TE 57, the slider steel sample performs a reciprocating movement achieving the lowest velocity values at its edge points A and B (actually the velocity is zeroed at these points), at the end of the sliding movement, while it achieves the maximum velocity at the centre point of the movement. The movement of the slider plate can be interpreted according to equations 59 and 60. Thus, the maximum surface velocity which can be generated by the sinusoidal movement of the rotary motor is 0.875 m/sec at 50 Hz, nearly half that of the scroll's expander, see figure 61.

Since the maximum velocity is found only at the centre point of the accelerated sliding motion by the motor, the average surface velocity had to be taken into account for the tests. Thus, the actual surface velocity (average velocity) used for the sliding tests was 0.5 m/sec for 50 Hz and 0.25 m/sec for 25Hz. The 50 Hz is the maximum rotational velocity the motor can achieve. The 25 Hz was chosen as an alternative motor speed for a better comparison of the

results and for a more coherent interpretation of the velocity effects during the steel-polymer sliding experiments.

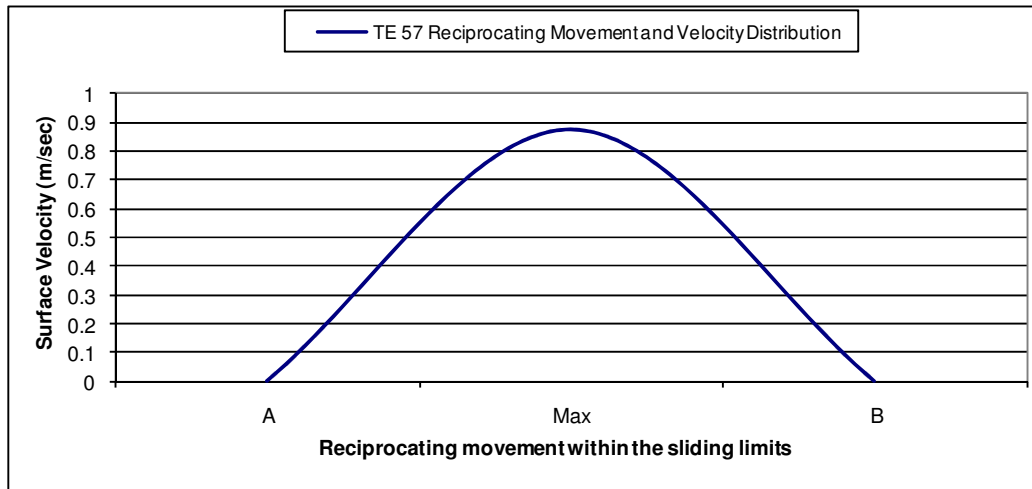


**Figure 61: The distribution of the sliding velocity according the sinusoidal movement of the TE 57 motor**

The calculation of the contact load was a complicated issue. To ascertain the contact condition in the scroll expander a unit was dismantled and measurements were taken. The actual contact pressure revealed the specific load which had to be applied for the friction/wear tests. Finally, the applied load was adjusted at 20 N and 40 N respectively (Appendix F).

Initially, the contact load at the start-up conditions of the scroll was estimated. This was achieved by measuring the friction torque and the static coefficient of the scroll during the start-up conditions. The friction torque which is required to turn the scroll expander when it is from a resting position was calculated to be around 1 Nm. A nut was installed on the shaft of the expander and a socket connected this to the spring Newton meter. After a few attempts with the spring Newton meter to set the scroll into motion the friction torque was successfully estimated.

The friction coefficient of the upper scroll material when is in sliding contact with the lower bottom one was measured. The friction coefficient of the tip seal against the steel plate was measured during the start up conditions of the scroll, when the scrolls were in close contact. This was performed using a sliding friction bench figure 62. The friction coefficient after several dozen measurements was effectively estimated to be among 0.2 and 0.25. This number correlates well with the experiments made with the TE 57 micro-friction machine when low loads between the tip seal and the steel plate were applied. Through the friction

torque and the friction coefficient, the applied contact load between the scrolls of the scroll expander during its start up conditions could then be easily identified. The normal contact load  $L$  (N) was estimated with the use of equation 61 assuming that the torque  $T$  (Nm) is equally distributed across the contact parts.

$$T = \mu Lr \quad (62)$$

where  $r$  (m) is the radius of eccentricity and  $\mu$  is the dimensionless static coefficient between the scrolls (tip seal/steel plate). The contact load was found to be between 800 and 1000 N. The contact parameters of the scroll had to be matched to those of the samples and the contact stress of the scroll correlated with that of the samples in the TE 57 in order that the contact load calculations made sense.



**Figure 62: Measuring the friction coefficient of the two involute scroll parts with the use of a sliding friction bench**

The contact surface inside the scroll was effectively calculated using SolidWorks software. The geometric profile of the scroll and of its main components was effectively scanned with the use of an appropriate optical laser scanning camera, the Vivid-900 Konica Minolta Scanner, and downloaded to the graphical environment of the corresponding software. The contact area was assumed to be the area of the tip seal since that is the smallest contact area which takes the whole contact load and is in constant close touch with the steel plate during the whole life cycle of the scroll, see figure 63. Thus, the contact pressure was calculated to be 0.35 to 0.4 MPa. Using the contact pressure parameter of the scroll expander the contact pressure per sample was calculated. Eventually the contact load was effectively determined [Appendix F].

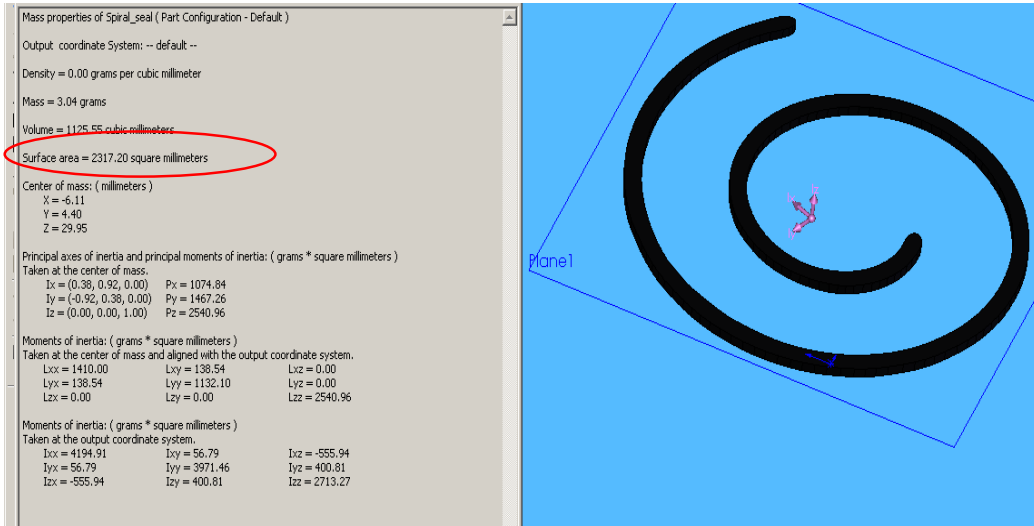


**Figure 63: Calculation of the tip seal surface area with the use of SolidWorks software**

The contact loads for the tests were chosen to be 20 N and 40 N respectively. The choice of the contact loads corresponded to an excessive contact pressure within the testing samples, of two and four times higher than the existing contact pressure among the scrolls. These contact parameters would possibly simulate a more severe wear regime similar to the scroll expander. Thus, wear results would be more comparable and the durability and performance of the materials easier evaluated.

Number of case studies	Description	Evaluation
Case 1	Dry and Lubricated Contact at constant time intervals	Investigating the changes of the contact pressure and the sliding speed over the friction coefficient
Case 2	Lubricated Contact in a Short Period of Time	Investigating the friction force, the friction coefficient and the wear rate of the tested samples under various lubrication regimes, contact loads and surface velocities.
Case 3	Lubricated Contact in a Long Period of Time	Investigating the friction force, the friction coefficient and the wear rate of the tested samples under various lubrication regimes, contact loads and surface velocities.

**Table 4: Description of the sliding experiments performed with the use of the TE 57 micro-friction machine**

The running time of the actual expander over its service life hypothetically could be in the order of 30,000 hours. However, the maximum running time under a consistent efficiency

operational mode was limited to 3,000 hours. The time target of 30,000 hours was impossible to simulate within the testing procedure but a representative correlation of the tip seal/steel plate wear performance was achieved. The running times for the major set of experiments was decided to be 20 and 60 hours respectively. This would enable the researcher to evaluate the friction and wear regime in a short and a long period of time and to come up with useful conclusions. Time intervals were chosen to be every 10 sec for better measurement accuracy. Finally the stroke length was set at 5 mm so as to better model the sliding motion of the scroll expander.

<b>Sliding Wear Tests-Experimental Conditions</b>				
<b>High Carbon Steel against Reinforced Fluoroelastomer-Pin on Plate Contact</b>				
Temperature (°C)	Frequency (Hz)	Contact Load (N)	Time (h)	Distance (km)
40	25	20	20	18
40	25	40	20	18
40	50	20	20	36
40	50	40	20	36
100	25	20	20	18
100	25	40	20	18
100	50	20	20	36
100	50	40	20	36
150	25	20	20	18
150	25	40	20	18
150	50	20	20	36
150	50	40	20	36
40	50	20	60	108
100	50	20	60	108
150	50	20	60	108

**Table 5: Sliding wear tests/ Test conditions**

Three sets of experiments were conducted (table 4). In the first set, a series of tests were run for different contact regimes and varying contact pressures in order to investigate the effects of the friction coefficient. The second set consisted of short period tests, lasting 20 hours, aiming to analyze the friction force, the friction coefficient and the wear rate of the tested samples under various lubrication regimes, contact loads and surface velocities. The third set of experiments had the same objective as the second bunch of tests but were applied for long time periods.

The two last sets of experiments are detailed in table 5. The number of tests conducted totalled 15. In order to obtain meaningful and comparable data a repeatable test regime was required. Hence, each of the tests was repeated at a minimum of 4 times and the results were interpreted using the average values of these tests.

#### 4.6.2 Cavitation Erosion

To assess the experimental conditions adjusted for the cavitation tests a similar philosophy had to be followed as for the sliding wear tests. The experimental conditions applied during the cavitation tests were mirrored as closely as possible to the real world case. In the cavitation experiments the test conditions were easier to identify than the ones applied in the sliding friction wear tests.

The experimental parameter which was crucial and had to be carefully identified was the temperature. The choice of the temperature parameter for the cavitation tests was made according to the operating temperature conditions of the scroll expander. However, the high temperature values that predominate inside the scroll could not be applied in the experiments as it could become extremely dangerous to recreate the actual scroll conditions in the ultrasonic tests. Hence, for safety reasons, the lubricant and refrigerant bubble behaviour were studied in a room pressure of 1 bar and temperature of  $23\pm 2$  °C.

Physical Properties	Water	Refrigerant	Lubricant
Ultrasonic Velocity inside Liquid (m/sec)	1476	990	1700
Liquid Density (kg/m <sup>3</sup> )	1000	625	995
Viscosity (mPa·s)	1	0.225	30
Surface Tension (mN/m)	54-59	33-35	49-53
Vapour Pressure(Pa) at 20 <sup>0</sup> C	2230	53328	1300
Acoustic Power (Watt)	6	3	9

**Table 6: Physical Properties of the experimental liquids at  $23\pm 2$  °C**

Initially, the lubricant was thought to be the most probable means of generating cavitation bubbles during the operation of the scroll expander. Thus, a much thinner lubricant from the same designated family was acquired to replace the actual lubricant of the scroll. Its properties in a room environment were closely matched with the properties of the lubricant inside the scroll environment. The aim was to obtain representative results regarding the lubricant's performance. The physical properties of the tested liquids are illustrated in table 6.

The liquids used for the tests were distilled water, a synthetic lubricant and a high molecular organic refrigerant. The distilled water was used as a reference fluid to provide more coherent results for the analysis of the cavitation bubbles. The viscosity and surface tension for all three fluids was measured in the ambient environmental conditions of the laboratory using appropriate experimental devices as described in paragraphs (4.3.3 and 4.3.4).

Test Cases	Description	Evaluation
Case 1	A full description of the size of the cavitation pits formed at their incubation time under various liquid environments.	Evaluating the typical depth, area and volume loss of the cavitation pits and compare them with their maximum values found in all the steel grade surfaces. Investigating the behaviour of the liquids environment and their impact on the formation of the bubbles.
Case 2	Cavitation tests for all the four steel grades were performed under various prolonged time periods in a water medium	Evaluating the durability of the steel grades looking at its erosion wear rate and its resistance to cavitation impact. The most durable material was revealed.

**Table 7: Description of the cavitation tests performed with the use of the Cavitation ultrasonic experimental apparatus**

Two test groups were conducted for cavitation experiments (table 7). In the first group, the pits incubation stage found on the surface of all the steel grades and formed by the destructive impact of the cavitation bubbles (cavities) within all the tested fluids, was thoroughly investigated. The use of the high speed camera was essential in these tests while the tested period lasted for 10 min for each case. Furthermore, the high speed camera results revealed the performance of all three tested liquids under cavitation conditions. The second group of experiments dealt with the durability of the four different steel grades used in these tests. All the tests were performed in a water environment over a prolonged period of time. The main objective of these tests was to effectively identify the most durable material.

The set of the thirty different configurations of cavitation experiments are detailed in table 8. In order to obtain meaningful and comparable data a repeatable test regime was required. Thus, each of the tests was carried out a minimum of 10 times for the group of the 10 min tests, at the incubation time, and 3 times for the tests in a prolonged period of time. The results were interpreted using the average values of these tests

<b>Duration (min)</b>	<b>Steel Samples</b>	<b>Environmental Conditions</b>	<b>Acoustic Power (Watt)</b>	<b>Tank (L)</b>	<b>Extra Equipment</b>
10	Chromium	Water	6	0.5	Fibre optic/Camera
10	Chromium	Lubricant	3	0.5	Fibre optic/Camera
10	Chromium	Refrigerant	9	0.5	Fibre optic/Camera
10	High Carbon	Water	6	0.5	Fibre optic/Camera
10	High Carbon	Lubricant	3	0.5	Fibre optic/Camera
10	High Carbon	Refrigerant	9	0.5	Fibre optic/Camera
10	Low Carbon	Water	6	0.5	Fibre optic/Camera
10	Low Carbon	Lubricant	3	0.5	Fibre optic/Camera
10	Low Carbon	Refrigerant	9	0.5	Fibre optic/Camera
10	Steel Plate	Water	6	0.5	Fibre optic/Camera
10	Steel Plate	Lubricant	3	0.5	Fibre optic/Camera
10	Steel Plate	Refrigerant	9	0.5	Fibre optic/Camera
60	Chromium	Water	6	5	No
120	Chromium	Water	6	5	No
180	Chromium	Water	6	5	No
300	Chromium	Water	6	5	No
480	Chromium	Water	6	5	No
60	High Carbon	Water	6	5	No
120	High Carbon	Water	6	5	No
180	High Carbon	Water	6	5	No
300	High Carbon	Water	6	5	No
480	High Carbon	Water	6	5	No
60	Low Carbon	Water	6	5	No
120	Low Carbon	Water	6	5	No
180	Low Carbon	Water	6	5	No
300	Low Carbon	Water	6	5	No
480	Low Carbon	Water	6	5	No
60	Steel Plate	Water	6	5	No
120	Steel Plate	Water	6	5	No
180	Steel Plate	Water	6	5	No
300	Steel Plate	Water	6	5	No
480	Steel Plate	Water	6	5	No

**Table 8: Cavitation erosion tests/ Test conditions**

## 4.7 Testing Samples

The tested samples which were used in this study were distinguished into two groups. In the first group were the samples used for sliding wear tests while the second group were the samples used for cavitation tests.

### 4.7.1 Samples for the TE 57

The samples used for sliding wear tests were constrained to the high carbon steel plate and the high performance fluoroelastomer tip seal. Thus, the performance of the steel plate against the tip seal under specific lubricated conditions was evaluated. An analytical investigation of the main components of the scroll expander was presented in paragraph (3.2.1). The chemical elements were defined and the structure of the materials was determined.

### 4.7.2 Samples for Cavitation

The high carbon steel plate was the only component in the scroll suffering from cavitation erosion. Thus specimens extruded by the steel plate of the scroll were used for cavitation bench tests.

Steel Grade	Chemical Composition %						
	C	Si	S	Mn	Cr	P	Al
<b>EN31</b>	0.95 - 1.05	0.2 - 0.25	0.005	0.31	1.45 - 1.60	0.01-0.015	0.005-0.01
<b>Ck10</b>	0.2-0.28	0.15-0.2	0.024	0.54	0.03	0.014	-
<b>Ck85</b>	0.80-0.90	0.20-0.25	0.005	0.5-0.55	0.05	0.008	0.005

**Table 9: Chemical analysis of the steel samples used for cavitation tests**

Another batch of steel samples consisted of a chromium steel, a through-hardened high carbon steel and a case hardened low carbon steel with similar physical properties to the steel plate which was used for cavitation experiments (table 9). The samples were commercial ball-bearings in a lower market price than that of the actual steel plate. Their designation grade was given by the manufacturer. A comparison of their durability performance was made, thus the best steel was revealed. The grain structure for each of the bearing samples was determined using the same method as explained in paragraph (3.2.1). The grain structures of the steel samples are presented in figure 64.

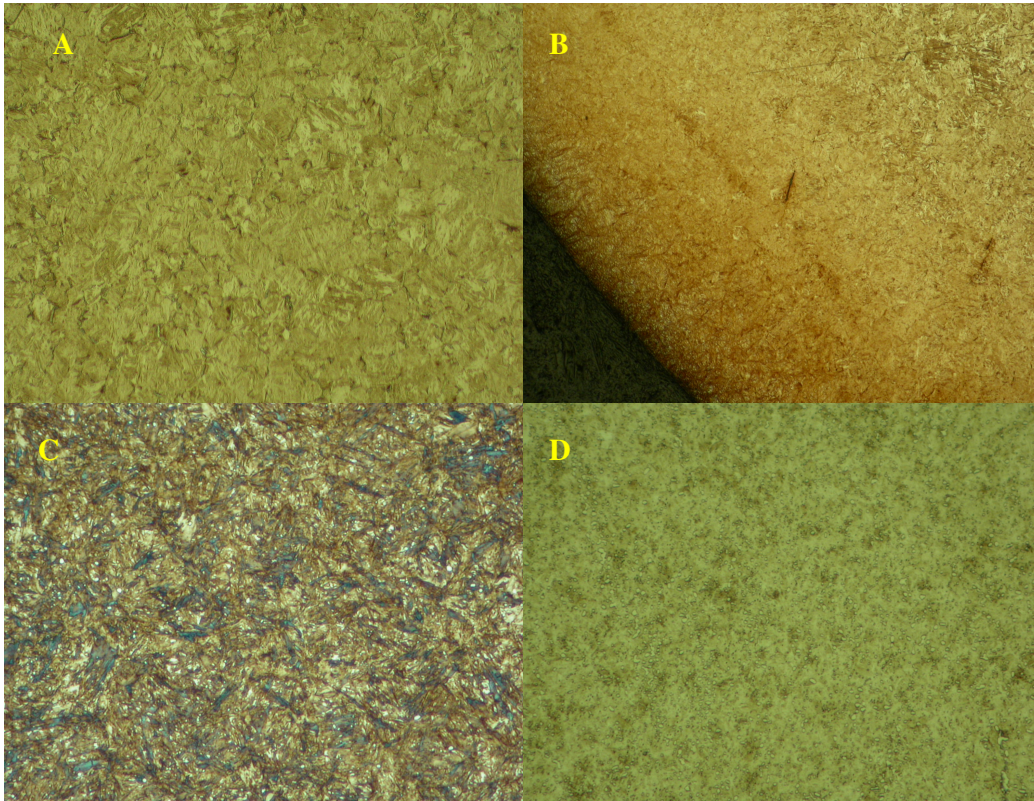


**Figure 64: Material structure of A&B) Low carbon steel C) High carbon steel D) Chromium steel**

The low carbon steel (Ck10) is a typical low carbon steel that had been case-hardened (figure 64 A&B). The first image shows the general core micro-structure of tempered martensite with small amounts of ferrite (dark spots). The second image shows the case and the core transition. The case-hardened zone (high hardness >1000 HV) is also lightly tempered martensite with some retained austenite (light etching). The total case depth is about 1 mm.

Material Properties	Various Steel Grades			
	Chromium	High Carbon	Low Carbon	Steel Plate
Tensile Strength (MPa)	2224	733	365	1335
Yield Strength (MPa)	2030	700	303	810
Density (kg/m <sup>3</sup> )	7834	7860	7860	7825
Hardness (Vickers)	840-880	850-875	950<	550-530
Young Modules E (GPa)	207	207	207	207

**Table 10: Mechanical properties of the steel samples used for cavitation tests**

The high carbon steel (Ck85) is a typical through-hardened steel which is hardened not just on the surface but also in depth (figure 64 C). The structure of the high carbon steel comprises predominantly tempered martensite with a small amount of bainitic (brown etching) and

lower transformation products such as ferrite (dark etching phases). A uniform dispersion of retained austenite (light etching) was also observed within the martensitic matrix.

The structure of the chromium steel (EN31) is comprised of fine, predominantly spheroidal carbides, mainly chromium carbides,  $\text{Cr}_3\text{C}_2$  (white spots), in a matrix of lightly tempered martensite (green etching) (figure 64 D).

Moreover the mechanical properties of all the steel samples are depicted in table 10. The properties for the high, low and chromium steel grades were provided by the manufacturer. The properties of the steel plate were accurately measured with the use of the Testometric machine (paragraph 4.3.2). The steel plate was accurately manufactured by the researcher in the shape of a bone sample, positioned in the Testometric machine and tension tests were performed. The mechanical properties of the steel plate of the scroll expander were successfully revealed.

## **4.8 Samples Preparation**

Wear and friction tests were conducted with the use of the micro-friction machine TE 57 and a suitable cavitation apparatus integrated with high speed camera equipment. Thus, two different manufacturing processes had to be followed. The first process produces samples appropriate for friction tests within the TE 57 micro-friction machine while the second one produces suitable samples for cavitation tests.

### **4.8.1 Samples Preparation for the TE 57 test rig**

Material test specimens were produced utilising the main parts of the scroll (figure 65). The steel plate and the tip seal were deployed to produce new samples for sliding friction tests. The steel specimens derived from the high carbon steel plate of the scroll expander were cut in appropriate dimensions with the use of the Accutom-5 cutting machine and attached to the top of auxiliary rectangular steel plates with the use of a strong adhesive.

The cutting process had to be very precise in order that the steel specimens did not bend or any undesirable cracks form. Any curvature on the specimen surface, after cutting, could make the sample useless for implementation on the auxiliary plate. The contact of the steel sample against the tip seal had to be constrained at several points instead of a flat on flat contact with the parallel surface of the elastomer. Thus, a delicate cutting technique was enabled.

Once the steel specimens had been mounted on their auxiliary steel plates the samples went for polishing (Appendix A). The plates were surface-ground, with SiC paper P120 and 1200 grade at about 250 rev/min with medium force for 2 min, to remove scratches, burs and surface anomalies providing the required surface finish. Then, they were polished using a 9 and 3 micron Metadi Supreme diamond slurry applying a medium force at 200 rev/min for about 5 min. The surface finish of the steel samples was properly measured by the ZYGO interferometer microscope and found to be  $R_a=0.05 \mu\text{m}$ . Then the steel samples were submerged in an ultrasonic bath, washed with acetone cleaning fluid and finally stored in a glass jar with moisture absorbing desiccant packets.

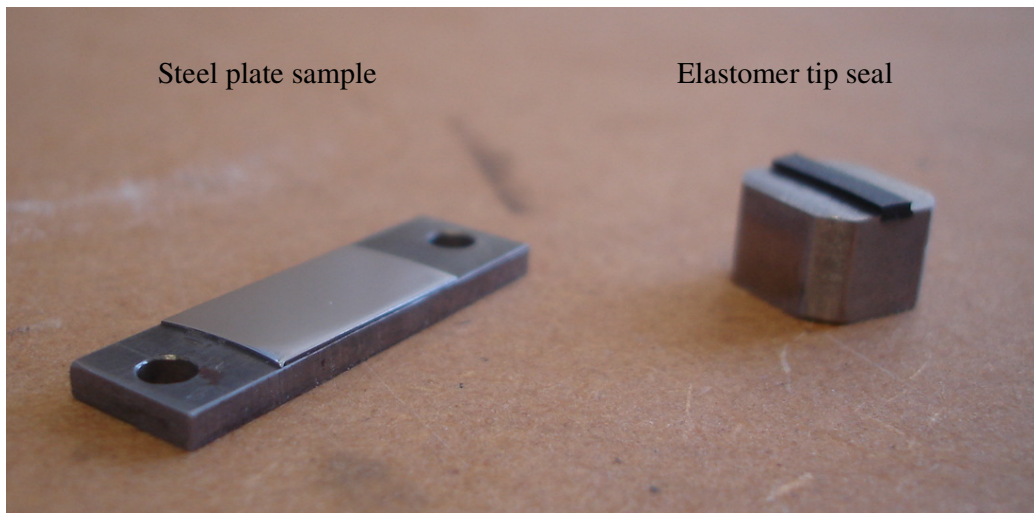


**Figure 65: The implementation of the testing samples used for sliding wear tests**

The high performance fluoroelastomer specimens made by the tip seal component, were carefully cut with a blade knife and placed on the surface of auxiliary rectangular steel samples. The tip seal specimens were mounted using the same method as the steel samples. Special holders were constructed to hold the auxiliary parts of the specimens. The nature of the elastomer specimens did not require any further special preparation for testing. For the fluoroelastomer samples the surface roughness was measured with the “Test Surf” machine using a sliding stylus across the surface. The  $R_a$  value was estimated to be 2 to 3  $\mu\text{m}$ .

The steel specimens had dimensions of (15, 10, 0.3 mm) while the fluoroelastomer specimens had dimensions of (7, 3.5, 1.5 mm). The hardness for the steel plate and for the tip seal was measured within the values of 530 HV and 90 HV respectively.

#### **4.8.2 Samples Preparation for the Cavitation test rig**

Suitable test samples for cavitation experiments were produced. Once again, constraints on the size of the scroll's steel plate were considered. Following effective modifications on the steel plate's shape, with the use of the Accutom-5 cutting machine, steel specimens were produced (Appendix A). Thereafter the specimens were mounted in a Bakelite base using the mounting machines and following a specific methodology (Appendix A). The steel samples were then ground and polished using appropriate polishing wheels, forming a very smooth flat surface. The greater the consistent flatness of the steel samples, the more coherent the results can be. The method was kept similar to the one described in the previous paragraph (4.8.1). The steel samples were thoroughly cleaned with the use of acetone in an ultrasonic bath and stored in a dehumidified glass jar ready for testing. The surface finish of all the steel samples was properly measured by the ZYGO interferometer microscope and the Ra roughness parameter found to be 0.01 to 0.025  $\mu\text{m}$ .

## **5 CHAPTER : FRICTION ANALYSIS AND WEAR MODES**

### **5.1 Introduction**

The experimental results produced by the TE 57 micro-friction machine, can be distinguished according to their test configuration. A combination of the applied load, the test duration, the sliding speed and the operating temperature are the basic parameters which affect the nature of the individual tests. In addition, the presence of lubricant significantly affects the wear contact and is indeed beneficial for a further attenuation of the friction coefficient. The experimental procedure which was followed in order to interpret the sliding wear and friction mechanisms of the steel against the reinforced fluoroelastomer, was distinguished in two parts.

In the first part the nature of the contact and the parameters which prevail during the tests are thoroughly analysed. The experiments initially were focused on the dry contact between the tip seal and the steel specimens. Then similar tests were performed using a lubricated regime. The results from the tests were utterly focused in the frictional data and a comparison between the dry and the lubricated contact was made. The process for each test lasted only a few minutes. The main parameters which affect the steel/fluoroelastomer contact in both regimes were revealed. These results were a first accurate indication of what was expected to be observed in the experiments over a prolonged period of time.

In the second bunch of tests the main group of experiments was conducted. The environment deployed for these tests was a synthetic lubricant. The results from the lubricated frictional data were gathered from the TE 57 micro-friction machine and plotted against the sliding distance for each test run. The wear data was derived from the measurements recorded from appropriate microscopes and was plotted against various parameters used in the tests.

### **5.2 Test Methodology**

In this first bunch of tests, a comparative study of the friction coefficient within lubricated and dry contact was conducted. The aim was to check the relationship of the friction coefficient, the applied load and the sliding speed in each case as this will be indicative of the contact conditions. The tests were performed using various applied loads at different speed variations. Friction was recorded using the in-built force transducer at intervals of 10 seconds. The applied load was manually increased with 5N being added every 5 minutes. Five minutes time was sufficient enough for a stable friction to be achieved prior to load changing. This was a good indication for a representative analysis of the friction coefficient. Eventually, the

effect of the two competitive aspects (load/speed) on the contact regime was successfully revealed. The tests were performed in a room temperature environment.

### **5.3 Friction Results Analysis (Running-in time)**

The variation of the friction coefficient of the fluoroelastomer tip seal with the steel plate counterface during the running-in stage, is shown in figure 66, where various normal loads, under dry sliding and lubricated conditions were used. The load range varied from 5 to 40N. The speed was kept constant at 50 Hz which corresponds to a sliding speed of 0.5 m/sec.

In both cases with the increasing normal loads the coefficient of friction gradually declined. The determinant was that in the case of the lubricated contact the friction coefficient was lowered to an average difference of 0.1 for load less than 20 N and around 0.6 for loads more than 30 N. Thus it can be seen that at higher loads the two curves converge to a corresponding value. This indicates that in lower loads where the real contact area is smaller, thermal effects cannot play a dominant role. The fillers stay well-mounted within the matrix of the bulk elastomer material. The contact is confined between the embedded hard fibres of the fluoroelastomer slider and the steel counterface. The wear mechanism at this stage can be characterised as a severe two-body abrasion. Thus, the friction coefficient produced by this rough contact is the highest under dry sliding and the wear rates are by far the largest. In the corresponding lubricated contact the friction coefficient is significantly lower since the film thickness prevents the severe contact of the hard asperities between the two samples.

Additionally, as the load increases, the decrease in shear strength for both regimes is dominant. Thermal effects are generating and the contact area is smoothening. Smoothening reduces viscoelastic deformation from the surface asperities while the poor thermal conductivity of the elastomer restrains the dissipation of the accumulated frictional heat. Apparently the friction coefficient is reduced. The phenomenon is generally explained by the relationship between the shear strength of the elastomer and the hydrostatic pressure, see equation 17. Moreover, lubrication accelerates the attenuation of the friction coefficient since it develops an extra protective layer between the rubbing surfaces. In contrast, the increment of load reduces the elastic modules resulting in an increase of the real contact area while it increases the viscosity at the lubricated contact points. The real contact area is greatly increased due to the serious decrease in stiffness. Thus, the friction coefficient is increased. Therefore, these two antagonistic effects determine the final friction coefficient. In the present study the friction coefficient, is further dropped with the increment of the applied load since the shearing effect prevails.

Additionally, the presence of lubricant can effectively dissipate and absorb the frictional heat. Eventually, the temperature between the rubbing counterfaces can be reduced. Hence, the dissipation of the frictional heat within the lubricant liquid protects the elastomer surface by severe shearing, resulting in a slight augmentation of the friction coefficient. This can be clearly depicted by the inclination of the lubricated curve which is levelled off in higher loads, over 30N. By contrast, the dry curve continues a steady reduction contour.

Moreover, the rolling effect (Chapter 2) in higher loads and sliding speeds is easier to generate since the combined effect of both parameters increases the interface temperature leading to deterioration of fibre matrix by shearing. The wear mechanism at this stage can be characterised as a three-body abrasion. The sheared surface of the tip seal degrades faster and more fibres are loosened leading to their free movement within the melted matrix of the polymer. Apparently, the peeled off fibres “float” within the viscoelastic matter of the fluoroelastomer material and the contact is relaxed. Thus, a combination of the rolling effect, the shear strength, the thermal effect and the viscoelastic nature of the fluoroelastomer material rapidly reduces the friction coefficient.

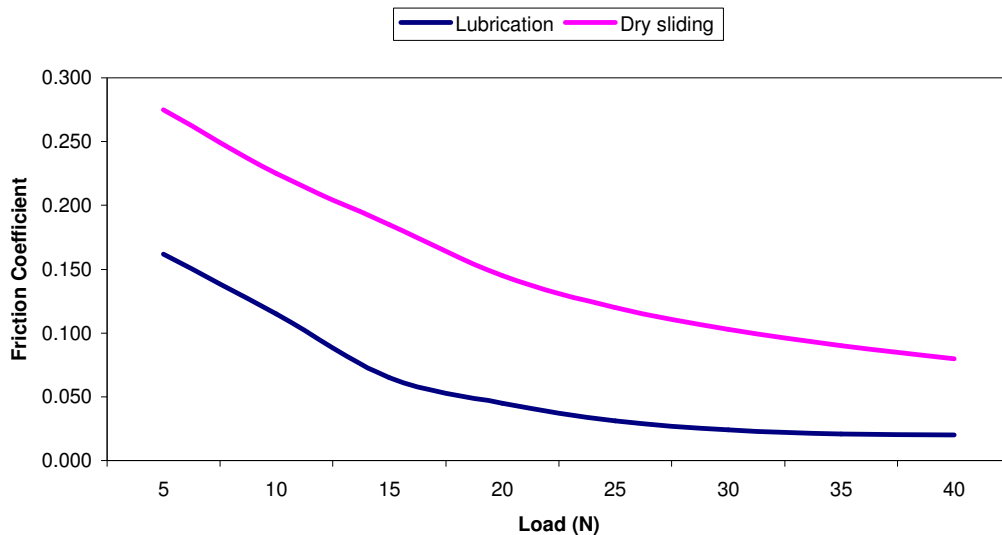


**Figure 66: Variation of friction coefficient with the applied load for different contact regimes**

Figure 66 presents the friction coefficient under different applied loads and reciprocating sliding is presented. Sliding speed and applied load are two competitive aspects which affect the friction mechanism of the rubbing materials. The importance of the sliding speed during the friction process is indicated.

It is clear from figure 67 that friction coefficient is significantly influenced by the sliding velocity rather than the applied load. The higher the sliding speed the higher is the rise in friction coefficient. As the velocity increases, the contact temperature reaches the softening point of the elastomer. As a result, the real contact area between the contact bodies tends to increase due to thermal expansion of the elastomer. Consequently, the adhesive component increases leading to higher friction coefficient values [86]. However, the drop of the friction coefficient, for the highest trend, as the load increases is significant. This can be explained by the severe contact and two-body abrasion of the steel asperities with the fillers of the elastomer in a low load stage. In higher loads since shearing dominates, accommodating the generation of the rolling effect, the friction coefficient is decreased and adjusted to similar values of the other two cases (0.2/0.25 m/sec).

Thus, from the aforementioned, it is reasonable to conclude that thermal effects and shearing mechanism seem to be the regulatory parameters for the performance of the elastomer steel contact under various sliding speeds and applied load conditions.

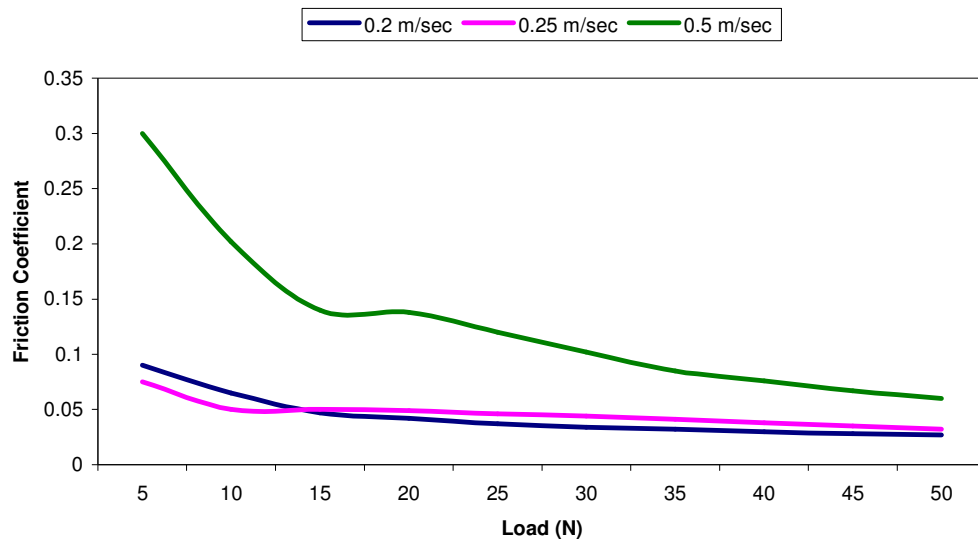


**Figure 67: Variation of friction coefficient with the applied load for different velocity conditions**

Figure 68 shows the variation of friction coefficient as a function of velocity/load parameter for the steel plate against the fluoroelastomer tip seal under dry and pre-lubricated conditions. Tests are performed under a number of dry and lubrication contacts to provide a representative picture of the variation of the friction coefficient. A comparative study between three different dry contacts and one lubricated contact was conducted. The dry contacts (dry

1/dry 2/dry 3) were distinguished according to their frequency range 20 Hz, 25 Hz and 50 Hz which corresponds to sliding speeds of 0.2 m/sec, 0.25 m/sec and 0.5 m/sec respectively. The lubrication contact was adjusted at the highest operating speed of the TE 57, in 0.5 m/sec.

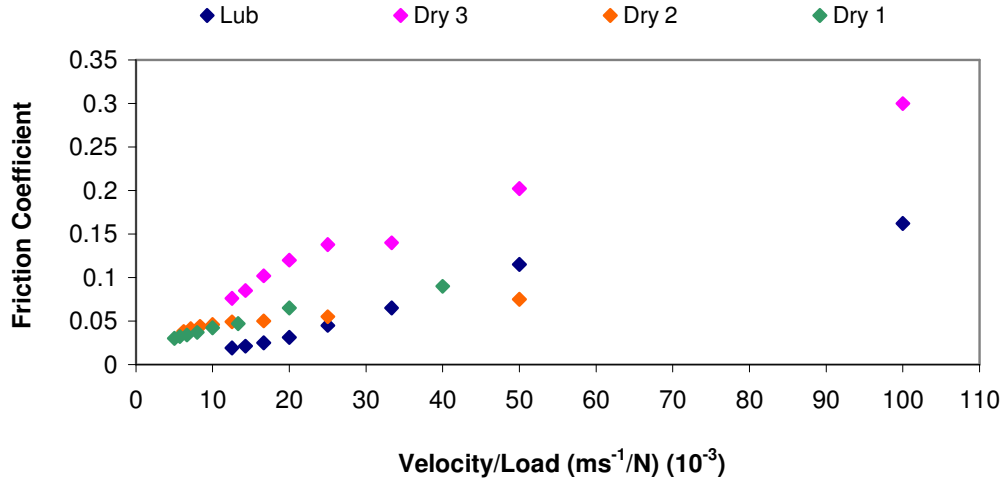


**Figure 68: Variation of friction coefficient as a function of velocity/load for the high carbon steel/high performance reinforced fluoroelastomer contact under dry and lubricated conditions**

It is depicted, that at constant sliding velocity the friction coefficient of the studied contact, in both of the regimes (dry/lubricated), decreases with the increase of load. Interestingly, the friction coefficient magnitude is seriously affected by the presence of the lubricant. A noticeable reduction in the higher loads is observed. The reduction of the friction coefficient is significant, achieving lower values than the corresponding dry contacts (dry1-dry2) with the lowest sliding velocities. Thus it is reasonable to say that lubrication can be considered as essential for an effective reduction of the friction coefficient in similar contact regimes. However an effective combination of the lubrication regime, the sliding velocity and the applied load can be proved efficient for an outstanding reduction of the friction coefficient, as will be discussed in section 5.5.

#### 5.4 Transfer films

The sliding process of the steel/elastomer contact during the running-in stage under dry/lubricated conditions results in the formation of transfer films across the steel surface. In figure 69, the elastomer transfer films formed across the surface of the high carbon steel plate under dry conditions are shown. Under the magnified view, the thickness, the continuity and the morphology of the transfer films can be observed. Using interferometer techniques the height of the transfer films was effectively measured. The height of the transfer films can reach up to 500 nm. This indicates that in the friction process the friction between the high

carbon steel and the reinforced fluoroelastomer tip seal can be transformed to a friction between the tip seal and its transfer films. Eventually, the friction coefficient is reduced.

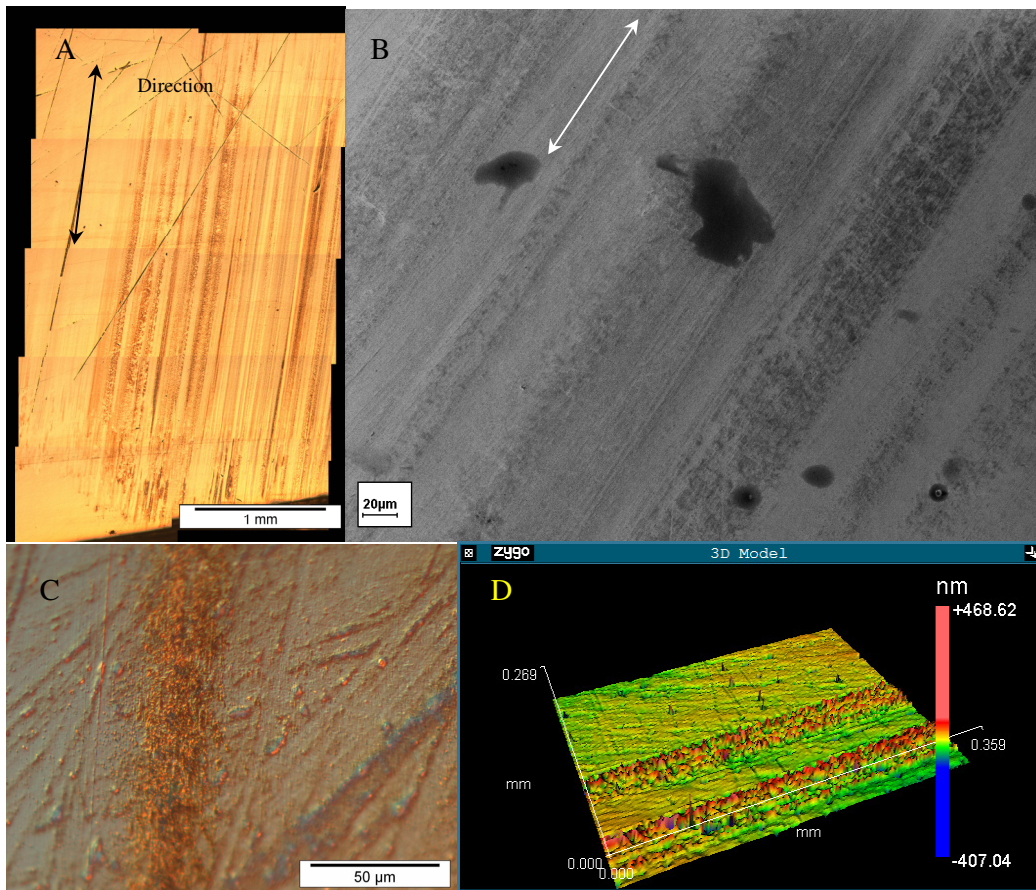


**Figure 69: A) Optical photograph of transfer films of the elastomer formed on the surface of the steel plate after 10 min test duration. B) SEM micrograph C) Optical micrograph D) ZYGO interferometer micrograph of the film deposition. (Load 40 N, sliding speed 0.5 m/sec)**

In addition, the explanation of the wear nature developed between the rubbing surfaces during the sliding test is explained by the transfer films. The amount of transfer films found on the surface of the steel plate was substantially higher, under the 40 N contact load. As the applied load increases to 40 N, considerable thermal effects are generated, softening the material structure. Apparently, the adhesive component is dominated the wear mechanisms, allowing elastomer traces to be embedded across the steel counterpart. In contrast, under 20 N applied load the real contact area prevails while severe thermal effects are constrained avoiding excessive melting of the matrix.

In figure 70, the elastomer transfer films formed under lubricated contact are shown. Under lubrication regime it can be seen that transfer film developed discontinuously across the

surface of the steel plate. The transfer film in dry sliding conditions is more compact and smooth. However, the coefficient of friction is significantly higher, especially at low loads, due to adhesion and abrasion mechanisms. In contrast, in lubricated conditions due to the “washing effect”, lubricant in due time removes most of the elastomer transfer layers from the steel surface. Only few layers scattered across the surface can be found. The height of the transfer film is substantially lower than in dry contact. Transfer films in lubricated contact are varying from 30 nm to 90 nm. In this case the lubrication film thickness can be more effective in lowering the friction coefficient of the contact than the corresponding elastomer thickness layer, However in higher loads the difference is not as significant between these two mechanisms as previously explained (paragraph 5.3).

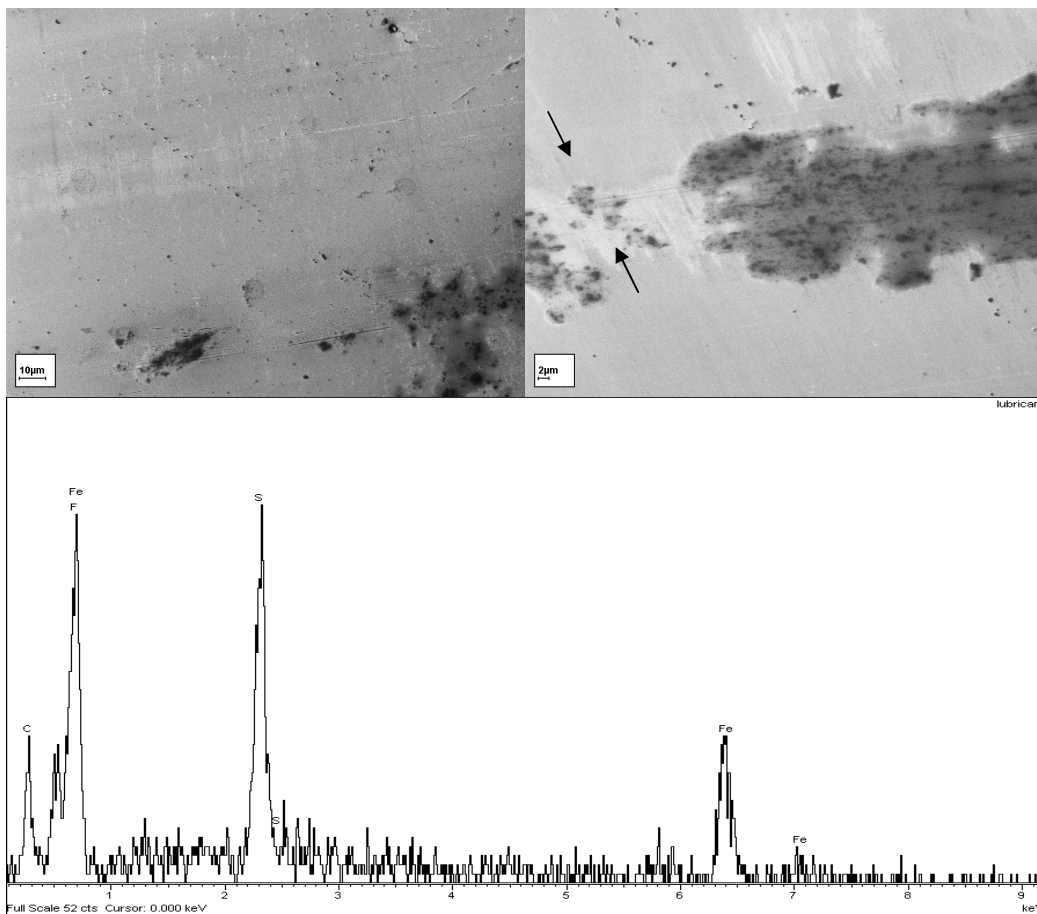


**Figure 70: Transfer films of the elastomer material detected on the surface of the steel plate after the completion of lubricated contact experiments. EPMA analysis graph reveals the presence of fluorine and sulphur, indicating the adhesive mechanism of the elastomer within a lubricant environment. Lubricant adhesion mechanism is highlighted.**

The chemical analysis, by the EPMA analysis graph figure 70, of the region in between the breaking parts of the transfer film, reveals that the contact nature is highly affected by the

presence of the lubricant. Apart from the main ferrous and fluorine elements which correspond to the steel plate and to the tip seal respectively, high levels of sulphur concentration were also monitored. This indicates that lubricant intermediates among the transfer layers disrupting the continuity formation. Eventually the “washing effect” of the lubricant removes these protective layers. However, as mentioned in paragraph (2.11) the interaction of the transfer films with lubricant can substantially reduce the friction coefficient.

## **5.5 Test results (prolonged period of time)**

The friction results can be divided into two distinctive groups, frictional data and wear data. The frictional data is gathered from the test machine and is plotted against the sliding distance for each test run. The wear data is measured and evaluated with the use of a ZYGO interferometer after the completion of the tests. The dominant lubricated friction regime for all the lubricant cases seems to be boundary lubrication. As the friction coefficient remains constant, indicated by Stribeck’s curve (figure 4), boundary lubrication occurs. The results from the contact sliding friction tests are presented below. For all the elastomer materials the coefficient of friction starts with a running-in period followed by a steady-state period.

A polymer layer, acting as a cushion, may transfer onto the steel counterpart surface during the running-in stage. The elastomer transfer film in combination with the lubricant film thickness, results in the relaxation of the contact during the steady-state period. At higher loads the frictional force is higher because of more contact area at the frictional material surface. However, the friction coefficient proportionally decreases with the augmentation of the applied load.

### **5.5.1 Friction Data**

The first batch of tests comprise the samples with low sliding contact speed 0.25 m/sec (25 Hz) at two different applied load levels, 20 N and 40 N. According to the sliding process of the two rubbing materials under those conditions and various temperature regimes, it can be seen that the reduction of friction occurs always after the initial wear stages. Thus, the friction force is significantly reduced after the running-in stage when thermal effects become active. In contrast, in the second batch of tests where an increment of the sliding speed at 0.5 m/sec occurred, the stabilisation of the friction parameters is instantly achieved in the very first stage of the running process. Thus, there is no running-in stage since the steady-state period starts immediately.

Initially the friction force was evaluated for all the test cases. In figures 71 and 72 it can be seen that the friction force increases rapidly, reaching a peak value in the very first stage of the sliding test while it then gradually decreases to a steady-state level. This behaviour was expected to happen in this low speed case. The thermal effects cannot be instantaneously generated, softening the substrate of the elastomer, leading the contact to a more relaxed regime. The kinetic energy is not sufficient to instantly melt the surface of the elastomer sample. Additionally, the lubricant at low speeds is more easily accumulated between the rubbing surfaces absorbing the contact heat and decelerating the melting process.

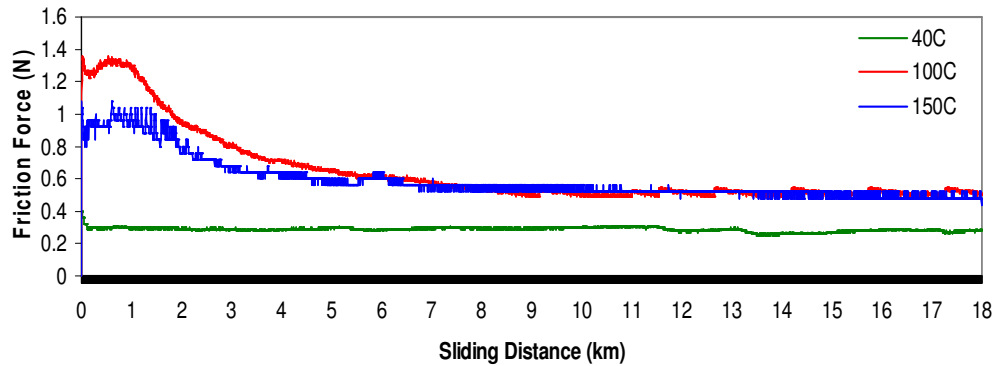


**Figure 71: Variation of friction force with sliding distance for various temperature regimes (V=0.25 m/sec, P=1.6 MPa, 20 hours)**

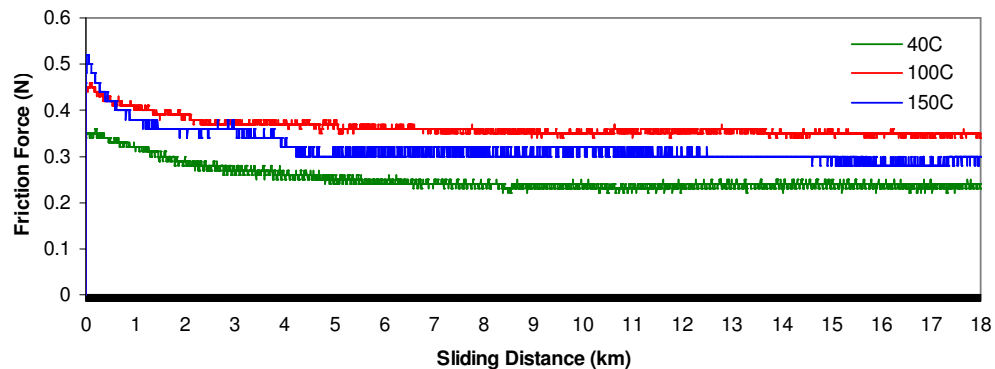


**Figure 72: Variation of friction force with sliding distance for various temperature regimes (V=0.25 m/sec, P=0.8 MPa, 20 hours)**

In figure 71 where the applied load is at 40 N the drop of the friction force starts at a distance slightly over the 1 km (after 1 hour of test). Then it declines until 6 km where it stabilises at a value of 0.6 N until the end of the test. This performance is observed only for the two higher

temperature regimes 100 °C and 150 °C. Interestingly, in the lower temperature regime at 40 °C, the friction force obtains a constant value from the very beginning of the test. The lubricant in this case has a dominant role, determining the contact nature. Obviously, this is the reason the wear rate is by far the lowest in this specific contact. In figure 72 where the applied load was adjusted to 20 N the drop of friction force started after 200 m of sliding (after 15 min) obtaining a constant value of 0.3 N at a distance of 3 km.

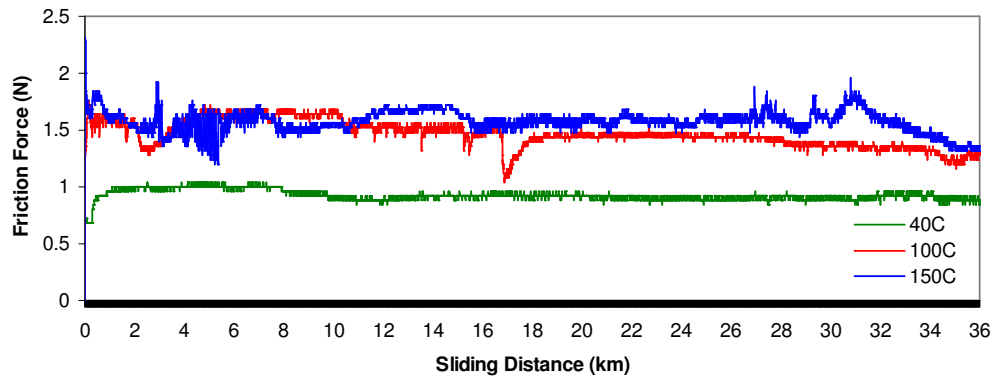


**Figure 73: Variation of friction force with sliding distance for various temperature regimes (V=0.5 m/sec, P=1.6 MPa, 20 hours)**

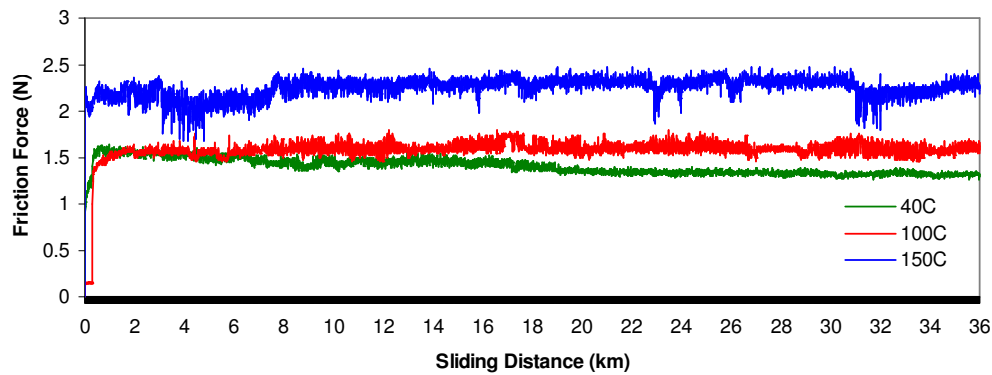


**Figure 74: Variation of friction force with sliding distance for various temperature regimes (V=0.5 m/sec, P=0.8 MPa, 20 hours)**

Figures 73 and 74 present the variation of frictional force as a function of sliding distance for 0.5 m/sec velocity. The running-in stage is restricted to a few hundreds metres. Thereafter, the steady-state stage is followed until the completion of the tests. Interestingly, as figure 74 reveals the friction force is higher than the corresponding force in figure 73 for all the temperature regimes. The friction force generated under 20 N applied load is slightly higher

than the one obtained at 40 N leading to higher friction coefficient values. The nature of contact is totally changed as the sliding speed increases. Subsequently, more severe wear and friction is monitored under low loads.

Even during the longest sliding distance of the 108 km (60 hours) the friction force remains at similar levels as in the 36 km test with a slight attenuation of its value throughout the test, as the slope inclinations reveal in figure 75, indicating a smooth, stabilised and relaxed contact over long periods of time. This excellent performance is promising for demanding long duration devices such as scrolls. The results are in very good agreement with the wear rates as will be analysed in the next session (5.5.2).

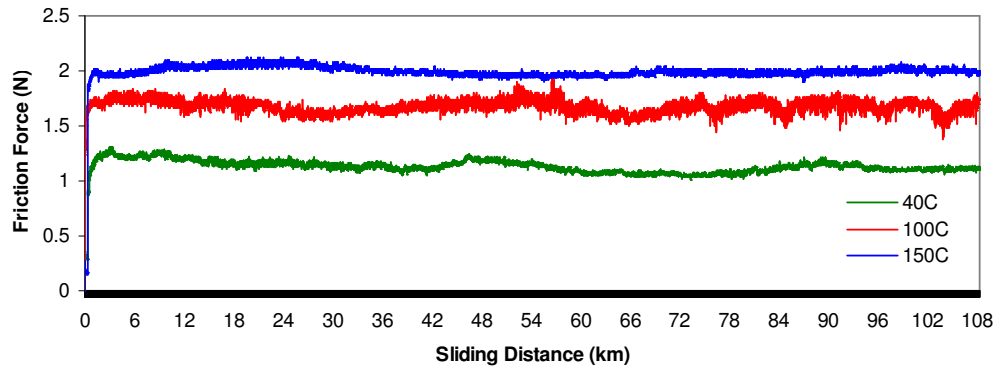


**Figure 75: Variation of friction force with sliding distance for various temperature regimes (V=0.5 m/sec, P=0.8 MPa, 60 hours)**

The low speed friction coefficient plots appear to follow each other very closely for all the temperature regimes as figures 76 and 77 depict. In particular, the 100 °C and 150 °C temperature regimes have identical friction coefficient behaviour for both the contact loads. The only appreciable difference is that the friction coefficient is rapidly increased to significantly higher values during the running-in stage for all the temperature regimes in figure 76. In contrast, the examination of the individual friction coefficient plots in figure 77 reveals that a full steady-state condition occurred quickly after the coverage of the very first metres by the rubbing samples. Thus, initially, both cases exhibit a rapid increment of the friction coefficient followed by declining trend before levelling off, after approximately 3 km. The 40 °C temperature regime obtains the lowest friction coefficient in both cases. By comparison, its friction coefficient is stabilised at of approximately half that of the other regimes. Overall the friction coefficient was slightly increased as the contact pressure was lowered.

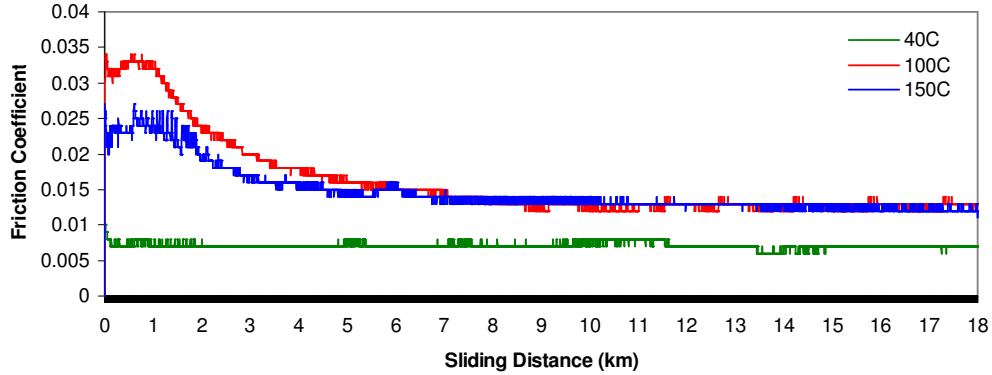


**Figure 76: Variation of friction coefficient with sliding distance for various temperature regimes (V=0.25 m/sec, P=1.6 MPa, 20 hours)**

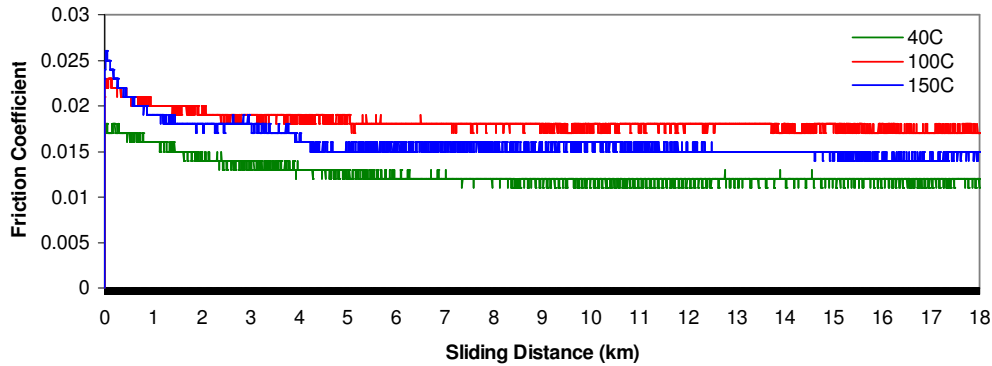


**Figure 77: Variation of friction coefficient with sliding distance for various temperature regimes (V=0.25 m/sec, P=0.8 MPa, 20 hours)**

Under higher velocity conditions the friction coefficients of the steel versus the elastomer counterface, in all the lubricated regimes, exhibit a steep increment until they reach their maximum values. Specifically, in figure 78 where the contact pressure adjusted at 1.6 MPa (40 N) the friction coefficient reached a maximum value of 0.045 for the 150 °C plot, followed closely by the 100 °C plot while the 40 °C plot obtains, once again, the lowest friction coefficient value of 0.025. In the case where the contact pressure was adjusted at 0.8 MPa (20 N), the friction coefficient is rapidly increased to significantly higher values for all the temperature regimes, as figure 79 depicts.

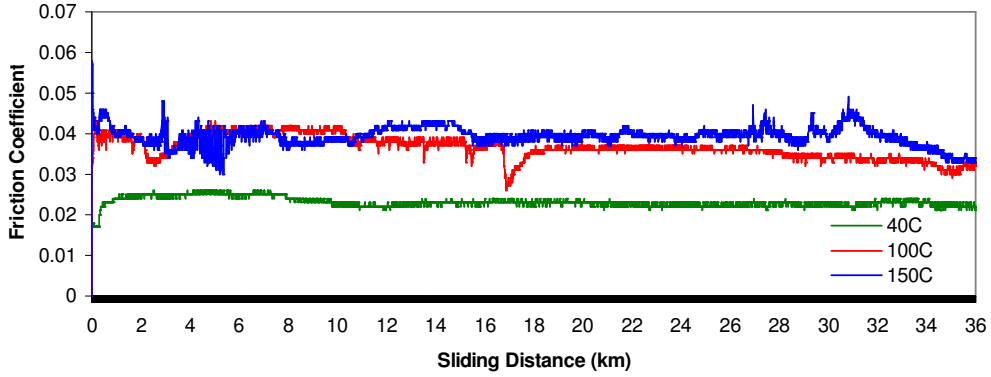


**Figure 78: Variation of friction coefficient with sliding distance for various temperature regimes (V=0.5 m/sec, P=1.6 MPa, 20 hours)**

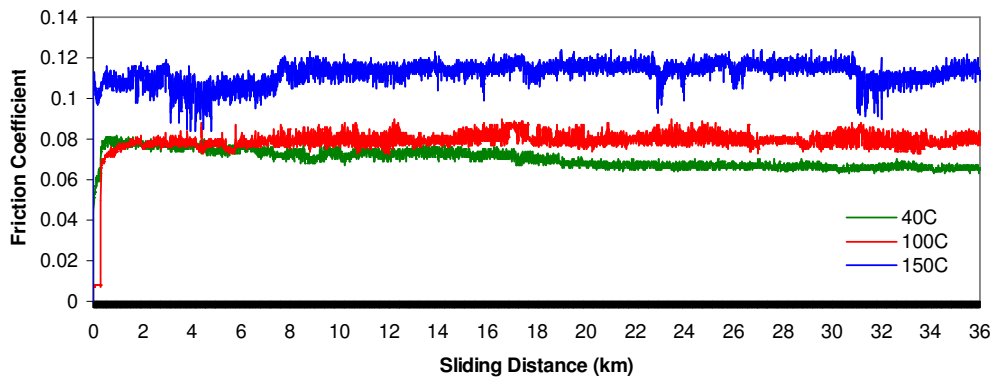


**Figure 79: Variation of friction coefficient with sliding distance for various temperature regimes (V=0.5 m/sec, P=0.8 MPa, 20 hours)**

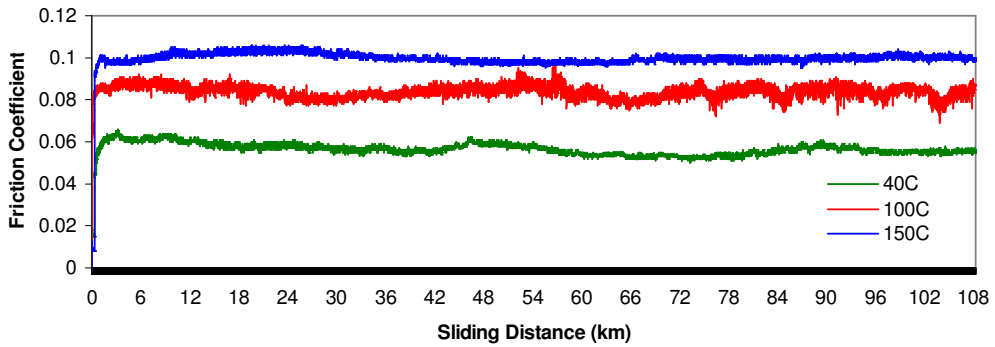


**Figure 80: Variation of friction coefficient with sliding distance for various temperature regimes (V=0.5 m/sec, P=0.8 MPa, 60 hours)**

Notably, the friction coefficient is increased more than twice in all the cases. The plots have an initial increment followed by constant friction coefficient throughout the duration of the tests. The 150 °C shows a substantial increment of the friction coefficient reaching an average value of 0.11. The 100 °C plot exhibits a friction coefficient in an average value of around 0.8. The 40°C plot significantly increases its value to an average coefficient of 0.7 approaching closely the 100 °C plot. Additionally, during the longest sliding distance of 108 km (figure 80) friction coefficient remains constant followed by a slow but steady fall, over the duration of the test. The smooth nature of the trace is reflected in the low wear rate for this combination.

### **5.5.2 Wear results analysis**

The wear analysis shows the performance of the testing samples against wear damage. It was initially planned to evaluate the wear resistance of both of the rubbing materials for a better comparison of their friction and wear characteristics. However, major inconsistencies in the surface measurements of the elastomer material, seriously affected the accuracy of the results.

The black surface of the elastomer was disturbing the light beam of the ZYGO interferometer hindering accurate measurements of the wear tracks. In addition using balance measurements were even worse since it was found that the final weight was greatly affected by the presence of lubricant and the attached steel particles. It was then decided to consider only the surface of the steel for evaluating the wear behaviour of the contact. Either way the main target was to evaluate the wear regime of the steel plate since it had suffered from excessive wear and this could significantly reduce the efficiency of the scroll by increasing the leakage points.

Initially the volume loss of the high carbon steel samples was estimated for all the 15 different cases (table 5). As can be seen by the trends in figures 81 and 82 the volume loss is always slightly higher in the case where the contact load was at 20 N. Specifically, in figure 81 a steep increment of the volume loss is observed where the maximum temperature regime of 150 °C is used. The volume loss was doubled compared to the case where the applied load was at 40 N. Thus a massive change in the surface morphology occurred while a substantial amount of volume was removed.

Looking at the trends in figure 82 it can be seen that this amount of volume is kept at similar levels even after the completion of the 108 km (60 hours) of sliding distance under the same operating conditions. The additional removed volume in the case of 150 °C is low, indicating a stabilised wear regime after the first 36 km (20 hours) of running. The same wear pattern is

observed for the 40 °C plot where the volume is at very similar levels, indicating that the wear damage started and finished even before the completion of the 20 hours test. Thereafter, the specific wear damage was maintained while the smooth contact combination of the lubricant and the possible transfer layer protected the steel sample from excessive wear. Finally the volume loss in the case of 100 °C is also slightly increased after the completion of the 108 km running showing evidence of a stabilised wear regime.

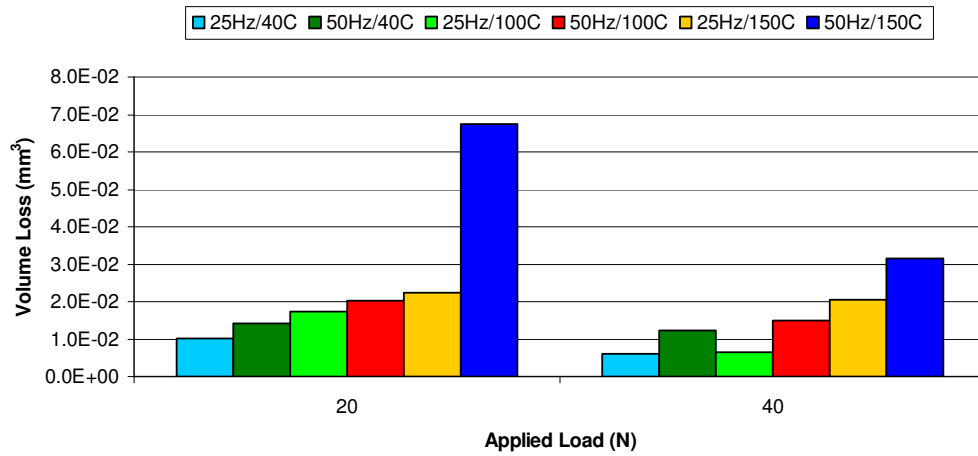


**Figure 81: Evaluation of the removed volume for various temperature regimes after 20 hours of running time.**

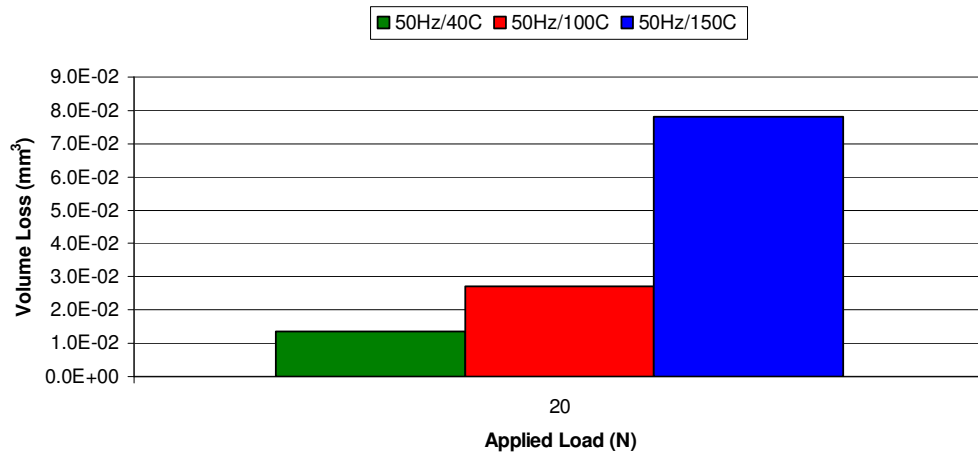


**Figure 82: Evaluation of the removed volume for various temperature regimes after 60 hours of running time.**

The series of figures from 83 to 86, collate the specific wear and friction characteristics of the high carbon steel against the reinforced elastomer contact under boundary lubrication conditions for three distinctive temperature regimes. The variation of wear with applied load is determined by keeping the load and the sliding velocity as constants. The specific wear rate of the steel samples is generally found to increase with the attenuation of the contact load and the augmentation of the sliding velocity. The specific wear rate follows the friction coefficient graphs, described above. Eventually, the wear rate on the steel plate proportionally increases with the increment of the friction coefficient while it decreases respectively with the decline of the friction coefficient.

The friction coefficient is observed high for lower loads and reduced for increase of applied loads. At lower loads, as already been mentioned (paragraph 5.3), the transfer film is more stable resisting rapid deterioration while the temperature rise is also low. Hence, friction coefficient is increased. At higher loads the transfer films are formed at a faster rate, while vigorous thermal effects are instantly generated. Consequently, excessive rising of the contact temperature occurs and the interactive sliding contact is softened. Thus, friction coefficient is decreased.

Additionally, the friction coefficient is also found to increase with the sliding velocity as figures 71 to 80 revealed previously. At higher sliding velocities the generation of the thermal effects is fast and lubricant is displaced, leading to a rapid degradation of the elastomer surface. Consequently, the contact becomes rougher and the friction coefficient is increased. On the other hand in lower sliding speeds, as the friction graphs earlier illustrated in figures 76 and 77, the maximum coefficient value is observed during the running-in stage where formation of transfer film on the interface is being developed. Subsequently, transfer film overlays across the contact and in combination with the existent lubricant layer, they rapidly decrease the friction coefficient. The low sliding speed also facilitates this behaviour.

Specifically in figure 83 the variation of the average values of the friction coefficient versus the applied load of 20 and 40 N after sliding distance of 18 km (corresponding to 20 hours time) is depicted. It can be seen that friction coefficient slightly decreases with the applied load. However, in the case of 150 °C the friction coefficient is of a similar value for both contact loads. Correspondingly, the wear rate follows the friction coefficient pattern as figure 84 shows. Only in the case of the 20 N applied load at 150 °C, where the friction coefficient was not the highest, does the wear rate obtain the largest value followed closely by the 100 °C wear plot.

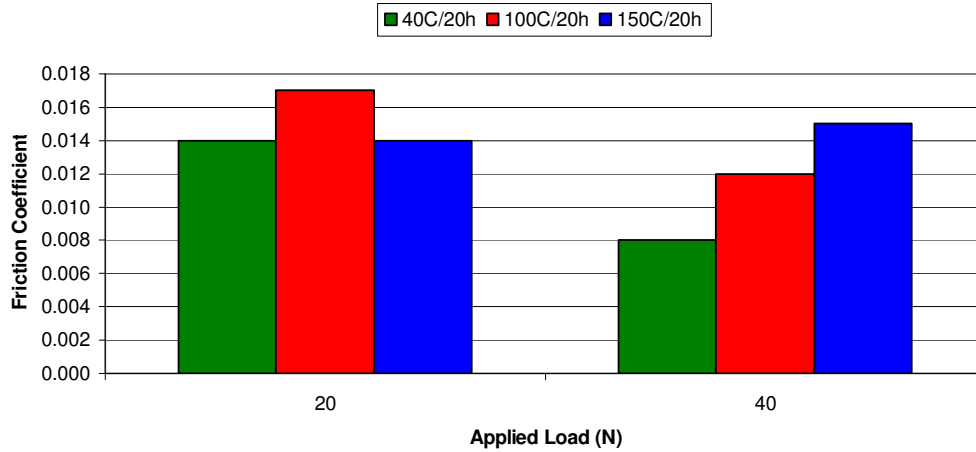


**Figure 83: The friction coefficient versus the applied load for different temperature regimes at a constant reciprocating velocity of 25 Hz (0.25 m/sec).**

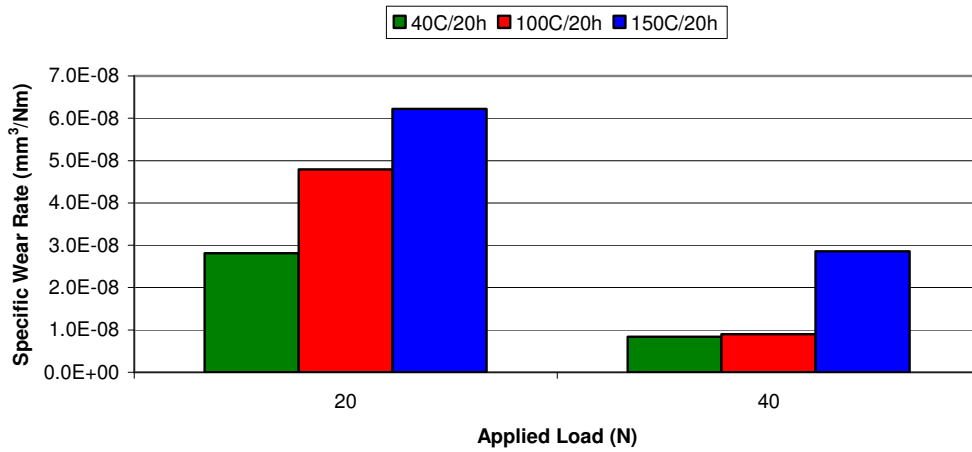


**Figure 84: The specific wear rate versus the applied load for different temperature regimes at a constant reciprocating velocity of 25 Hz (0.25 m/sec).**

Figures 85 and 86 depict the influence of the sliding velocity in the average values of the friction coefficient and the corresponding specific wear rates. The applied loads were kept the same, at 20 and 40 N respectively, while the sliding speed is increased to 50 Hz. Consequently, the wear sliding distance was increased to 36 km for the 20 hours case and to 108 km for the 60 hours case. The average values of friction coefficient remained similar for both cases as the friction graphs previously revealed. In the 20 hours case with 40N applied load the friction coefficient was by far the lowest for all the tests.

According to the friction coefficient graph a correlation with the specific wear rates was achieved. It is clearly depicted in figure 86 that the wear rate in all the cases corresponds to

the increment of the friction coefficient. Especially in the case of the 20N/150<sup>0</sup>C/20h there is a steep increment of the wear rate reaching a peak value. However, this aggressive wear rate is further relaxed throughout the test process, dropping its value an average of three times, as the maximum sliding distance stage (20N/150<sup>0</sup>C/60h) reveals. The rest of the temperature regimes maintain quite low levels of wear rates having similar values.

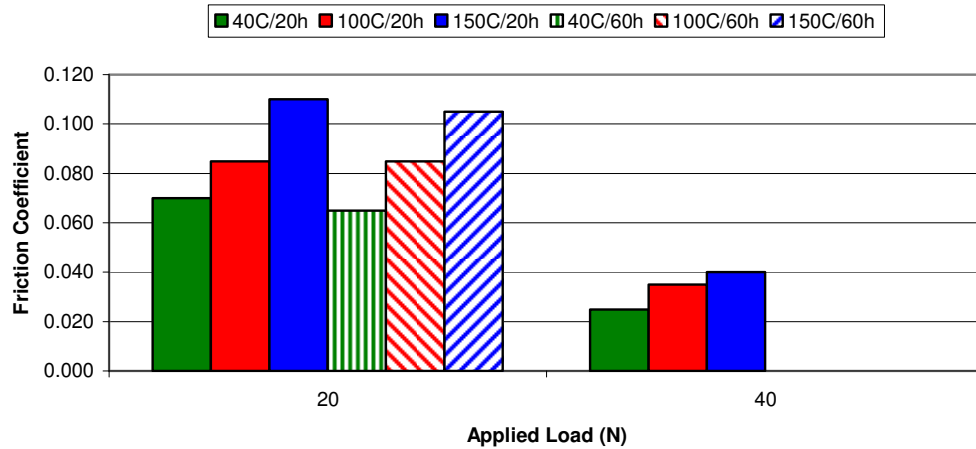


**Figure 85:** The friction coefficient versus the applied load for different temperature regimes at a constant reciprocating velocity of 50 Hz (0.25 m/sec).

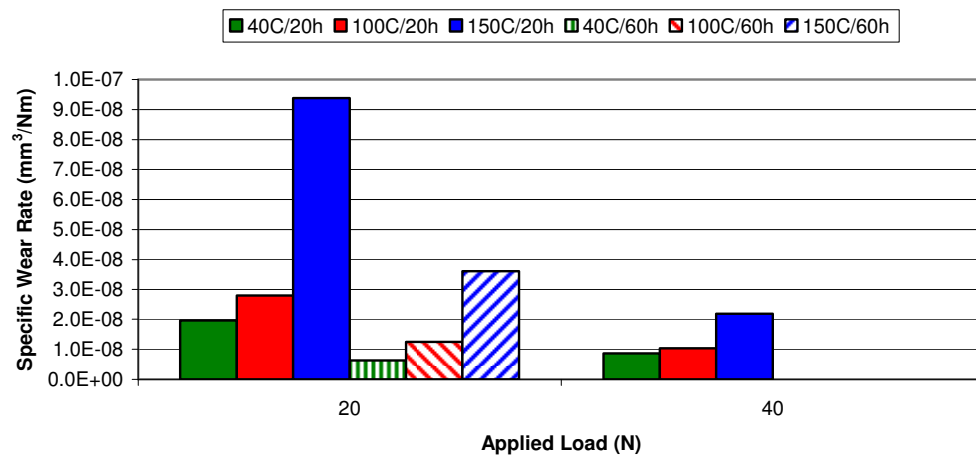


**Figure 86:** The specific wear rate versus the applied load for different temperature regimes at a constant reciprocating velocity of 25 Hz (0.25 m/sec).

From the above it is clear that the friction coefficient and the wear rate are strongly dependant on the sliding velocity, the contact load as well as the time duration. For a better understanding of the influence these parameters have on the specific contact the PV product

was used. Figures 87 and 88 present the friction coefficient and the time-related depth wear of the rubbing materials as a function of the PV (Pressure  $\times$  Velocity) factor. The material's tribological performance can be effectively described by the maximum value of the PV product which the material can withstand.

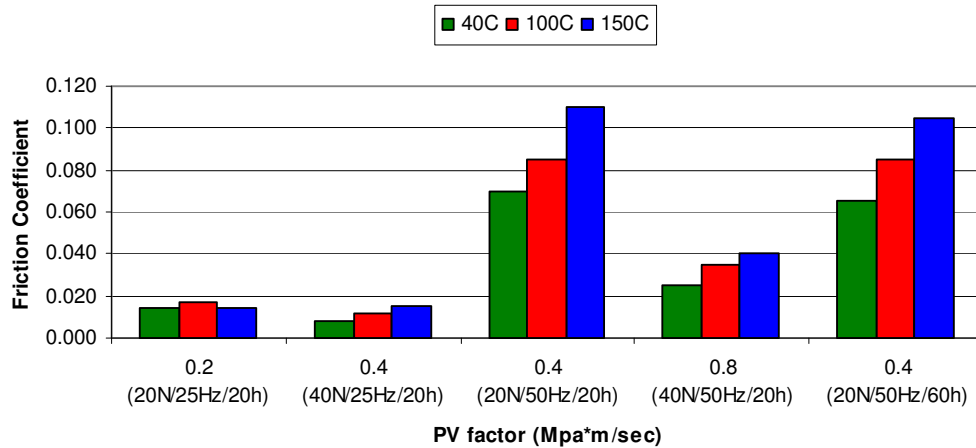


**Figure 87: Variation of the friction coefficient as a function of the PV factor for various temperature and time sliding regimes.**

In figure 87 the PV contact is depicted against the friction coefficient for the three different temperature regimes after 20 and 60 hours of running time respectively. As expected, the friction coefficient increases with the augmentation of the sliding velocity and decreases as the apparent contact pressure is lowered. The effect of the temperature conditions is also notable leading the rubbing materials to higher friction coefficients. Specifically, the friction coefficient gradually increases with the increment of the lubricant's bulk temperature.

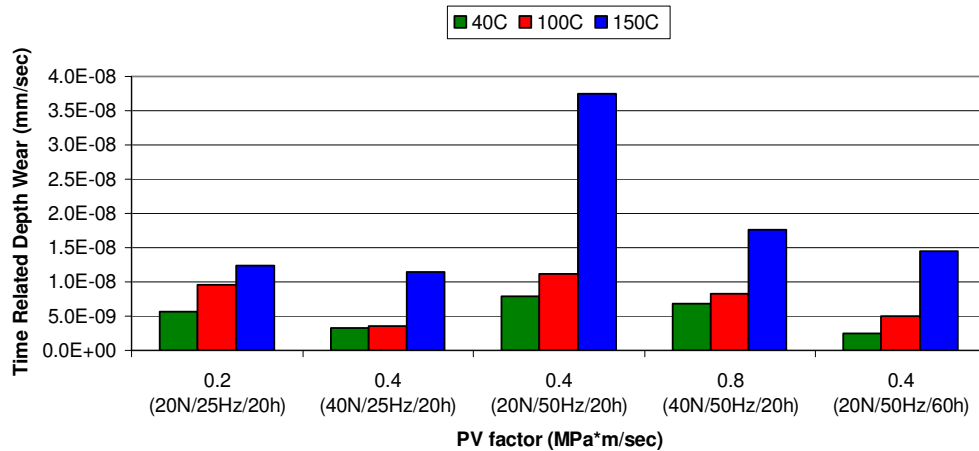


**Figure 88: Variation of the time related depth wear as a function of the PV factor for various temperature and time sliding regimes.**

In figure 88 the time related depth wear as a function of the PV contact is illustrated. It can be observed that the influence of the sliding speed on the wear rate is much higher than the applied load. Interestingly, in the lower temperature conditions (40 °C and 100 °C) the wear rate is similar for both PV cases. However, when the temperature reached the highest value of 150 °C the wear rate of the steel/elastomer contact was steeply increased to a magnitude of about 3 times more than that of the other lubricated conditions. In general, the reduction of the lubricant viscosity leads to a significant rise of the friction coefficient and wear rate values.

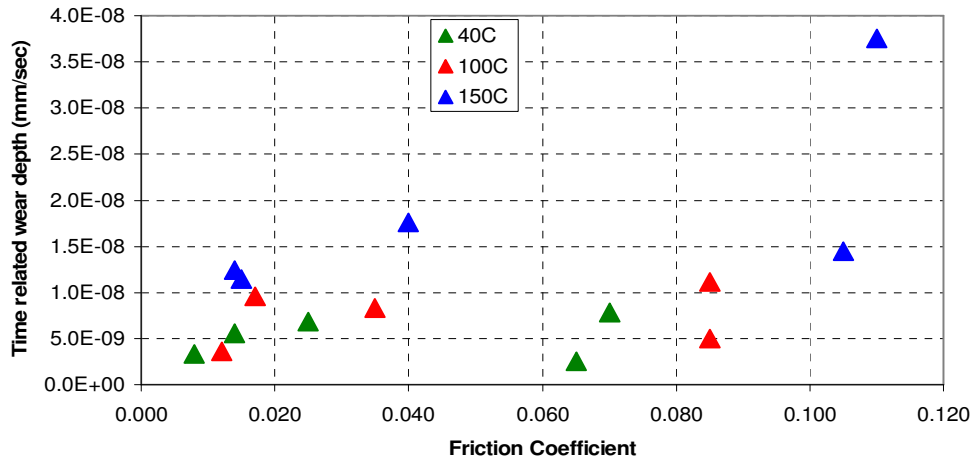


**Figure 89: Change in specific wear rate with friction coefficient**

The relation between the time-related wear depth and the friction coefficient for all the studied cases is presented in figure 89. The wear depth increases exponentially with the increment of the friction coefficient. However, noticeable wear occurred for friction coefficient 0.04 and beyond 0.1 for the temperature of 150 °C. This result indicates that even for lower friction coefficient rates, if sliding speed is the factor, the wear rate can be significantly increased. Interestingly, with the increment of the environmental temperature conditions the wear damage significantly increases.

The wear resistance for all the case studies was estimated. The assumption derived from the observation of the 108 km (60 hours) graphs in figure 80, indicating that the wear resistance of the specific steel/elastomer contact gradually increases over a long period of time, is successfully interpreted by the plots in figure 90. Interestingly, the wear resistance rapidly increases, as the sliding contact progresses throughout the time. In particular, for the 150 °C case, which is the critical operating temperature of the scroll, the wear resistance is significantly improved. The wear resistance after 60 hours of running is much higher

compared to the corresponding case (0.4-(20N/50Hz/20h)) of the 20 hours test. Furthermore this behaviour suggests a gradual change in the wear regime from severe to mild. Thus, this performance of the tip seal versus the steel plate can be proved beneficial for long operating devices with demanding environmental conditions like the scroll systems.

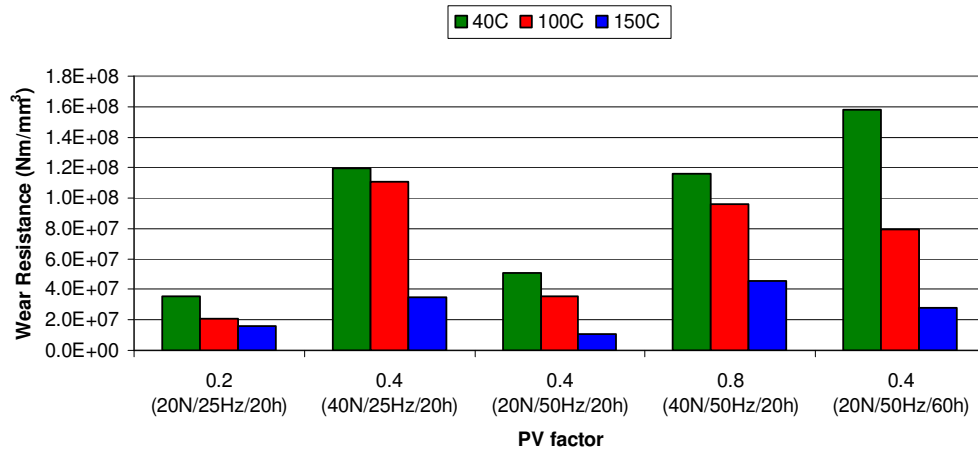


**Figure 90: The wear resistance of the steel plate as a function of the PV factor for different temperature and time sliding regimes.**

Since the friction coefficient remains steady for the duration of the 60 hours experiment and the contact is smoothened, it can be assumed that the time-related depth wear stabilises at the value of around 1.5E-08 mm/sec even for longer test periods. This result correlates well with the depth of the wear marks found on the 300 hours scroll. Thus, assuming that the tip seal can sustain its mechanical/chemical properties and its robust structure without completely deteriorating for the duration of the 30,000 hours, the average depth of the time related depth wear can reveal approximately the surface loss after the end of the process. Thus, this hypothesis can lead to a surface reduction of the steel of up to 1.5 mm under the 150 °C temperature regime, while in the low pressure region where the temperature is 100 °C it can be reduced by up to 500 microns. Thus, the proportional reduction for the high pressure region can be up to 3 times higher in comparison to the low pressure region.

The estimated wear damage over that huge period of running time, 60 hours, has shown that it is possible to achieve an overall surface reduction of the steel plate within the circular grooves of about 1.5 mm. The intimate contact of the tip seal fibres with the steel plate can theoretically increase the depth of the circular grooves to that catastrophic for the scroll system depth. However, this reduction of 1.5 mm cannot be applied under a real case scenario since the pressure contact between the tip seal and the steel plate is not equally distributed and

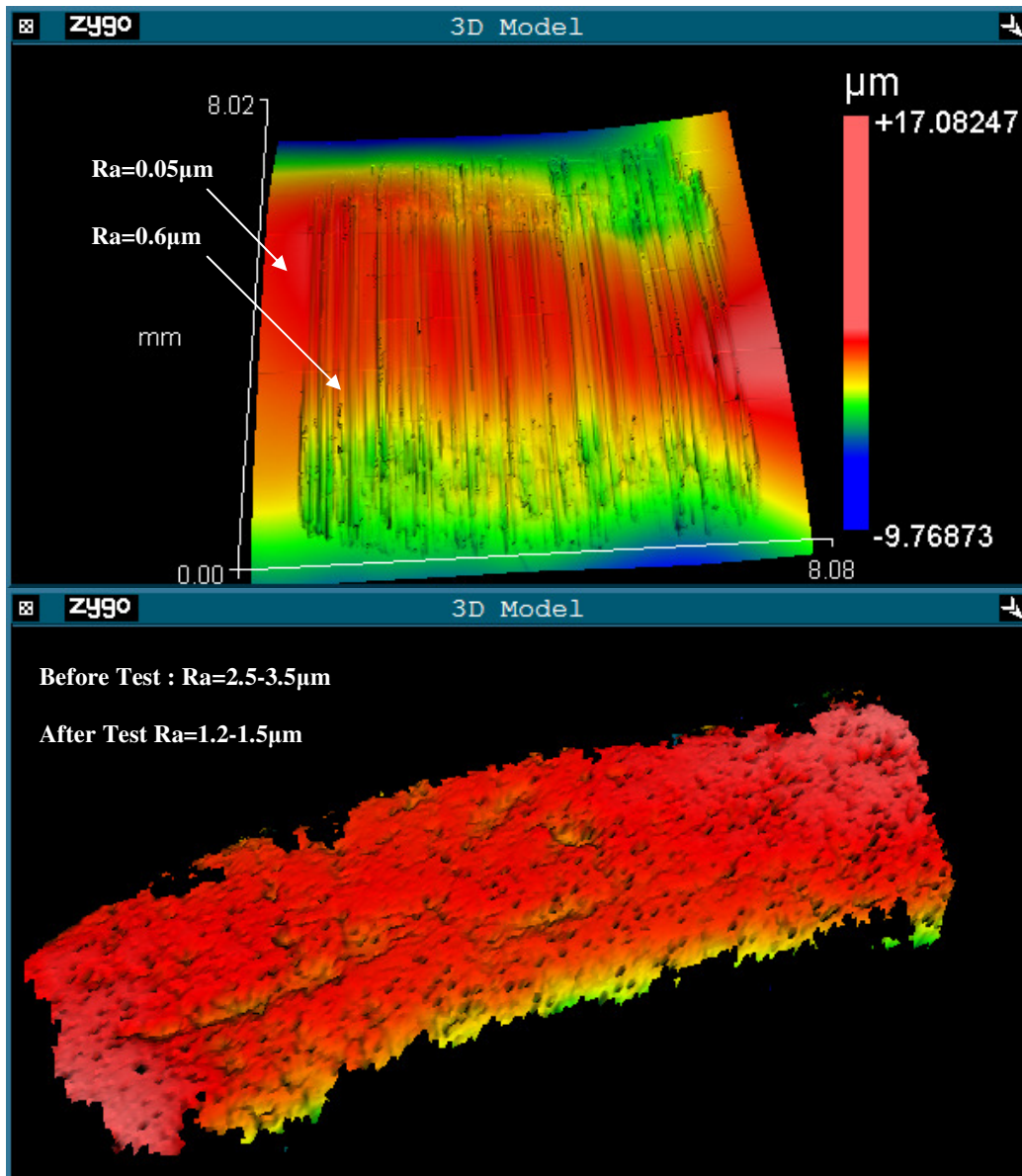
the wear damage is random. This was revealed by the nature of the circular lines in Chapter 3. The circular wear lines were found at random points with different heights, widths, patterns and directions. Also, the wear marks found on the 1000 hours scroll were of a similar average depth to the ones in the 300 hours scroll, indicating a relaxation of the overall sliding wear regime. Thus, a coherent interpretation of wear damage to the scroll steel plate after 30,000 hours of running period is not possible.

The specific wear rate of the fluoroelastomer tip seal against the steel plate is highly affected by the change of the sliding speed but less by the change in the applied load. These results are in a very good agreement with the results obtained by J.P Davim et al, Z.P Lu et al and Kukureka et al [87,181-182]. Particularly, it was shown that the specific wear rate and the friction coefficient of the rubbing materials steeply increase with the increment in the sliding speed. By contrast, the specific wear rate of the material is also influenced to a lower extent by the alterations of the applied pressure. The reduction of the apparent contact stress has expressed itself as an increase of the specific wear rate and the friction coefficient. The outcomes of the study are in a good agreement with the results obtained by Unal et al [86].

### **5.5.3 Roughness Analysis**

Figure 91 illustrates the surface profile of a typical worn out steel sample. The roughness difference before and after the test is notable. The initial surface roughness of the steel counterpart was about 0.05  $\mu\text{m}$ . After the completion of the tests, roughness increased to an average of 0.6  $\mu\text{m}$ . The correlation of the Ra roughness parameter versus the friction coefficient and the specific wear rates is presented in figures 92 and 93.

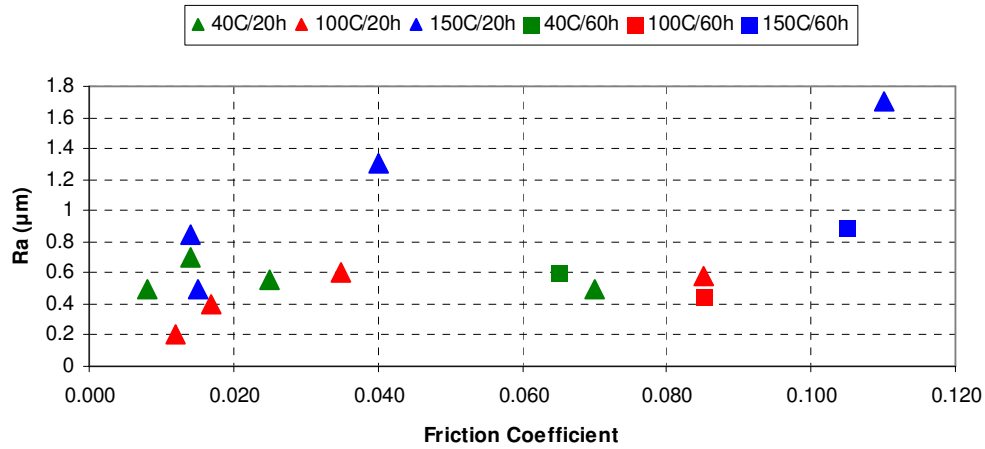
The morphology observations of the tested surfaces with the use of the ZYGO interferometer microscope reveal the mild character of the wear damage. The fine shaped grooves are equally distributed in a parallel direction across the steel surface having similar depths. The elastomer surface was initially heat-treated due to thermal effects then was gradually melted while the sliding steel counterpart was simultaneously “ironing” the surface, improving the flatness of the elastomer and reducing its roughness of about 1 to 2  $\mu\text{m}$ . Additionally, during the friction process the fine parallel position of the tested blocks and the high friction force generation, cause a smoothening effect on the rubbing parts by removing asperities from the surface. This in turn generates uniform distribution of the real contact pressure across the surface. Consequently, further relaxation of the real contact area is achieved and substantial attenuation of the friction coefficient occurs. Eventually, a good correlation between the roughness and the friction/wear parameters can be achieved.



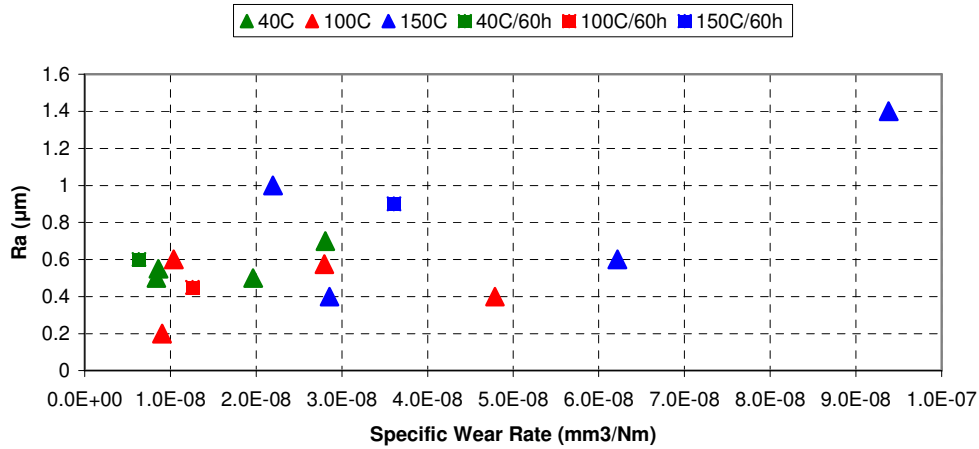
**Figure 91: Surface profile of the worn regions across the steel and the elastomer surfaces. The experimental conditions were 0.5m/sec, 0.8MPa, 100C, 20hours.**

Figure 92 summarizes the variations of the friction coefficient of the steel/elastomer contact with the Ra roughness parameter for the different temperature regimes. Interestingly it can be seen that in the areas where the Ra is higher the friction force obtains a maximum value, (see friction force graphs figure 71-75). For example, in the cases of the ( $T=150^{\circ}\text{C}$ ,  $V=0.5\text{ m/sec}$ ,  $P=1.6/0.8\text{ MPa}$ ,  $t=20\text{ hours}$ ) where the friction force is highest, the surface texture becomes very rough obtaining the highest Ra value. In the same case under the 60 hours running period, although the friction force is similar, around 2 N, the Ra is much lower. This roughness reduction indicates the smoothening effect on the rubbing parts by removing

asperities from the surface while the contact becomes further relaxed over that prolonged period of time.



**Figure 92: Variation of the Ra roughness parameter as a function of the friction coefficient for all the 15 cases.**



**Figure 93: Variation of the Ra roughness parameter as a function of the specific wear rate for all the 15 cases.**

In figure 93 the specific wear rate is presented against the Ra parameter. It can be generally said that the specific wear rate is proportional to the augmentation of the surface roughness. Notably the specific wear rate significantly increases as the Ra roughness parameter goes beyond the 0.6  $\mu\text{m}$ . Once again, an increment of the Ra parameter is observed in the highest temperature regime. The lubrication film thickness is further reduced, generating severe boundary contact and rougher steel surfaces. The elastomer surface becomes smoother.

## 5.6 Lubrication analysis

Oil analysis was developed as a condition-based maintenance technique to offer solutions in the operation of demanding systems like scroll expanders. In this study oil analysis is mainly focused on the wear debris and their contaminants, found in an after-test oil lubricant. Three different oil samples removed from the sliding micro-friction TE 57 system and were thoroughly investigated. The samples were distinguished according to their temperature operating regime at 40 °C, 100 °C and 150 °C respectively. The specific oil analysis involves a particle profile and identification of solid contamination in order to assist in understanding the degradation and the failure mechanisms of the steel/elastomer contact.

More specifically, the ISO Code with the patch picture will both quantify the particles present and show a snap-shot of the debris. The International Organization for Standardization created the cleanliness code 4406:1999 which is assigned to quantify the number of particles per unit volume. The ISO code includes all particles of the specified size or greater than 4, 6 and 14 microns and it is expressed in 3 distinctive numbers: a/b/c. Each number represents a contaminant level code for the correlating particle size as the code chart reveals (Appendix H). Moreover, an oil that runs at a higher temperature is likely to be more oxidised which should be reflected in the total acid number (TAN) and possibly viscosity. Elemental analysis will show things like wear metal quantities and any contamination. PQ Index will show if there is an increase in the quantity of magnetic ferrous debris (including larger particles).

Approximately 10ml of each lubricant solution were used for the analysis. Initially, part of the lubricant was filtered, leaving any solid contamination on a filter paper. With this process the amount of particles (ISO code) was estimated. A visual inspection was then carried out on each individual sample using a low-powered optical microscope to identify the debris profile. Then the tested lubricant was dissolved prior to being fed into the ICP-OES system (paragraph 4.3.6). With the ICP-OES method the rest of the oil parameters were identified.

Table 11 summarizes the oil parameters before and after the sliding tests. For comparison purposes the properties of the clean oil were also measured. At first glance it can be seen that in all the oil samples ferrous and silicon debris were detected while the water content and the acidity levels had risen. In particular, in the case of the 40C the oil presents some abnormal silicon levels with moderate iron content. The ISO code 21/20/14 reveals that there are 10,000 to 20,000 particles per million (ppm) greater than 4 µm, 5,000 to 10,000 ppm greater than 6 µm and only 80 to 160 ppm of greater than 14 µm in size. The larger size particles are in higher than normal levels and are mainly silicon particles. This indicates the breakage of the

fibres with a length of maximum 100  $\mu\text{m}$ . From the steel surface with a smooth roughness profile it is more difficult to generate this size of particle. Finally the viscosity seems unaffected while the overall oil conditions are considered as marginal. Apparently no critical wear can be produced.

Oil Analysis Results					
Lubricant Test Samples		Clean Oil	40 <sup>0</sup> C	100 <sup>0</sup> C	150 <sup>0</sup> C
Elements (ppm)	Iron	0	32	47	75
	Chromium	0	0	2	2
	Aluminium	0	0	0	0
	Copper	0	0	1	8
	Lead	0	0	0	1
	Nickel	0	0	1	1
	Tin	7	3	9	7
	Manganese	0	0	1	1
	Titanium	0	1	0	0
	Silver	0	0	0	0
	Molybdenum	1	2	0	0
	Zinc	0	4	9	16
	Phosphorus	6	0	34	31
	Calcium	0	2	6	7
	Barium	0	0	1	0
	Magnesium	0	0	2	0
	Silicon	1	72	186	102
	Sodium	4	6	7	9
Physical Tests	ISO Code	15/14/12	21/20/14	20/19/14	22/21/17
	PQ	6	6	8	6
	Water (ppm)	296	856	863	863
TBN/TAN	TBN				
	TAN	0.04	3.61	3.91	5.34
Viscosities	Visc @ 40°C	157	158	158	261
Condition		Satisfactory	Marginal	Marginal	Marginal

**Table 11: Oil analysis of the lubricated samples, used for sliding wear tests.**

The properties of the 100<sup>0</sup>C oil sample are found to be at similar levels to the 40<sup>0</sup>C sample. The determinant is that the quantity of ferrous and silicon particles is steeply increased. This indicates a more severe contact between the steel and the elastomer under these experimental conditions. The lubricant loses its efficiency while the elastomer tip seal can deteriorate faster due to substantially higher number of silicon particles. The ISO code 20/19/14 reveals that for all the particle sizes, the quantity levels are identical to the 40<sup>0</sup>C oil sample. The conditions once again can be characterized as marginal while the wear damage can be successfully prevented.

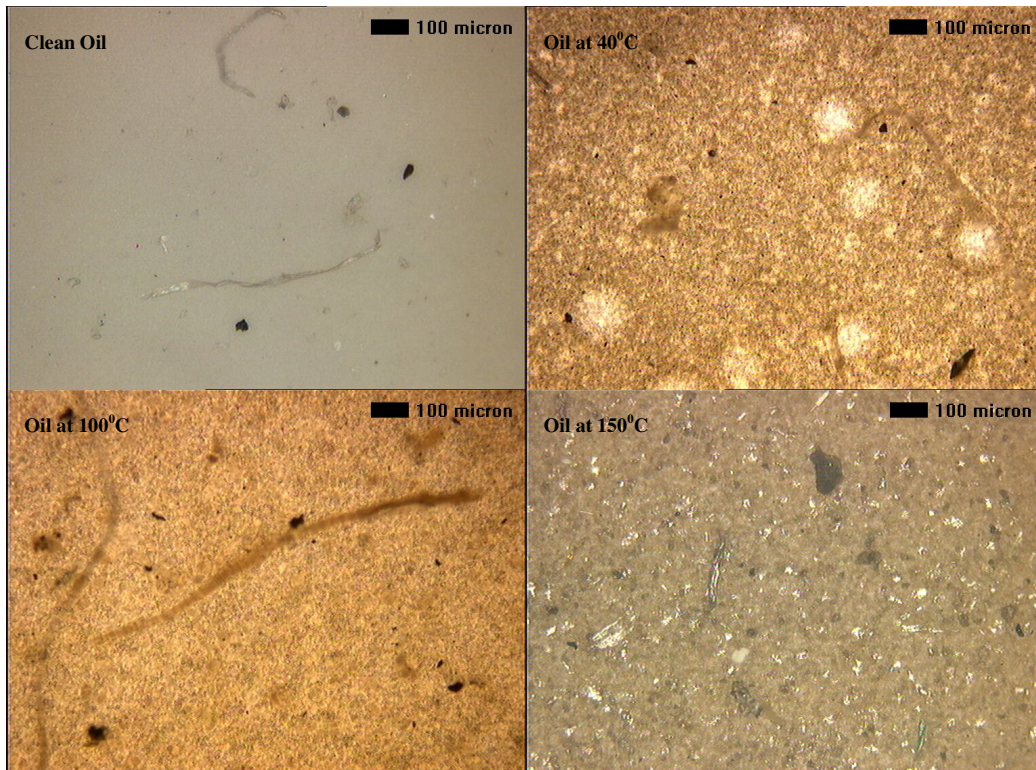


**Figure 94: Optical examination of the after test lubricant samples at 40 °C, 100 °C and 150 °C**

The analysis of the 150 °C oil sample, showed an extremely high number of particles in the filtered contamination, the majority of which were ferrous and silicon debris. The filtered oil sample had also revealed a moderate proportion of copper particles and various other metallic fragments, some of which appeared to be a wear product. Specifically, the ISO code 22/21/17 reveals that for particles with a size greater than 3 and 6  $\mu\text{m}$ , there were no significant differences in the amount of the detected particles compared to the other two tested oil samples. However for the larger size particles, greater than 14  $\mu\text{m}$ , the amount of debris was steeply increased reaching a significantly high number of particles between 640 and 1300.

In addition, high levels of the acidity (TAN) and viscosity parameters were observed. The acidity level compared to clean oil is extremely high which indicates an oxidation process. Specifically as the oil's TAN increases with the passage of time and its exposure to high running temperatures, the oil becomes oxidised (high temperatures cause oil molecules to react with the oxygen within the air). Oxidation severely affects the oil's ability to protect internal components and can also affect the viscosity. The viscosity is substantially higher than the corresponding clean oil, indicating a possible oxidation process due to high temperatures.

The condition of the oil can be once again determined as a marginal. However in this case a replacement of that aged oil has to be considered. This is a very interesting outcome since the demanding areas within the scroll expander operate in similar high temperature regimes or even higher. Thus, a regular inspection of the oil condition in those areas is needed, in order to maintain the proper operation of the whole unit and to avoid oil breakdown.

In figure 94 the analysis of the deposited particles on a filter patch are depicted for each case separately. The wear results (paragraph 5.7) are in a good agreement with the wear size debris trapped in the filter patches. In all of the images some black particles appeared which are oxide particles. In the case of the 40 °C and 100 °C sample, a silt layer of translucent particles with submicron size is depicted. The contrast with the golden colour of the oil reveals the amount of these particles (white areas). In both cases it was more unlikely for larger particles to be detected. By contrast, in the case of 150 °C sample a large amount of metallic parts are deposited on the filter patch. The majority of the metallic debris is in the low few micron size. However, there are a few larger particles with sizes up to 100 µm as the micrograph of the 150 °C lubricant sample reveals.

All samples contained a large amount of particles of which a significant number were ferrous and silicon. Apparently the ferrous particles derived from the wear damage on the steel plate surface and the silicon particles derived from the deterioration of the elastomer surface and the hard fibre breakage. The presence of ferrous and silicon debris within the lubricant solutions after the completion of the tests, justifies that the wear damage in both surfaces derived from severe two- and three-body abrasion wear.

## **5.7 Wear Mechanisms**

The wear mechanisms on the high carbon steel plate and the reinforced high performance fluoroelastomer tip seal were successfully interpreted. In figure 95 (A-B) the steel samples after the completion of the tests are presented. The wear track is clearly visible, even with the naked eye, and it widens as the applied load increases from 20 to 40 N. A representative image of the wear track across the steel plate surface corresponding to all the tested steel samples is illustrated in figure 95 (B). It can be seen that wear lines are equally distributed across the steel surface while a significant part of the surface has been removed. The wear depth of the steel samples can reach up to few micrometers overall as the time related wear graph revealed in figure 88.

The challenging part was that of the elastomer material because of its nature and its black colour which was partially disturbing the ZYGO interferometer microscope. As can be observed from figure 95 (C-E), a detailed overview image showing the wear damage and distinguishing the wear mechanisms across the elastomer surface was impossible to be taken. Thus, the analysis of the wear mechanisms of the reinforced elastomer tip seal focused on a nano-scale level using advanced techniques of the microscope devices. The wear mechanisms of the bulk elastomer material and particularly of its embedded hard fibres were thoroughly investigated and effectively determined.

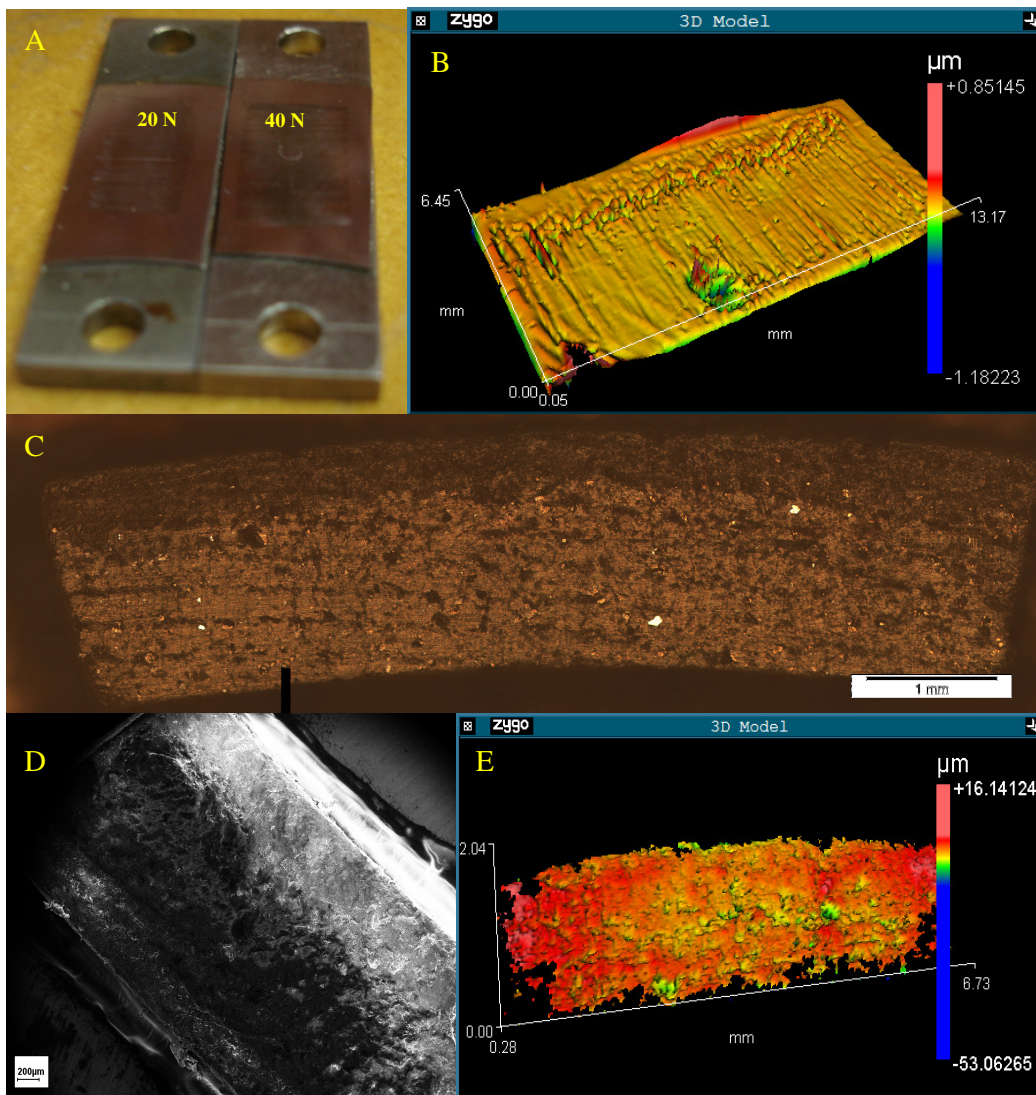


**Figure 95: An overview of the wear pattern formed due to sliding wear on the surface of the steel samples: A) Photo image of the steel samples for different applied loads, at 20N and 40N respectively. B) ZYGO interferometer image of the steel plate at 100°C-20N-50Hz-20hours. Overview micrographs, of the reinforced elastomer tip seal sample after the completion of the test at 100°C-20N-50Hz-20hours, taken with C) Optical microscope D) SEM E) ZYGO interferometer**

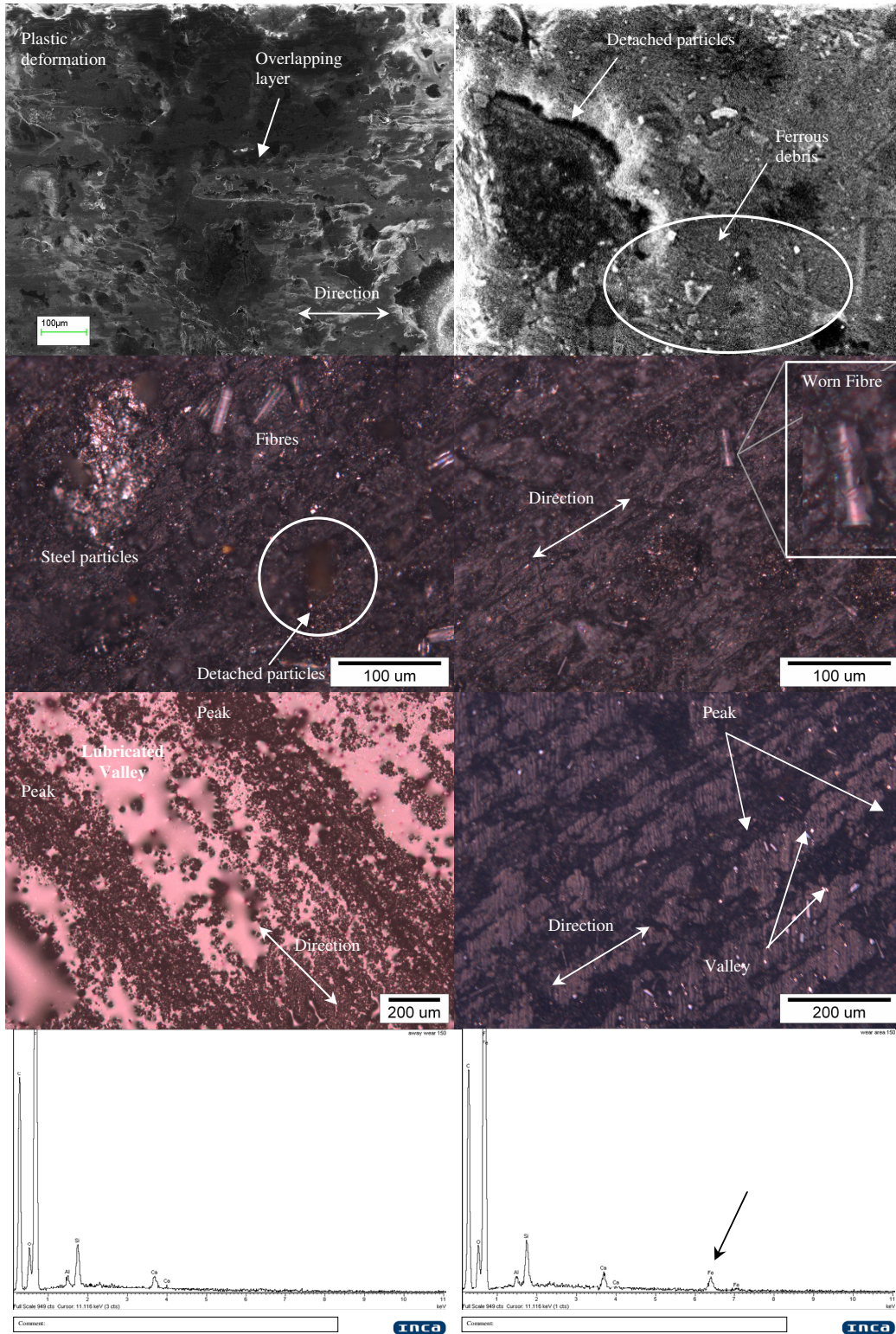


**Figure 96: Fluoroelastomer sample after the end of 20 hours sliding test (40N/0.5msec<sup>-1</sup>/100<sup>0</sup>C). The plastic deformation of the surface, overlapping layers due to thermal/melting effects, the deterioration of the substrate, the worn fibres disorientation, the detached particles, the embedded steel particles, the formation of peaks and lubricated valleys, is shown.**

In figure 96 distinctive damage patterns developed across the fluoroelastomer tip seal are shown after 20 hours of test. A typical plastic deformation of the bulk material is shown. Overlapping layers are formed due to the thermal and cooling effects. The thermal effects melt the bulk material and instantly allow the formation of overlapped elastomer layers after the viscoelastic material cools down. A characteristic interfacial debonding of the fibres within the matrix of the elastomer is observed. The very hard fibres found on the surface of the elastomer during the friction process interact with the asperities of the steel plate producing abrasion on the steel surface. Deep grooves parallel to the sliding direction can be observed on the magnified image of a typical worn fibre.

In addition, steel particles are embedded in the surface of the elastomer after their removal from the steel surface. Steel particles were successfully detected with the use of the surface chemical analysis method provided by the SEM microscope. No evidence of metal particles was observed in a default area prior to test. However, in the same area after the test a peak by ferrous element is monitored. Thus it can be said with certainty that steel particles embedded on the elastomer surface after their removal from the steel surface generating a third-body contact between the rubbing surfaces. Hence, two different types of third-body contact are generated which simultaneously damage the surfaces during the sliding contact. The first one is derived from the broken fibre particles of the elastomer and the second one from the steel particles of the steel samples.

Further analysis of the micrographs shows the detached particles from the polymer surface. The detached particles are easily trapped in the contact and form a third-body which separates the rubbing materials and relaxes the friction. Finally, both of the micrographs show undulations “beach marks” across the surface of the samples. The polymer is softened due to thermal effects. The softened material can now easily displace to the sides creating peaks and valleys as the asperity contact mechanism progresses. The peaks are constituted by the original material, hence not much damage is observed. The valleys are mainly formed due to the micro-ploughing mechanism which leads to fatigue damage at a later stage.

On a lubricated substrate after the completion of the test, it has been observed that some of the long linear valleys turned into fluid pools. Consequently, the lubricant seals off the valleys creating a smoother surface during the sliding contact. Additionally, in the presence of lubricant, the accumulation of wear debris onto the subsurface is prevented. This can be proved to be beneficial for the elastomer surface preventing excessive sliding wear damage by three-body abrasion.

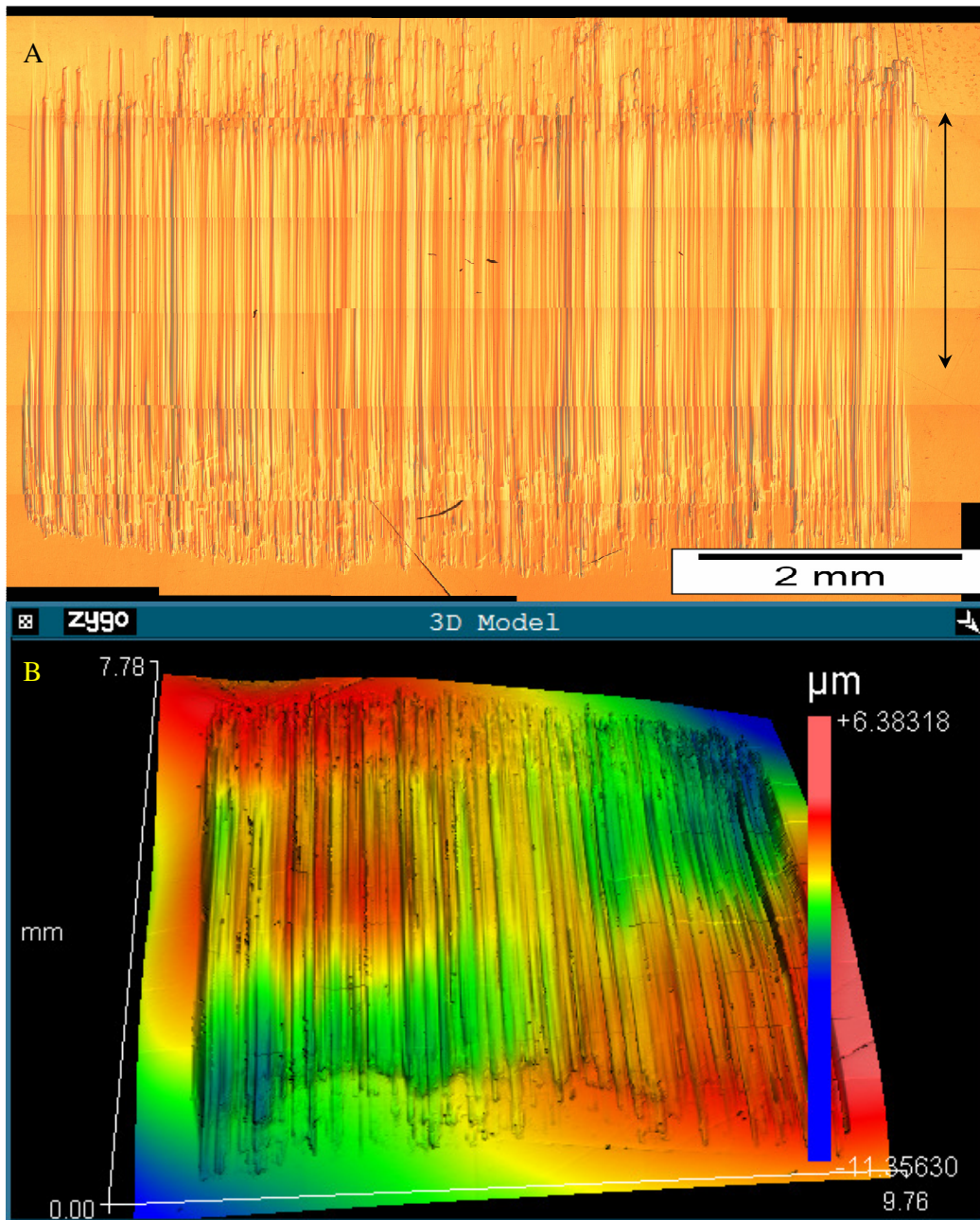


**Figure 97: A typical pattern of the wear damage formed on the surface of the steel plate sample after the completion of the experimental process with the following conditions: 100<sup>0</sup>C-50Hz-60hours-20N. A) Optical microscope B) ZYGO interferometer**

Figure 97 shows a typical image of the influence the reinforced elastomer has on the surface of the steel plate under lubricated conditions. Arrow lines marked the sliding direction. As can be seen, the presence of oil plays an important role in the wear behaviour of the sliding contact since no traces of elastomer material are visible across the steel surface. Thus, in contrast with the corresponding image (figure 69) of the dry contact, no noticeable elastomer particles embedded on the steel surface were detected. Additionally, the contact load seems to

be uniformly distributed over the entire surface of the steel plate producing these identical wear marks. The similarities between the surface texture and the shape of the ploughed grooves indicate that lubricant film was captured and maintained between the surface irregularities, providing a smoother and more equal contact of the rubbing surfaces. Most of the worn surface of the steel plate consisted of smooth stripes without significant depth, as the ZYGO interferometer revealed. Grooves parallel to the sliding direction are clearly observed which suggest the wear process is governed by abrasive wear mechanism as figure 98 depicts. The wear lines with their abrasive character are characterised by the combination of micro-ploughing and micro-cutting modes as will be further analysed in the following sections. The average depth of these specific wear lines is around 1  $\mu\text{m}$ . Eventually, the wear mechanism is characterised as a two-body abrasion.

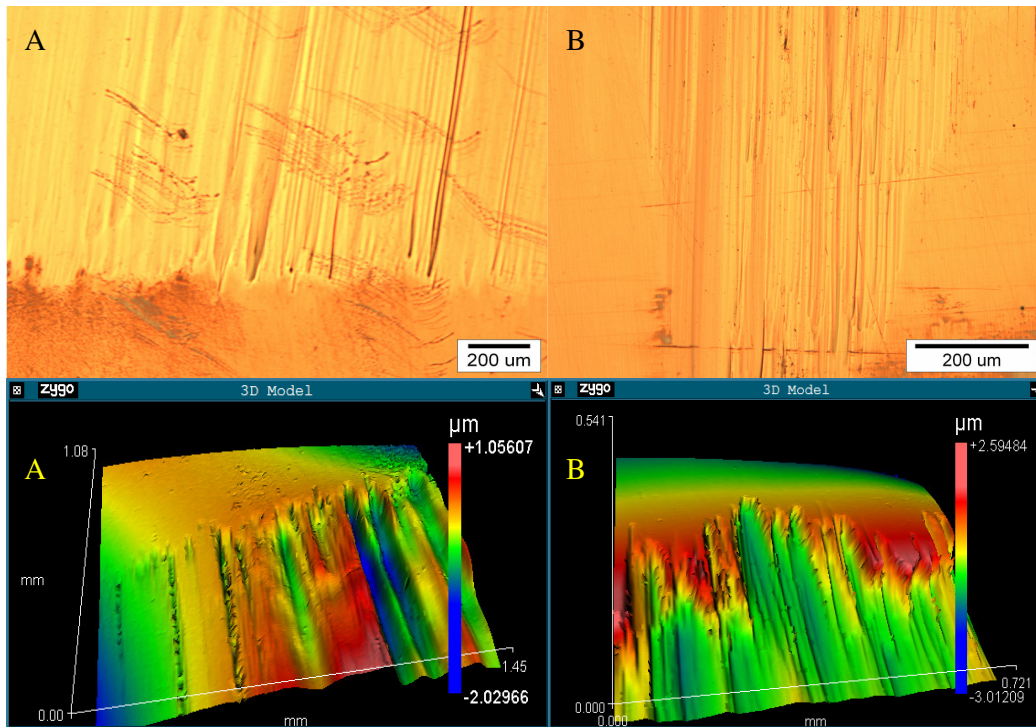


**Figure 98: Surface morphology of the wear lines distributed on the steel counterpart surface A) 0.8MPa, 0.5m/sec, 150<sup>0</sup>C, 20hours and B) 0.8MPa, 0.5m/sec, 100<sup>0</sup>C, 20hours**

Moreover, many evidences of three-body abrasion wear were also found in figure 99. Across the surface of the linear scratches many consecutive indentations were observed. As can be seen by the higher magnification of the SEM micrograph for a typical worn area with accumulated indentations, three-body wear is the clue to the damage on the steel surface. Apparently, the shape, the size and the direction of these cracks reveal the impact of three-body wear mechanism in that region.

In figure 100 the surface of the elastomer material is presented for two different test conditions. All the testing parameters were kept the same, except the sliding velocity which was doubled. It was found that the worn surface of the elastomer and the amount of the detached particles rapidly increases with the increase in reciprocating sliding frequency. The sample surface after the lower speed test is characterised by shearing waves and viscous flow while surface plastic deformation is accompanied by shallow detached particles. After the higher speed test it is clearly visible that many detached particles damaged the surface creating a cratered area. The worn surface is characterised by severe plastic deformation and deep hollows while a tenacious transferred film was formed on the counterpart steel surface. The chemical analysis of the detached particles found on the steel surface showed that the embedded particles were derived from the bulk elastomer material. The diameter of these cavities is maximum of 100  $\mu\text{m}$  while their depth can reach up to 5  $\mu\text{m}$ .

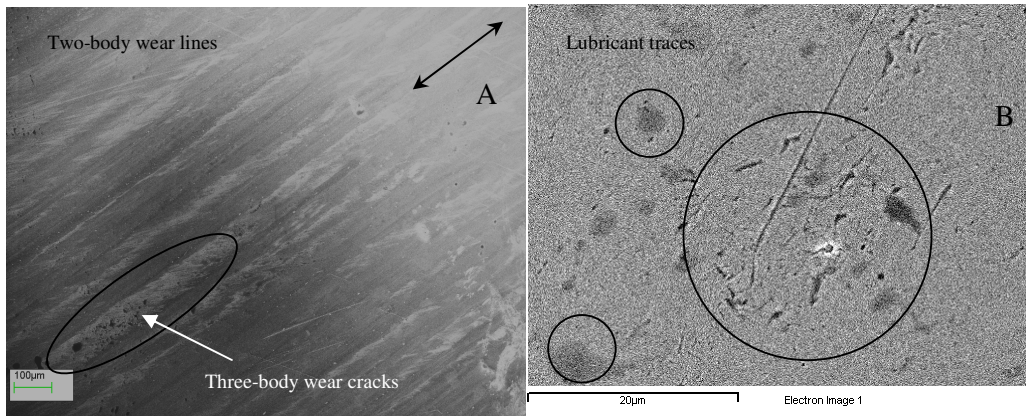


**Figure 99:** A) Consecutive indentations across the linear wear lines of the steel plate, indicating the three-body abrasion mechanism B) A close up image reveals the indentations by the third-body particle

The SEM micrographs show a severely damaged matrix and subsequent removal of bulk material leading to exposed reinforced fibres. With the increment of the contact pressure the contact temperature was greatly increased leading to an accelerative breakage of the matrix especially in the interfacial region. The extent of damage on the surface of the elastomer was increased with fibres peeling-off. The exposed fibres were subjected to most of the load and were tilted due to impaction by the asperities of the counterpart. Eventually, some of the protruded fibres were thinned and fractured (figure 101).

In contrast, the specific length of the fibres enhances the wear performance of the elastomer material. In this study the length of the fibres is up to 100 microns. The fibres can be determined as short ones. Short fibre reinforcements have been successfully used to improve

the strength the load carrying capacity of the elastomers [182]. According to Chang et al [98] short fibre reinforcements like carbon and glass fibres, could generally improve the mechanical properties of the composites and result in wear reduction.

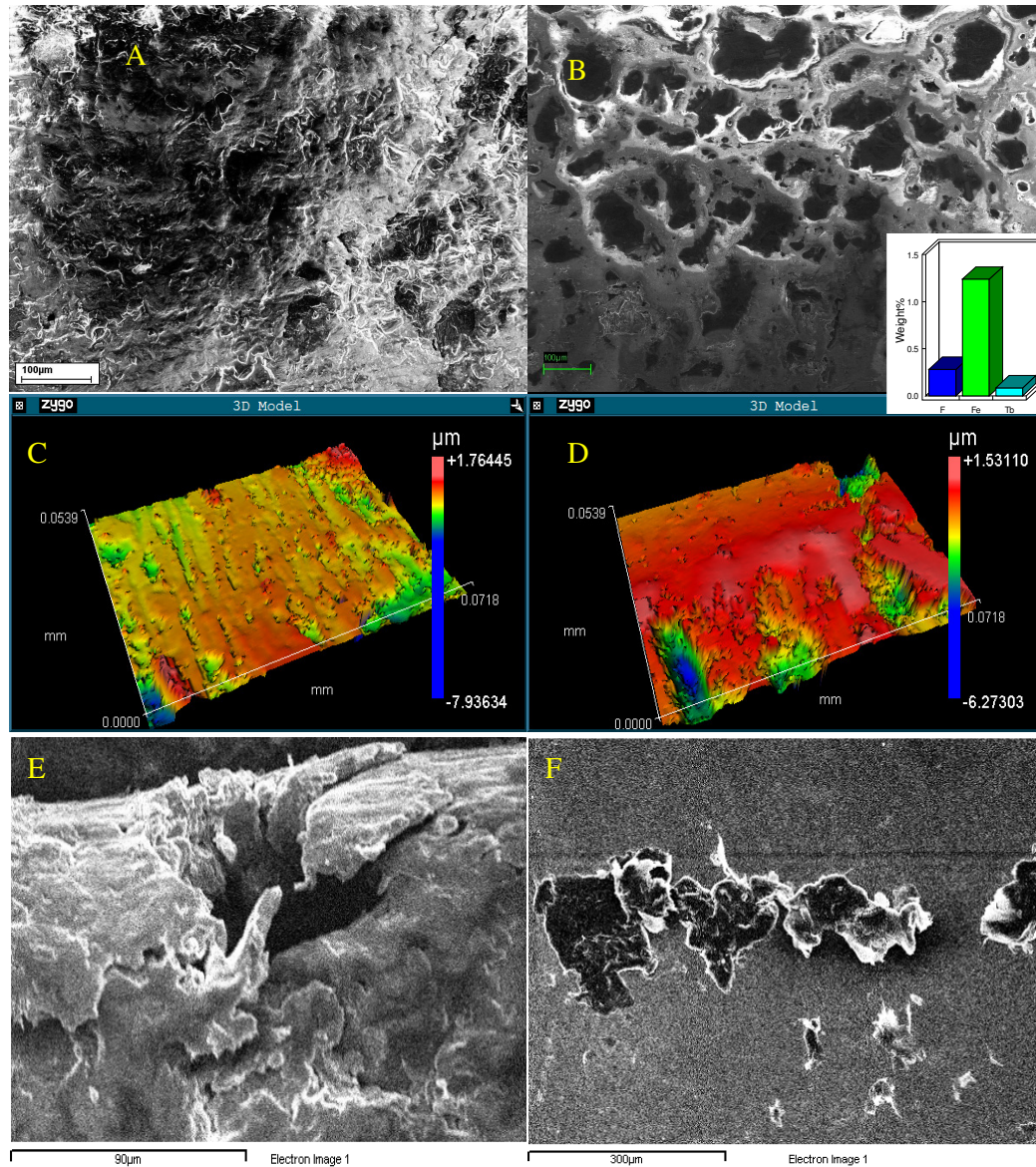


**Figure 100: Fluoroelastomer surface after A) 20h-100°C-20N-25Hz, B) 20h-100°C-20N-50Hz. Surface morphology for C) 25Hz reciprocating frequency, D) 50Hz reciprocating frequency. SEM micrograph of a E) detached particle, F) elastomer particles found on the steel plate/chemical analysis**

A close-up observation reveals local micro-cracks occurred within the matrix (figure 102). The formation of these cracks is probably caused by fatigue. Interestingly, the distinction between the regions with fatigue crack and detached particles can be observed in figure 102 B and C. The fatigue cracks are formed by overlapping layers which in due time fracture due to

the repeated loads. On the other hand detached particles are mainly caused by the adhesion mechanism.

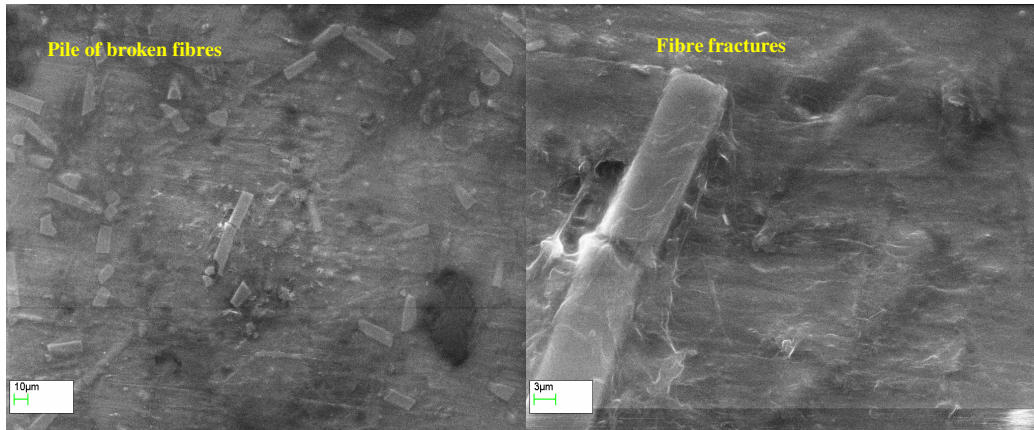


**Figure 101: SEM micrograph of an after test elastomer surface: a) A pile of broken fibres b) High magnification of a broken fibre**

Additionally, nano-scale grooves parallel to the sliding direction were observed on the fibre surfaces as figure 102 (D) illustrates. The fibres are well mixed with the bulk material of the elastomer and only under higher magnification would it be possible to examine their damaged surface (figure 102 E). Interestingly, consecutive wear linear strips were detected across the fibre surface. Their depth is very shallow and superficial and could not be accurately measured. The width of the grooves is in a range of 600-1000 nm. The width of these grooves is much lower compared to the hard fibre size with a width size around 5-6 µm. However, the broken hard fibres which are in the same order of size as the grooves seem to be responsible for this wear type (figure 101 and 103).

It can be considered that the individual hard fibre particles, after their breakage, were possibly mounted on the counter surface of the steel plate. The fibre debris was constantly scratching the surface of the implemented fibres within the elastomer matrix, indicating a two-body nano-ploughing abrasion mechanism [101], [183]. Furthermore, the rolling effect between the fibres and the detachment of tiny parts is also responsible for the generation of the superficial abrasion lines on the fibres' surface [101]. In addition, the high carbon steel debris exposed in between the rubbing surfaces can be also responsible for the formation of these shallow scratches across the hard fibres' surface.

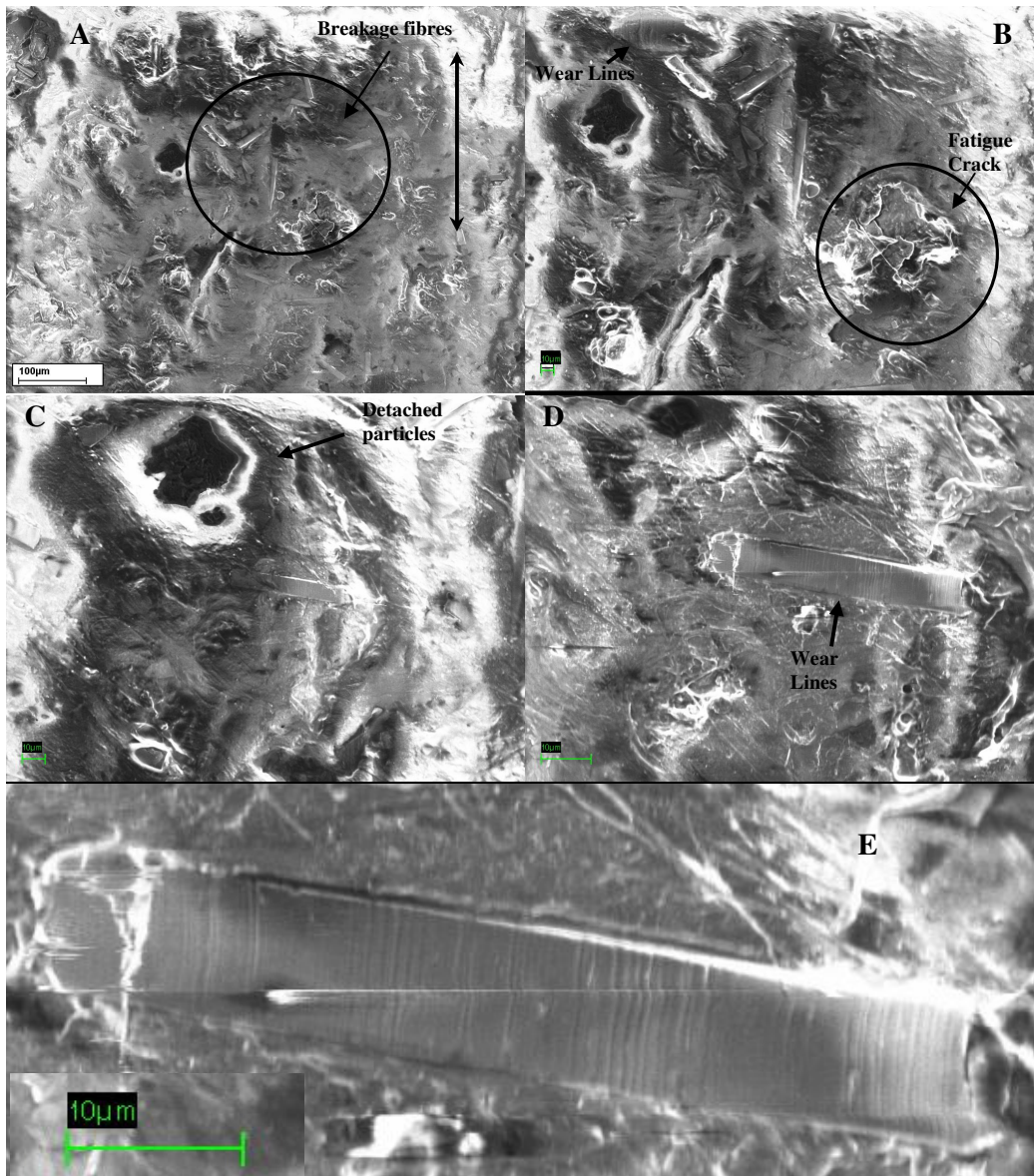


**Figure 102: SEM micrograph of an elastomer surface after the completion of sliding test A-C) Broken fibres, fatigue cracks and detached particles are depicted D-E) Wear linear scratches found on the surface of a fibre are illustrated**

Moreover the linear sliding grooves on the fibres' surface can be well matched with similar grooves found on the surface of the steel plate as figure 104 illustrates. These tiny grooves were in the same direction as the main body of the abrasion mechanisms. However they were a few microns long and very superficial. Their width ranged between 1-1.5 µm while their depth was in the range of 200-400 nm. In this case it is reasonable to hypothesize that the hard tiny breakage particles of the elastomer matrix are responsible for the nature of these marks. Once again it seems that a combination of the rolling effect creating consecutive indentations and the sliding mechanism forming linear grooves occurs. Figure 104 also highlights the

formation of a possible fatigue crack developing along the direction of motion and initiated by the fibre debris.

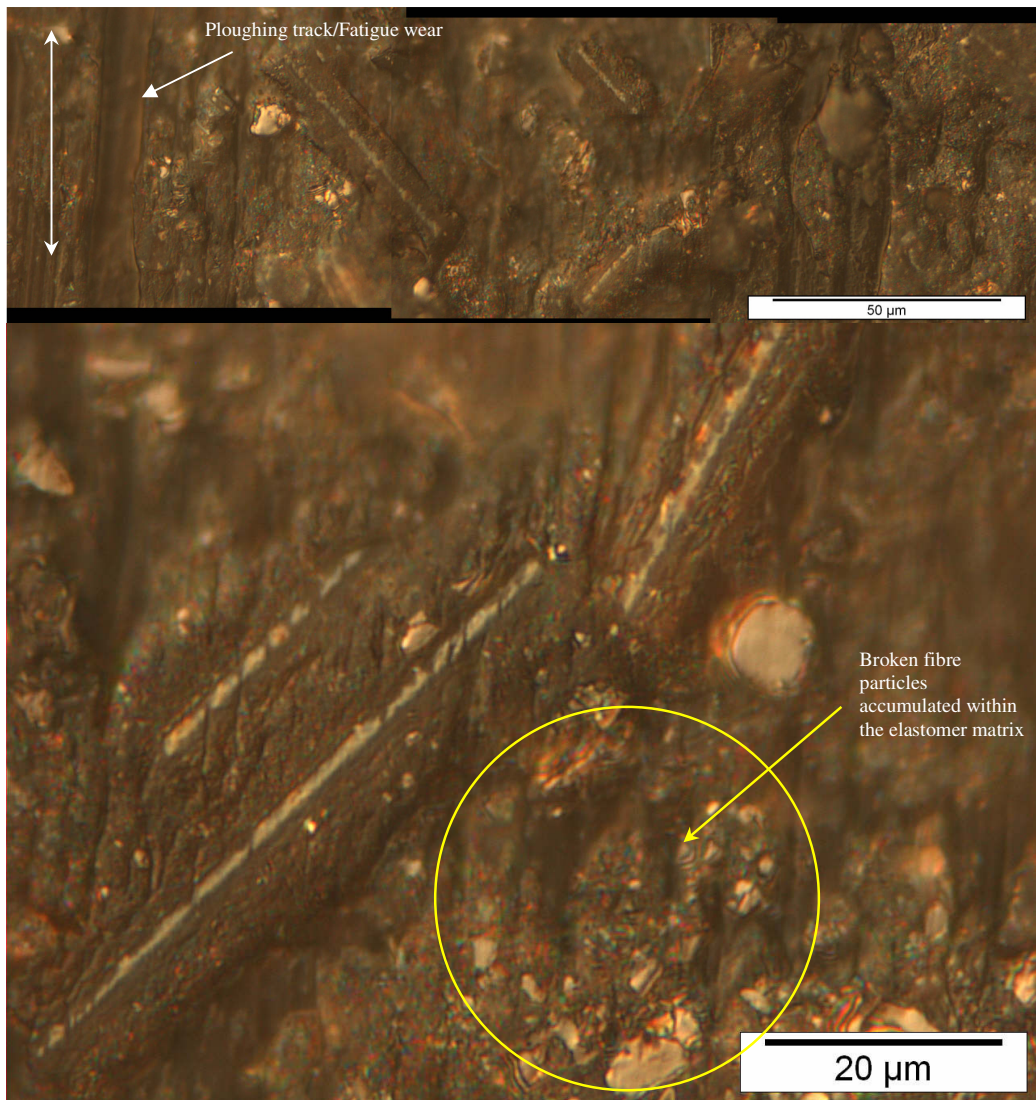


**Figure 103: Optical micrograph of A) accumulated fibres within the elastomer matrix B) detailed representation of the damage surface of the fibres**

The sliding contact creates undulations and ploughing cracks leading to fatigue damage. Specifically, many ploughed tracks were observed across the surface of the elastomer. In figure 105 a ploughed tracked is presented. It is characterised by plastic deformation creating a linear smooth crevice. A higher magnification reveals that the inside folds of the crevice have deteriorated. Several parts of the elastomer matrix are detached forming elastomer-like flake particles and fatigue mechanism prevails.

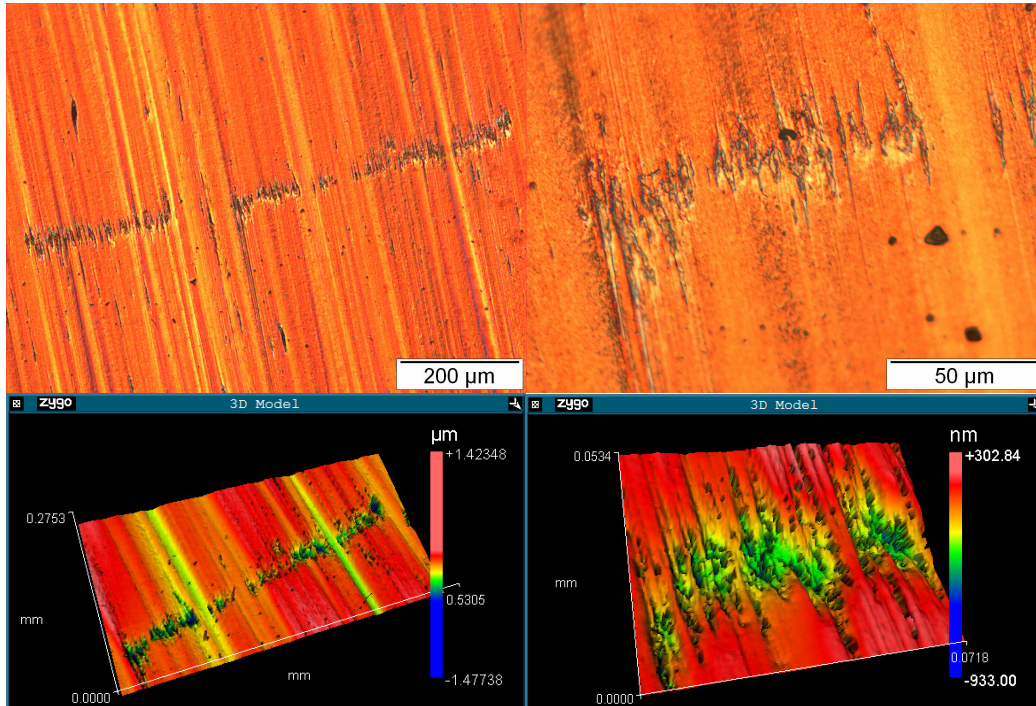


**Figure 104: Optical microscope images of the fatigue crack developed by three-body abrasion particles. Zygo interferometer microscope reveals the size and the depth of this track.**

Moreover with the ZYGO interferometer microscope we were able to measure the depth and monitor the morphology of a typical ploughed track formed on the elastomer surface, see figure 106. The depth can reach up to 1 micron while the width ranged between a few micrometers up to 200  $\mu\text{m}$ . The crack dimensions also matched well with the size of the fibres and the debris which was detected within the tested lubricants. Additionally, the length of most of the cracks expanded to a few millimetres range. This indicates that contact with the blunt asperities of the steel surface is continuous and constant avoiding severe wear but generating fatigue.

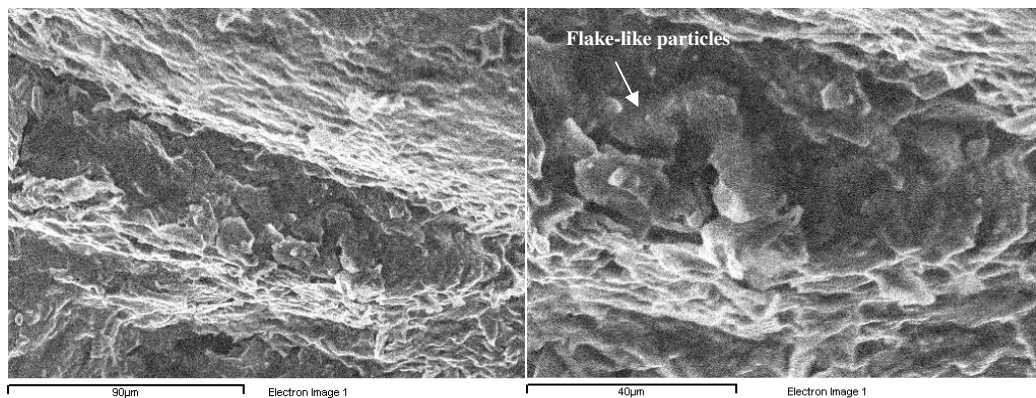


**Figure 105: High magnification SEM micrograph illustrates the degradation of the inside folds of the crack shows a ploughed crack developed across the surface of the elastomer material.**

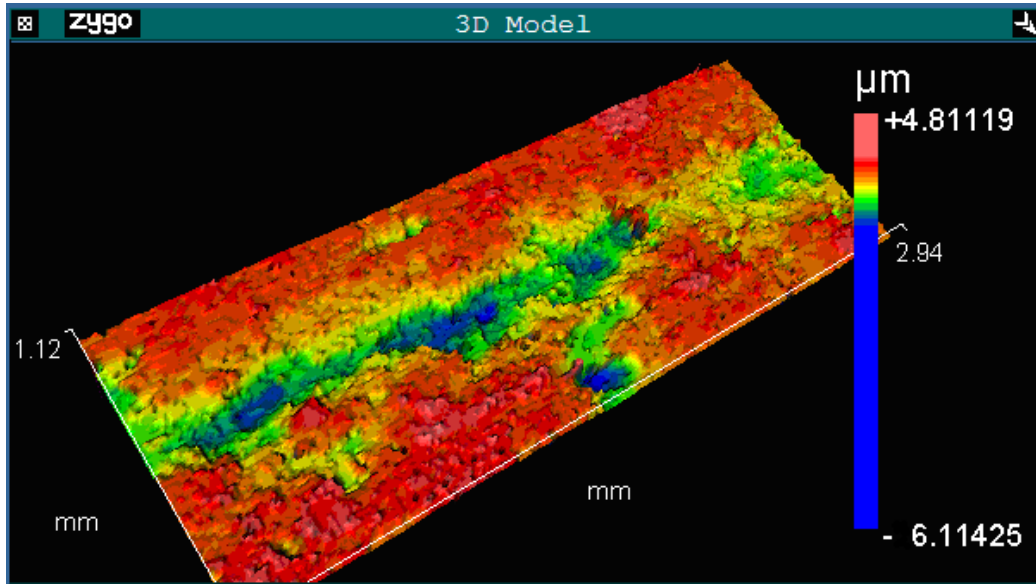


**Figure 106: ZYGO interferometer image shows the morphology of the inside folds of fatigue track.**

In figure 107 the different behaviour of the fibres is depicted. In all the images the peeling mechanism is highlighted except in figure 107 (A) where the fibre is still embedded within the matrix of the elastomer. This indicates that strong bonding between the bulk material and the fibre occurs preventing the peeling-off mechanism. Hence, the wear on the polymer surface is further reduced. This performance can be observed in the lower speed and applied load regimes. The rest of the figures 107 (B-D) present the peeling mechanism of the worn fibres. Three distinctive patterns were revealed. In the first and most common one (figure 107 B) the fibre after the relaxation of the elastomer matrix, loosens and emerges on the viscous surface. Consequently, the fibre surface obtains an intimate contact with the asperities of the counterface steel plate and severe wear is generated. The height of the exposed fibre is about 1  $\mu\text{m}$ . Interestingly, the exposed fibre height coincides with the average depth of the corresponding steel counterpart, presented previously (figure 104). This is a very good indication of the wear damage mechanism, highlighting the hard fibres of the elastomer matrix.

In the second pattern an interesting fibre damage mechanism is observed (figure 107 C). The fibre is found to be damaged by forming an oblate-like shape. This morphology is possibly derived by a third-body fibre particle which was trapped in between the rubbing surfaces and simultaneously started squeezing the fibre surface with a specific pressure angle causing deterioration on the fibre's surface. On closer inspection it can be seen that a step has been formed across the top edge of the fibre. Knowing that the direction of movement is tangential

to that step it can be assumed that during the sliding process the third-particle was trapped between the step and the counterface of the steel plate. The particle was pushed aggressively onto the formed step every time the reciprocating movement was in that direction. This mechanism looks like the wedge forming mechanism where a wedge-like wear particle is formed at the tip of the grooving asperity and stays there working as a kind of built-up wedge. Thus, only a part of the fibre obtains this oblate-like shape and is formed opposite to the edge step.

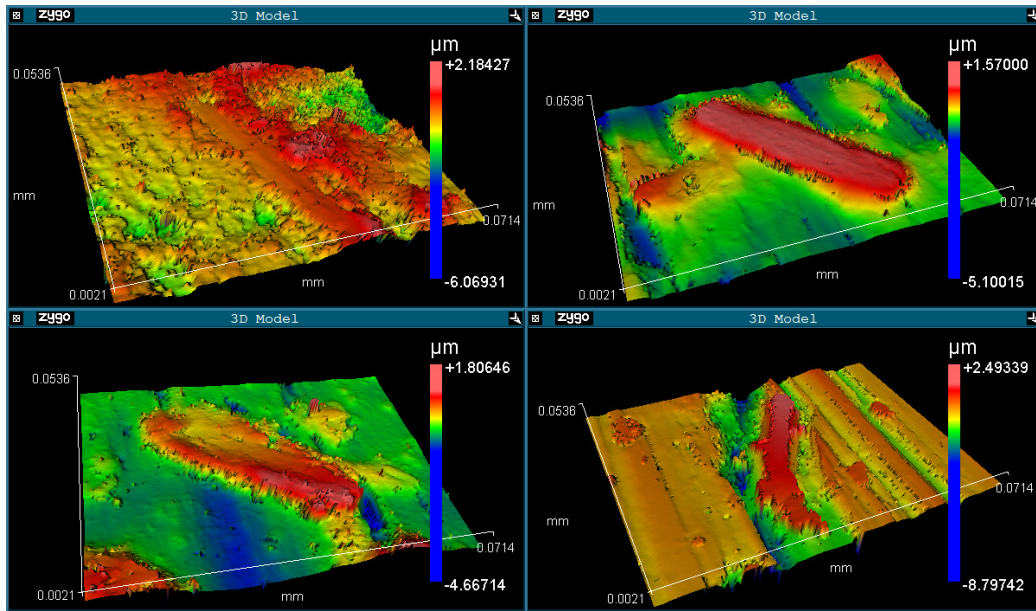


**Figure 107: Fibre analysis on the surface of the fluoroelastomer. a) position of the fibre within the original surface (before test) b) fibre revealed on the surface (after test) c) fibre damaged “oblate shape” d) fibre between a micro-crack and a micro-ploughing wear mark**

Finally, the last pattern is a combination of a crack and a surface fibre (figure 107 D). This fibre looks like the one described previously in figure 107 (B). The determinant is that the actual fibre sits in a higher position, on top of a ridge formed by plastic flow, having direct and aggressive contact with the higher asperities of the steel plate. Thus, wear damage on the steel plate surface is inevitable. Additionally, the fibre is embedded in a very vulnerable and loosened region. The fibres in that region damaged by wear lines can be easily peeled or rolled off. These kinds of fibres are responsible for the generation of third-body particles in similar sliding contacts.

In the series of images of figure 108, the main wear mechanisms found on the steel plate samples, are presented. The evaluation of the steel samples in all the testing environments showed that two-body abrasion prevails in relation to the wear mechanisms on the steel

surface. Two-body abrasion is generated by the sliding contact of the opposing asperities. The wear becomes more severe as the temperature increases.

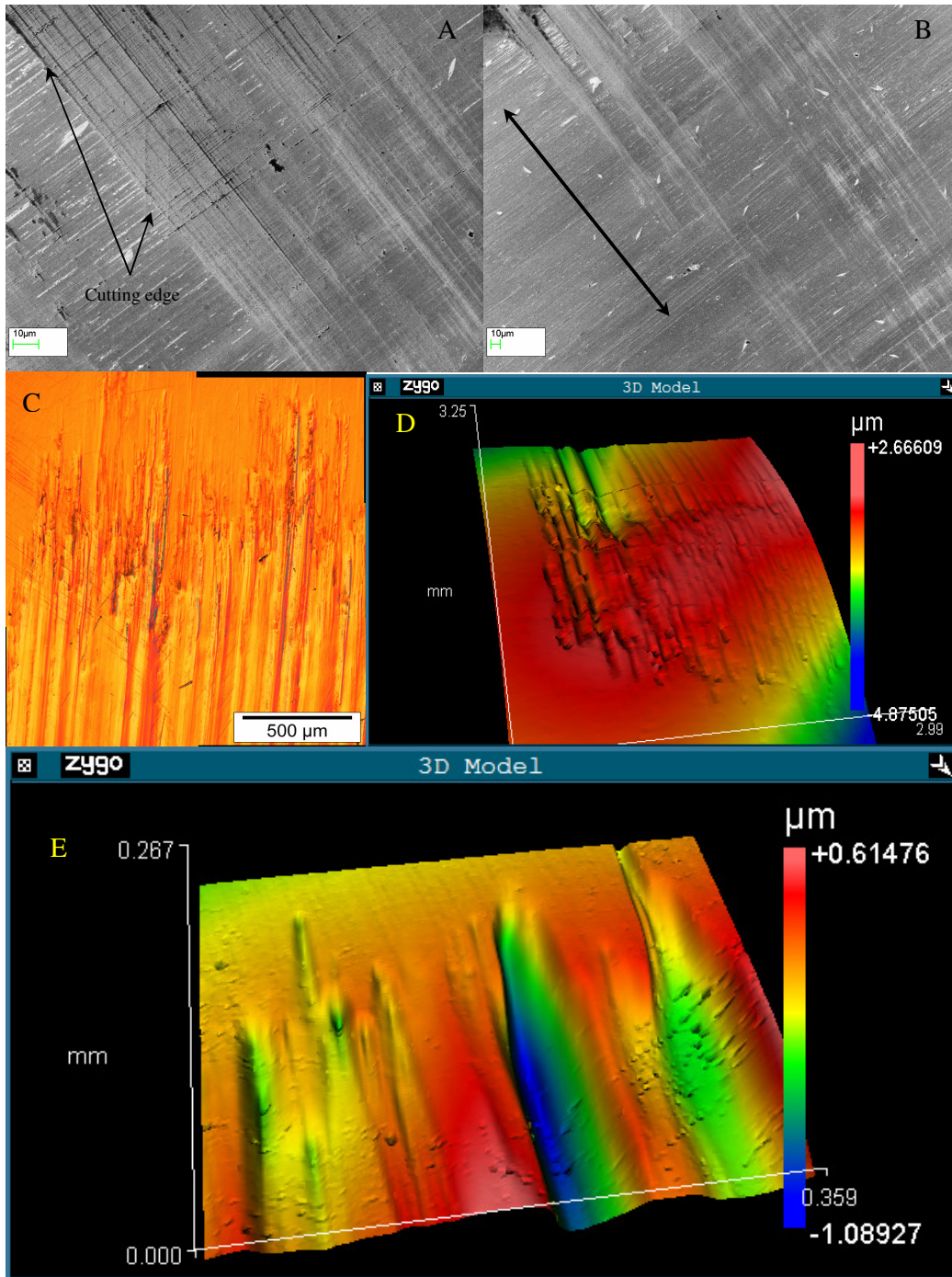
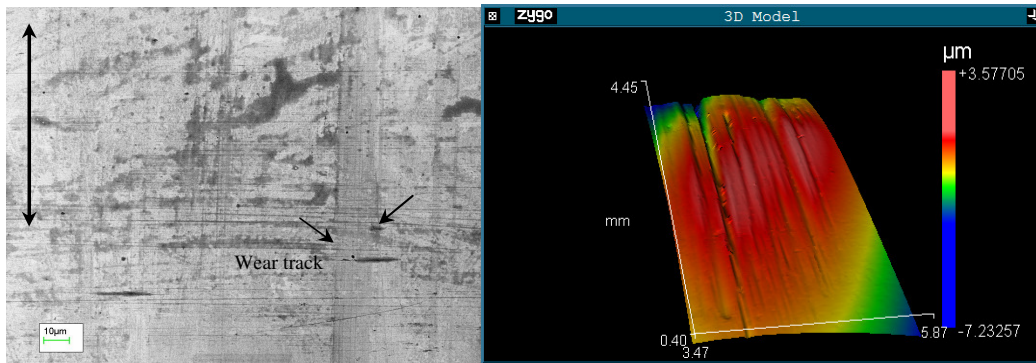


Figure 108: Typical steel plate wear damage. Test conditions were adjusted at 150<sup>0</sup>C-60hours-20N-50Hz. A-B) Precise fine perpendicular cut across the edge of the steel surface by the reciprocating movement of the reinforced elastomer is observed. C-D) The main body of wear is governed by wear linear marks. E) A detailed representation of the steel edge ploughing mechanism is depicted

Detailed observations of the linear abrasion grooves by the ZYGO interferometer microscope showed that the major abrasive mode can be determined as ploughing (figure 108 E). The round finish of the grooves at both edges and their smooth curving shape obtained during the sliding process by the contact asperities of the polymer matrix, reveal the micro-ploughing mechanism. In micro-ploughing mode the material flows down the front face of the particle. Thus no material volume is removed. However since a lot of debris was found on the surface of the elastomer material and within the lubricant samples, a combination of micro-ploughing and micro-cutting mode co-exists. In micro-cutting mode the material flows up the front face of the particles while substantial volume is removed by chip generation. Thus, it can be said with certainty that two-body abrasion wear on the steel plate derives from the combined effects of micro-ploughing and micro-cutting modes. Additionally, both modes contribute to the ridge formation on both sides of a groove (figure 109).



**Figure 109: A representative wear track with the ridge formation on both sides. Experimental conditions were adjusted at 40<sup>0</sup>C-60h-20N-50Hz.**

Moreover, three-body abrasion seriously damaged some parts of the samples. The third-body particles either adhered to the hard surface and slid on the softer surface, or were caught and rolled between the two surfaces. In this case due to the nature of the contact surfaces, the latter mechanism mainly occurs. The hard fibres of the elastomer roll frequently, creating a series of indentations rather than linear grooves. Three-body wear clearly appears in the high temperature regimes while the amount of the abrasion cracks is significant. Abrasion cracks were found accumulated in many areas within the abrasion lines. This is something which was expected to be seen since the elastomer matrix is filled with hard fibres playing the role of the third-particle during the sliding wear process.

In figure 110 different patterns of indentations formed by the rolling effect of a third-particle are shown. The trapped particle creates a series of identical indentations on the surface of the steel samples, indicating that the three-body wear occurs between the specimen surface and

the abrasive particles. These indentations are varying in size and depth. In most of the cases the depth is constricted to a few nanometers, with a maximum depth of 1000 nm (figure 110 B). However, in some cases the abrasive particles can create more severe indentations with a depth of up to 2  $\mu\text{m}$  (figure 110 D).

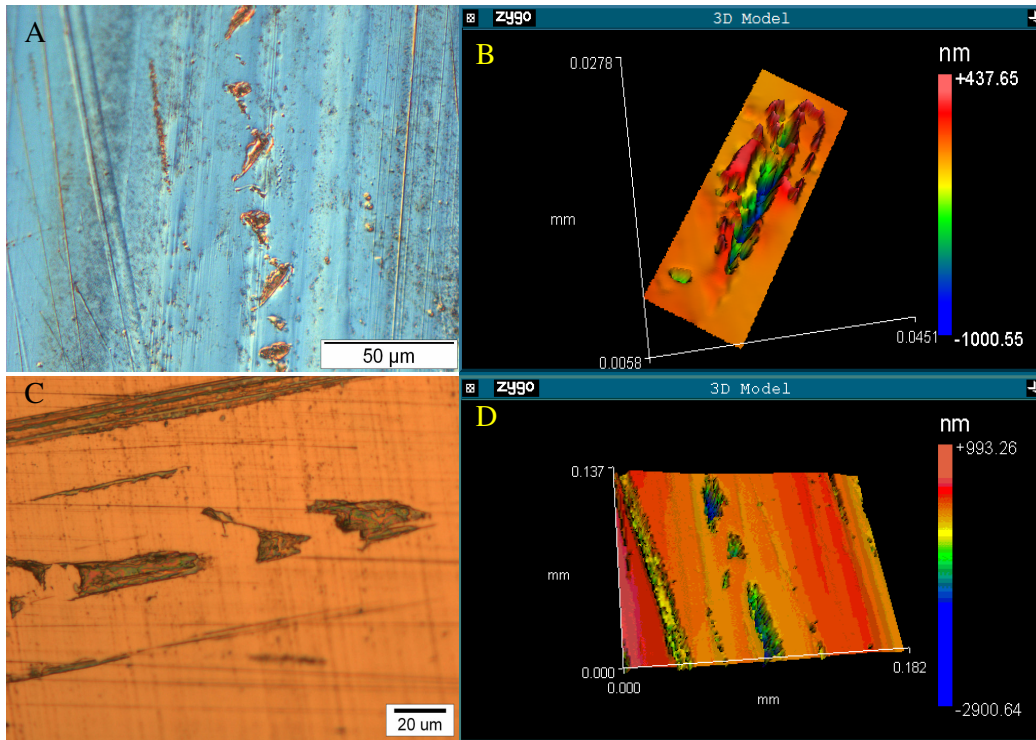


**Figure 110: Three-body wear abrasion cracks formed at 100°C on the surface of the steel plate a) average depth b) maximum depth**

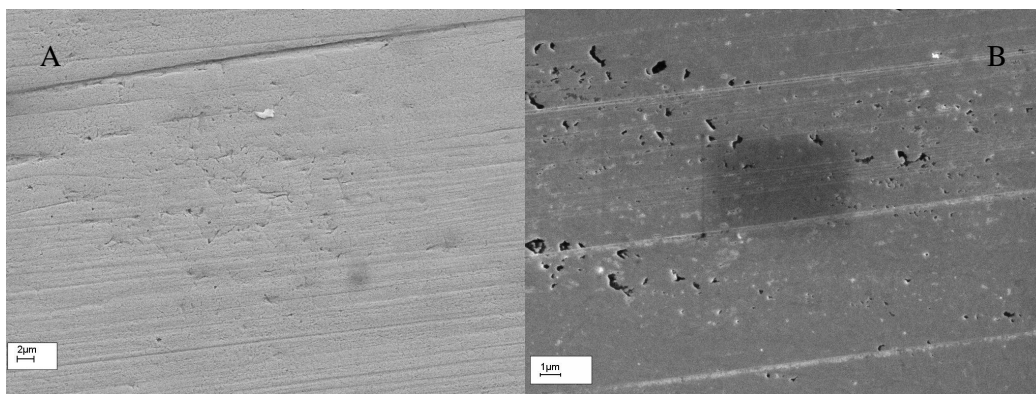


**Figure 111: SEM micrographs of cluster of cracks generated by three-body wear mechanism. Test conditions: A) 20N-60 hours-50Hz-40°C, B) 20N-60 hours-50Hz-100°C**

Additionally, SEM micrographs show the formation of indentation clusters by abrasion particles in different areas. In figure 111 a series of third-particle indentations is depicted. In figure 111 (A), plastic deformation is initiated, creating superficial damage on the steel plate's surface. The test regime was at the lowest operating temperature conditions enhancing the performance of the lubricant. Hence, the damage on the steel surface was the minimum possible. By contrast, in higher temperature regimes the abrasive particles were more aggressive and vigorous, creating a cluster of holes and cracks across the steel surface (figure 111 B). The size of these indentations remains similar in both testing regimes.

Three-body abrasion is not as rigorous as two-body abrasion, minimizing the possibility of severe damage. It is well known that three-body abrasion is 10 times lower than that of two-body wear. The wear reduction by three-body contact is generally attributed to the rolling effect of the abrasion particles. The rolling effect strongly depends on the sliding conditions, the hardness of the particles as well as their size and shape [184-185]. Thus three-body wear is more beneficial than two-body abrasion in terms of keeping the wear rates at low levels. Eventually, the friction coefficient is significantly reduced as well as the overall abrasion wear rate. In this study as has already been mentioned the rolling effect of the short fibres protects the deterioration of the rubbing surfaces.

## **5.8 Summary and discussion**

### **5.8.1 Wear/Friction Modes**

The main goal was to identify the tribological behaviour of the high carbon steel plate sliding against the reinforced fluoroelastomer tip seal of the scroll expander. The contact regime was changed with variable speed and load values. Initially the wear mechanisms responsible for the reduction of the friction coefficient and the specific wear rates were thoroughly investigated. Afterwards a correlation of the friction coefficient and the wear rate with various parameters was conducted. Finally, a comprehensive surface investigation of the steel/elastomer contact revealed the wear damage modes under various lubricated regimes.

### **5.8.2 Wear Mechanisms**

The wear mechanisms of the main components of the scroll expander, the high carbon steel plate and the high performance reinforced fluoroelastomer tip seal can be synoptically summarised with the following block diagrams, figures 112 and 113 respectively.

## Steel Plate Wear Mechanisms

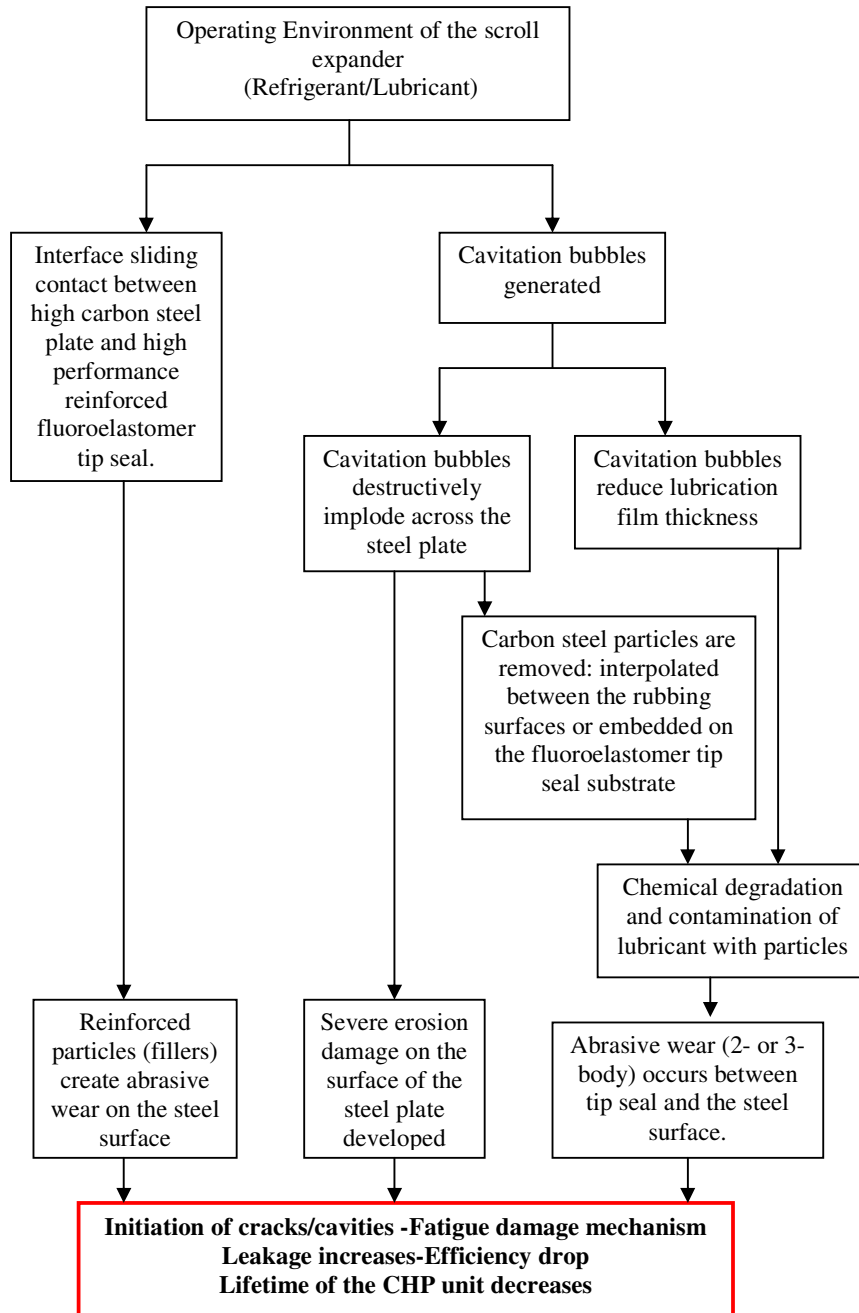


**Figure 112: Classification of the sliding friction process leading to wear of the steel plate.**

## High Performance Reinforced Fluoroelastomer Wear Mechanisms

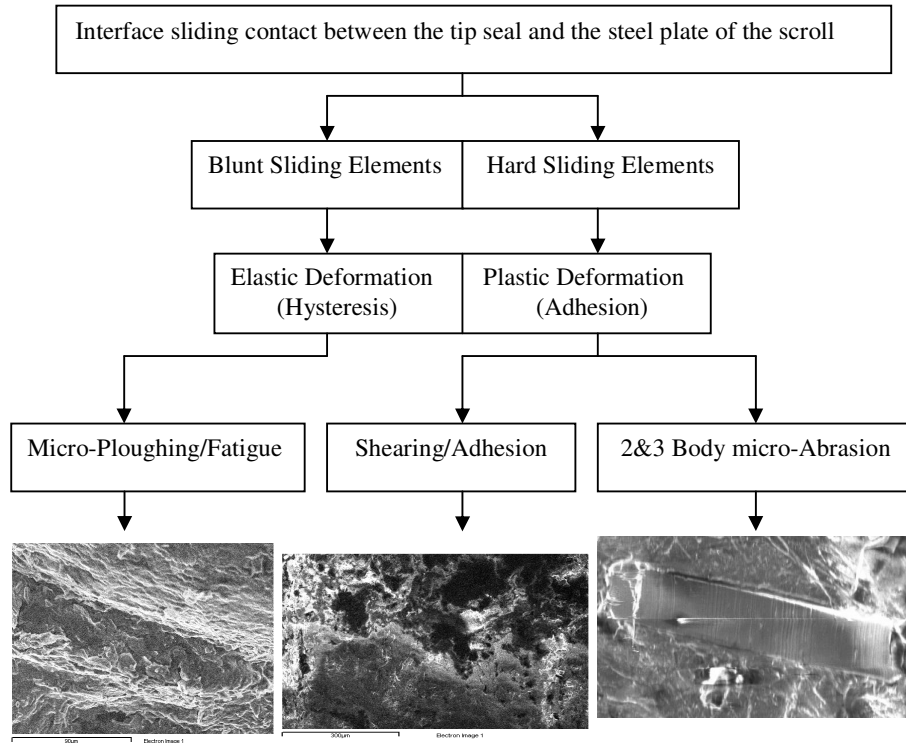


**Figure 113: Classification of the sliding friction process leading to wear of the elastomer tip seal.**

### 5.8.3 Friction/Wear Analysis

In sliding wear contacts of elastomer against steel counterparts, the friction coefficient component resulting from adhesion equalled the product of the real contact area and the shear strength of the elastomer [79], [98], [101]. Thus, after the evaluation of the parameters which affect the friction coefficient of the high carbon steel against the high performance reinforced fluoroelastomer contact, two competitive mechanisms were revealed. On one hand the lubricant dissipates part of the frictional heat and increases its viscosity due to the increment of the applied load. Additionally, due to thermal expansion of the elastomer and the softening effect, the real contact area increases. The result is the rise of the friction coefficient. On the other hand, the viscosity of the lubricant is reduced due to the generation of thermal effects caused by the augmentation of the sliding velocity and the applied load. Moreover, the poor thermal conductivity of the elastomer accumulates an amount of frictional heat accelerating

the melting of its bulk material. Hence, the asperity contact increases, resulting in a shear mechanism on the elastomer's material surface facilitating the generation of the rolling effect.

In this study, the results showed that for higher applied loads (40 N) shearing prevails, substantially softening the overall contact. The friction coefficient is thus decreased. By contrast for lower applied loads (20 N) of the steel/elastomer contact, the real contact area prevails, restricting excessive shearing due to absence of elevated thermal effects. Eventually, the friction coefficient is substantially increased. The abovementioned competitive mechanisms are well represented by the schematic diagram in figure 114.

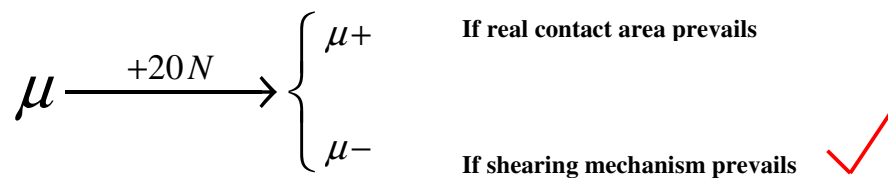


**Figure 114: Schematic diagram of the two competitive mechanisms generated during the steel/elastomer contact.**

In addition, the strong coupling between the fibres and the elastomer matrix prevents the rubbing-off mechanism, resulting in increased friction coefficient. This indicates that in lower loads, where the real contact area is smaller, thermal effects do not play a dominant role. The fillers stay well mounted within the matrix of the bulk elastomer material. The contact is confined between the embedded hard fibres of the fluoroelastomer slider and the steel counterface. Thus the friction coefficient rapidly increases. However, due to higher pressure contact and sliding velocities, contact temperature is elevated, which results in a serious softening of the elastomer matrix. Thus, fibre removal is seriously aggravated since the softened elastomer matrix is not capable of preventing fibres from peeling-off. Hence, a rolling effect is generated. The combination of the lubrication and adhesion contact with the rolling effect can substantially reduce the friction coefficient.

However, there is still a debate in the scientific community, regarding the sliding contact of the reinforced elastomers against steel materials. On one hand some researchers believe that the friction coefficient decreases with the increment of the applied load due to the excellent performance of the fillers while it increases with the rise of the sliding speed [79], [98], [101], [103], [105]. This research agrees with those outcomes. On the other hand others believe that the fibres under a given applied load provide a stronger interfacial adhesion leading to rapid wear of the elastomer surface and consequently the friction coefficient is increased [186-187].

Additionally they found that with the enhancement of the sliding velocity the friction coefficient is reduced. Thus more investigation on the sliding contact of the reinforced elastomer against steel materials under dry and lubricated conditions is needed in order to achieve a coherent and generally accepted determination of their tribological mechanisms.

Furthermore, in low sliding speeds the friction force proportionally increases with the increment of the applied load. Interestingly, in higher sliding speeds the friction force is also increased as the applied load is reduced, leading to higher friction coefficient values and more severe wear rates. This indicates that a severe contact between the exposed hard fibres and the steel asperities has occurred. The real contact area remains mainly unformed and excessive shearing is restricted, while the cohesive bulk material restrains any possible peeling mechanisms of the fibres. Shearing is not a dominant factor and the real contact prevails. Consequently the friction coefficient and the wear rates are rapidly increased.

According to friction coefficient graphs a detailed evaluation of the wear rates for all the tested cases was performed. It was found that the wear rate of the steel samples increases according to the friction coefficient. The interpretation of this mechanism can be found on the two competitive wear mechanisms described above. Since the real contact is dominant for lower applied loads, the contact is restricted between the well-mounted fibre particles of the elastomer bulk material and the asperities of the steel plate. This was also indicated by the small amount of the elastomer transferred onto the steel sample after the completion of the sliding test. Thus the wear rate increases. In contrast, for higher loads, the wear rate was found to be substantially lower. Thermal effects are generated while the free roll fibres carry most of the load in the friction process alleviating the rough contact. This performance was enhanced by the fact that substantial elastomer traces were found across the steel surface. Interestingly, the wear rates after a long period of time are stabilised and the actual wear regime is reduced. The wear resistance was radically improved suggesting a gradual change in the wear regime from severe to mild. This excellent performance of the tip seal/steel plate contact can prove beneficial for devices with long operating times in demanding environmental conditions like the scroll systems.

After the evaluation of the wear modes of the tip seal over the steel plate it can be said with certainty that the friction coefficient of the high carbon steel over the high performance reinforced fluoroelastomer is proportionally decreased with the increment of the contact load and the attenuation of the sliding speed. This result can be effectively used in the design of the scroll expander. The actual rotation speed of the scroll is already in the minimum operating levels. It cannot be significantly reduced as this will seriously affect the efficiency

of the scroll. Furthermore, the actual contact load of the scroll is too low. Hence, with a possible increment of the intimate contact pressure of the involute scrolls and assuming that the contact will be constrained between the tip seal and the steel plate, the wear regime can be significantly reduced. Thus, the service life of the main components of the scroll and the whole micro-CHP unit will be enhanced. Additionally, the increase in contact load in correlation with the adhesive wear mechanism will directly improve the sealing performance of the expander since the size of the gaps and the leakage points will be minimized and the tendency of the working fluid to flow through these areas will be further confined. However, more applied load may result in the generation of cavities due to the squeezing film theory, although the researcher believes that cavitation, as discussed in chapter 3, is most likely produced by the high jet stream velocity in the inlet scroll and not by the squeezing surfaces. The enhanced contact load obviously has to target the limitation of the wear regime and the improvement of the scroll's overall efficiency.

Finally the effect of the sliding time is crucial for long working period applications like the scroll expander. The time-related wear rate for the 60-hour running experiment is significantly reduced and stabilised at 3 times less than the corresponding rate after 20 hours of running. This performance indicates a relaxation of contact is achieved after the running-in period of the steel/elastomer, leading to a less severe regime over that period of time.

#### **5.8.4 Lubrication Analysis**

The oil analysis revealed the condition of the oil samples and the interaction debris responsible for the wear damage. The presence of ferrous and silicon debris within the lubricant solutions after the completion of the tests, justifies that the wear damage in both surfaces derived from severe two- and three-body abrasion wear. Interestingly, the 150 °C oil sample found that due to oil degradation replacement oil may subsequently be needed after a short period of time. Under these conditions the lubricant seems to be degraded with loss of its stability and its overall performance. It is well-known that different loads and speeds in correlation with the higher temperatures in a lubricating system increase the rate of oxidation which automatically determines the level of the lubricant's degradation [188]. This can be proved critical for the operation and the efficiency of the scroll expander. A regular inspection of the oil performance within the scroll is required.

#### **5.8.5 Surface Analysis**

Several wear mechanisms have been proposed and observed microscopically explaining the contact nature of the high performance fluoroelastomer tip seal sliding against the high carbon

steel plate. Moreover, the material removal process from the rubbing surfaces was also thoroughly investigated. Specifically, on the steel surface, deep grooves parallel to the sliding direction clearly observed which suggests the wear process is governed by abrasive wear mechanisms. The evaluation of the linear grooves in all the testing environments showed that two-body abrasion prevails among the wear mechanisms on the steel surface. Two-body abrasion is generated by the continuous sliding contact of the opposing asperities. The wear lines with their abrasive character are characterised by the combination of micro-ploughing and micro-cutting modes. Additionally, both wear modes contribute to the ridge formation on both sides of a groove. The wear becomes more severe as the temperature increases.

Furthermore, evidence of three-body abrasion wear was also observed as many consecutive indentations were detected across the surface of the linear grooves. Three-body abrasion seriously damaged some critical parts of both samples. The third-body particles either adhered to the hard surface and slid on the softer surface, or caught and rolled between the two surfaces. Finally, the tiny linear sliding grooves on the fibres' surface could be matched with similar grooves found on the surface of the steel plate. A combination of the rolling effect creating consecutive indentations and the sliding mechanism forming linear grooves occurs.

The SEM micrographs show severely damaged matrix and subsequent removal of bulk material leading to exposed reinforced fibres. Viscoelastic ploughing and removal of material appeared to be the main dissipative processes giving rise to friction and wear during the sliding of the high carbon steel plate against the reinforced elastomer tip seal, as seen in the present study. All the elastomer samples were characterised by plastic deformation of the bulk material and undulations (beach marks) across the surface. Valleys are mainly formed due to the micro-ploughing mechanism which leads to fatigue damage wear mode at a later stage.

Additionally, overlapping layers are formed due to the thermal and cooling effects while interfacial debonding of the fibres within the matrix of the elastomer is generated, producing large amounts of detached particles. Detached particles from both materials generate two different types of third-body contact. The first one is derived from the broken fibre particles of the elastomer and the second one from the steel particles of the steel samples embedded on the smooth elastomer surface.

In all the experimental cases the peeling-off mechanism of the fibres is highlighted. The very hard exposed fibres during the friction process interact with the steel asperities producing abrasion lines across the steel surface. Interestingly, parallel nano-scale linear strips were also detected on the surface of a typical worn fibre. Their presence indicates that an aggressive,

vigorous and consistent contact within the steel asperities is achieved. This in turn generates the continuous deep abrasion pattern formed on the steel surface samples.

Based on the ZYGO interferometer measurements an interesting observation was made. The height of the exposed fibres coincides with the average depth of the steel counterface roughness. This indicates, to a large extent, that the two-body abrasion wear damage is probably derived from the severe contact of the exposed fibres with the smooth steel surface. It seems that this is the initial source of damage for the steel surface followed by the rubbing combination of the fibres and their detached particles in later stages.

The transfer films had a smaller effect on the tribological performance of the rubbing surfaces under lubrication regime. The cooling and the boundary lubricated effects of the lubricant medium dominate the contact and substantially reduce the friction coefficient. In addition, lubrication prevents the accumulation of wear debris in critical areas where otherwise the contact would have significantly increased. By contrast, in dry contact the formation of transfer layers is more noticeable while the corresponding contact is restrained between the surface of the elastomer and the elastomer transferred films. Under low loads, the friction coefficient is much higher in dry contact compared to the lubricated one. However it reduces as the load increases approaching the values of the corresponding lubricated contact.

Use of a less viscous lubricant could possibly be beneficial for the operation of the scroll since the wear performance of the tip seal against the steel plate was proved to be very efficient and reliable. A thinner lubricant, with significantly lower viscosity at 40 °C and 100 °C degrees than the actual one used in the sliding experiments, could possibly even protect the contact by sealing the grooves, hence reducing the wear and the leakages respectively. Concomitantly, because of its high fluidity in various temperatures it will prevent any accumulation in the circulation tubes of the micro-CHP system avoiding any further reduction of its thermal efficiency.

The operation of the scroll expander with the absence of lubricant can possibly be another scenario to be considered. The increment of the applied load between the scrolls, assuming that the contact is strictly constrained between the elastomer tip seal and the steel plate, can reduce the friction and wear rates. Moreover, the accumulation of oil on the inside of the heat exchanger tubes will be avoided. The heat transfer and the thermal conductivity will be further improved. Consequently, the overall performance of the micro-CHP system will be enhanced. However, the formation of grooves on the steel plate surface during the sliding process would probably affect the efficiency of the scroll. In those areas leakage will be

enhanced due to the absence of lubrication. In contrast, the elastomer adhesion mechanism will be able to seal these gaps reducing the leakage and maintaining the efficiency at high levels. Thus, the performance of the scroll will be determined by these two contradictory mechanisms.

## **6 CHAPTER : CAVITATION EROSION FAILURE MECHANISMS**

### **6.1 Introduction**

Cavitation is a complicated failure mechanism and it is often difficult to assess the material resistance and performance. Cavitation erosion is a two-fold phenomenon dealing with fluid mechanics and material science. Following the interesting findings in Chapter 3 the experimental procedure which was followed in order to interpret the cavitation mechanism was distinguished in three parts.

In the first part the behaviour of three different types of cavitation bubbles is presented. Measurements with the use of a high speed camera revealed three different behaviour patterns for each of the testing liquids (water-lubricant-refrigerant) respectively. The second part investigates the formation of the pits in their incubation stage for four different commercial steel grades including the actual scroll steel plate. The experiments were performed in three different testing environments (water-lubricant-refrigerant). Finally, the third step involved ultrasonic cavitation tests over a prolonged period of time.

In the first and the second experimental procedure the performance of the liquid environments is interpreted. The correlation of the bubble photographic results with the inception results of the cavitation pits reveals the level of contribution of the liquids to the cavitation mechanism. In the second and the third experimental procedure the performance of the steel samples is interpreted. The results from the initiation of the cavitation pits in correlation with the results over a prolonged period of time reveal the endurance of the materials against cavitation attack. The tests were performed using three different commercial steel grades and the scroll's steel plate in order that their durability performances could be compared. The alteration of the steel hardness properties was also analysed. The environment deployed was distilled water.

### **6.2 Camera Results Analysis**

#### **6.2.1 Test Methodology**

The bubble behaviour is studied with the use of high speed photography. The images were focused on three critical regions. On the tip of the ultrasonic probe where the bubbles were generated, on the boundary (chromium steel) wall where bubbles were destructively collapsed and in the area in between where the descent of the bubbles was monitored. This was performed for all three liquid types. Consequently, an evaluation of various bubble images

using the camera software was conducted and a range of graphs was produced. In each of the liquid environments more than 20 different bubble behaviours were thoroughly monitored.

Three distinctive patterns of bubble behaviour, which represent the general outcomes for each of the liquids, are finally characterised. In the first pattern the mechanism of the generation of cavitation bubbles for all the tested fluids was investigated during their incubation period of time around the ultrasonic source. The performance of the bubbles was monitored and recorded during their descent to the solid surface. Consequently, the behaviour of the bubbles across the solid boundary and their impact attributes were indicated. Finally the maximum bubble radius and velocity were calculated for all the liquid environments. The sample used in all the experiments was made of chromium steel.

### 6.2.1.1 Region around the Ultrasonic Source

The bubbles generation and the expansion mode on the tip of the horn revealed three different behaviours for each of the liquid environments (water-lubricant-refrigerant) respectively. Interestingly, the refrigerant bubbles maintain a robust shape avoiding the bubbles which are generated by the oscillation movement of the horn to separate, escape and finally collapse.

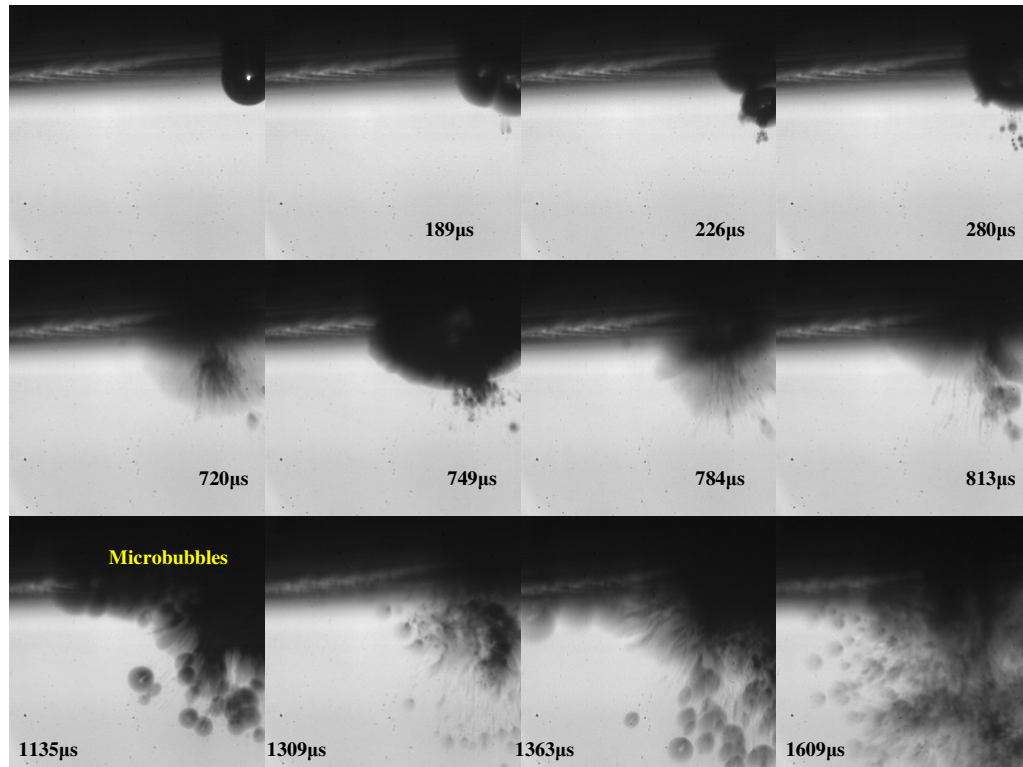
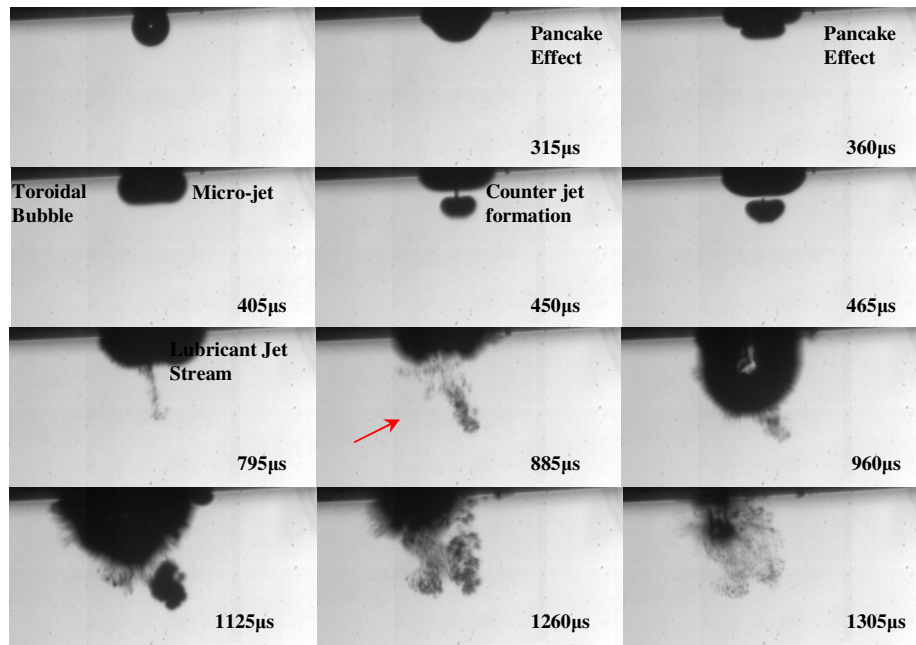


Figure 115: Expansion mode of an acoustic cavitation water bubble at its incubation stage onto the lower surface of the horn. The frame size is 0.5×0.5 mm.

More specifically, in the case of the distilled water figure 115, a typical generation cavitation phenomenon was observed. The bubbles imploded due to pressure variations creating a jet stream which in turn can damage the material surface (frame 5-8, figure 115). Moreover, the bubbles mainly collapsed asymmetrically and spread in all directions inside the liquid. From the series of images in figure 115 it can be observed that after a 1000  $\mu\text{s}$  period of time micro-bubbles generated (frame 8-9) are 10-12 times smaller than the primary bubble.



**Figure 116: Expansion mode of an acoustic cavitation lubricant bubble on the tip of the horn. The frame size is 1 x 0.5 mm.**

In the lubricant environment a “pancaking” effect at the site of the bubble collapse can be observed (frames 2-3, figure 116). The “pancaking” shape is formed only when the initial bubble is very close to the wall during the incubation period. Thereinafter the bubble rapidly obtains a toroidal shape. Then a micro-jet is formed which is usually difficult from that identified in the “pancaking” effect mode, leading eventually to a counter-jet generation (frames 5-6, figure 116). As the bubble takes the rebound and grows, in an almost round spherical shape (frame 9, figure 116), it then rapidly collapses (frame 10-12, figure 116). It is interesting that a linear jet stream, which is comprised of many tiny bubbles, emanates from the middle of the collapsed bubble. Over time, this linear jet stream becomes asymmetric, taking the shape of a cloud, and is eventually spread along the neighbouring liquid volume. At a later time step, figure 122-124, this cloud of micro-bubbles is extended inside the lubricant. The cloud is spread across the material surface creating a thin lubrication layer. This layer

plays the role of a cushion as it absorbs the impact from the micro-jet impact, thus its destructive power is significantly reduced.

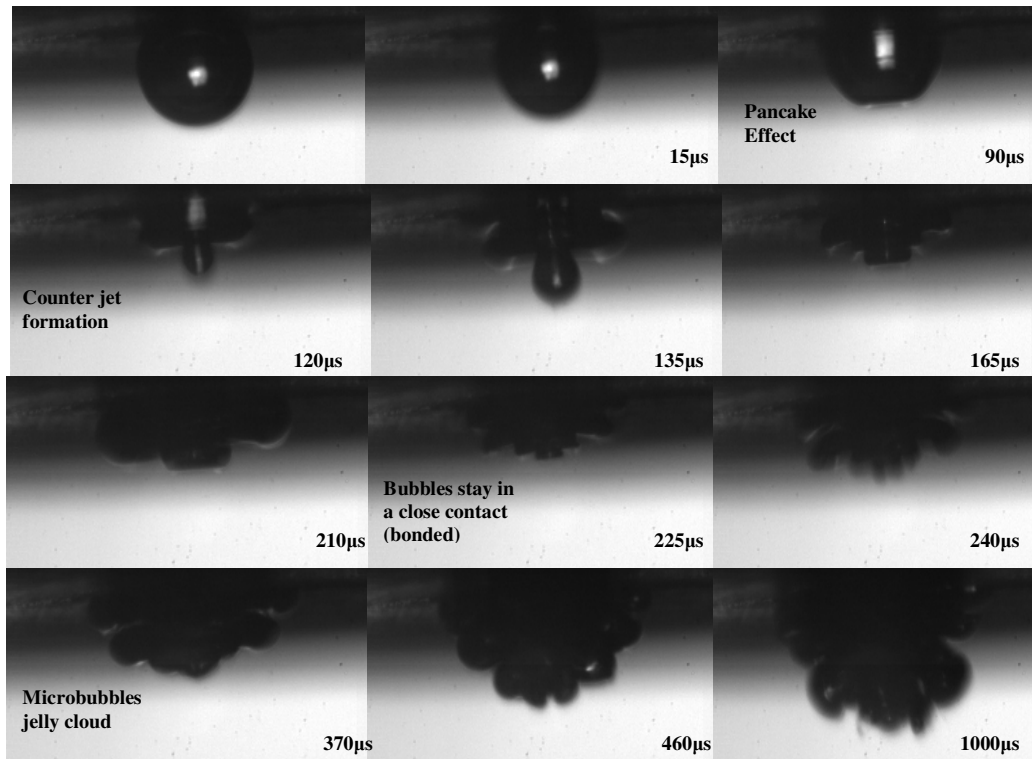


**Figure 117: Expansion mode of an acoustic cavitation refrigerant bubble on the tip of the horn. The “jelly” cloud shape is shown. The frame size is 1×0.5 mm.**

In the case of the refrigerant, initially the spherical bubble is formed to a “pancaking” shape (frame 3, figure 117) followed by a counter-jet (frame 4-5, figure 117). Then it can be clearly seen that hundreds of small bubbles are connected in a “jelly” cloud shape (frames 9-12, figure 117). Contrary to the previous cases (water, lubricant) during the cavitation process in the liquid refrigerant there is no bubble diffusion. In most cases even the bubbles which escape from this “jelly” cloud do not implode. Molecules cannot overcome the surface tension and other cohesive forces maintaining their bubbly shape. The bubbles cannot resist the attractive forces creating strong bonding.

Looking at the expansion mode images near the surface of the horn, the different behaviours of the liquid bubble implosion over a period of time is highlighted. During the experiments a single isolated bubble for each of the liquids respectively was chosen to be observed. When water was used, the deformation of the water bubble at its incubation stage started after 189  $\mu\text{s}$ . In the case of the liquid refrigerant it was measured to be at 90  $\mu\text{s}$  while for the lubricant it was around 315  $\mu\text{s}$ . Furthermore the time step where the jet stream was generated was at 280

$\mu\text{s}$  and at  $795 \mu\text{s}$  for the water and the lubricant respectively. Interestingly, for the refrigerant a similar liquid-jet stream was never formed since the bonding between the bubbles did not allow that.

### 6.2.1.2 Region between source and solid surface

During their descent to the boundary wall the lubricant and water bubbles merged or split due to pressure variations figure 118. Thus, when the pressure increased the bubble imploded and divided into smaller bubbles (frame 7 in figure 118). When the pressure decreased their radius increased and they eventually merged to a single bubble (frames 14-16 in figure 118). On the other hand, as it is shown the pressure variations did not affect the wobbling behaviour of the refrigerant bubbles.

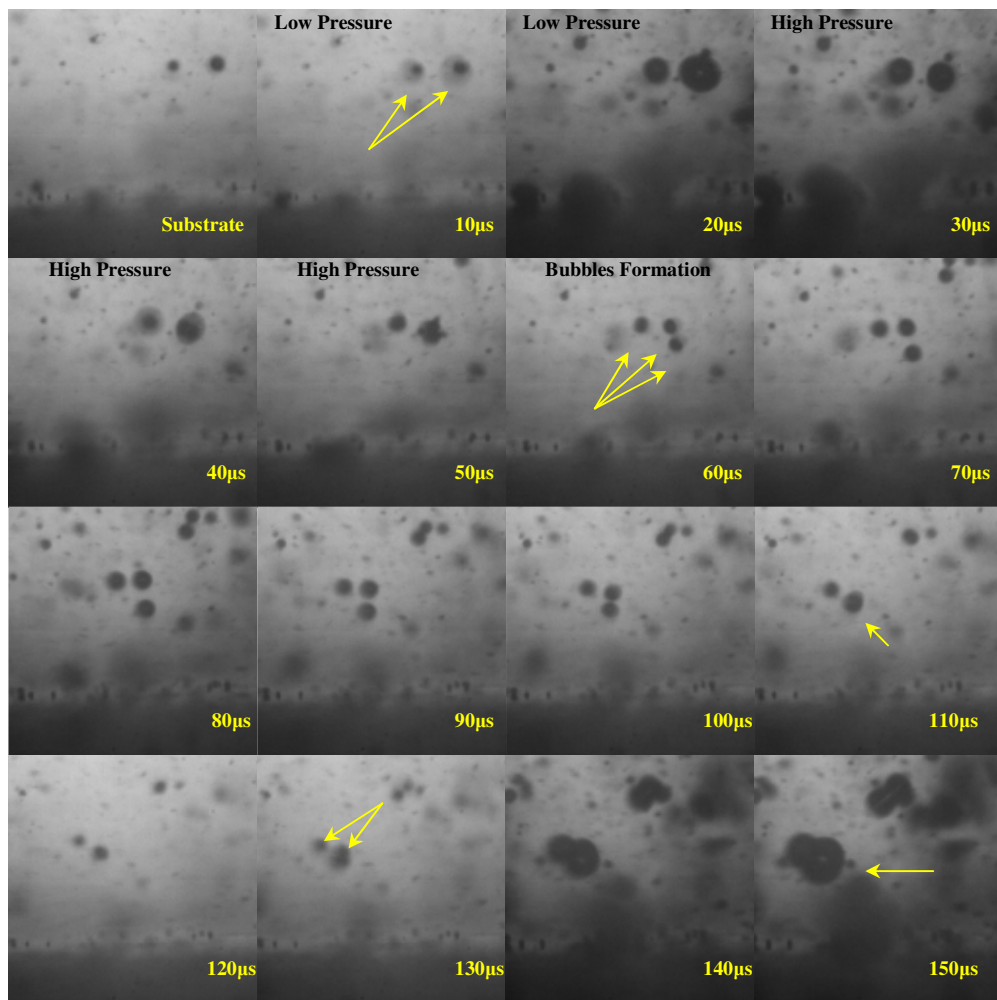


**Figure 118: The merging and splitting mechanisms of the water and the lubricant bubbles due to pressure variations. The frame size is  $0.5 \times 0.5 \text{ mm}$ .**

In the case of the refrigerant, the adjacent unstable bubbles, present a distorted shape leading to an increase of their volume and their size. Larger bubbles absorb the smaller ones. The tendency to merge is higher than in the other two liquids. Frame 7 in figure 119 captures how the detachment mechanism of the amoeboid shaped refrigerant bubbles is achieved (suck like effect). The adjacent bubbles are connected leading temporarily to an elongated bubbly shape prior to obtaining another amoeboid shape of a different size. The bubbles within the refrigerant solution have a more vigorous behaviour than in the other liquid mediums. The pressure variations generate the wobbling behaviour of the refrigerant bubbles affecting their movement. The bubbles appear to be electrified by a massive amount of energy, maintaining a higher state of wobbling movement. This is possibly related to the lower resistance (viscosity) of the refrigerant fluid allowing the bubbles more freedom of movement.

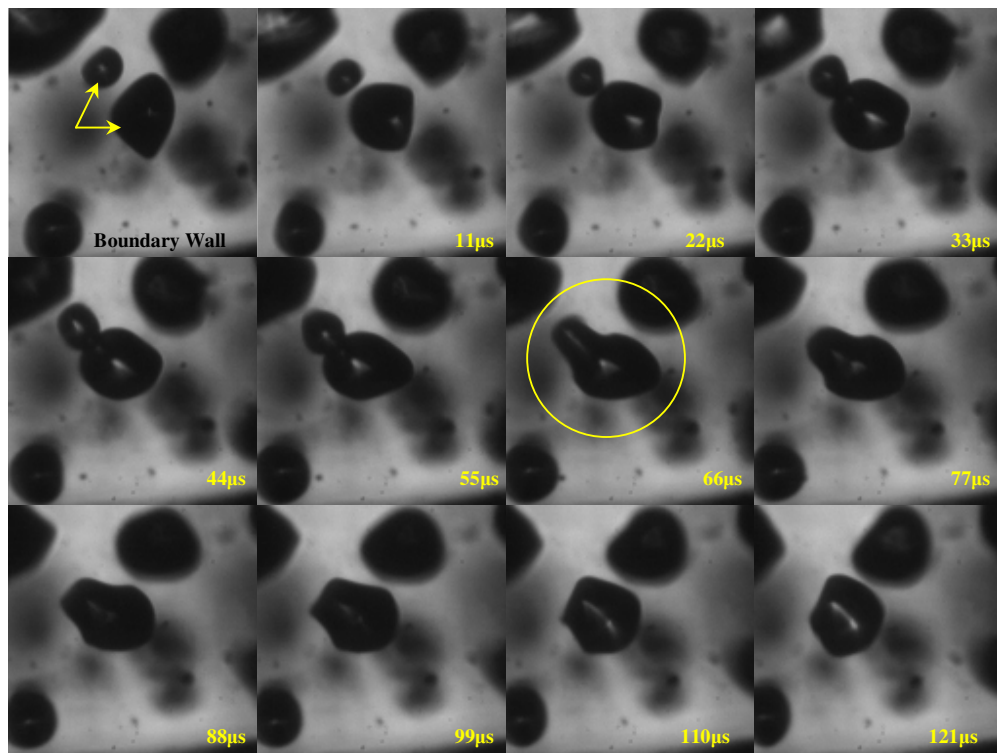


**Figure 119: The merging mechanisms- the so called suck like effect- of the refrigerant bubble. The larger bubble absorbs the adjacent bubble. The frame size is 0.5×0.5 mm.**

Observing the two different mechanisms of bubbles merging an interesting conclusion can be drawn. The merging mechanism of the lubricant and water bubbles maintains a spherical shape across the bubble periphery with a significant increment on the size. In the case of the refrigerant bubble, the bubbly round shape cannot be obtained while the size of the bubble after merging is further reduced. Additionally, a series of images shows the typical behaviour of the bubbles in correlation to the normalized distance before their final collapse onto the

solid boundary, figure 120. The normalized distance reduces as the bubble approaches the boundary wall. The normalised distance drops from a 6.9 value to 3.9 reaching the boundary wall, just before the bubble collapses for last time, at a value of 0.96. Implosions are observed in regular time steps (frames 4, 11, 16 in figure 120). The difference in the lubrication regime is that the layer of lubricant has to be penetrated by the micro-jet for surface damage to occur. Moreover the determinant of the refrigerant bubbles compared to the other bubbles during their descent onto the rigid wall is the absence of implosions.

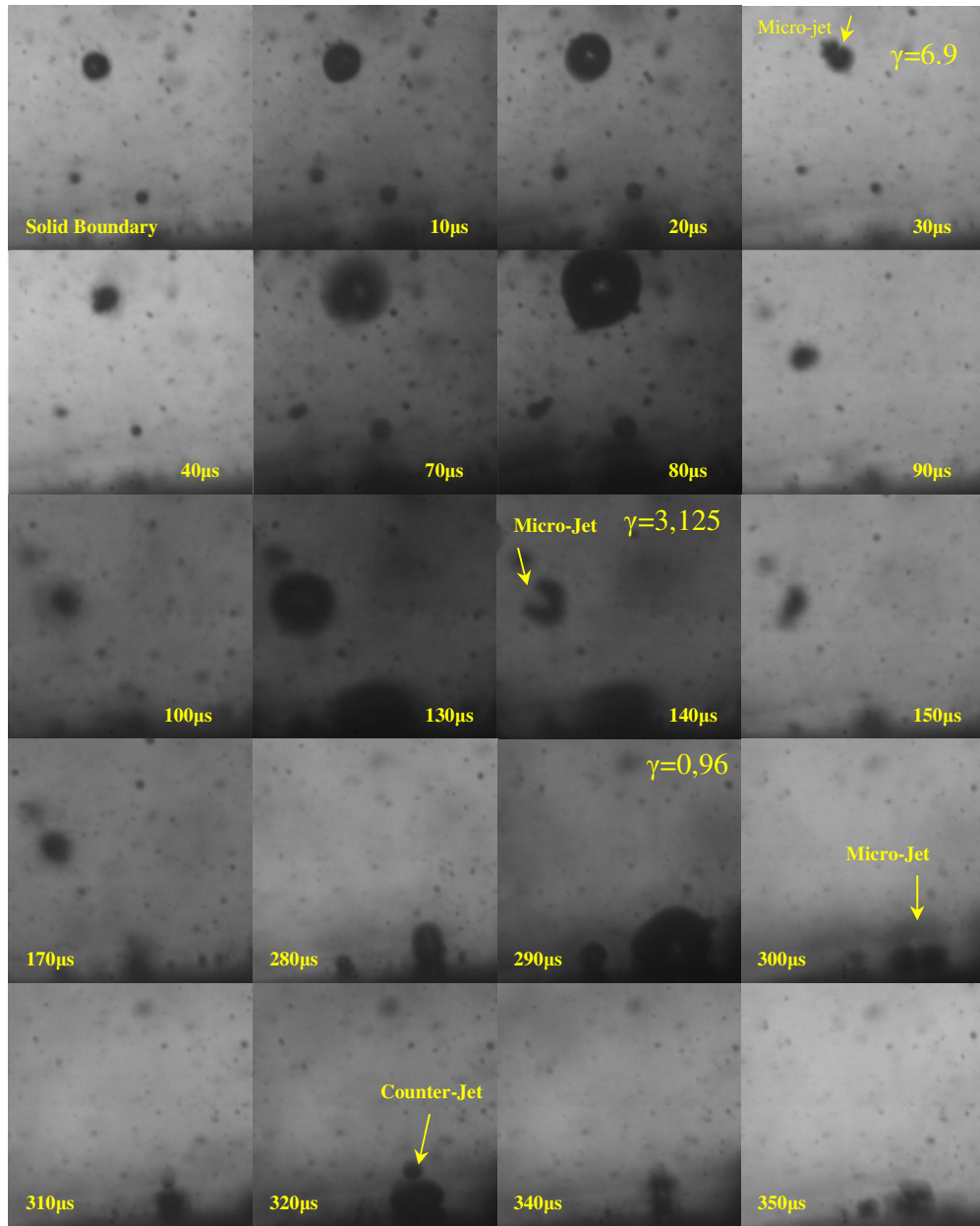


**Figure 120: Behaviour of an acoustic cavitation water bubble in correlation to the normalized distance as it approaches the rigid boundary. The frame size is 0.5×0.5 mm.**

### 6.2.1.3 Region near the solid surface boundary

The bubble implosion near the rigid boundary revealed three distinctive behaviours for each of the tested liquids respectively. Initially in the case of the distilled water, a typical behaviour of a cavitation bubble is described. The steps of the cavitation mechanism are presented in figure 121 since previous researchers have well explained the phenomenon [189-193].

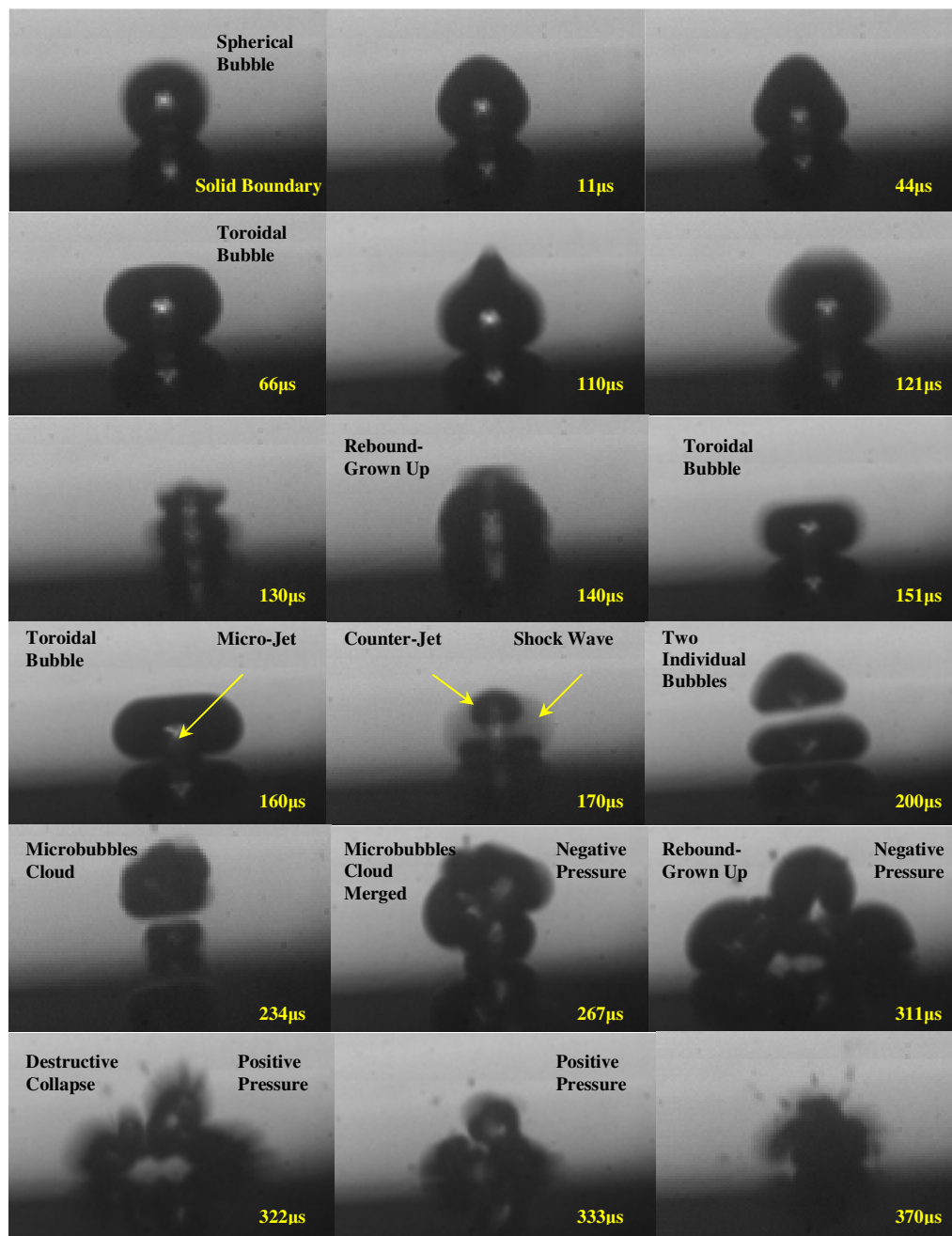
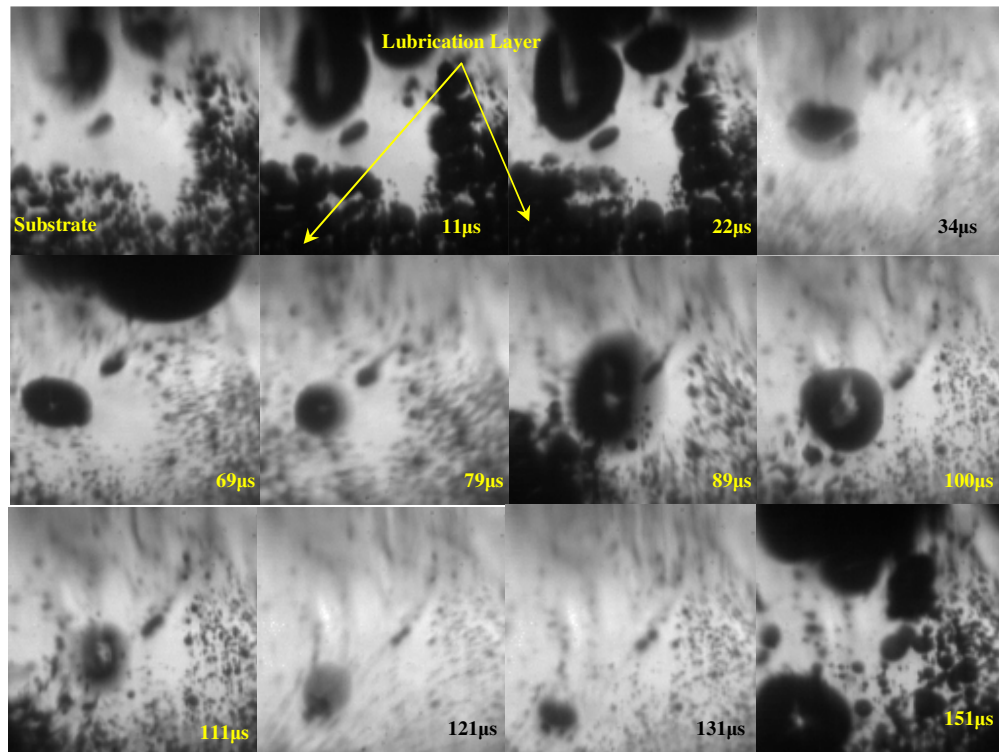


Figure 121: Characteristic collapse and rebound of an acoustic cavitation water bubble near the solid boundary. The frame size is 1×0.5 mm.

The life cycle of the bubble can be determined by the acoustic cycles. The bubble grows reaching its maximum diameter cycle and then collapses during one ultrasound cycle [190]. It can rebound instantly and this process can be repeated several times. The spherical bubble starts to deform because of the pressure variations as is shown (frames 1-3 in figure 121). Afterwards, as positive pressure prevails, the attractive Bjerknes forces deform the spherical bubble to a toroidal bubble as shown (frames 4-6 in figure 121) [194]. The third series of frames shows how the bubble deforms in a period of 30  $\mu\text{s}$  until it reaches the maximum toroidal diameter where the micro-jet is formed (frame 10 in figure 121) [132-133]. Then it collapses creating a very clear counter-jet [133], emitting a powerful shock wave (frame 11 in figure 121) [191-192]. Then the bubble becomes unstable and is separated into two individual small bubbles which in turn generate two micro-bubble clouds, the so-called splashing effect (frames 12-13 in figure 121) [193]. Thereafter the two clouds merge into one, growing in size until they finally collapse releasing a high velocity destructive impact to the boundary wall damaging eventually the material surface.



**Figure 122: Collapse of an acoustic cavitation lubricant bubble near the solid boundary. A lubrication layer is formed. The frame size is 0.5×0.5 mm.**

In the case of the lubricant, the bubbles have a similar behaviour to that of the water, figure 122. They were generated in low pressure areas and then they collapsed in regions where the pressure was higher, creating severe damage on the surface of the material. What was found

to be interesting is the lubrication layer which is generated during the cavitation process (frames 2-3, fig 122). The lubrication layer can affect the destructive impact of the collapse mechanism of the bubbles. It can protect the material surface by acting as a cushion, absorbing and reducing the impact of the implosion. Thus, despite the fact that the impact pressure from the lubricant bubbles is higher than in the water (paragraph 6.2.2), the actual damage should be considerably less (paragraph 6.3.2).

This it can be well observed in figure 123 where an isolated lubricant bubble is approaching the boundary wall. In all the frames of figure 123 the lubrication film thickness appears. During the destructive collapse of the cavitation bubble the lubrication film can effectively absorb the impact reducing the surface damage. The thin layer consists of small bubbles with a radius less than  $5\ \mu\text{m}$  as frame 3, in figure 124 reveals.

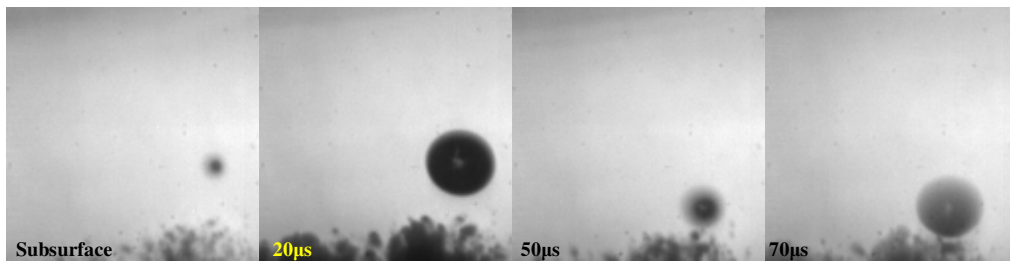


**Figure 123: Lubrication layer formed across the surface of the rigid boundary, prior to bubble's implosion. The frame size is  $0.5 \times 0.5\ \text{mm}$ .**

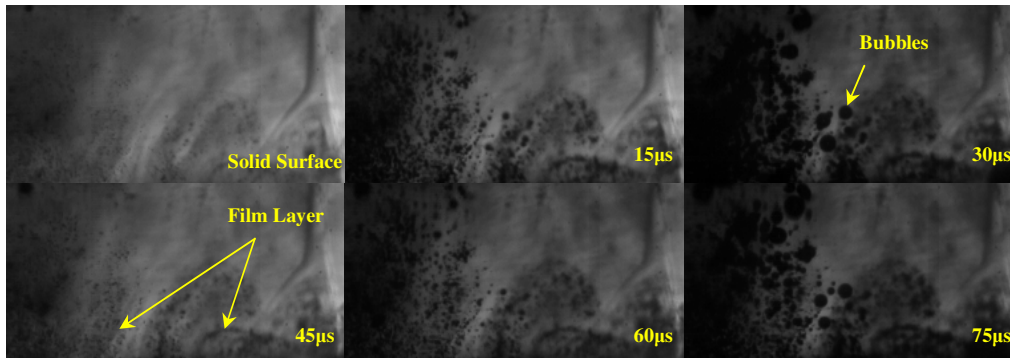


**Figure 124: The extended lubrication layer across the surface of the rigid boundary. The frame size is  $1 \times 0.5\ \text{mm}$ .**

When refrigerant was used, bubbles had a remarkable behaviour while approaching the surface of the chromium steel, figures 125 and 126. The refrigerant bubbles sustain a seemingly random movement in a continuous oscillatory motion without imploding. A ceaseless wobbling effect was also noted. Most of the refrigerant bubbles wobble instead of collapsing. Eventually the refrigerant bubbles obtained an amoeboid shape. This incredible

performance significantly increases their lifecycle reducing the probability of a destructive impact. The bubbles, instead of growing and collapsing in regular time steps as normal cavitation bubbles, are driven by this wobbling behaviour for a prolonged period of time prior to their collapse.

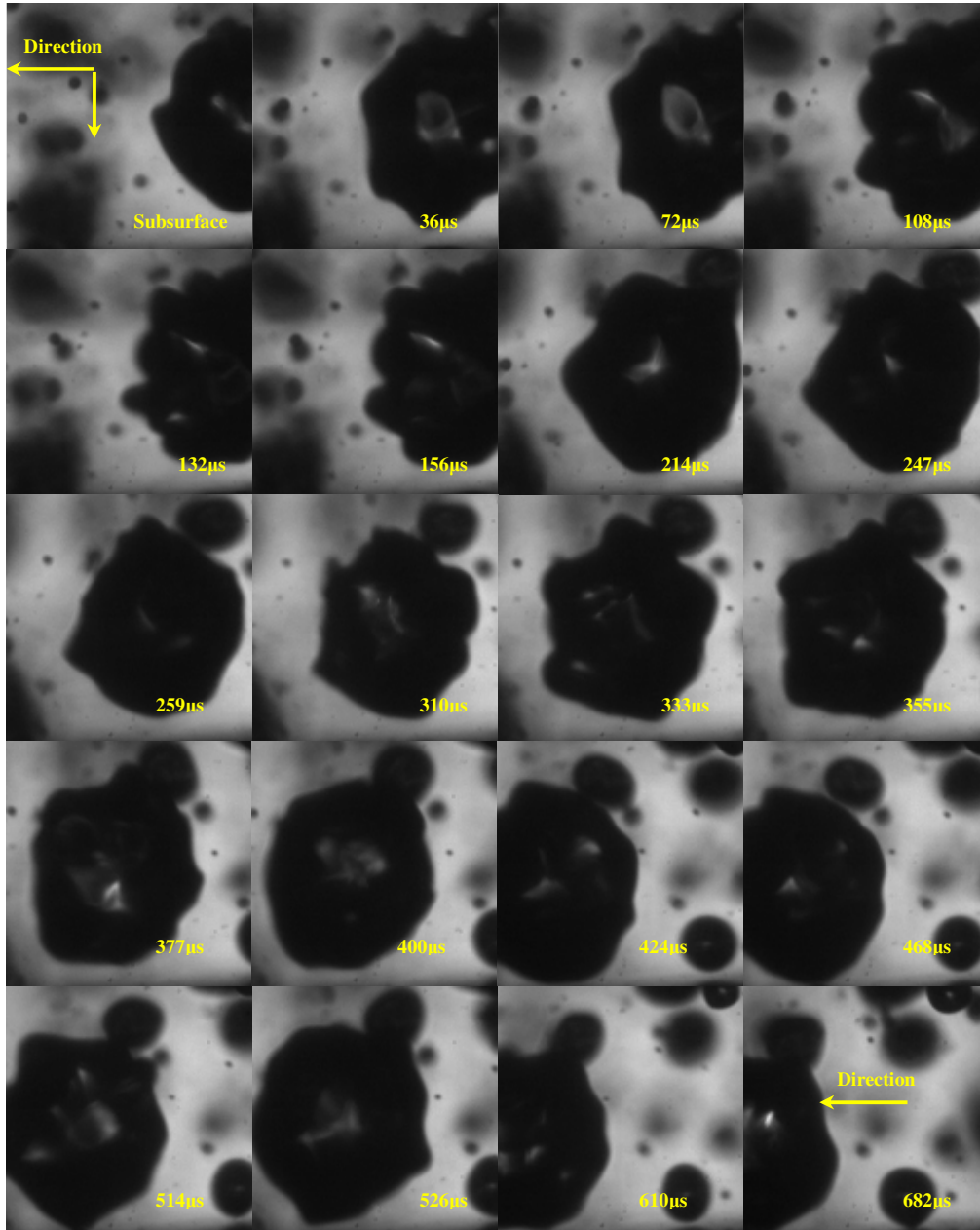


**Figure 125: The ceaselessly wobbling movement of an acoustic cavitation refrigerant bubble near the solid boundary. The frame size is 0.5×0.5 mm.**

Typical results in figure 125 show the journey the refrigerant bubble follows prior to its collapse. After reached the maximum size, the refrigerant bubble follows an oscillating

motion instead of starting the collapse process, until gradually escaping from the image. It is clear that even after 700  $\mu\text{s}$  the time where the bubble leaves the image, the size of the bubble remains the same and there is a total absence of implosions. However the shape slightly changes to similar amoeboid forms. By contrast, in the other two environments, as the figures 120-122 revealed, the cavitation bubbles under this prolonged time period had already collapsed.

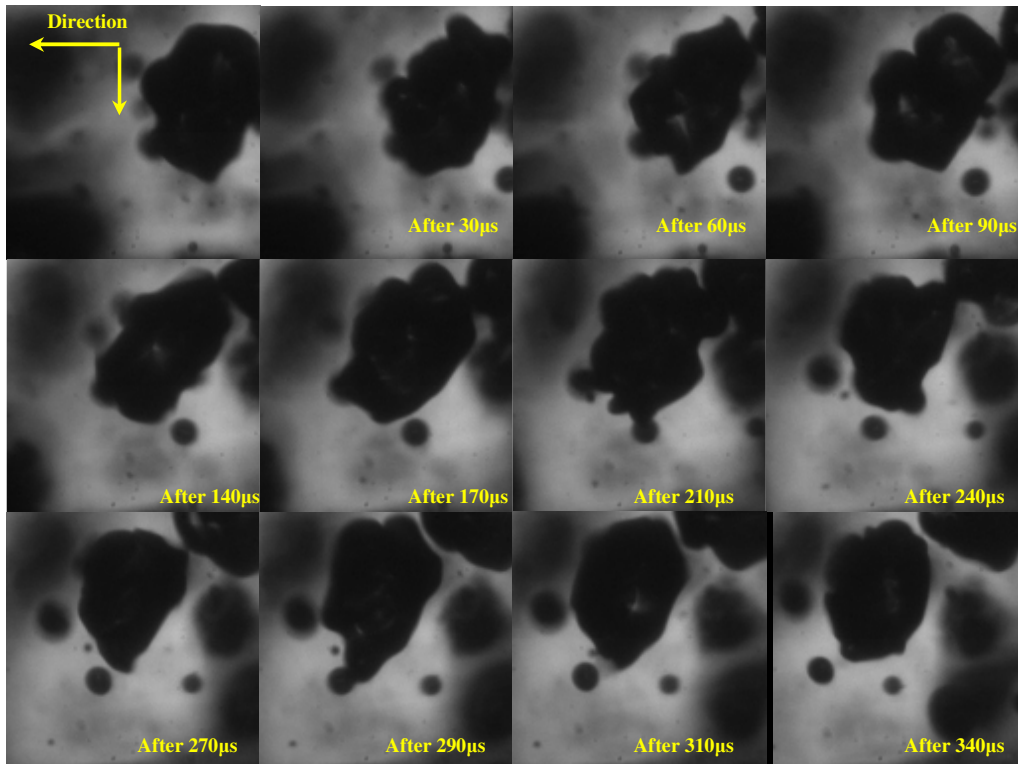


**Figure 126: The different shapes the cavitation refrigerant bubble obtains in its maximum radius. The frame size is 0.5×0.5 mm.**

Figure 126 captures another refrigerant bubble with more distinct phases of an amoeboid formation. Immediately after the bubble attained its maximum size it moved from one side of the image to the other without collapsing. Interestingly, in frame 4 a separation procedure mechanism appears. However, the attraction forces of the bubble restrain this phenomenon keeping the bubble in a robust single shape. Then, in frame 8 the bubble obtains a round amoeboid shape and is subsequently elongated, reaching its maximum length in frame 10. Surprisingly instead of collapsing it returns to a bubbly round shape.

The interaction of the surface tension and the viscosity forces of the refrigerant liquid can explain the behaviour of the refrigerant cavitation bubbles. It has been reported in previous

studies that viscous forces giving rise to perturbations tend to abet the breakup of the cavitation bubbles while surface tension tends to prevent bubbles from collapsing [191]. In the present study the refrigerant has a substantially lower surface tension and viscosity than the water and the lubricant (table 6). The implosion frequency of the refrigerant bubbles is not as consistent as with the other two liquids. Thus, it seems that in the case of the refrigerant, surface tension forces prevail, the viscous forces maintaining a bubbly wobbling pattern among the cavities preventing them separating and collapsing. The opposite phenomenon was observed within the water and lubricant solutions, as the viscous forces prevail, leading the bubbles to consecutive oscillations, separating the bubble body into smaller cavities. This in turn generates regular implosions among the bubbles.

The actual surface tension and viscosity values of the tested fluids indicate this remarkable behaviour. The refrigerant has the highest surface tension/viscosity ratio overall (table 6), implying a higher resistance to the bubble collapsing mechanism. The above behaviour also enhances the probability of the refrigerant bubbles to get connected in a cloudy shape as presented in paragraph 6.2.1.1.

A similar behaviour was also noted by Schneider et al [195] in his latest study, using another type of refrigerant flowing in micro-channels, where the bubbly flow morphology of low surface tension liquid in a fully developed hydrodynamic cavitating flow was highlighted. Similar results were also found by Mishra et al [196] in his recent work using de-ionised water with substantially higher surface tension and viscosity values to the refrigerant solutions. Mishra showed the disturbances the body of a water bubble experiences and the tendency of the bubble to implode during the cavitation process.

## **6.2.2 Results Analysis**

In the comparison graphs, in figures 127-129, in order for a representative bubble analysis to be conducted, a cavitation bubble of the same diameter range was chosen to be recorded and evaluated in all the liquid environments.

Figure 127 presents the fluctuations of the bubble radius as a function of time for each of the liquids respectively. Lubricant and water bubbles after their first implosion take the rebound by re-forming in a smaller size. Then they implode again and reform. At the level of the boundary wall they reach their maximum size before the final collapse. The refrigerant bubbles keep a linear fluctuation behaviour on their size. Their radius is not significantly

altered since the wobbling behaviour prevails. The only implosion is observed at the level of the boundary wall where the refrigerant bubble obtains its maximum bubble size.

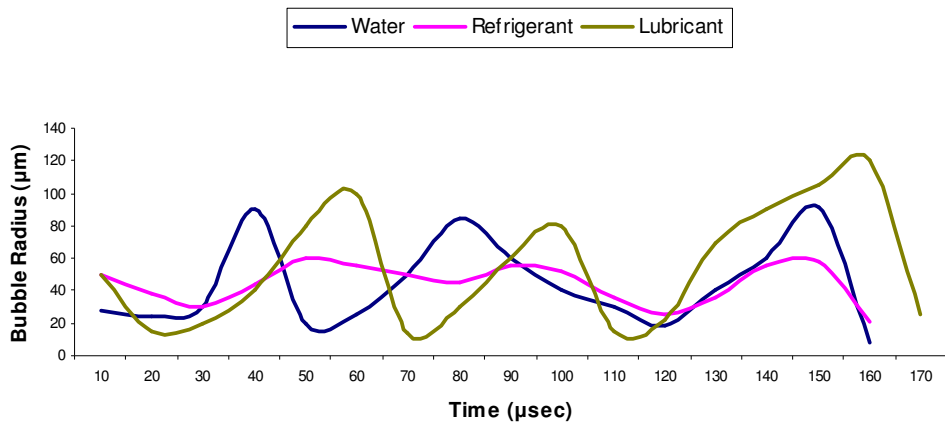


Figure 127: Variation of cavitation bubbles radius as a function of time

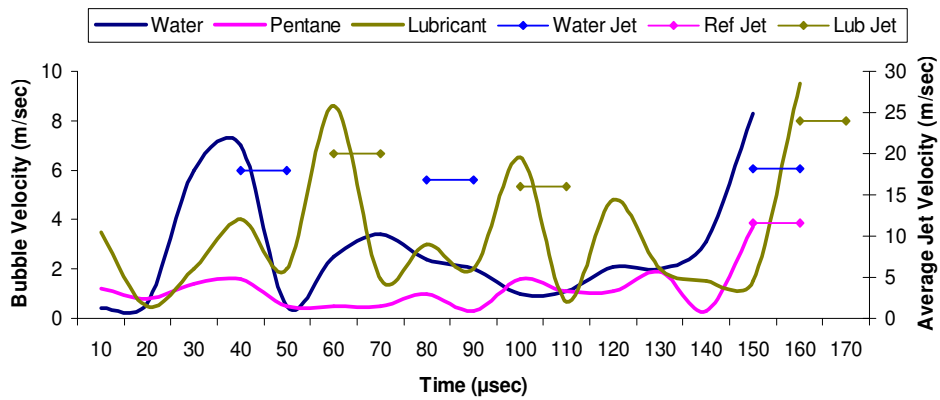


Figure 128: Variation of bubble velocity and the jet velocity versus time

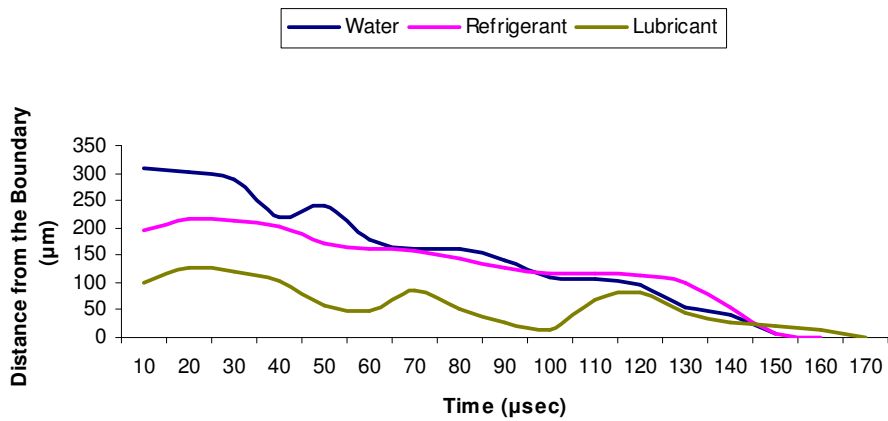


Figure 129: Variation of the bubble distance approaching the boundary wall

Figure 128 shows the bubble velocity and the average jet velocity during the descent of the bubbles to the boundary wall. The bubble velocity was calculated during the expansion and the shrinkage mode of the bubbles prior to their final collapse onto the solid boundary. The average jet velocity is estimated by the assumption that the jet flow develops during the shrinkage of the bubble from its maximum radius (equation 37). Lubricant and water bubbles show significant alterations in their velocity following their radius fluctuation patterns.

The lubricant bubbles achieve by far the highest bubble and jet velocity. The refrigerant bubble implodes only once having the lowest jet velocity of the tested bubbles. This happens only close to the boundary wall. In addition, the refrigerant bubble keeps a constant velocity during its entire route reaching its maximum speed just before the implosion with the solid surface. The velocity achieved by refrigerant bubbles has the lowest impact potential.

Figure 129 shows the variation of boundary distance over time as each of the bubbles approaches the boundary wall. The water bubble, according to the inclination of the graph, has the fastest descent to the solid surface followed by the refrigerant and the lubricant bubbles. The viscosity in the lubricant liquid is higher than the other liquids, decelerating the movement of the bubbles. Apparently, the refrigerant bubble having the lowest viscosity cannot achieve the fastest movement. The absence of oscillations in correlation with the wobbling effect, highly affect the bubble's motion reducing its velocity inside the liquid refrigerant.

It is reasonable to report that the combination of the surface tension and the viscosity properties (table 6) of the bubbles affect the cavitation mechanism. The bubbles produced in the refrigerant environment with the lowest surface tension had the largest size among the bubbles while their collapsing time was the lowest reducing the risk of damaging the material to a minimum extent. Thus the probability of damaging the surface by consecutive destructive implosion impacts is unlikely to happen in the refrigerant environment. The results are in good agreement with Liu's et al [130] and Benhia's study [128] which found that the bubble tends to grow larger in lower surface tension and viscosity solutions reducing the collapse duration time.

In regards to viscosity, a theoretical correlation between the viscosity and the jet velocity can be determined. The bubble and jet velocity increases as the viscosity increases. Thus the maximum impact pressure can be found within the lubricant bubbles since the lubricant has the highest viscosity among the tested fluids. However, in practise this cannot be applied since the lubrication layer which was formed across the surface of the chromium steel plays

the role of cushioning the jet impact. Hence, the actual impact damage will not be so severe in comparison with the corresponding jet velocity generated by the bubbles and estimated by the high speed camera images. The results are in agreement with Meged's study [127] since no direct correlation between the viscosity and the impact potential of the bubbles was drawn.

Figures 130 and 131 illustrate the average jet velocity and the bubble energy as a function of the normalized distance when the bubble approaches the wall boundary. The bubble energy (equation 38) was calculated assuming that the radius correlates to a spherical representative shape for all the testing liquids respectively. In all the liquids when  $\gamma$  (figure 8) moves toward the normalized distance of one, the average jet velocity and the bubble energy reach their highest value. At this point the lubricant bubble acquires its highest average velocity jet and energy compared to the other testing liquids. Interestingly the refrigerant bubble implodes only once. This happens only close to the boundary wall.

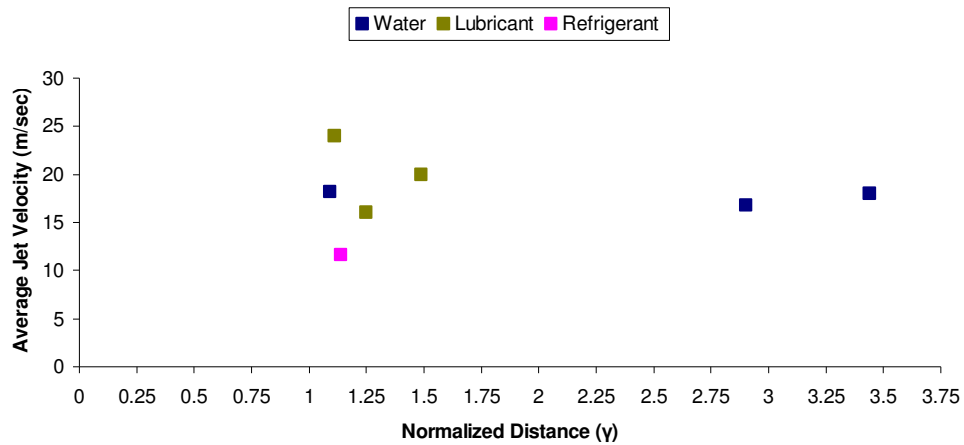


Figure 130: Average jet velocity of the cavitation bubbles as a function of normalized distance.

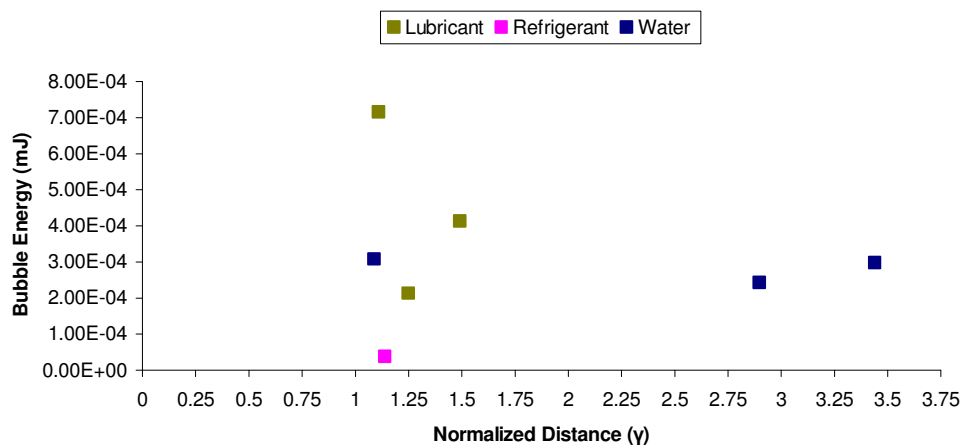
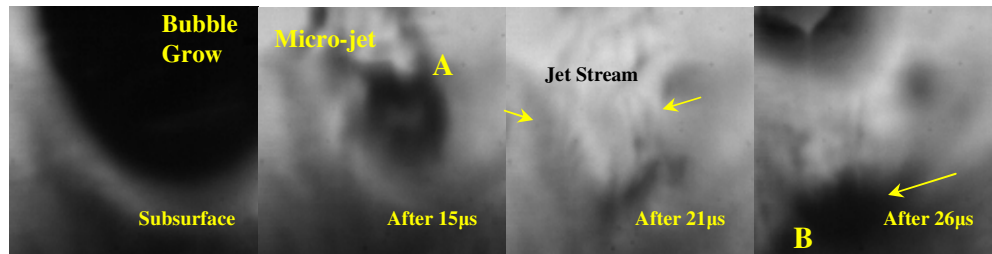


Figure 131: Energy of the cavitation bubbles as a function of normalized distance.

Finally, table 12 shows the impact pressure of the bubbles striking the material surface (equations 35-36). The micro-jet velocity during the implosion of a bubble was recorded by the high speed camera and evaluated using the camera software observations, figure 132. The results reveal that the highest impact pressure can be developed in the lubricant environment. Refrigerant bubbles have the minimum impact pressure and cause the least damage on the material surface. The results indicate that in viscous liquids the impact effects of the collapse of cavities are stronger than collapse in less viscous liquids. This is in agreement with the ultrasound theory [197].

Moreover the acoustic power produced by the ultrasonic transducer agrees with the above outcomes. The probe of the ultrasonic transducer was submerged into the fluids in order to keep the same operational amplitude for all the testing liquids it had to consume different amount of energy in each of the fluids respectively. The lubricant obtained the maximum acoustic power producing the most powerful cavitation bubbles.



**Figure 132: Characteristic implosion of the lubricant bubble from point A to point B. Jet fluid velocity was calculated to be 150 m/sec. Frame size is 1.025x1.025 mm.**

Fluid	Water	Refrigerant	Lubricant
Average Micro-jet Velocity (m/sec)	95	60	140
Impact Pressure (MPa)	140	40	236
Ultrasonic Transducer Acoustic Power (Watt)	6	3	9

**Table 12: Calculated average micro-jet velocity and impact pressure of the experimental fluids.**

Unfortunately no experimental data on the refrigerant and lubricant bubbles relating to their velocity and impact attributes are available in literature. The impact pressure and jet velocity results for water environment are in agreement with results from previous studies [117-118], [136], [145].

### **6.3 Incubation Stage-Pits Analysis**

The incubation time is a critical period for cavitation augmentation. Specifically, the formation of cavities in a scroll expander system enhances the probability of creating severe damage in its main components while its performance can be significantly reduced.

At the implosion spots of the material surface, inception of cavitation pits, cracks and grooves occur. Upon further excitation the pits are joining together causing loss of mass. The mass loss contributes to a change of geometry causing changes to the local flow conditions accelerating the erosion. The cavitation pits attract the bubbles' implosion, rapidly increasing in size. The growth of cavitation pits is caused largely by the linking up of nearby pits or cracks. Their enlargement into craters is a time and history dependent process. The craters can seriously affect the performance of the system increasing its leakage points and reducing its efficiency. Thus, the prevention of cavitation erosion pits during the early stages of a process can prove vital and essential for the lifecycle of the system.

#### **6.3.1 Test Methodology**

The inception time of the cavitation pits, was a critical parameter for this bunch of tests. On one hand the time duration had to be kept as short as possible to prevent liquids from increasing their internal temperature. On the other hand time duration had to be sufficient to enable pits formation. Thus a balance had to be achieved between these parameters.

Testing time was selected at 10 minutes, in order to prevent the temperature of the tested fluids from rising more than two to three degrees during the cavitation process. The liquids' temperature was constantly measured (every minute) with a laser digital thermometer. Furthermore, the amount of the isolated incubation pits formed on the surface of steel samples, after 10 minutes of experimental process, was adequate for a thorough analysis and interpretation.

Initially, measurements were carried out using only the actual steel plate of the scroll in all the three environments. Consequently, the impact pressure by the bubbles' implosion was thoroughly analysed and effectively correlated with the damage produced by the erosion pits on the scroll's steel plate surface. Thereinafter, three different types of industrial market steels were used in order that their durability performance against the formation of erosion pits could be compared with that of the actual steel plate of the scroll.

### 6.3.2 Experimental Results

Initially, the behaviour of the tested liquids to cavitation phenomena is analysed in an indirect way. The impact by the cavitation bubbles is evaluated measuring the morphology of the cavitation pits. Thus, the more severe the pits the more destructive the impact by the bubbles. Then the experimental results were compared to the camera results and a coherent interpretation of the liquids performance was conducted.

The figure 133 below shows the inception of the erosion pits at the centre of the test sample, after 10 minutes of ultrasonic power. The number of pits formed by lubricant bubble implosion were fewer compared to the refrigerant ones for the same period of time. In addition, the size of the pits in both liquids is very tiny with a maximum average value of a few micrometers, as it will be later analysed in detail.

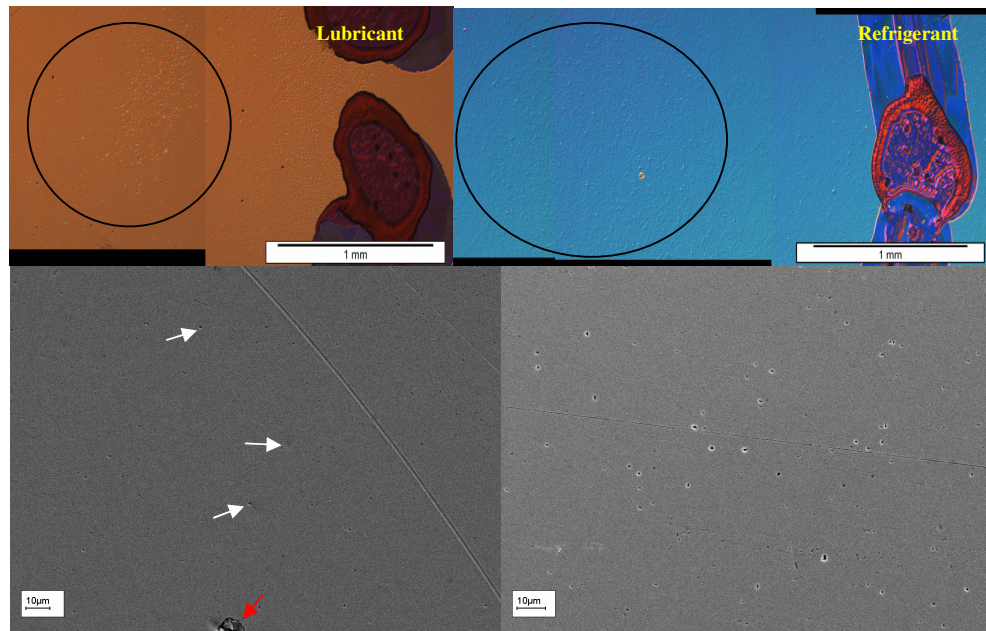


**Figure 133: Cluster of cavities formation on steel plate surface after 10 minutes of testing. Optical micrographs showing the cavities formation: in lubricant and refrigerant environment. High magnification SEM micrographs showing the cavitation pits formed in these areas.**

In terms of the lubricant, the small size of the pits (white arrows) is mainly due to the implosion of the tiny bubbles which comprise the lubrication film thickness. In addition, as the lubrication layer cushions or restricts the penetration of the jet-impact by larger bubble implosion, the camera images revealed, that the size of the erosion pits is further minimized. However, some pits generated in the lubricant environment had a very destructive impact, initiating deep cracks (red arrow) on the sample's surface. This can be interpreted by the fact

that the impact pressure by the lubricant bubble was measured to be the highest among the tested fluids paragraph 6.2.2. Thus a strike away or through the film thickness can generate destructive pits. By contrast, the erosion pits generated in the refrigerant solution were denser although very shallow. These results clearly depict the low impact pressure the refrigerant bubbles have due to their remarkable bubbly behaviour.

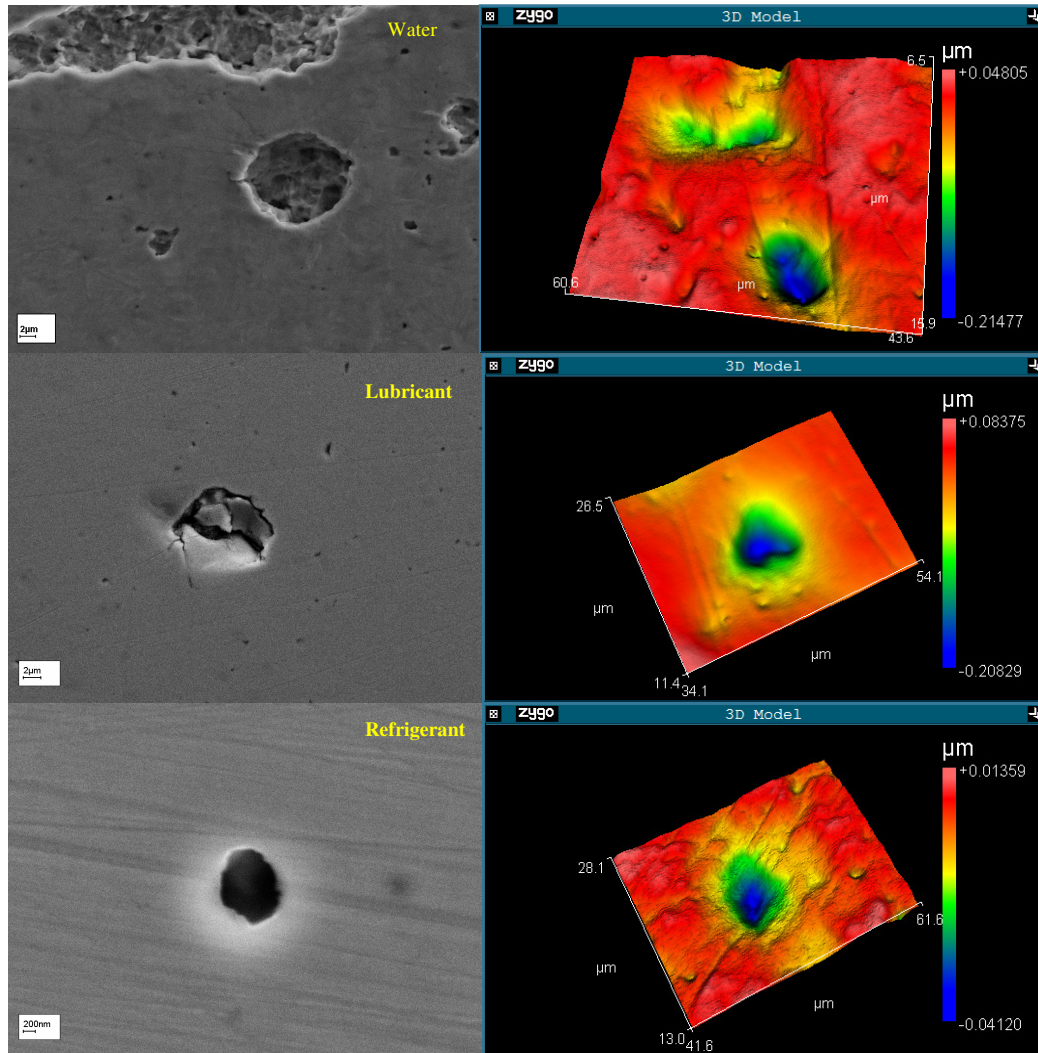


**Figure 134: SEM and high magnification ZYGO micrographs showing a typical cavitation erosion pit formed in water, lubricant and refrigerant solution.**

A close-up of the erosion pits are shown in figure 134. A typical destructive cavitation pit, produced in water, lubricant and refrigerant environment is presented. The SEM image clearly illustrates the nature of the pit and its shape. The depth is close to the average typical depth produced by a bubble's impact in all the liquid environments. The size of the pits, as the SEM images reveal, is similar in the water and lubricant environment at around 0.2 µm deep and substantially smaller and more superficial in the liquid refrigerant at around 0.04 µm. The

cavitation pits produced by refrigerant bubble implosion are very shallow and cannot be considered as destructive for the material surface. Thus, the determinant between the different types of erosion pits according to their liquid environments is their depth level.

In regards to the performance of the steels, during the incubation period, interesting outcomes were drawn. The tests were performed in a distilled water environment since in this time step the analysis focused on the mechanical performance of the steel materials and their durability behaviour against the formation of erosion pits. At the very early stages of the cavitation process, the impact energy released during cavity collapse on the surface is absorbed without any material deformation. Then, plastic deformation occurs which propagates into the grain boundary of the material displacing the grain's structure. Subsequently, within the 10 minutes of the experimental process, cracks are initiated in the high carbon steel, martensitic lathings on the low carbon steel, thermal pits on the chromium steel while plastic deformation is very significant and cavitation pits are formed in all the steel samples.

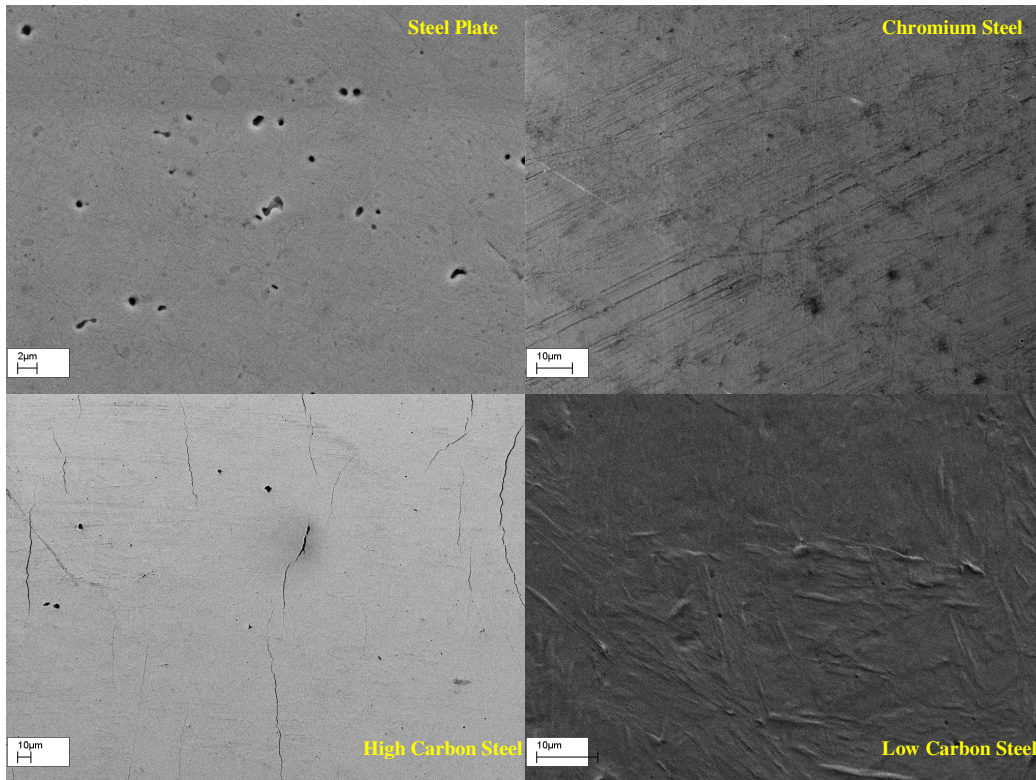


**Figure 135: SEM micrographs showing the deformation of the tested steel types after 10 minutes of exposure to cavitation in a water solution.**

The energy absorption without or with a minimum material damage is directly related to the resistance of the steel samples to cavitation erosion. The retained austenite which was found

in the high and low carbon steels can lead the material to a higher cavitation resistance (paragraph 2.11). This is due to the fact that the retained austenite can be transformed into fresh martensite ( $Fe\gamma$  BCC  $\rightarrow$   $Fe\alpha$  FCT) absorbing cavitation energy and hence could become more resistant to cavitation erosion. However, the cavitation erosion of the studied steels might also be reduced because of thermally softened effects [158-160]. In addition, the small amount of bainite found in the structure of the high carbon steel can improve its yield strength and toughness, increasing the exposure period to cavitation impact. On the other hand, the structure of the chromium steel consists of martensite and chromium carbides (extremely hard ceramic material). This combined structure network can significantly improve the durability and the cavitation resistance of the chromium steel storing higher amounts of energy than the high and low carbon steels. The steel plate of the scroll has a similar performance to that of the chromium steel since the spherical carbides and the martensitic structure can enhance its endurance improving its mechanical properties.

High magnification images of the damaged regions caused by cavitation impact are shown in figure 135. The scanning electron micrographs of the four tested steels exhibit differences in the eroded surface after 10 minutes of exposure to cavitation. The erosion pits are clearly depicted on the surface of the scroll's steel plate. They are sharp and broad, penetrating the substrate of the steel plate. Upon further testing, this eroded region would eventually contribute to substantial material loss. By contrast, on the chromium steel surface with a similar reinforced structure of chromium carbides ( $Cr_3C_2$ ), only limited plastic deformation pits were revealed. This is thought to be due to the large difference in their hardness and mechanical properties as will be seen in paragraph 6.4.2. At this stage the plastic pits formed on the chromium steel cannot be considered as a critical threshold for cavitation-erosion inception. However, using advanced optical microscope techniques in combination with appropriate polarizing filters some thermal pits were revealed on the chromium steel surface.

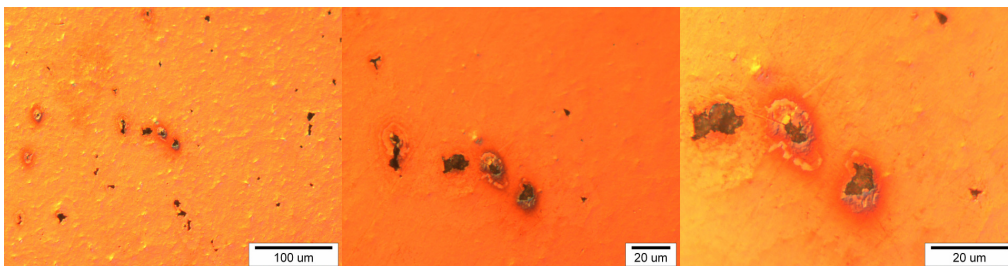


**Figure 136: Optical micrographs showing thermal pits formed on the surface of Chromium steel.**

The accumulation of thermal pits figure 136, can significantly affect the strength of the metal surface, making it more vulnerable to erosion damage. The appearance of the needle-like pit

in the centre of the cavity and the iridescent colour area around it indicates a thermal pit according to Haosheng et al and Wang et al [198-199]. In addition, it is well known that surface hardness reduction occurs in thermal influenced areas [145]. Therefore, a drop in hardness can seriously affect the cavitation erosion resistance of steel materials. Fewer in number and mainly isolated thermal pits were also observed on the high carbon steel surface. In the low carbon steel, there was an absence of thermal pits. The absence of thermal pits also indicates the percentage of carbon content within the steel structure since thermal pits are more likely to be formed in high carbon materials.

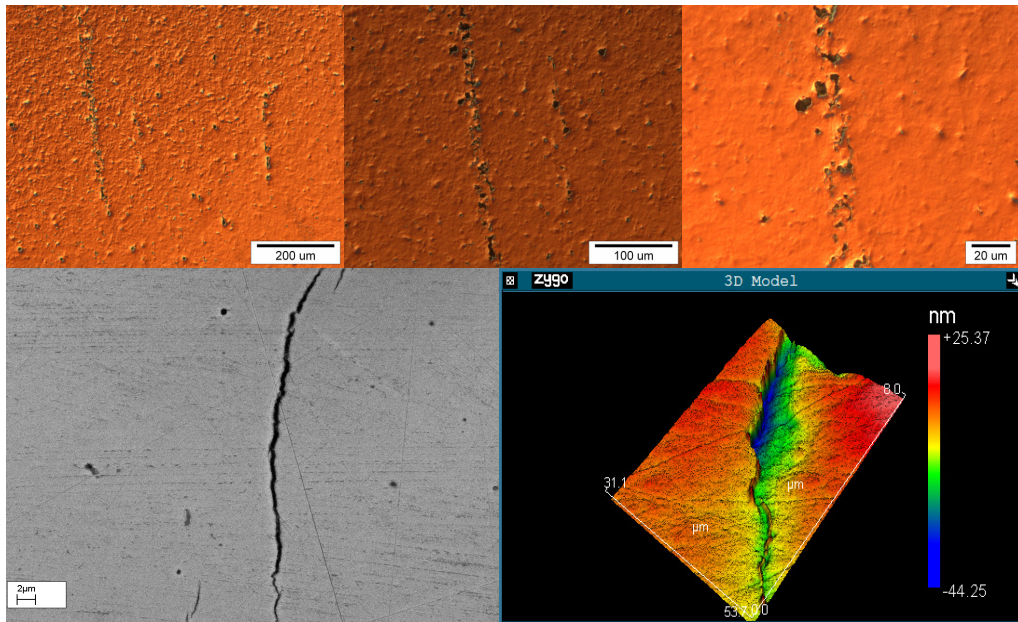


**Figure 137: Optical microscope images showing the accumulation of cavities along the cracks of the High Carbon steel. SEM micrograph shows the morphology of the crack. High magnification ZYGO interferometer image shows the step of the crack.**

On the through-hardened high carbon steel surface a lot of micro-cracks were also observed (figure 137) apart from the formation of the erosion and thermal pits,. The propagation and the growth of these micro-cracks can increase the erosion rate. Any preliminary surface defects such as cracks on the testing materials encourage cavitation by providing a favourable condition for a bubble nuclei to grow. Apparently, the presence of bainite makes the material stronger but more brittle. Thus, high carbon steel cannot withstand extreme impact pressure, as this results in cracking. At the level where impact stress builds up in the material structure due to the ultrasonic waves, the strain threshold increases and the accumulated potential energy is released as strain energy. This in turn causes intergranular fractures and micro-cracks are formed. Using the advanced software of the ZYGO interferometer the structure of these cracks was effectively analyzed. The depth of these micro-cracks rises to a few

nanometers while their length can be up to a few tenths of microns. These weaken areas are no longer able to withstand any further impact pressure by the bubble implosion and hence they get eroded much faster than the smooth adjacent surface.

The hypothesis of the formation of micro-cracks is probably related to the cutting process and the brittle crystalline structure of the sample. The cracks were initially generated as the cut off wheel was penetrating the steel ball. Many different options were used during the cutting process in order to avoid the formation of those cracks like changing the cutting speed, the feeding speed, the ball's condition (rotating or keeping it steady) but the results were the same. Many superficial cracks were hidden below the surface. Even inspection after sectioning the ball, with the maximum objectives of the SEM and ZYGO microscopes, did not detect their presence. Thus, the only way for these micro-cracks to come up on the surface was by the destructive impact of the cavitation bubbles, a similar mechanism to an earthquake.

In regards to the low carbon steel, the ultrasonic cavitation impact seems to create severe cavitation defects on the surface of the sample. The low carbon steel is case-hardened having a very hard and brittle surface layer (over 900 HV) which has been carburized. However as you approach the core the surface becomes softer. Under cyclic action of cavitation pulses degradation has developed along the entire surface of the steel. Dislocation movement occurs resulting to plastic deformation across the grain boundaries (figure 138 A-C). Cavities are formed by the stress concentration at a grain boundary junction when dislocations occur [200]. Simultaneously, thermal effects arise and plastic strains appear. The deformation of the surface layer is mainly restrained in martensite lathings, which in a later stage can cause delamination on the material's surface. Delamination weakens the mechanical properties of the material reducing its endurance.

The close up of these erosion lathings revealed some micro-tunnel pits on the top of the undulation surface (figure 138 B, white arrows) mixed with the localized plastic deformation pits (figure 138 B, red arrows). These micro-tunnel pits were initially identified on the surface of austenite steel by Krella et al [152], [201] in his latest work. However they have not been determined yet because of their tiny dimensions. Thus, using advanced metrology techniques with the ZYGO scanning interferometer this problem was overcome (figure 138 D-G). These micro-tunnel pits which are formed in the early stages of the cavitation process, trap small amounts of liquid and nuclei. Thus, they construct cavitation sources for bubbles inception. In addition, the morphology of the martensitic lathings in combination with the micro-tunnels in those weak regions can create severe grooves and cracks over a prolonged period of time.

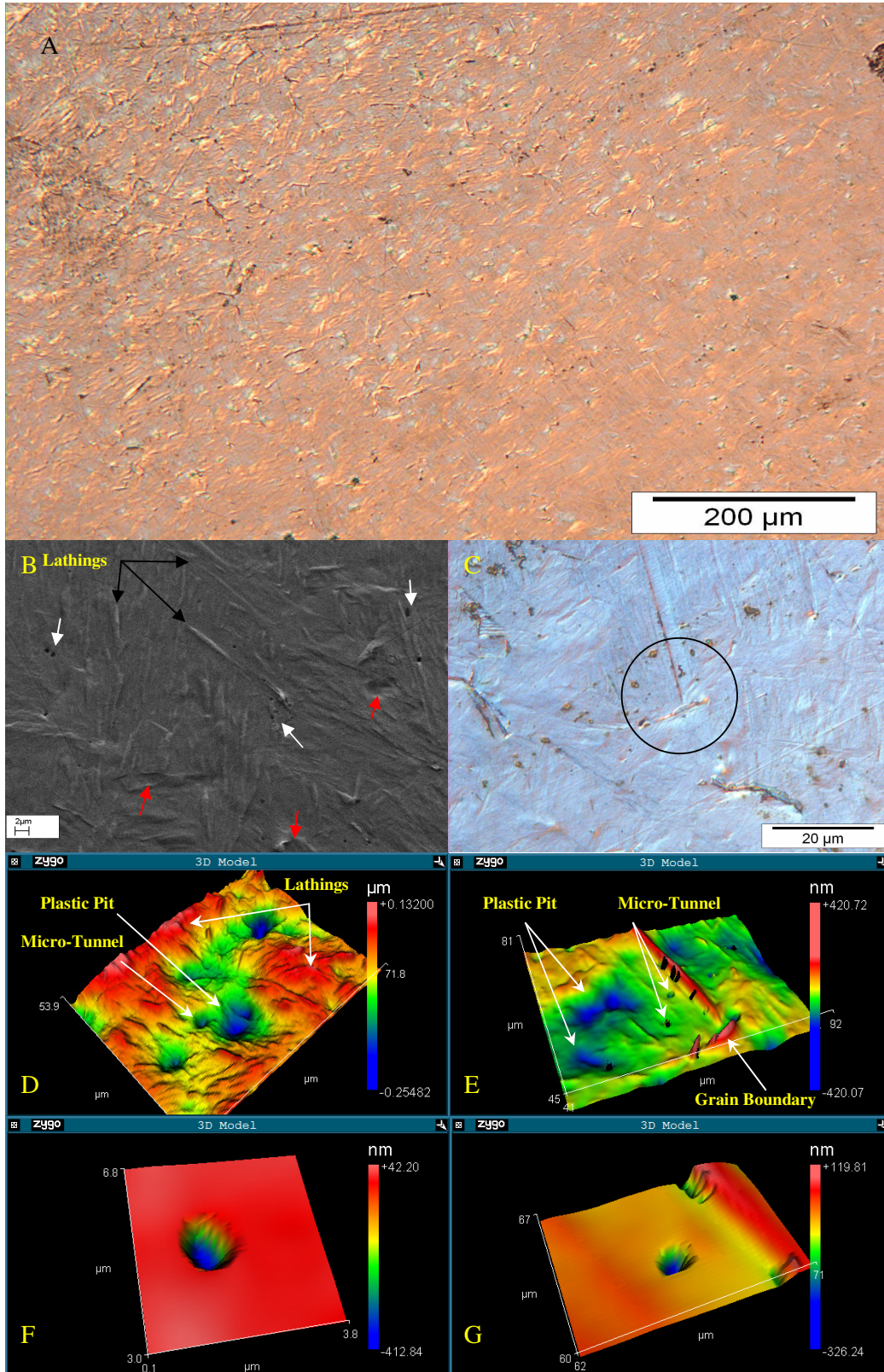


**Figure 138: Optical and SEM images of cavitation damage arisen on Low Carbon steel surface after 10 min of exposure to cavitation. A-C) Martensitic lathings and intergranular fracture revealed. ZYGO interferometer image shows a typical eroded area surface. D-G) Micro-tunnel and deformation pits are depicted.**

The radius of the micro-tunnel pits can vary from a couple of micrometers to a few nanometers (figure 138 F-G). Interestingly a thorough investigation in the cavity of these tunnels revealed their depth. The depth is around 0.4 microns which is slightly higher than the average depth of the erosion pits formed on the surface of the low carbon steel. The micro-tunnel pits which were produced by micro-jetting degradation can become sources for violent impacts in the substrate of the material. The implosion of the bubbles on the deep bottom of those pits can transfer a very intense shocking impact in the core of the substrate crystal structure of the material, accelerating its degradation rate. Thus, these tiny holes on the top of the martensitic lathings having a highly relevant depth can significantly reduce the steel's life time.

Surface scanning measurement techniques give precise details of the depth and the shape of the pits, the volume of material removed and the size of the eroded area of the cavitation pits. Thus, surface alterations due to cavitation erosion were effectively measured and the steel samples were properly evaluated, ranking their resistance to cavitation.

The following series of graphs shows the estimation of the typical and the maximum depth of the pits, volume loss and size of the eroded area around the pit. The typical values were produced taking the mean average values of the cavitation pits after thorough measurements of around 50 different pits in each material's surface. The maximum pits were produced by following a similar procedure taking the average maximum values of the pits in a sum of around 10 different pits for each sample.

In figure 139 the typical and maximum depth of the cavitation pits against the tested steel samples in the three liquid environments is shown. The water cavitation bubbles have the strongest impact on the samples' surface creating the deepest pits among the liquid environments. The lubricant bubbles, with the highest micro-jet and impact pressure, as the camera observations earlier revealed (paragraph 6.2.2), produce smaller in depth pits than the water bubbles but substantially higher compared to the refrigerant bubbles. This result can be well interpreted by the fluid film thickness which absorbs the jet impact and was recorded by the high speed camera during the collapse of the lubricant bubbles in the vicinity of the steel surface.

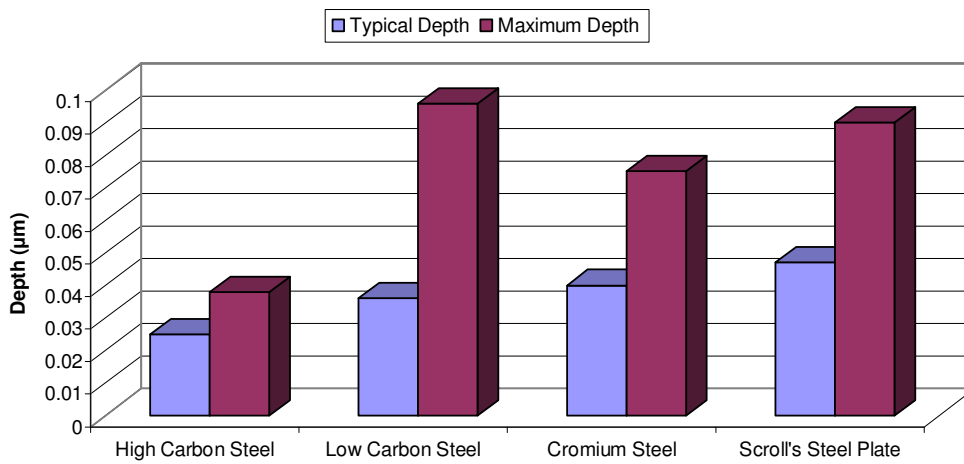
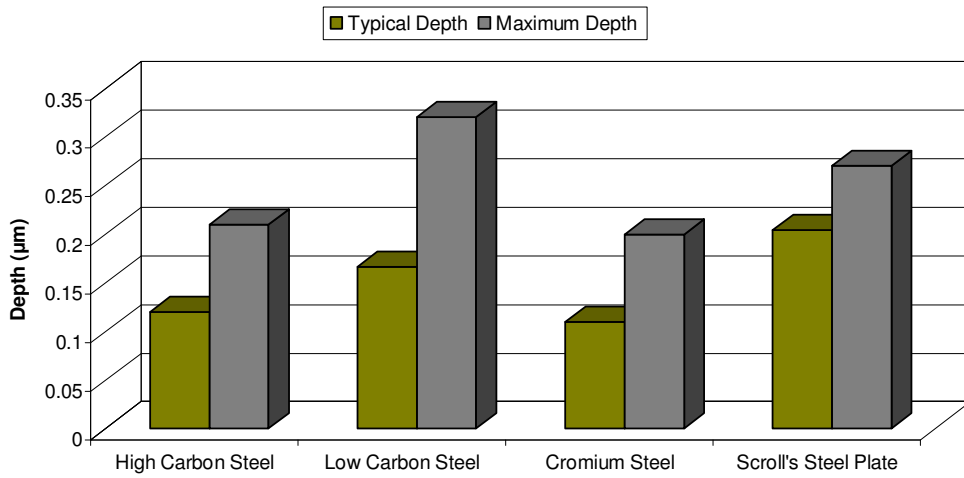
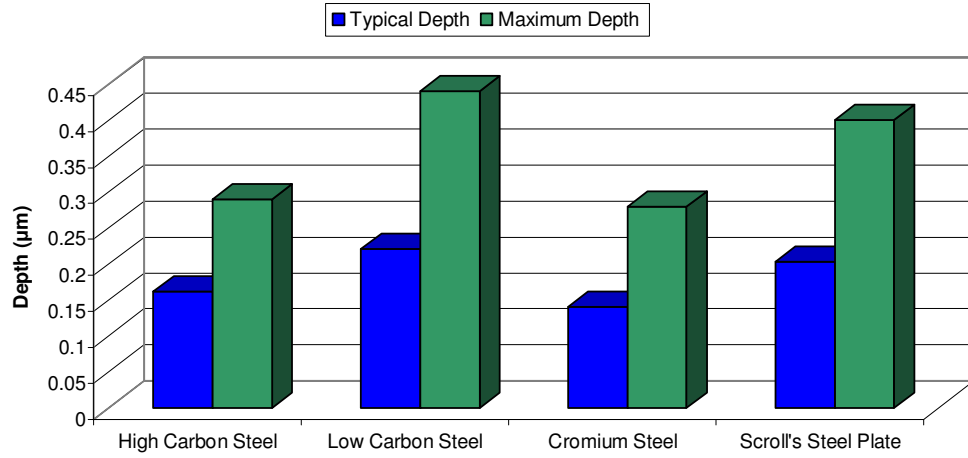


**Figure 139: Comparison of the average typical and maximum depth of the cavitation pits in a) water b) lubricant c) refrigerant environments**

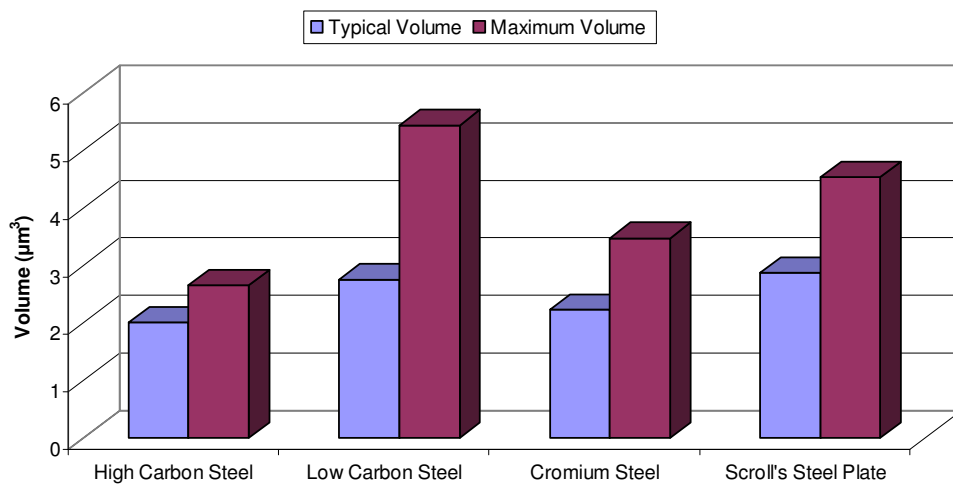
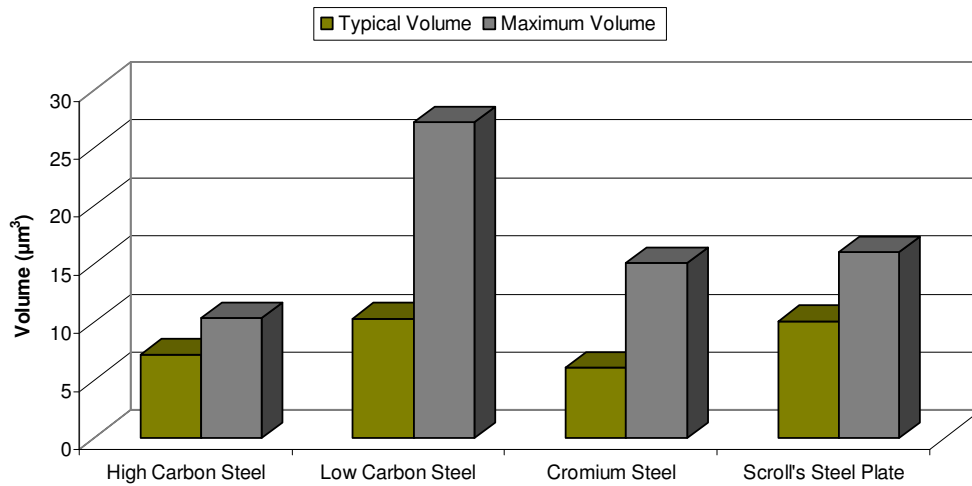
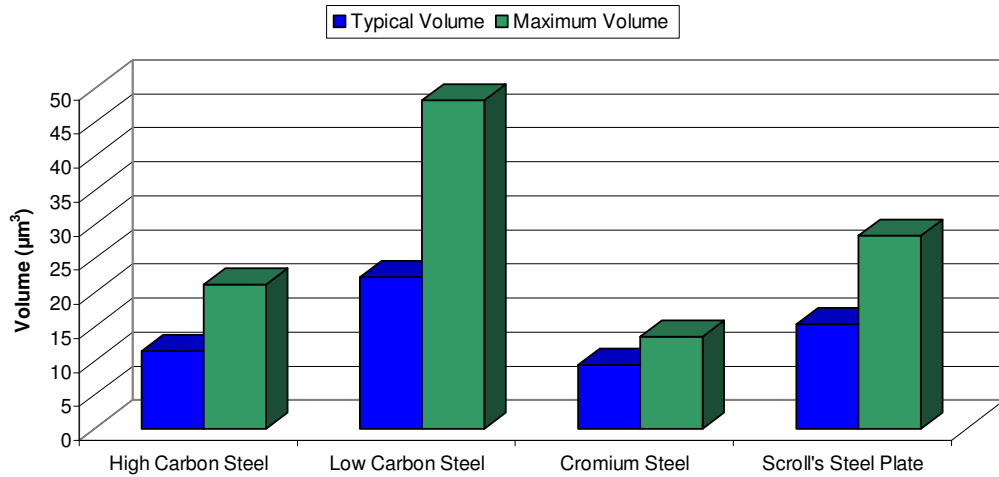


**Figure 140: Comparison of the average typical and maximum volume removed of the cavitation pits in a) water b) lubricant c) refrigerant environments**

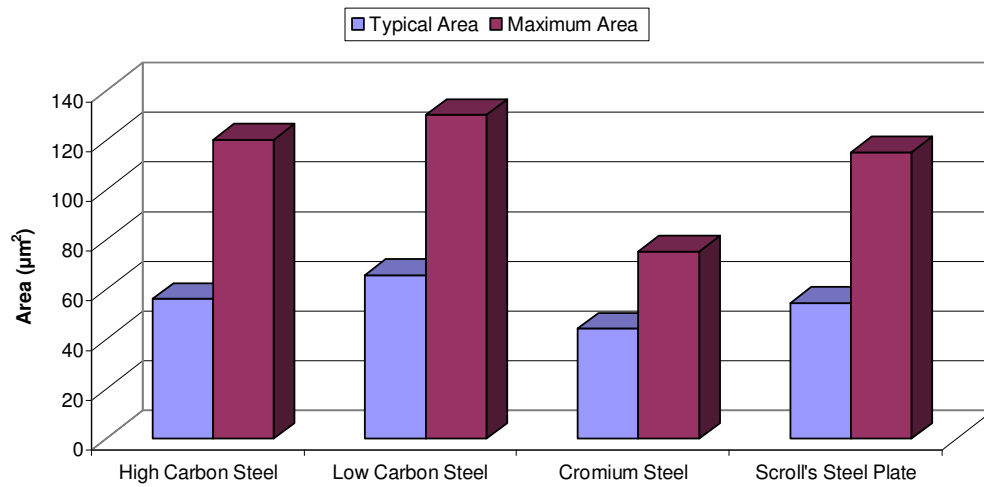
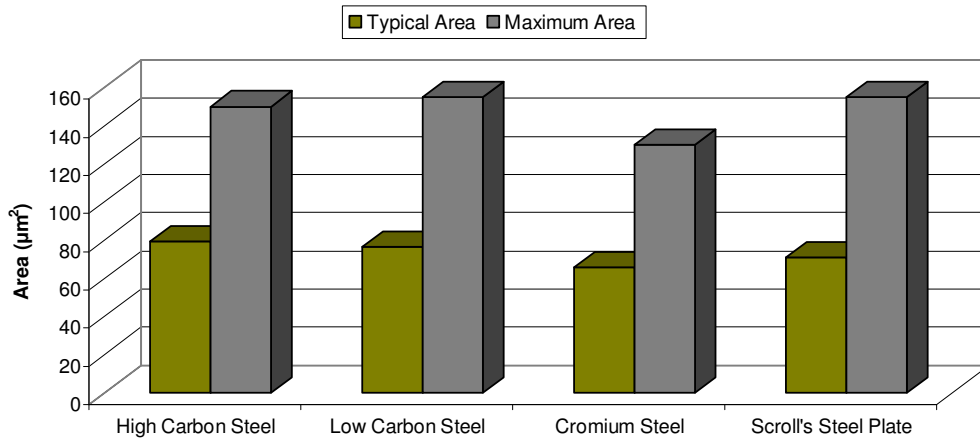
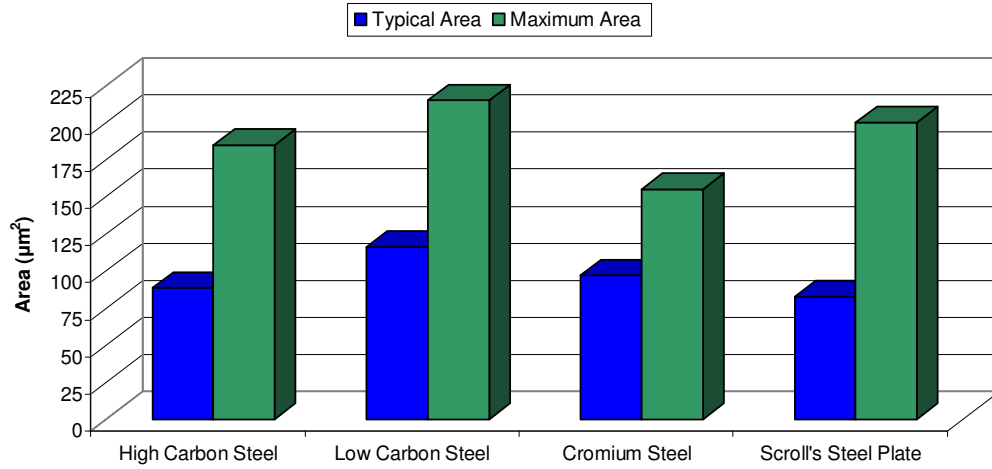


**Figure 141: Comparison of the average typical and maximum eroded area of the cavitation pits in a) water b) lubricant c) refrigerant environments**

The cavitation pits produced within the lubricant environment are on average 4-5 times deeper than the ones found on the refrigerant environment under the same exposure time. In addition, the average depth of the larger pits produced by lubricant bubbles was found to be 3-5 times higher than the pits generated by the implosion of the refrigerant bubbles. Thus, the experimental results of the minimum refrigerant bubble impact on material's surface can be perfectly matched with the photographic results and the peculiar behaviour of the refrigerant bubbles. Chromium and high carbon steel samples lead the performance of the steels against cavitation erosion having the smallest pits depth, followed by the low carbon and the scroll's steel plate.

In regards to volume loss, tests have shown a varying rate in the cavitation process among the steels. In figure 140 the results from volume loss measurements for each liquid case are illustrated. The differences in the shapes of the diagrams are identical to the previous ones figure 139. Generally, during the incubation period the material surface is plastically deformed. However, many erosion pits were also indentified. The material removed was accurately measured with the 3D optical interferometer microscope. The maximum objective was utilised for detailed analysis.

The volume loss was significantly higher within the lubricant bubbles compared to the refrigerant bubbles. Specifically, the volume loss in the lubricant environment is, on average, 3.5 times more than that of the refrigerant environment. In addition, the average volume loss of the larger pits shows the same pattern. Thus, in any case, the lubricant bubbles are much more destructive than the refrigerant bubbles, producing severe pits. Furthermore, water having less impact pressure than the lubricant produces more damage on the surface of the steel samples removing more volume. In the cases of the low and high carbon steels the volume loss is almost doubled. The reason as previously mentioned is related to the lubrication film thickness.

Finally the size of the eroded area around the pit was measured, figure 141. The area on the high carbon and scroll's steel plate pits are close for the water and the lubricant. Once again chromium exhibits a well-balanced performance keeping its overall average standards against cavitation on the top of the ranking. Low carbon steel has the largest eroded area across the pits in all the liquid environments. In the refrigerant environment the eroded areas were restricted to very small formation patterns. The impact of the refrigerant bubbles is the least among the tested fluids.

The experimental results are in a very good agreement with the photographic results. The water bubbles produce the maximum damage among steel samples, followed closely by the lubricant bubbles and finally by the refrigerant bubbles which have potentially the smallest cavitation impact. Apparently, water provides the most hostile environment for the steel samples regarding the growth and the size of the pits. Thus, in the next bunch of experiments, where the durability and the toughness of the steel materials will be tested, water is used.

From the morphology evolution as well as the depth and volume loss of erosion pits of the four tested steels, it can be deduced that during the formation of the cavitation pits in the early stages of cavitation erosion, the best durability performance by far is possessed by the chromium steel, closely followed by the high carbon steel, the scroll's steel plate and finally the low carbon steel. Thus, according to the structure investigation and the evaluation criteria of the erosion pits, a superior performance is expected from the chromium steel over a prolonged period of time.

## **6.4 Maximum Erosion Stage**

### **6.4.1 Methodology**

A comparative study on the maximum erosion stage of three low cost market steels against the steel plate of the scroll expander was conducted. The maximum erosion stage is crucial since it shows the actual cavitation resistance of the steel samples after many hours of exposure to cavitation impacts. The cavitation damage inside the scroll can be significantly reduced. However, to totally extinguish the cavitation mechanism inside the scroll expander is a difficult issue because of the scroll's geometric profile and its demanding operational conditions.

For this last bunch of tests, selected time was 1,2,3,5 and 8 hours respectively. The samples were installed on the bottom of a 0.5 litre plastic tank. The temperature during the running period of the experiments was kept constant. The surface roughness for all the samples was identical avoiding any erosion augmentation in the early stages of the test. The surface of the cavitation testing transducer was regularly inspected to ensure optimal performance. The ranking of the steel samples against the cavitation erosion mechanism was indentified. The best performance of the steel samples to cavitation according to their endurance was evaluated. The strongest steel can be used in future scroll devices.

## 6.4.2 Experimental Results

Over a prolonged period of time, the pits which were formed in the early stages of the cavitation mechanism can significantly grow by linking up with nearby pits, cracks and groves. The surface roughness substantially increases accelerating the erosion rate of the materials. The enlargement of the pits is accompanied by additional volume loss. The mechanism of pit growth leads to the formation of deep and wide craters penetrating the sample's surface. These areas were named "ring areas" because of the shape they obtain after the end of the cavitation process.

The cavitation intensity is higher in the centre of the eroded area followed by the area across the periphery of the ring. The area in between obtains the least damage since the intensity of the implosion impacts is minimum. Thus, images were focused in two distinctive areas for all the samples: in the crater where maximum damage is found and in the area between the crater and the outer annulus where the minimum damage is observed.

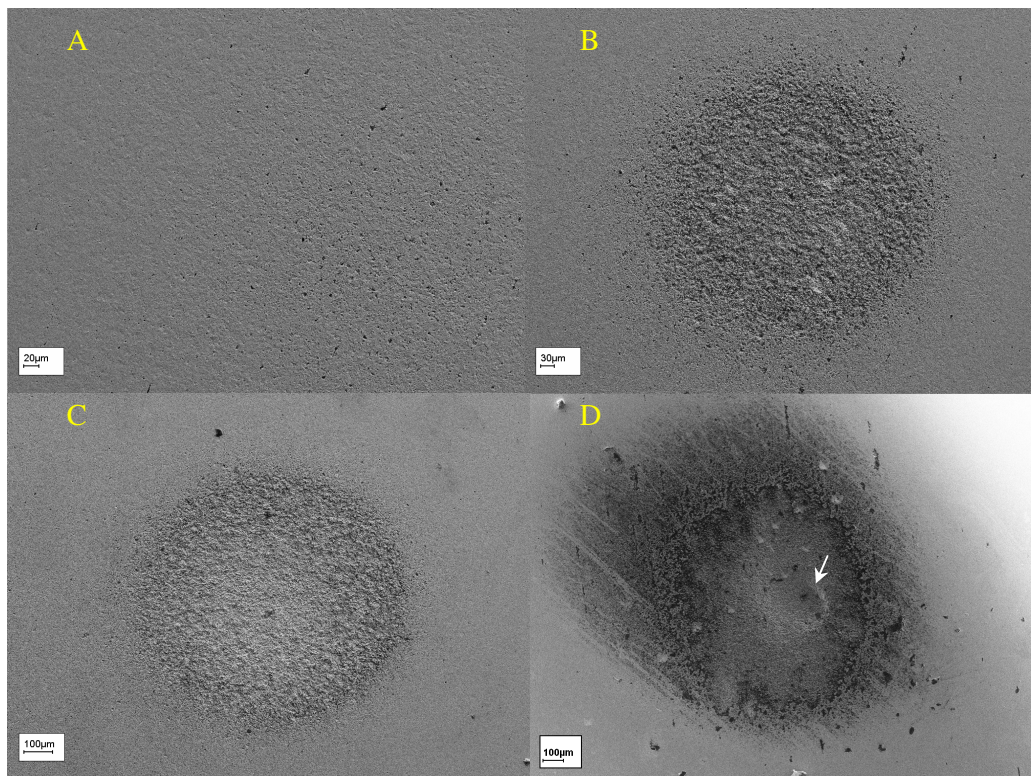


**Figure 142: SEM images of eroded areas at different stages: A) 1 h B) 3 h C) 5 h D) 8 h**

A series of SEM micrographs shows the eroded surface of the scroll's steel plate at different stages of the cavitation process (figure 142). The images were taken in each of the selected

test intervals in order to get an overview of the attenuation of the pits and their formation into craters. The first image figure 142 (A) shows the initial stage of erosion pit formation after 1 hour of testing. The next stage is after 3 hours of exposure and a crater shape is formed. The periphery of the crater is clearly visible. Its core consists of pits which show increased density and size. After 5 hours of testing the centre area was significantly eroded but still no substantially material loss was observed and the depth remained superficial. Finally after 8 hours of testing the crater was severely eroded forming a deep valley. The edges of the periphery were very sharp and sloppy while huge loss of material was noticed. Closer observation demonstrated the increased depth of the crater (figure 142 D white arrow).

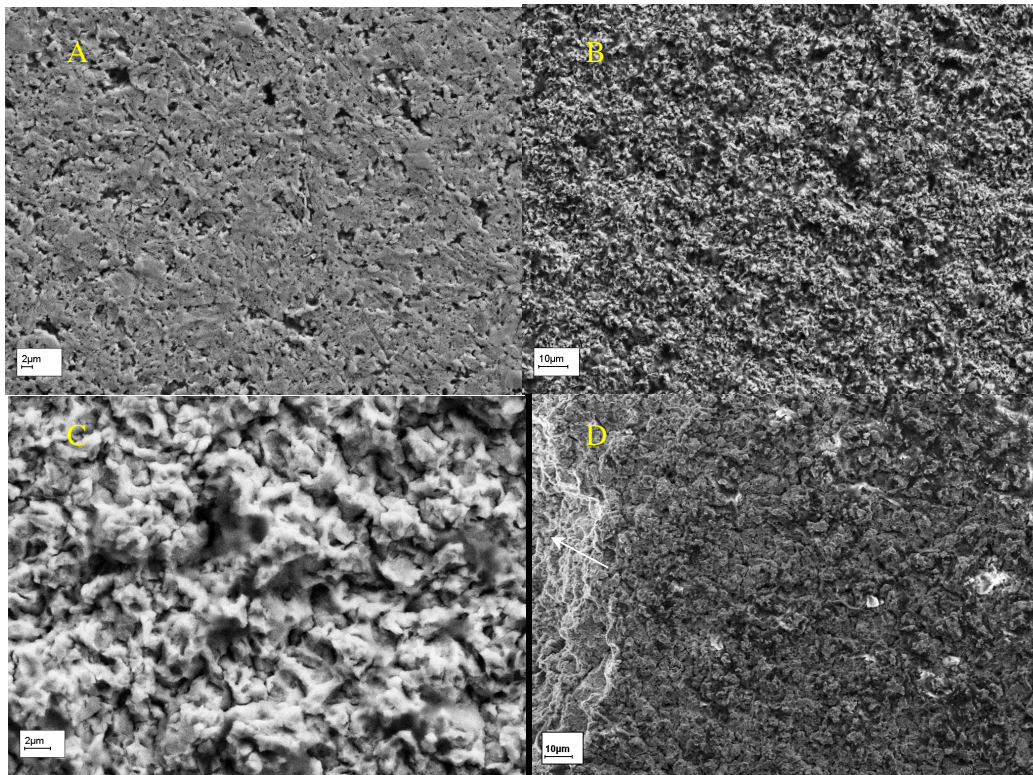


**Figure 143: A close up series of SEM micrographs showing the damage by cavitation erosion impact at different stages: A) 1 h B) 3 h C) 5 h D) 8 h**

High magnification of the crater's structure reveals the nature of the damage as figure 143 depicts. After an hour of testing, a field of concentrated strains caused intergranular fracture at the grain boundaries resulting in enhanced dislocation movements. Many pits were formed with their adjacent areas plastically deformed. After 3 hours the roughness increased while it became very hard to distinguish the pits and the cracks from the previous eroded region. The surface layers vanished and a very rough surface was formed. The crater was progressively becoming rougher and deeper. As marked in figure 143 (C) many consecutive cracks were formed showing a brittle failure fraction which significantly accelerated the erosion rates. At

the final stage of 8 hours, erosive wear had sufficiently propagated, penetrating the surface. Eventually, the depth of the erosive region rapidly increased while large craters were formed. A height difference between the core of the crater and the original surface due to material loss was observed, figure 143 (D).

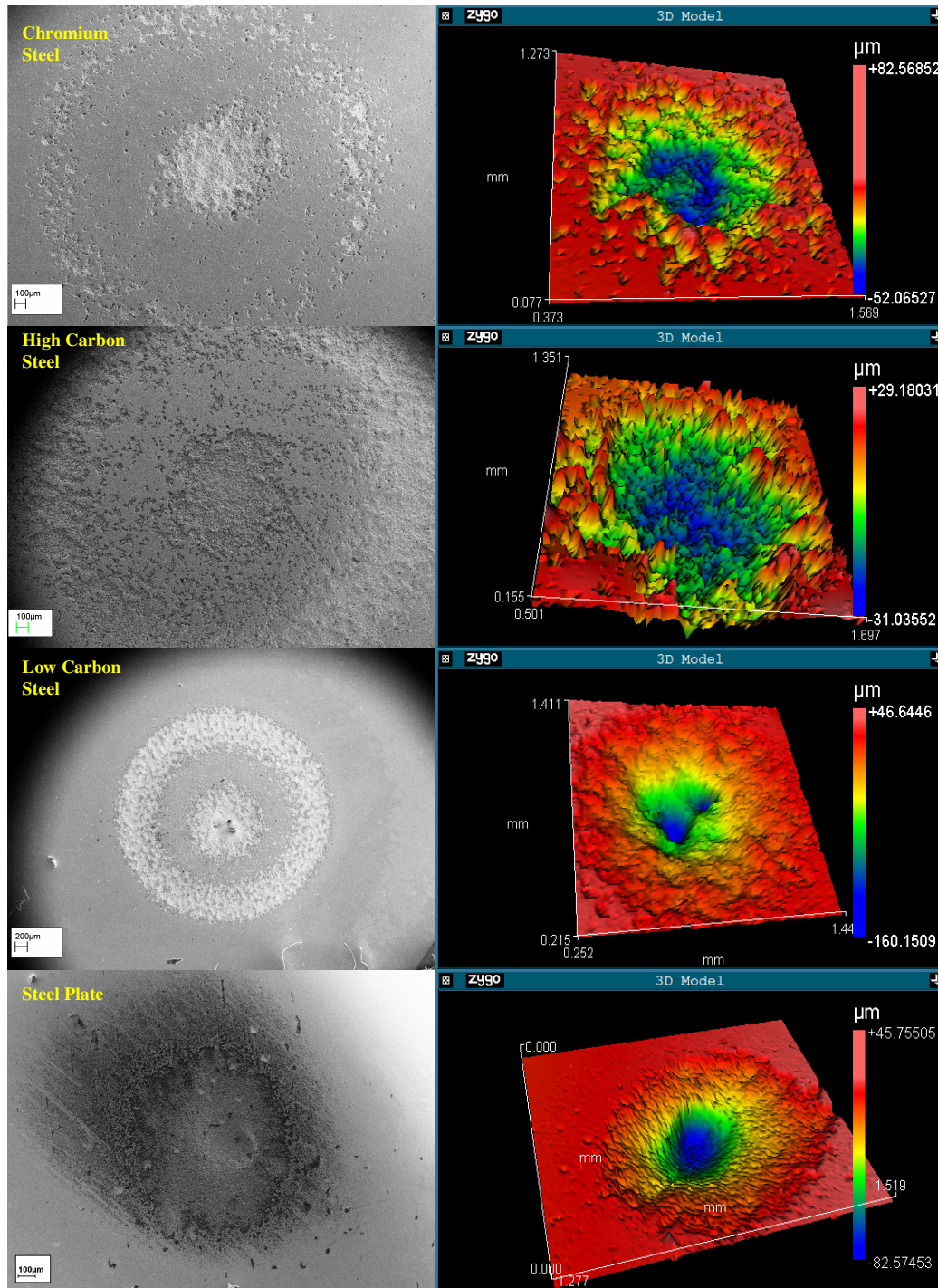


**Figure 144: Morphologies of the steel samples after 8 hours exposure to cavitation erosion.**

The level of damage on different steel materials after 8 hours of exposure to cavitation impacts is shown in figure 144. The effect of cavitation in all the materials is identical to the steel's plate described previously. Pits are formed during the early stages of the cavitation mechanism progressing into deep craters in later time steps. Specifically, the observation of the bird's eye SEM and ZYGO interferometer images of the erosive ring areas allows the evaluation of the surface transformation and the extent of the erosion damage. The morphology of the craters revealed that low carbon steel has the deepest crater overall. The maximum eroded area was found to be on the high carbon steel. These results indicate that there is no direct correlation between the material's resistance and its erosive parameters. A combination of all the erosion parameters (e.g cavity depth, area of erosion and volume loss) should be taken into consideration when calculating the actual resistance of the materials. Additionally, crater formation leads to increased roughness and attenuated severity of the erosion damage.

Prior to the evaluation of the fundamental erosion parameters, the damage mechanisms of the steel samples are investigated with the use of SEM micrographs, figure 145. The majority of volume loss in all the samples derives from the centre of the ring. In general, the resulting surface damage was found to be similar for all the steel types. The damage is characterised by the formation of undulations, fatigue cracks, deep craters and protruding steps.

From images it can be seen that the fracture that occurs on the chromium steel surface has a transcrystalline and a brittle character. Cracks propagate in places where slip lines developed along the grain boundaries (figure 145 E). The chromium carbides contribute to an increase in the material's strength. It seems that even after 8 hours of exposure to cavitation, carbides have not been removed from the low intensity area creating a blistering effect (figure 145 A). There are no evidences that carbides accelerate the erosion. On the contrary carbides are well embedded within the crystalline matrix, resisting cavitation impacts and thus enhancing the material's lifetime. However, when the matrix around the carbides is becoming severely eroded, the carbides lost support and eventually dislodged out of the sample's surface [202]. Moreover a large amount of carbides produces higher brittleness in the chromium steel [203].

Additionally, the blistering effect observed on the surface of the chromium steel can be derived from another scenario. According to Haosheng [204] in his recent study, the spherical particles found on the surface of a chromium steel sample after cavitation erosion tests, are the results of the thermal effects in high temperature regimes. The spherical particles can form from a molten state after experiencing a rapid cooling process. Thus a combination of spherical carbides with spherically formed particles can co-exist. An intensive chemical

analysis of these particles should be the answer to that blistering effect. Nevertheless, a reliable chemical analysis of such a tiny particles is very difficult.

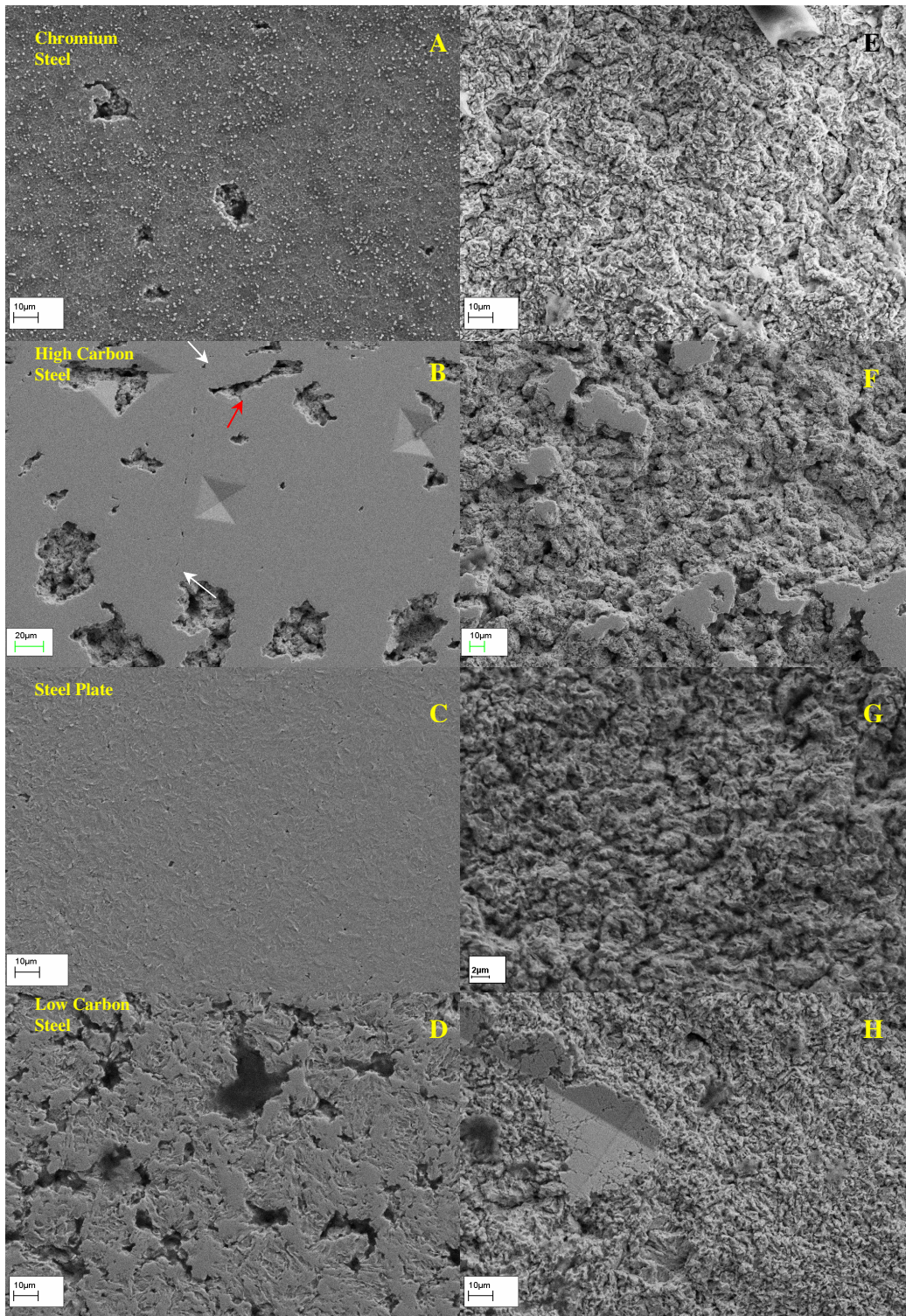


**Figure 145: Cavitation erosion damage: in the low intensity area in between the crater and the outer annulus (A-D) and in the high intensity area in the centre of the ultrasonic source (E-H).**

A lot of nearby cracks can be found on the high carbon steel sample in the area between the crater and the outer annulus,. The extension of the linear cracks observed in the early stages, are shown (figure 145 B). In the high carbon steel some of the cracks were propagated deeper to the surface, forming wedge shapes (red arrow) while others kept their original form (between the white arrows). The cracks are wide and elongated while they tend to join together forming bigger grooves. However, the area adjacent to cracks is not plastically deformed showing the strength of the material. The low density of the bubble implosion in this area is not sufficient to create serious damage on the high carbon steel's surface. The micrograph results (figure 145 F) suggest that a brittle failure fraction surface occurs. Intergranular fracture occurs along the grain boundaries. Interestingly, on the high carbon steel sample, partially original surface layers are still standing without any traces of severe damage on their surface. The erosion morphology and the unaltered surface layers highlight the strength and the brittleness of the material. The roughness was measured to be similar to that of the chromium steel.

The damage found on the steel plate's surface between the crater and the outer annulus was restrained to a few cracks and to a lot of martensite lathings (figure 145 C&G). This implies the good performance the steel exhibits away from the cavitation source, since its ductility plays an important role absorbing the energy impacts avoiding severe damage. In addition, the martensite lathings are thinner and smaller in the steel plate compare to the low carbon steel. The steel plate having higher carbon content and more cohesive forces between the primordial grains, as the chemical analysis revealed, creates a very strong surface restricting the growth of martensite lathings. A few short cracks initiated in this area were observed. These cracks were difficult to be developed perpendicular to the surface because they restrained due to martensite lathings [205]. However, under the massive cavitation strike by the source of the ultrasonic horn the extent of the erosion damage can be critical as the size and the depth of the crater reveals. Eventually, the damage in this stage is due to the brittle character of the material and the appearance of fatigue striations decreases the lifetime of the material.

As the cavitation erosion goes on the surface of the low carbon steel gets seriously damaged and the shape of the martensite lathings found in figure 138 vanishes (figure 145 D). In addition, the erosion process is accelerated by the fact that ferrite, which comprises the structure of low carbon steel, is less resistant to the attack of micro-jets and is removed from the surface earlier than the austenite. In low carbon steel the surface is heavily eroded by ductile fracture. Figure 145 (H) clearly illustrates the cavitation cracks which were formed on the surface of the low carbon steel material. The growth of bubbles within those cracks and the low hardness of that region increase the severity of the cavitation impacts encouraging

material removal. Notable displacement of material is observed since the cracks are found to be very deep. The concentration of the martensitic lathings mentioned in paragraph 6.3.2 is in correlation with the existing cracks after 8 hours exposure to cavitation allowing displacement in large areas resulting in delamination wear. Even in that area of low cavitation intensity the sample's surface suffers from severe erosion damage.

Measurements were carried out to monitor the erosion rate and the erosion resistance of the steel samples over the different stages of the cavitation erosion tests. The erosion rate of the chromium steel is measured to be the smallest among the steels while its resistance was calculated to be the highest.

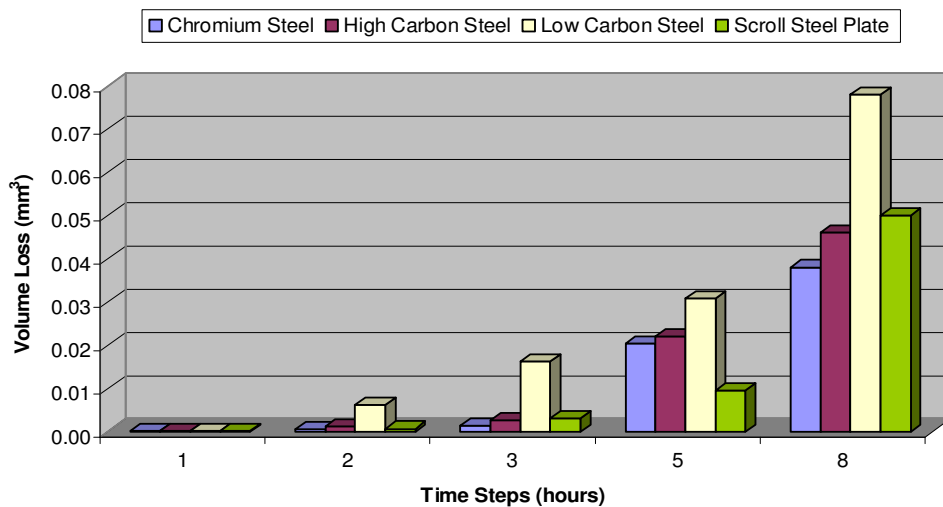


**Figure 146: Variation of volume loss with cavitation time for the steel samples overlay in water.**

According to figure 146 the volume loss proportionally increases with time for all the steel samples. Chromium steel overall has the lowest volume removed. High carbon steel comes second while the steel plate cannot maintain its excellent performance in the previous stages rapidly increasing its volume loss in the maximum erosion stage. Finally, low carbon steel has by far the maximum volume loss in all the time steps.

Figures 147 and 148 show the mean depth erosion rates (MDER) and the mean depth erosion (MDE) of the tested steels as a function of time for all the cavitation stages respectively. Chromium and high carbon steel after the completion of the 8 hours test tend to flatten out their MDER to a similar value. It seems that after this stage the MDER in both steels slightly changes stabilizing its value. The MDE was found to be around 2.5  $\mu\text{m}$  and 3  $\mu\text{m}$  for the chromium and the high carbon steel respectively. By contrast, low carbon steel has a linear

increment of the MDER in proportion to the time period for all the erosion stages. There are no evidence of reducing the MDER even after the end of the maximum run test. The MDE for the low carbon steel is nearly twice that for the chromium steel over the same time step. Interestingly, a dramatic increment of the steel's plate MDER and the MDE from 5 to 8 hours is noticed. Until the 5 hours exposure to cavitation, the steel plate had the lowest MDER and MDE among the steel samples. Then, its endurance was dramatically reduced and the erosion rate was steeply increased. The dislocation movements were possibly restricted, increasing their density in those areas with the consequence that the increase in hardness and brittleness of the material made it vulnerable to cavitation. Hence, over a prolonged period of exposure to cavitation impacts, the steel plate of the scroll faced inevitable severe damage.

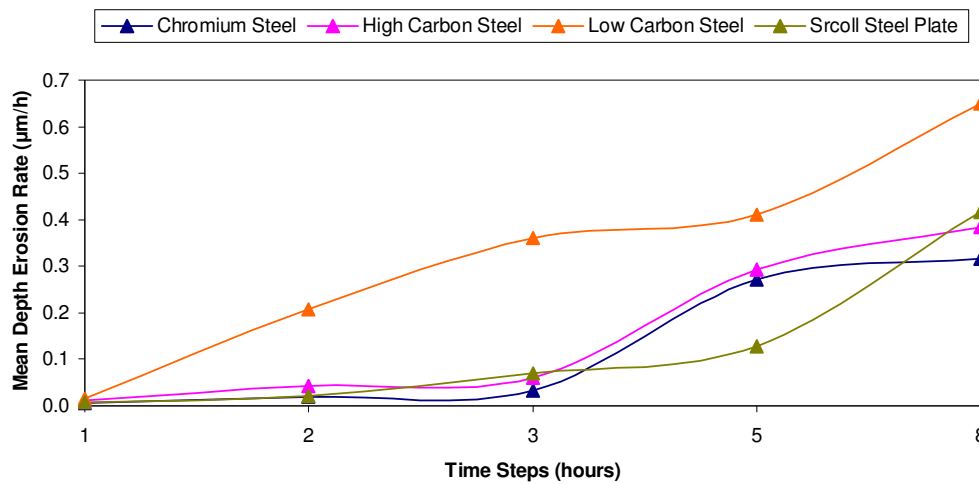


Figure 147: Mean depth of erosion rate as a function of the tested time for the evaluated steels.

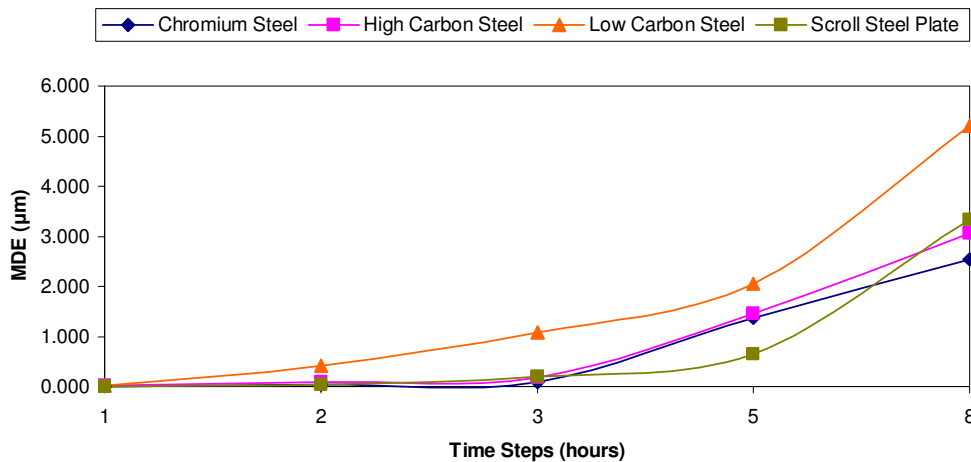
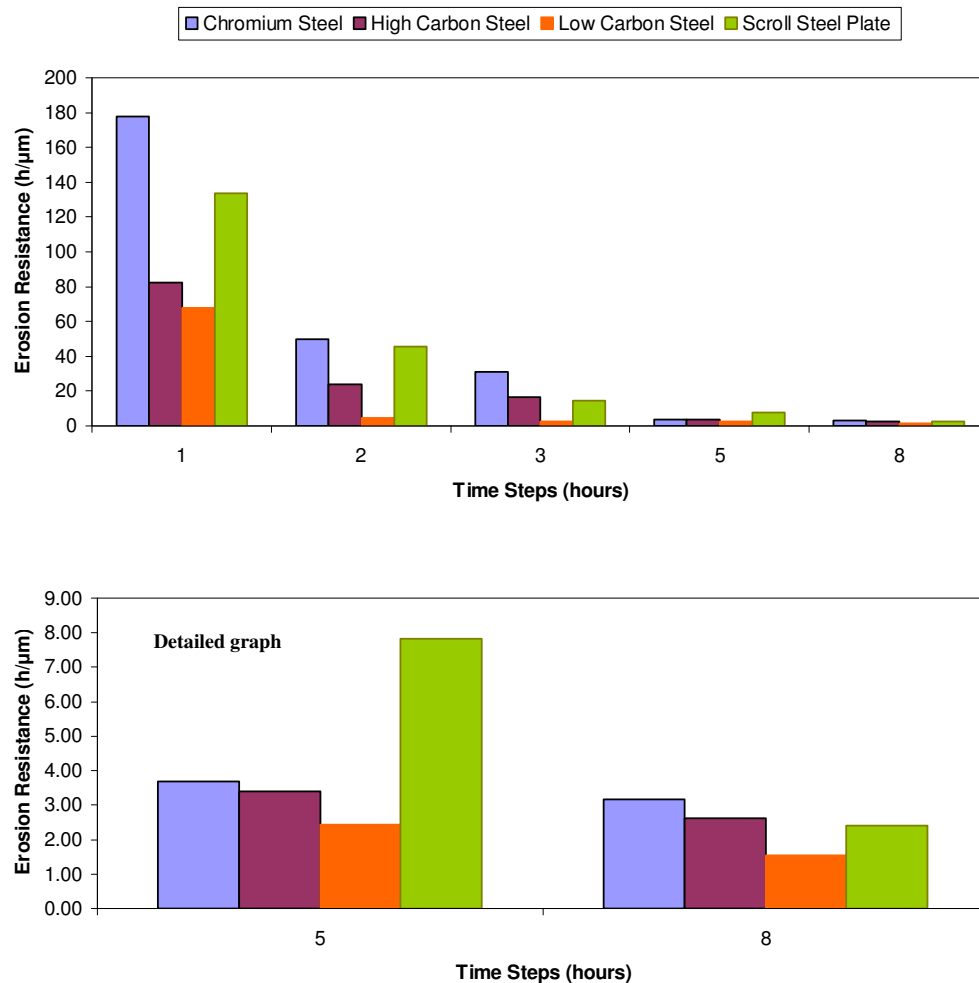


Figure 148: Mean depth of erosion as a function of tested time for the evaluated steels.

According to the abovementioned performance of the steel samples their erosion resistance was successfully calculated (figure 149). Once again the chromium steel shows its superior performance against the other steel samples. Chromium steel keeps a consistent performance achieving the maximum erosion resistance in all the stages except the 5 hour test. High carbon follows a similar trend to the chromium steel. Steel plate loses its resistance after 5 hours exposure to cavitation. In the low carbon steel even from the second stage of the 2 hours test, a steep reduction of its erosion resistance ( $5 \text{ h}/\mu\text{m}$ ) is observed, reaching the minimum value of  $1.5 \text{ h}/\mu\text{m}$  at the maximum erosion stage of the 8 hour test. The aforementioned results confirm that the cavitation erosion performance of the chromium steel in comparison to the rest of the steel materials is the highest.



**Figure 149: Correlation of cavitation erosion resistance as a function of time a) for five different time stages b) a detailed representation of the last two critical stages of the tests, 5 and 8 hours.**

In general, the roughness of the tested materials increases with the exposure duration [157]. In this study the roughness was estimated by measuring the eroded area in the vicinity of the crater including the crater. It can be seen that the largest increment correlates to the acceleration stage of cavitation erosion for all the steels. As shown in figure 150 low carbon steel in comparison to the other steel samples, has the highest roughness at the initial stages of 2 hours, gradually increasing that trend during the following hours. This is in good correlation with all the aforementioned graphs (figure 146-149). Additionally, the high carbon steel which obtains the smallest roughness does not have the highest resistance. Thus, even if the roughness attenuation generally reveals the behaviour of the steels against cavitation it cannot be considered as a key factor for a qualitative analysis. A precise correlation between the roughness parameters and the erosion resistance of the steel samples cannot be established.

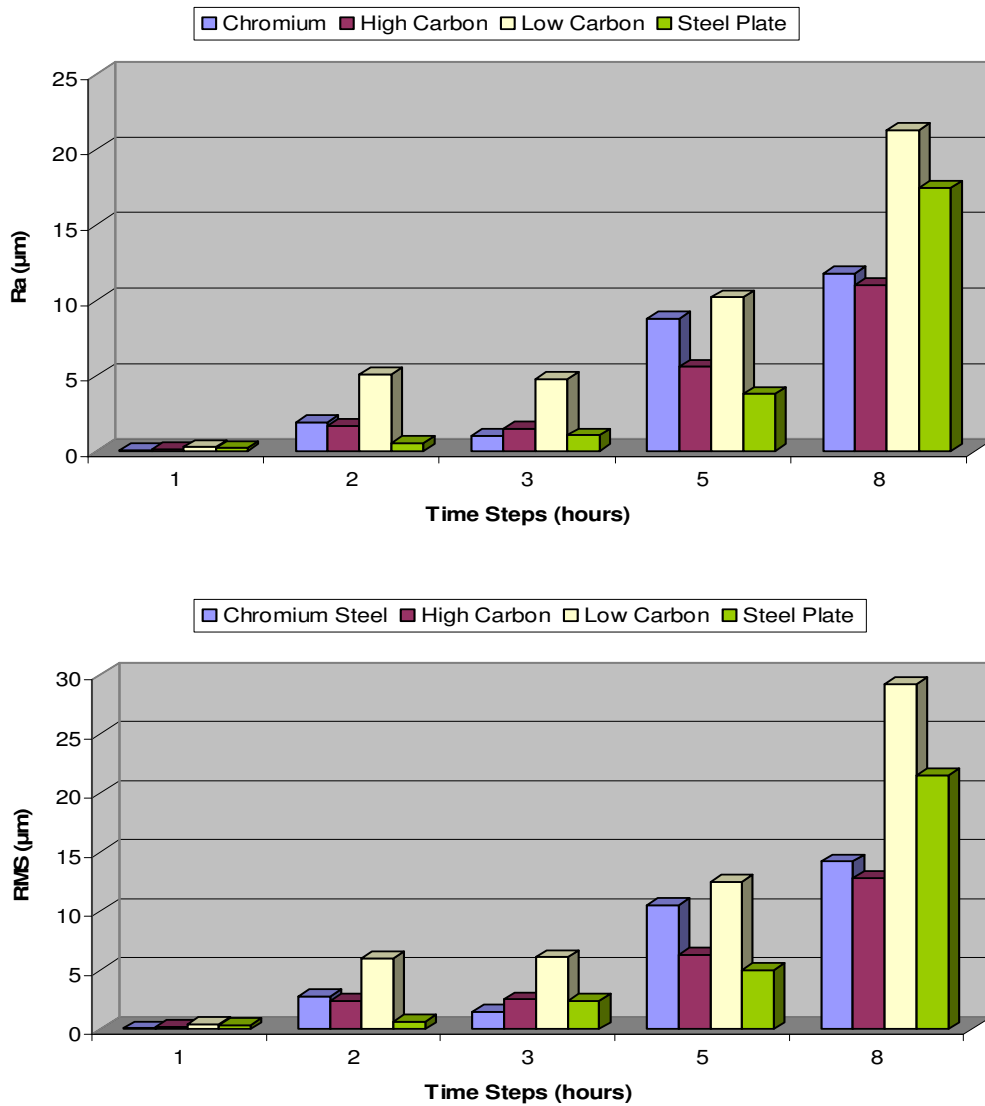
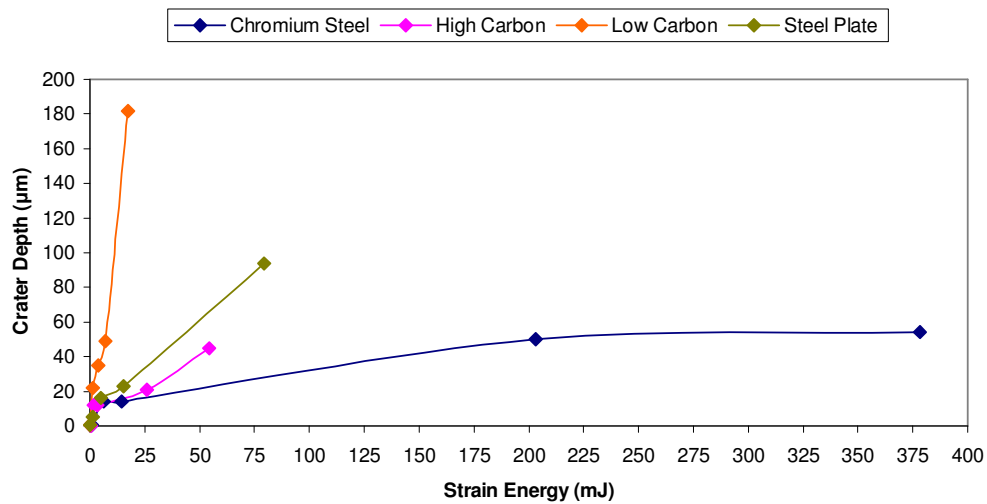
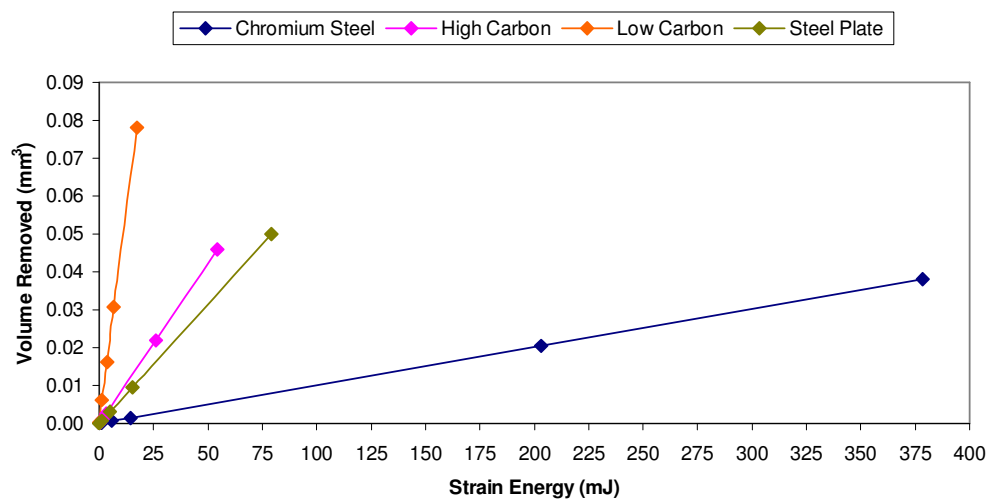


Figure 150: Evolution of the roughness parameters (Ra and RMS) in cavitation erosion tests.

The cavitation erosion mechanism has a fatigue character; hence the damage needs time to be developed. Since the erosion damage is caused by consecutive impacts similar to a fatigue phenomenon, the accumulated strain energy can indicate the critical point where the damage becomes crucial for the steel. The dependency of the accumulated strain energy as a function of the crater depth and the volume loss of the steel samples is depicted in figures 151 and 152. As shown on these figures, when the strain energy exceeds the limit of the 15 mJ the eroded damage is localised forming deep craters. In this value of strain energy a notable volume loss is also observed while the erosion rates are significantly accelerated.



**Figure 151: Correlation between the accumulated strain energy and the crater depth.**



**Figure 152: Correlation between the accumulated strain energy and the volume removed.**

Interestingly, the superior performance of the chromium steel against the other steels is noticed. In the maximum erosion rate the sample requires a massive amount of accumulated strain energy in order to produce the corresponding volume loss. This trend explains how hard

and strong is the chromium steel. On the other hand the low carbon steel instantly starts to deform when the strain energy is in the value of 15 mJ and the damage is already enormous compared to the other steel samples. Such a behaviour can be explained by the ductility of the low carbon steel which can be coupled to the low mechanical properties (table 10) leading the sample to a rapid fracture.

The high carbon steel requires lower accumulated strain energy than the steel plate to remove the same corresponding volume from the surface. This implies the brittleness of the material. The high carbon steel and the steel plate are very close in the steel grades with their distinctive property to lie on their hardness. Hardness of the high carbon is substantially higher than the steel plate. The steel plate accumulates more strain energy in order to produce the same level of damage as the high carbon steel. Hence, from the behaviour of the steel plate it can be said that it is more ductile than the high carbon steel (the high brittleness of the high carbon was also observed during the cutting process appendix A) increasing its resistance to cavitation. Interestingly, and contrary to the erosion rate and resistance graphs, the trends of the accumulated strain energy reveal that steel plate can perform slightly better than the high carbon steel. However, the big difference in the crater height can prove catastrophic for the steel plate in longer cavitation exposure time.

In figure 153, the section of a ring area formed by cavitation impacts over a prolonged period of time is illustrated. Consecutive indentations were performed in critical areas across the sample's surface where the micro-hardness was supposed to have changed. At points 7 and 8 where the damage was very rough, restricting precise micro-hardness calculations, several measurements were required. Hence, in both areas more than one indentation was performed for better accuracy. The applied force in all of the samples was 8.825 N.

In all the graphs the micro-hardness decreases gradually as it approaches the crater. After the 3 hours cavitation process chromium and high carbon steel show a peak on the 6<sup>th</sup> point. This is due to the hardening which both of the steels experience during the process, increasing their hardness properties and becoming more durable against cavitation. In that region the intensity of impacts is lower than in the centre and there is an absence of severe damage. By contrast, on the same region, the hardness of the steel plate remains the same while for the low carbon steel it is significantly decreased. The obtained hardness drop is due to the thermal effect. In the 5 hours stage a similar behaviour by the samples was observed. No significant alterations in their hardness value as they approached the crater were observed. Chromium and high carbon steel follow a similar trend while steel plate once again it seems unsusceptible, maintaining a linear pattern.

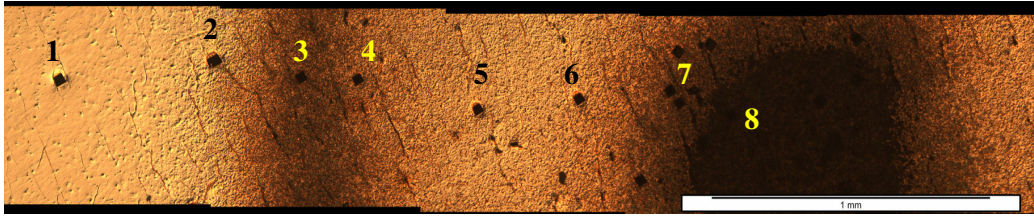


Figure 153: Representative section of cavitation damage for all the steel samples. The points where the hardness indentations were made are presented.

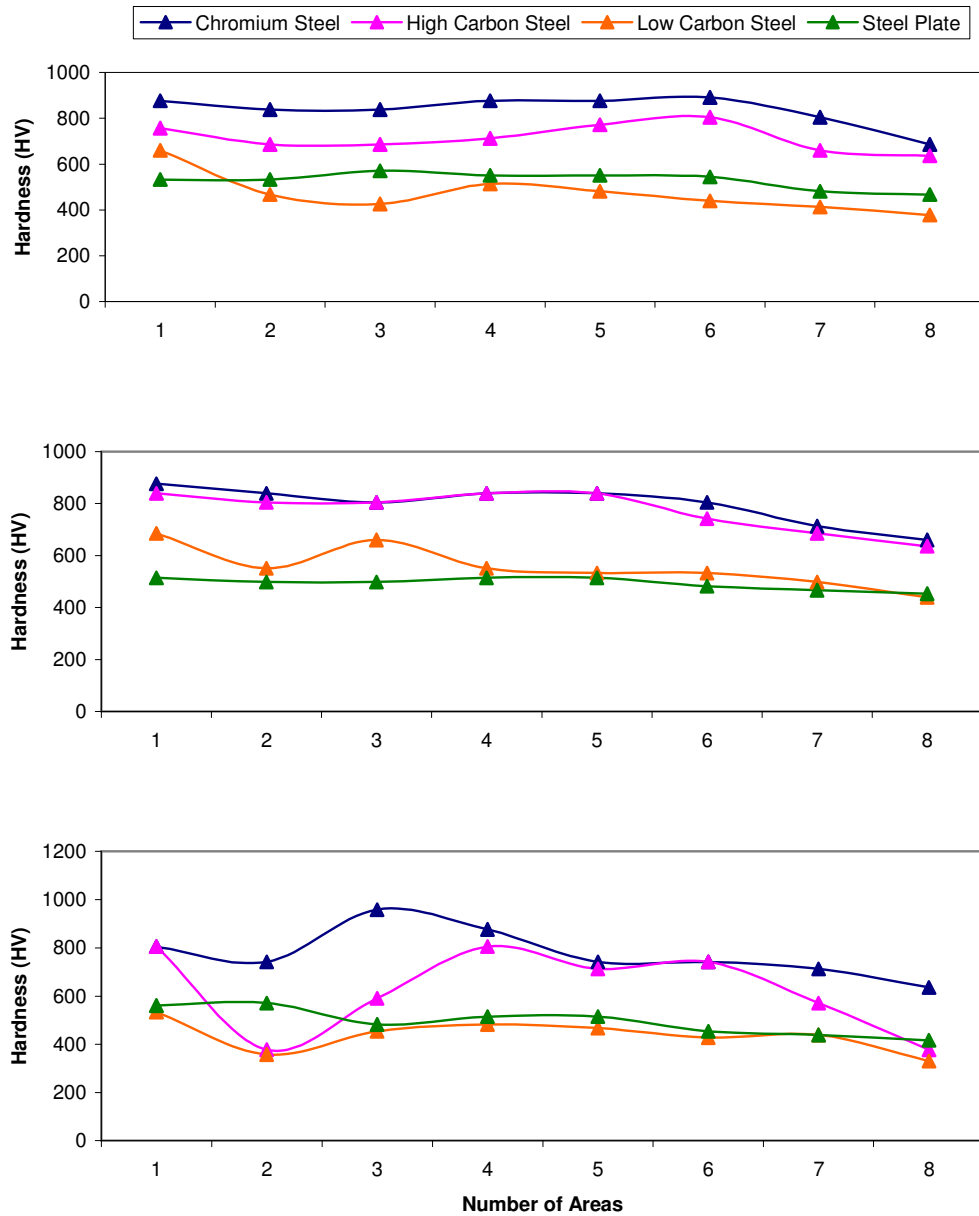


Figure 154: Hardness measurements after 3, 5 and 8 hours of exposure to cavitation. The number of areas is in accordance to figure 153.

In the maximum accelerated stage of cavitation erosion interesting trends are depicted, figure 154. The chromium steel reaches a maximum peak on region 3. In this region the impact of cavitation is less intense than in the centre. Seemingly, during the 3 hour stage the micro-structure of the chromium increases its hardness due to martensite work-hardening, and then decreases as a result of crack initiation and propagation, local fracture and subsequent crater formation. Moreover, it seems from the increment of the hardness values that under these experimental conditions of 8 hours of less intense impacts, work hardening of the chromium steel is achieved. Thus, the chromium steel allows martensitic deformations within the martensitic lathings, increasing its surface hardness. The cavitation erosion resistance for materials with martensite structure was considered to be dependent on the hardness material [205].

High carbon steel in region 4 shows a peak. In region 3 the cavitation impact severity has significantly reduced its hardness. This point is in the periphery of the outer annulus. In general high carbon shows its brittle character, incapable of resisting the massive striking of the micro-jets, lowering its hardness values to the level of the low carbon steel. Steel plate has a considerable reduction of its hardness at more than 100 HV, implying the rapid reduction of its erosion resistance which was observed at this stage. In the low carbon steel the hardness levels seems to be stabilised after the 8 hour test with no steep inclinations on its linear graph. The low carbon steel has a peak on the region 4, found inside the outer annulus showing the work hardening due to dislocations blockage which that area experiences under specific time and intensity of the cavitation power.

The change in hardness can be closely correlated with the erosion resistance of the steel samples. Generally, higher resistance implies higher hardness values. In every steel sample the hardness alterations depend on the intention and the time duration of the cavitation impacts. If conditions are suitable, work hardening on the steel samples is occurs, otherwise rapid damage can occur. Hardness is proved to be one of the key factors in increasing the lifetime of the steel materials. The more brittle the material is, the more significant the fluctuations in its hardness levels are. Interestingly, the materials with the lower hardness at the end of the tests proved to be the most eroded as the figures 146-152 earlier revealed.

Finally, the influence of the manganese (Mn), phosphorous (P) and sulphurous (S) elements can seriously affect the hardness and the cavitation performance of the steel materials. The stacking fault energy is significantly influenced by the amount of the manganese found in the crystal structure [206]. Increased manganese levels enhance stacking fault energy and allow higher dislocation movements. Thus, in a martensitic structure the hardness and the cavitation

erosion resistance can be decreased. In this study the tested steels consist of small amounts of manganese. The chromium steel having the smallest amount of manganese compared to other steel samples can slightly enhance its cavitation erosion resistance. In addition, as low carbon steel contains relatively high concentrations of phosphorous and especially of sulphur this can substantially reduce its erosion resistance. It is well known that those elements diffuse to the grain boundaries and decrease the strength of the material, leading to rapid fracture [147].

### 6.5 Actual Scroll Steel Plate Erosion Damage

The morphology of the cavities found on the surface of the scroll's steel plate after the end of its service period (1000 hours) (figures 26-30 at Chapter 3), was analysed and evaluated (Appendix K). Various pits were used from random areas across the steel's plate surface for a more representative analysis. However, only the larger pits were taken into account for this analysis. The number of selected pits was 100 in total. Many small regions were found dominated by erosion pits. Nevertheless, this analysis is focused on the region where a massive and dense production of pits occurred. This region was next to the inlet port of the scroll, starting from the tip of the steel plate, going across the upper peripheral edge of the steel plate and covering a total area of around 200 mm<sup>2</sup> (figure 25 at Chapter 3). This critical area is very important to be maintained for the smooth operation of the scroll. The reason is that in the suction area the pressure drop is inevitable (paragraph 1.1 and 3.2.1). Thus, any further pressure drop due to a failure mechanism in that area it can prove catastrophic for the efficiency of the integrated scroll system.

Pits	Ra(μm)	RMS(μm)	Depth(μm)	Volume Loss(mm <sup>3</sup> )	Area(mm <sup>2</sup> )	Time(h)	MER(μm/h)	REC(h/μm)
100	0.77	1.19	5.16	8.00E-05	7.37E-03	1000	1.52E-03	1284

**Table 13: Average erosion characteristics after the evaluation of 100 individual pits across the surface of the original steel plate.**

Pits	Volume Loss(mm <sup>3</sup> )	Eroded Area(mm <sup>2</sup> )	Time(h)	MER (μm/h)	REC (h/μm)
8000	1.60E-01	2.00E+02	1000	8.00E-04	1250

**Table 14: Measurements of the critical severe damaged area lie next to the inlet port.**

Initially the average volume loss for each pit was calculated (table 13). Then by detailed micrograph analysis of the 200 mm<sup>2</sup> critical area the number of pits was estimated. There were found to be around 8000 pits. Then using the average volume loss for each individual pit and multiplied by the number of pits found in that area, the average volume loss of this area was estimated. According the hours of operation the MER and REC values were calculated

and presented in table 14. The average values of MER and REC were successfully identified and correlated with the lifecycle of the scroll expander and by the aforementioned test results.

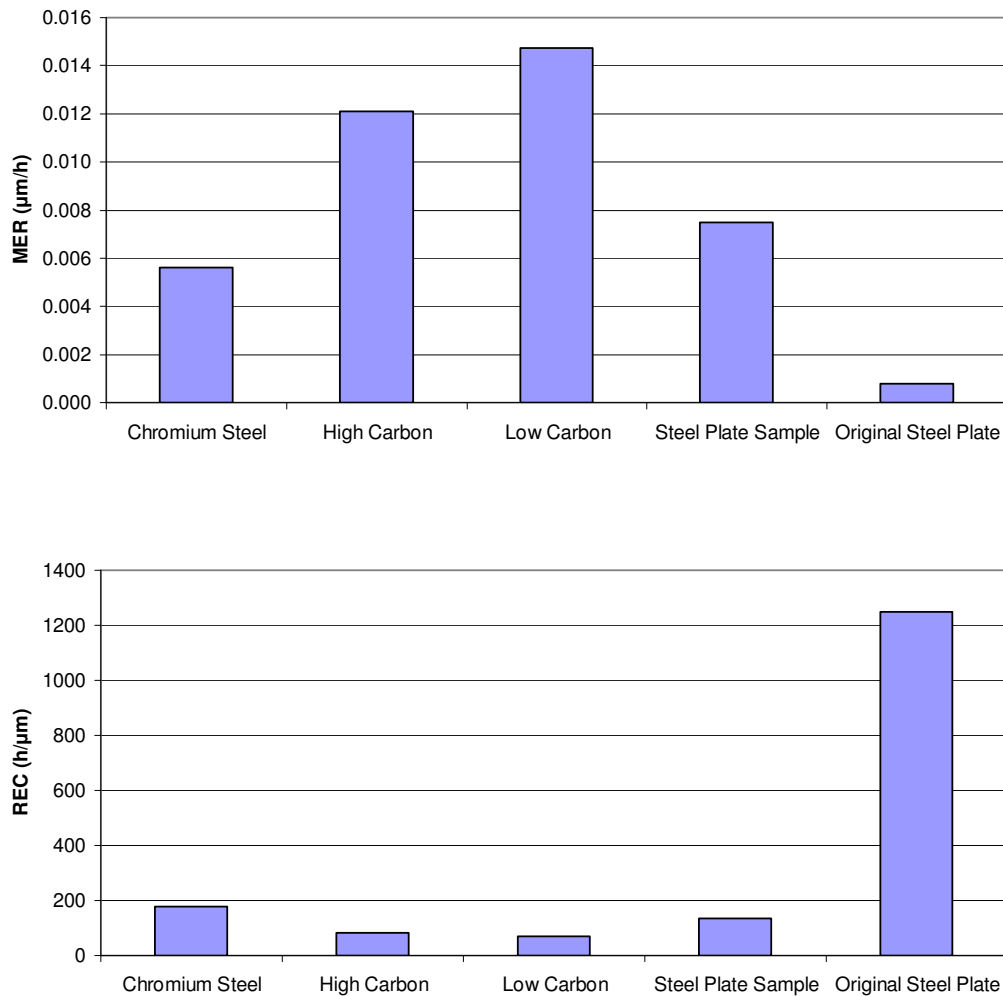


**Figure 155: Correlation of the mean erosion rate and the cavitation erosion resistance of the tested steels against the original steel plate of the scroll expander. The testing time was 1 hour for the steel samples overlying in a water liquid and 1000 hours for the actual steel plate of the scroll exposed to its extreme operational environment.**

The effect of the impact pressure from the bubble implosion on the actual steel surface of the scroll expander during its operation is not as intense as in the experiments performed by an ultrasonic transducer. This can be noticed by the average MER and REC values of the cavities. The MER of the actual scroll's steel plate is substantially lower than the corresponding steel plate sample. Even in the lowest testing time of 1 hour it is seven times lower than that of the steel plate sample (figure 155). In addition, its erosion resistance is 10 times more than the corresponding resistance of the steel plate sample after 1 hour exposure to cavitation impact by water bubbles. Thus, the correlation which can be made is that after

1000 hours of random cavitation impacts within the scroll expander the intention of its cavitation properties can be matched with the damage produced in a water environment with consecutive powerful impacts by the bubble implosion for less than 1 hour.

This difference is due to the following two reasons. Firstly, the sample is subjected to low intensity cavitation impacts by the implosion of the refrigerant bubbles as previously revealed. The impacts are random and not very regular without any particular direction and order. In contrast, the cavitation produced by the ultrasonic system is consistent with high intensive pulses producing severe wear in a small area and short time duration. Secondly, the medium which produces cavitation inside the scroll expander is found to be the refrigerant (paragraph 3.3). Eventually, as the performance of the refrigerant bubbles is not severe, the damage expected on the steel surface even after this very long time duration of 1000 hours is generally low. However, the surface investigation revealed that the extent of damage after 1000 hours of operation can be considered as critical showing evidences of a rapid increment in an additional prolonged period of time.

Looking at the MER value of the scroll steel plate after the 1000 hours of service an approximation of the failure mechanism of the scroll system can be made. Assuming that the maximum operational period is 30,000 hours for the scroll and that after the formation of pits and grooves with an average depth of 10  $\mu\text{m}$  the efficiency of the scroll will be significantly reduced due to leakages, the maximum lifetime was estimated to be around 12,000 hours. Thus, after 12,000 hours of operation, the scroll expander could face severe damage by cavities collapse and a significant drop in its efficiency.

This approximation shows the best possible scenario of the scroll's failure mechanism by cavitation. However, cavitation by the refrigerant bubble implosion within the scroll expander can rapidly be increased especially after the formation of deep cracks, up to the 5  $\mu\text{m}$  average depth, and rough surfaces. Apparently, cavitation becomes more aggressive striking these weak areas and accelerating the erosive wear rates. Thus, an accurate correlation is difficult to achieve. Nevertheless, the cavitation resistance of the scroll can be significantly increased by replacing the damaged steel plate with chromium steel EN 31. The chromium steel was found to be 25% more durable and tougher than the steel plate during the 1 hour and the 8 hours of testing. Thus, chromium steel will initially delay the formation of the cavities, restricting and slowing down the erosion damage growth while after a prolonged period of time it would prevent any steep increment of the erosion rates. Hence, the lifecycle of the scroll and simultaneously of the micro-CHP's system can be significantly enhanced.

## 6.6 Summary and discussion

### 6.6.1 Photographic Results

The lubricant and water bubbles have similar behaviour as they approach the rigid boundary. They expand in a continuous motion, due to pressure variations, keeping a spherical shape. In the case of refrigerant, the pressure variations affect the shape but not the size of the bubbles. Eventually the refrigerant bubbles obtained an amoeboid shape.

During their descent to the boundary wall, water and lubricant bubbles produce micro-jet impacts at various normalized distances from the sample's surface. This sequence of events is repeated until they reach the boundary wall of the chromium steel sample where they destructively collapse. Conversely, the refrigerant bubbles keep an oscillatory and wobbling motion, without implosions on their way down to the boundary. The only implosion which was observed was slightly before the bubble touches the surface of the chromium sample. More experimental work is needed to fully comprehend the remarkable performance of the refrigerant bubbles.

Interestingly, during the expansion mode of the bubbles in their incubation period, three different bubble behaviours were observed respectively for each fluid. The water bubble implodes generating hundreds of micro-bubbles. These micro-bubbles, with a size 10-12 times smaller than the primary bubble, diffuse to the water liquid with orientation to the boundary wall. The lubricant bubble has a similar behaviour to the water bubble. The semantic differential is that it creates a lubricant layer consisting of many tiny bubbles (around 10  $\mu\text{m}$  diameter) which absorb the destructive impact from the imploding bubbles. On the other hand, the refrigerant bubble shows a totally different behaviour. When the refrigerant bubble collapses, micro-bubbles are generated, creating a "jelly" shaped cloud. Camera observations showed that the attraction forces between the refrigerant micro-bubbles are very strong, preventing their diffusion into the liquid refrigerant. In addition, during the incubation time period, jet stream was only observed in the lubricant and water environment. A similar jet stream was never formed in the refrigerant.

Furthermore, it was interesting to observe the merging mechanism of the refrigerant bubbles. It was different to that of the lubricant or the water bubble. The merging is achieved by the powerful attraction of individual adjacent refrigerant bubbles to other unstable bubbles as the camera observations revealed.

Finally the actual impact pressure of the lubricant bubble is determined to be the highest among the testing liquids. Apparently the lubricant layer takes on the critical role of cushioning the jet impact, protecting the material surface. Thus the damage produced could be significantly less than expected. Overall refrigerant has the lowest impact pressure and it cannot be considered as a destructive medium of cavitation.

## **6.6.2 Experimental Results**

A comparison between the erosion damage produced on the steels' surface in their incubation and in their maximum erosion stage was conducted. The performances of the steels were thoroughly evaluated. The chromium steel had by far the best performance against cavitation erosion impact. Chromium steel was proved to be the most durable and resistant material compared to the other three steel samples.

### **6.6.2.1 Incubation Stage**

The experimental results of the bubble behaviour at the incubation stage are in a very good agreement with the photographic results. The water bubbles produce the maximum damage among steel samples, closely followed by the lubricant bubbles and finally by the refrigerant bubbles which have by far the smallest cavitation impact. Apparently, water provides the most hostile environment for the steel samples according to the growth and the size of the pits.

From the morphology evolution of the steel samples, it can be deduced that during the formation of the cavitation pits in the early stages of cavitation erosion, the best performance is exhibited by the chromium steel, closely followed by the high carbon steel, then the scroll's steel plate and finally the low carbon steel. The cavitation pits produced on the chromium surface in all the liquid environments are very superficial with the lowest depth and volume loss.

Interestingly, by observations of the damage area on the high carbon steel samples, the ultrasonic cavitation mechanism can be proposed as an alternative method for tiny hidden cracks to be revealed on the surface. A fluorescent dye penetration technique is often used to reveal any presence of surface cracks. However, this method takes time and the results are indistinct and hardly identifiable, especially when dealing with tiny superficial micro-cracks a few nanometres deep. Although cavitation is a destructive mechanism it can be considered to be an effective and rapid method for revealing nano-crack defects.

In addition, micro-tunnels found on the surface of the low carbon steel were successfully investigated. The micro-tunnel cavities produced by micro-jetting degradation can become sources of violent impact in the substrate of the material. The destructive implosion of tiny bubbles on the bottom of those apparently deep pits, can transfer a very intense shocking impact wave in the core of the substrate crystal structure of the material, accelerating its degradation rate.

### **6.6.2.2 Accelerated Stage**

The results of the present study show the performance of various steel grades with martensitic structure and different mechanical properties against cavitation damage. The erosion parameters were found to be significantly lower levels compared to the investigation in previous studies (see Chapter 2) where similar steel grades with austenitic structures and lower hardness values were used.

The evaluation of the SEM images and their corresponding graphs showed the nature of the damage mechanism on the steel samples. Low carbon steel suffers from severe ductile fracture due to low concentration in carbon, high concentration in phosphorous and sulphurous and low hardness. The erosion damage is rapidly developed after the end of the first stage. When the accumulated strain energy exceeds 2 mJ the erosion process is notable, leading to the next stage of large scale material removal and the formation of deep craters. The rest of the steel samples suffer from brittle fracture due to a high carbon concentration. Interestingly, mechanical properties and hardness play an important role in the steel performances. The steel plate having similar chemical composition to the high carbon steel but substantially lower hardness, shows a more ductile character as it acquires more accumulated strain energy in order to achieve the same level of damage with the corresponding one, measured on the high carbon steel sample. Finally, all the steel samples demonstrate a fatigue character induced by the level of the cavitation intensity, the bubble implosions and the amount of the pits and cracks on the surface of the samples. The fatigue process contributes to the accelerating failure of the steel samples.

Hardness is considered to be one of the key properties in cavitation resistance. It was also noticed that the increase of hardness increases the cavitation erosion resistance of the steel materials. Interestingly, the materials with the lower hardness suffered extensive wear damage at the end of the tests. In addition, the formation of martensitic lathings decelerates the penetration within the substrate of the material. Thus, steels with martensitic structure and high hardness properties can significantly enhance the lifetime and the mechanical endurance of a system.

On one hand, after the thorough investigation of the scroll working fluids it is found that the presence of refrigerant (rather than the liquid lubricant) as the major medium of cavitation within the scroll expander complies with the optimum scenario of keeping cavitation at low levels. Overall, cavitation within the refrigerant environment has the lowest impact on the steel surfaces. On the other hand, the steel plate is proved to be less resistant to cavitation than high carbon and chromium steel. Moreover the specific steel plate is the most expensive in the market among the tested samples. Thus the damage of the scroll by cavitation impacts can be significantly reduced by replacing the steel plate with a chromium steel plate.

### **6.6.3 Comparison Results**

The evaluation of the cavities, found on the surface of the original steel plate, according to their depth and the material loss, showed that the material damage can be correlated with the damage found in the sample of the steel plate after the first hour of test within water liquid. This comparative study revealed the real case scenario for the lifetime of the scroll. The maximum operational period without any critical drop of pressure according to the erosion rates (MER) of the scroll's actual steel plate was estimated to be around 12,000 hours. In addition, the depth of the cavities and their correlation with the erosion rate revealed refrigerant as the responsible medium of cavitation. Thus, as the erosion rate is low enough, refrigerant should be considered as the main reason for the generation of cavities within the scroll. The experimental results of Chapter 6 are in a good agreement with the analytical results of Chapter 3.

The REC of the chromium steel in the early stages of cavitation is 25% higher than that of the steel plate. If the scroll is supposed to operate for 30,000 hours the actual damage could be significantly higher since the steel plate suffers a steep reduction in its erosion resistance in the following hours. However a coherent estimation of the cavitation damage inside the scroll and its progress after a few thousand hours of running cannot be made since cavitation is a random phenomenon and refrigerant bubbles implode in a non-consistent way. In addition, as cavities are formed across the surface, cavitation will propagate easily increasing the depth of the existing cavities, hence the gaps and the leakage points will be enlarged.

Overall, at the early stage of the cavitation process, refrigerant bubbles have a low impact pressure and they cannot be considered to be a destructive medium of cavitation. However, over a prolonged period of time (1000 hours) the surface investigation revealed the critical damage produced by the refrigerant bubbles. Looking at the extent of damage between the

water and refrigerant bubbles it was found that refrigerant is 5 times less destructive than water according to their hydrodynamic behaviour and impact pressure. Moreover, the resistance of chromium steel over 8 hours of testing is 2 times higher than that of the actual steel plate.

The cavitation produced by the refrigerant is difficult to avoid due to the geometrical profile and the demanding environmental conditions of the scroll. However since refrigerant is the less severe medium of cavitation the other option would be to replace the actual steel plate of the scroll with a chromium steel one. Thus the damage produced after 1000 hours of the scroll expander's operational period can be significantly reduced. Eventually, the lifecycle and the durability of future scroll devices will be enhanced. The combination of the existent environment with chromium steel material can radically enhance the lifecycle of the scroll expander and the micro-CHP's system.

## **7 CHAPTER : CONCLUSIONS & FUTURE WORK**

### **7.1 Conclusions**

The wear mechanisms between the main interacting materials of the scroll are successfully indentified. Two-body abrasive wear prevails across the steel plate deriving from the consecutive asperity contact of the rubbing materials. Three-body abrasion wear is also indentified due to the sliding/rolling process of breakage steel and fibre debris. Cavitation is generated due to elevated pressure fluctuations. Refrigerant is the fluid medium which generates cavitation bubbles inside the high pressure gas pockets of the scroll expander. This finding resolves the question of how the refrigerant which enters the scroll in a gas phase produces cavitation. This is really an exceptional situation. Usually cavitation occurs in an environment where basically the fluid in motion is in liquid phase, which at low pressure is transformed into gas, producing cavitation bubbles. In this situation the fluid in motion is in gas phase, which is locally liquefied under very high pressure, producing cavitation bubbles within the high pressure region. It has not been possible to discover a similar finding in any published literature.

The understanding of the tribological friction and wear mechanisms, of the high carbon steel plate sliding against the high performance fluoroelastomer tip seal of the scroll expander, in dry and lubricated environment, under specific temperature, velocity and load conditions is achieved with the use of the TE 57 micro-friction machine. The results showed that for higher applied loads and sliding velocities, shearing prevails substantially softening the overall contact. The friction coefficient is thus decreased. By contrast for lower applied load and sliding velocities the real contact area prevails, restricting excessive shearing due to absence of elevated thermal effects. The friction coefficient is significantly increased. This result can be effectively used in the design of the scroll expander effectively improving the service life of the whole micro-CHP unit. Moreover the excellent performance of the hard fibres in reducing the friction coefficient and wear rates of the tested materials is highlighted. When the fillers stay well mounted within the matrix of the bulk elastomer material the contact is mainly confined between the embedded hard fibres of the elastomer composite slider and the steel counterface. Thus the friction coefficient rapidly increases. However, due to higher pressure contact and sliding velocities, contact temperature is elevated, which results in a serious softening of the elastomer matrix. Thus, fibre removal is seriously aggravated since the softened elastomer matrix is not capable of preventing fibres from peeling-off. The fibres emerge to the elastomer surface and their hard exposed surface interacts with the steel asperities producing abrasion lines across the steel surface. Interestingly, parallel nano-scale

linear strips were also detected on the surface of a typical worn fibre. Additionally the fibre's rolling effect is generated. The combination of the lubrication and adhesion contact with the rolling effect can substantially reduce the friction coefficient.

An effective correlation between the friction force, the friction coefficient and the wear rate parameters is achieved under specific lubricated regimes. In low sliding speeds the friction force proportionally increases with the increment of the applied load. Interestingly, in higher sliding speeds the friction force is also increased as the applied load is reduced, leading to higher friction coefficient values and more severe wear rates. This indicates that a severe contact between the exposed hard fibres and the steel asperities has occurred. Shearing is not a dominant factor and the real contact prevails. Consequently the friction coefficient and the wear rates are rapidly increased. Furthermore, according to friction coefficient graphs it was found that the wear rate of the steel samples increases according to the friction coefficient. Finally the effect of the sliding time is crucial for long working period applications like the scroll expander. The time-related wear rate for the 60-hour running experiment is significantly reduced and stabilized at 3 times less than the corresponding rate after 20 hours of running. This performance indicates a relaxation of contact is achieved after the running-in period, leading to a less severe regime.

A thorough evaluation of the tested lubricants is achieved and their impact on the actual contact is revealed. The condition of the oil samples and the interaction debris responsible for the wear damage are identified. The presence of ferrous and silicon debris within the lubricant solutions after the completion of the tests, justifies that the wear damage in both surfaces is derived from severe two- and three-body abrasion wear. Interestingly, the 150°C oil sample found that due to oil degradation replacement oil may subsequently be needed after a short period of time. A regular inspection of the oil performance within the scroll is required.

Consistent monitoring of the cavitation bubbles behaviour is achieved with the use of an appropriate experimental cavitation test rig integrated to a high speed camera. The lubricant and water bubbles have similar behaviour as they approach the rigid boundary. They expand in a continuous motion, due to pressure variations, keeping a spherical shape until they collapse. In the case of refrigerant, the pressure variations affect the shape but not the size of the bubbles decelerating the collapse process. Interestingly, during the inception of the ultrasonic horn, vapour bubbles are monitored to have emerged, and three different behaviours were observed. The water and lubricant bubbles implode generating hundreds of micro-bubbles diffused to the liquid with orientation to the boundary wall. The determinant is that the lubricant creates a film thickness which absorbs the destructive impact from the

imploding bubbles. When a refrigerant bubble collapses, micro-bubbles are generated, creating a “jelly” shaped cloud. Camera observations showed that the attraction forces between the refrigerant micro-bubbles are strong enough to prevent any bubble diffusion into the liquid refrigerant. Across the solid surface the refrigerant bubbles have a very peculiar performance. They obtained an amoeboid shape avoiding any regular implosions. This behaviour is due to the surface tension forces as they prevail to the viscous forces, sustaining an elongated bubbly morphology of the refrigerant cavities. The refrigerant bubbles can continue travelling in that amoeboid shape for a significant period of time prior to their collapse. Finally the actual impact pressure of the lubricant bubble is determined to be the highest among the testing liquids. Apparently the lubricant layer takes on the critical role of cushioning the jet impact, protecting the material surface. Thus the damage produced is significantly less than expected. Overall refrigerant has the lowest impact pressure.

Moreover, the most hostile liquid environment for the life-cycle of the tested materials is revealed. The water bubbles produce the maximum damage among the steel samples, closely followed by the lubricant bubbles and finally by the refrigerant bubbles which have by far the smallest cavitation impact. Therefore water provides the most hostile environment for the steel samples according to the growth and the size of the pits. Additionally, from the morphology evolution of the steel samples, it can be deduced that during the formation of the cavitation pits in the early stages of cavitation erosion, the best performance is exhibited by the chromium steel, closely followed by the high carbon steel, then the scroll's steel plate and finally the low carbon steel. The cavitation pits produced on the chromium surface in all the liquid environments are very superficial with the lowest depth and volume loss. Moreover, micro-tunnels found on the surface of the low carbon steel were successfully investigated.

An effective correlation between the volume loss, the cavitation erosion rate, the strain energy and the hardness of 4 different steel grade materials including the actual steel plate of the scroll is achieved. The results from the initiation of the cavitation pits in correlation with the results over a prolonged period of time revealed the endurance of the materials against cavitation attack. The chromium steel was found to be 25% more durable and tougher than the actual steel plate of the scroll during the 1 hour and the 8 hours of testing. Thus, chromium steel will initially delay the formation of the cavities, restricting and slowing down the erosion damage growth while after a prolonged period of time it would prevent any steep increment of the erosion rates.

Moreover a comparative study revealed the real case scenario for the lifetime of the scroll prior to be failed by the cavitation mechanism. The maximum operational period without any

critical drop of pressure according to the erosion rates (MER) of the scroll's actual steel plate was estimated to be around 12,000 hours. However alterations of the geometric profile of the scroll expander (e.g increasing the inlet port diameter, the height of the spiral wall or diverted the nozzle) could possibly minimize the possibility of cavitation mechanism development. On the other hand such a decision carries significant risks. The performance of the scroll can be seriously affected and the efficiency of the micro-CHP unit will be significantly reduced. Thus, since the geometry and the ambient environmental conditions of the scroll are not to be changed, the safest option is to enhance the lifetime of the scroll device by replacing the components which underwent cavitation damage by similar cheaper and stronger materials like chromium steel.

## **7.2 Future Work**

### **7.2.1 Sliding Wear**

Sliding friction/wear experiments will be performed using the tip seal/steel plate contact under various refrigerant/lubricant combinations in order that the wear and friction mechanisms can be assessed. This will be performed using a special modified test rig of the existing TE 57 sliding micro-friction machine (figure 156). A viscosity device will be integrated into the circulation loop to monitoring the viscosity, the density and the shear stress of the refrigerant/lubricant mixture in various pressure and temperature conditions. Additionally, a second pressurized chamber will be deployed to mix the refrigerant with the lubricant prior to it being fed into the circulation pipes. The mixture will then be introduced to the environmental chamber and the sliding wear/friction process will start.

Preliminary tests of the steel plate against the elastomer tip seal under liquid lubricated mixture (lubricant/refrigerant) were conducted with the TE 57 sliding micro-friction machine. The ambient conditions for the experiments were adjusted at 40 °C temperature and 1 atm pressure. The preliminary results showed that refrigerant can seriously reduce the friction coefficient of the specific contact surface. Specifically the addition of refrigerant increases the friction coefficient by about 20-40% at higher speeds (50 Hz) and 50-70% at lower speeds (25 Hz). This can prove crucial for higher operating temperatures and longer time duration tests. As the wear rate proportionally increases with the friction coefficient, as this study revealed, the specific wear rate can be significantly increased under more demanding operating conditions.

Moreover, a comparative study of the dry contact wear rates to the lubricated ones is required. It is suggested by J. Jia et al [91] and O. Jacobs et al [93] that the wear rates of a

steel/polymer contact under lubrication conditions are increased. Thus, a further study of the wear rates of the specific steel/elastomer contact, of this project, under dry sliding conditions could be an important issue for consideration. Subsequently, a complete investigation and a coherent interpretation of the tribological performance of the steel plate against the tip seal under both contact (dry/lubricated) regimes, could be conducted.

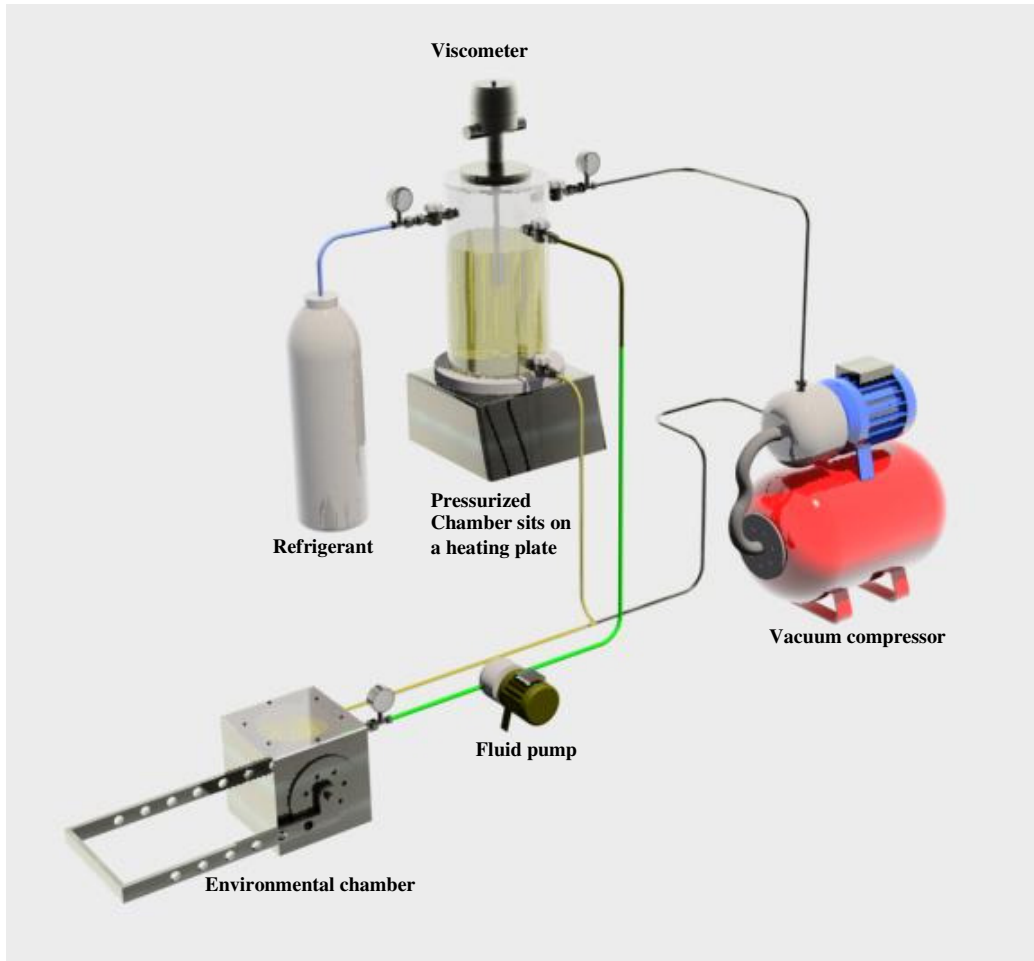


**Figure 156: Schematic representation of the modified TE 57 test rig**

Furthermore, the use of a thermal camera will enable the researcher to control and measure the temperature between the two rubbing surfaces of the tip seal and the steel plate (figure 157). The critical temperatures for polymer melting will be correlated with the variations of the applied load and the different sliding speeds. Thus, a coherent determination of the thermal effects with the friction and wear parameters of the specific steel/elastomer contact will be achieved. Consequently, instant alterations of the wear regime will be precisely determined.

Finally, a coherent interpretation of the main interaction wear mechanisms between the sliding walls of the scroll is needed. The adhesion component seems to prevail while the nature of the contact gradually changes, accelerating the wear rates across the side walls. Thus, a thorough tribological investigation with the use of the TE 57 micro-sliding machine of the coating wall against the aluminium side wall of the scroll under sliding lubricated conditions is suggested. The specific experimental procedure is considered to be essential in maintaining a quality performance of the scroll. Eventually the overall lifecycle of the micro-CHP unit will be enhanced. Additionally, with the use of the thermal images the dissipation of the frictional heat and the temperature augmentation within the lubricant can be estimated. This will also reveal the real temperature conditions developed within the ambient environment of the scroll expander in a real case scenario.

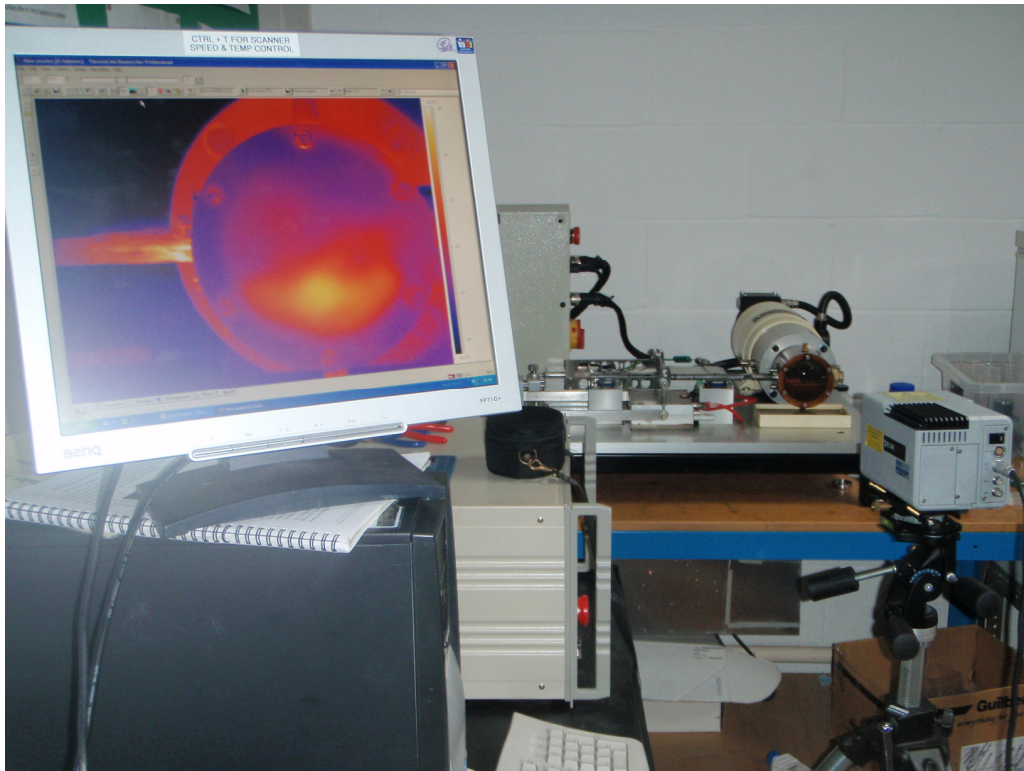


**Figure 157:** The thermal imaging system FLIR ThermoCAM SC3000 integrated to the TE 57 sliding micro-friction machine.

### **7.2.2 Cavitation**

A suitable viscosity measurement apparatus based on the current state of the art will be designed and assembled. With the use of the specific apparatus (figure 158) the lubricant/refrigerant physical properties will be measured in various temperature and pressure

conditions. This will enable the researcher to accurately determine the viscosity, the density, the surface tension and the shear stress of the mixture. Moreover the miscibility of the mixture can also be measured with the use of an appropriate sensor. The percentage of the refrigerant/lubricant miscibility will be correlated with the apparent friction and wear contact. Finally the vapour pressure of the mixture at different temperatures and various refrigerant concentrations will be measured. This can be done with the use of a typical technique called thermogravimetry.

The measurements of the above values will provide the researcher with suitable correlations of the cavitation mechanisms over the physical properties of the mixture refrigerant/lubricant. Thus, the probability of the generation of cavitation bubbles for the refrigerant/lubricant mixture during the operation of the scroll expander, in the critical area of the suction port, will be accurately determined. In addition with the results from the above measurements, the performance of the lubricant will be determined while the lubrication regime will be interpreted across that area.

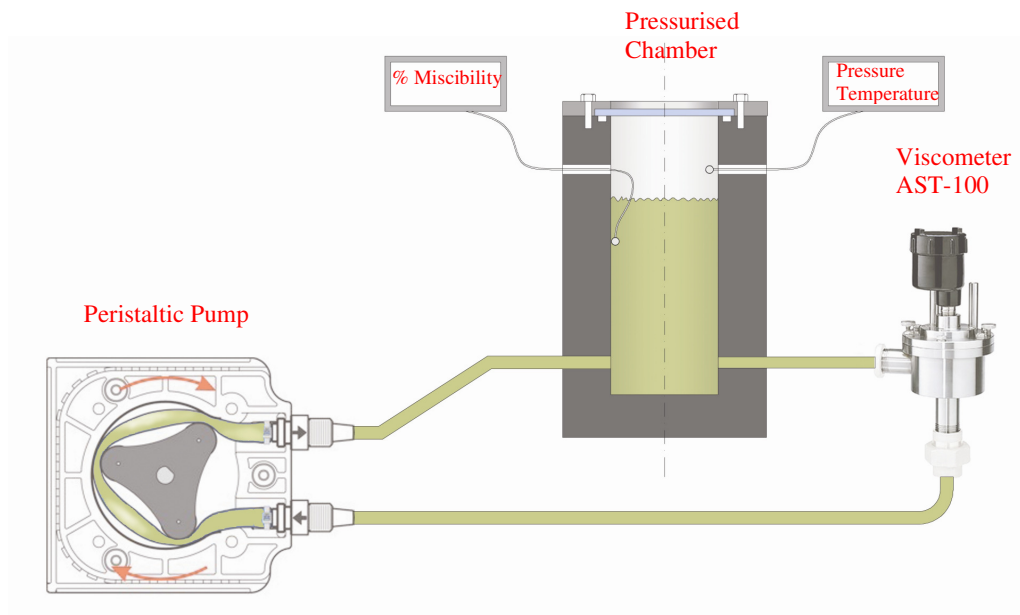


**Figure 158: Schematic representation of the viscosity test rig.**

The above results in combination with the design concepts of the scroll expander will help to improve the design parameters of the scroll. Thus the mechanical performance and efficiency of the scroll will be improved while the cavitation phenomena and the excessive wear mechanisms will be constrained to a minimum extent.

Furthermore an analytical 3D simulation of the working fluid performance when it is instantly introduced inside the central expansion chamber of the scroll has to be performed. This will show in detailed the alteration of the initial environmental conditions with respect to time and the orbiting movement of the scroll. The cavitation impact regions onto the main components of the scroll during the expansion process will be also determined.

Finally with the use of a thermal camera, the temperature distribution during the miscibility of the fluids inside the chamber will be monitored. This will help in the interpretation and the control of the miscibility mechanism of the tested liquids. Apparently the cavitation mechanisms can be further restricted.

# Appendices

## Appendix A: Auxiliary devices for experimental preparation



**Figure 159: A) Mounting press B) Polishing wheels C) Cutting machine D) Ultrasonic bath**

The sample was initially cut in appropriate shape and dimensions by the cutting machine and then was installed into the chamber of the mounting press where Bakelite powder was added. The sample when mounted on the Bakelite base sample was sent for grinding and polishing. Special polishing pastes and lubricants were used. Finally the steel sample was send into an ultrasonic bath for thorough cleaning. This same cleaning process was also used after the end of the some of the experiments.

## Appendix B: Chemical analysis-Characteristic analysis tables of the steel samples

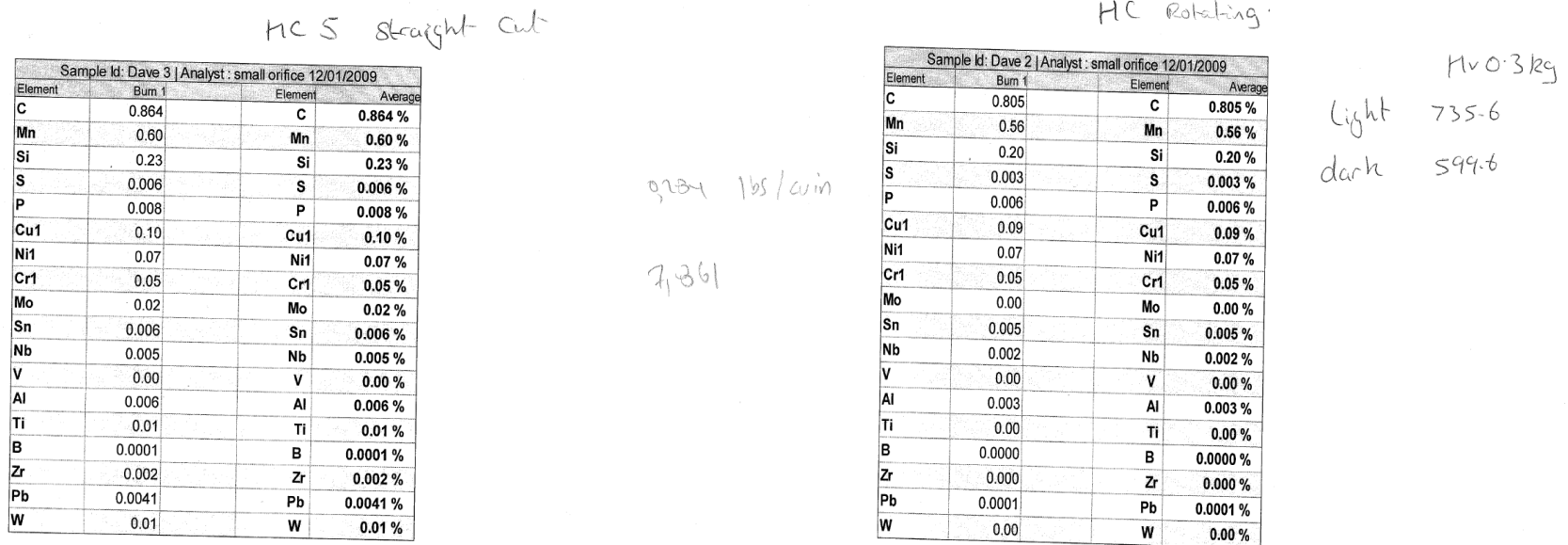


Figure 160: High carbon steel chemical analysis/Raw data

## Appendix B: Chemical analysis-Characteristic analysis tables of the steel samples (continued)

CR

Sample Id: Dave 4   Analyst: small orifice 12/01/2009			
Element	Burn 1	Element	Average
C	1.048	C	1.048 %
Mn	0.31	Mn	0.31 %
Si	0.19	Si	0.19 %
S	0.003	S	0.003 %
P	0.010	P	0.010 %
Cu1	0.11	Cu1	0.11 %
Ni1	0.07	Ni1	0.07 %
Cr1	1.58	Cr1	1.58 %
Mo	0.02	Mo	0.02 %
Sn	0.009	Sn	0.009 %
Nb	0.002	Nb	0.002 %
V	0.00	V	0.00 %
Al	0.005	Al	0.005 %
Ti	0.00	Ti	0.00 %
B	0.0004	B	0.0004 %
Zr	0.000	Zr	0.000 %
Pb	0.0001	Pb	0.0001 %
W	0.00	W	0.00 %


  
 Light -> Ferrite  
 Dark -> Perlite

LC ?

Sample Id: Dave B   Analyst: small orifice 12/01/2009			
Element	Burn 1	Element	Average
C	0.910	C	0.910 %
Mn	0.31	Mn	0.31 %
Si	0.24	Si	0.24 %
S	0.005	S	0.005 %
P	0.015	P	0.015 %
Cu1	0.16	Cu1	0.16 %
Ni1	0.15	Ni1	0.15 %
Cr1	1.45	Cr1	1.45 %
Mo	0.05	Mo	0.05 %
Sn	0.033	Sn	0.033 %
Nb	0.006	Nb	0.006 %
V	0.01	V	0.01 %
Al	0.011	Al	0.011 %
Ti	0.01	Ti	0.01 %
B	0.0005	B	0.0005 %
Zr	0.002	Zr	0.002 %
Pb	0.0087	Pb	0.0087 %
W	0.02	W	0.02 %

No. 3 kg.  
 792-9  
 806-4  
 Corrosion Area  
 882-1  
 886-1  
 2% HNO<sub>3</sub> Nitric acid  
 in meths / methanol.  
 98% meths  
 acid -> meth  
Nital

Figure 161: Chromium steel chemical analysis/Raw data

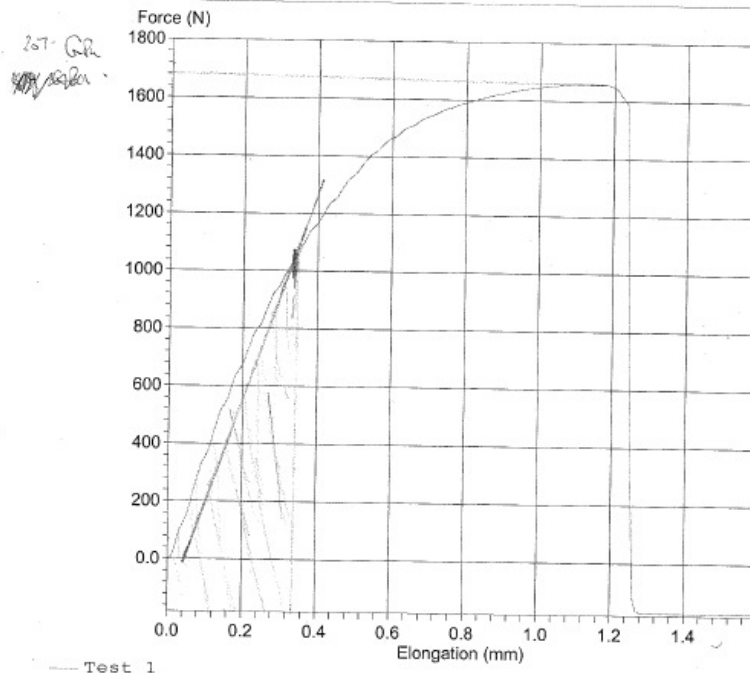
## Appendix C: High carbon steel plate tensile test

Ref 1 :  
 Ref 2 :  
 Ref 3 :  
 Test Name : Steel Plate  
 Test Type : Tensile  
 Test Date : 01/07/2009 14:55

Test Speed : 6.00 mm/min  
 Width : 4.200 mm  
 Thickness : 0.300 mm  
 Pretension : Off  
 Sample Length : 20.000 mm

Test No	Youngs Modulus (N/mm <sup>2</sup> )	Elong. @ Break (mm)	Stress @ Peak (N/mm <sup>2</sup> )	Strain @ Peak (%)
1	208517	1.6000	1318.3	5.7000

STEEL PLATE



Elastic:  $F = 1020 \text{ N}$

$A = 0,3 \times 4,2 = 1,26 \text{ mm}^2$

$\Rightarrow P = 810 \text{ N/mm}^2 \Rightarrow$

$P = 810 \text{ MPa}$

Elastic:  $F = 1680 \text{ N}$

$P = 1,35 \text{ GPa}$

## Appendix D: Tables of $\tau_0$ and $\alpha$ in regards to the applied pressure

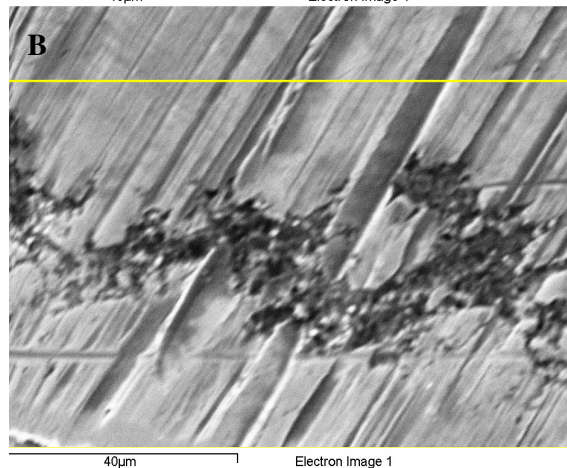
Metal	$\alpha$	$\tau_0$ (Mpa)	$\mu_{\text{eff}}$ (at $p=1\text{MPa}$ )
Fe	0.075	173.82	0.246
Cu	0.049	107.61	0.16
Ag <sup>a</sup>	0.036	109.04	0.144
Au	0.029	91.82	0.123
Al	0.035	47.56	0.082
Sn <sup>a</sup>	0.012	12.3	0.024
In <sup>a</sup>	0.006	5.65	0.011

Table 15: Dependence of saturation shear strength and friction of metals on the applied pressure (<sup>a</sup> Commonly used solid lubricants) [207]

## Appendix E: Evidence of corrosion within the cavities of the steel plate of the SE<sub>1000</sub>



Element	Weight%	Atomic%
P K	1.03	1.84
S K	0.44	0.76
K K	0.62	0.88
Fe K	95.83	94.93
Cu K	0.88	0.76
Br L	1.2	0.83
Totals	100	



Element	Weight%	Atomic%
O K	11.47	30.61
P K	1.93	2.66
S K	0.8	1.06
K K	0.76	0.83
Mn K	0.73	0.57
Fe K	82.65	63.16
Cu K	1.65	1.11
Totals	100	

Figure 162: Two different regions of cavities A) Typical cavities B) Cavities with accumulated Oxygen. The cluster of cavities with O<sub>2</sub> is distinctive showing a corrosive pattern rather than a cluster of typical cavitation craters and cracks (the yellow lines indicating the analysis area).

## Appendix F: Calculation of the contact load within the scroll expander

Scroll with Seal				Friction Coefficient		
Load (kg)	Weigth (kg)	Weigth of Scroll (kg)	Scroll with Seal	0.196	0.212	
4.5	0.55	0.332	Scroll Without Seal	0.185		
4.5	0.55	0.332	Scroll with Seal and Lubricant	0.241		
4.5	0.55	0.332				
4.5	0.55	0.332				
<b>4.5</b>	<b>0.55</b>	<b>0.332</b>	Start Up Conditions of the Scroll			
Load (kg)	Weigth (kg)	Weigth of Scroll (kg)	Measurments	A	B	C
5	0.800	0.332	Friction Torque (Nm)	1	1	1
5	0.700	0.332	Friction Coefficient	0.241	0.2	0.25
5	0.740	0.332	Radius of Ecentricity (m)	0.005	0.005	0.005
5	0.680	0.332				
<b>5</b>	<b>0.730</b>	<b>0.332</b>	Contact Load (N)	<b>829.876</b>	<b>1000</b>	<b>800</b>
Scroll Without Seal						
Load (kg)	Weigth (kg)	Weigth of Scroll (kg)	Area (mm <sup>2</sup> )	2320		
5	0.6	0.33	Sample Area (mm <sup>2</sup> )	25		
5	0.59	0.33	Number of Samples	92.80		
5	0.59	0.33		90		
5	0.6	0.33				
5	0.59	0.33	Contact Load Per Sample in TE 57 (N)	9.221	11.111	8.889
<b>5</b>	<b>0.594</b>	<b>0.33</b>				
Scroll with Seal and Lubricant						
Load (kg)	Weigth (kg)	Weigth of Scroll (kg)	Contact Pressure Measurements			
5	0.870	0.332	Contact Pressure (Mpa) inside scroll	0.36	0.43	0.34
5	0.850	0.332	Contact Pressure (Mpa) per sample TE 57 20N	0.80		
5	0.900	0.332	Contact Pressure (Mpa) per sample TE 57 40N	1.60		
<b>5</b>	<b>0.873</b>	<b>0.332</b>				

## Appendix G: Friction/Wear results (A)

**Process:** Characterization of the contact nature of the steel plate versus the tip seal for dry and lubricated conditions

**Test Rig:** TE 57 sliding micro-friction machine.

**Materials:** High carbon steel plate against the high performance reinforced fluoroelastomer tip seal

Friction Coefficient				Velocity (m/sec)			Load (N)	Ratio V/L		
50Hz (Lub)	20 Hz (Dry)	25 Hz (Dry)	50 Hz (Dry)					20 Hz	25 Hz	50 Hz
0.019	0.027	0.032	0.06	0.2	0.25	0.5	40	0.0050	0.0063	0.0125
0.021	0.028	0.035	0.067	0.2	0.25	0.5	35	0.0057	0.0071	0.0143
0.025	0.03	0.038	0.076	0.2	0.25	0.5	30	0.0067	0.0083	0.0167
0.031	0.032	0.041	0.085	0.2	0.25	0.5	25	0.0080	0.0100	0.0200
0.045	0.034	0.044	0.102	0.2	0.25	0.5	20	0.0100	0.0125	0.0250
0.065	0.037	0.046	0.14	0.2	0.25	0.5	15	0.0133	0.0167	0.0333
0.1	0.042	0.049	0.202	0.2	0.25	0.5	10	0.0200	0.0250	0.0500
0.162	0.047	0.05	0.3	0.2	0.25	0.5	5	0.0400	0.0500	0.1000

## Appendix G: Friction/Wear results (B)

**Process: Pin on Plate sliding contact**

**Test rig: TE 57 sliding micro-friction machine.**

**Materials: High carbon steel plate against the high performance reinforced fluoroelastomer tip seal**

**Experimental Data of High carbon steel against reinforced fluoroelastomer (Pin on Plate Contact)**

Tests	Conditions	Stroke (mm)	Time (sec)	Frequency (Hz)	Average Velocity (m/sec)	Normal Load (N)	Contact Area ( mm <sup>2</sup> )	Contact Pressure (MPa)	Sliding Distance (m)
1	40°C-25Hz-20h	10	72000	25	0.25	20	25	0.80	18000
2	40°C-25Hz-20h	10	72000	25	0.25	40	25	1.60	18000
3	40°C-50Hz-20h	10	72000	50	0.5	20	25	0.80	36000
4	40°C-50Hz-20h	10	72000	50	0.5	40	25	1.60	36000
5	100°C-25Hz-20h	10	72000	25	0.25	20	25	0.80	18000
6	100°C-25Hz-20h	10	72000	25	0.25	40	25	1.60	18000
7	100°C-50Hz-20h	10	72000	50	0.5	20	25	0.80	36000
8	100°C-50Hz-20h	10	72000	50	0.5	40	25	1.60	36000
9	150°C-25Hz-20h	10	72000	25	0.25	20	25	0.80	18000
10	150°C-25Hz-20h	10	72000	25	0.25	40	25	1.60	18000
11	150°C-50Hz-20h	10	72000	50	0.5	20	25	0.80	36000
12	150°C-50Hz-20h	10	72000	50	0.5	40	25	1.60	36000
13	40°C-50Hz-60h	10	216000	50	0.5	20	25	0.80	108000
14	100°C-50Hz-60h	10	216000	50	0.5	20	25	0.80	108000
15	150°C-50Hz-60h	10	216000	50	0.5	20	25	0.80	108000

**Appendix G: Friction/Wear results (B continued)**

<b>Wear/Friction Measurements of High carbon steel against reinforced fluoroelastomer (Pin on Plate Contact)</b>				
<b>Tests</b>	<b>Wear Volume Loss (mm<sup>3</sup>)</b>	<b>Specific Wear Rate (mm<sup>3</sup>/Nm)</b>	<b>Wear Resistance (Nm/mm<sup>3</sup>)</b>	<b>Time Related Depth Wear (mm/sec)</b>
1	1.01E-02	2.81E-08	3.56E+07	5.62E-09
2	6.02E-03	8.36E-09	1.20E+08	3.34E-09
3	1.42E-02	1.97E-08	5.08E+07	7.87E-09
4	1.24E-02	8.61E-09	1.16E+08	6.89E-09
5	1.72E-02	4.79E-08	2.09E+07	9.58E-09
6	6.50E-03	9.03E-09	1.11E+08	3.61E-09
7	2.01E-02	2.80E-08	3.57E+07	1.12E-08
8	1.50E-02	1.04E-08	9.61E+07	8.32E-09
9	2.24E-02	6.22E-08	1.61E+07	1.24E-08
10	2.06E-02	2.86E-08	3.50E+07	1.14E-08
11	6.76E-02	9.38E-08	1.07E+07	3.75E-08
12	3.17E-02	2.20E-08	4.55E+07	1.76E-08
13	1.37E-02	6.33E-09	1.58E+08	2.53E-09
14	2.71E-02	1.26E-08	7.96E+07	5.03E-09
15	7.80E-02	3.61E-08	2.77E+07	1.44E-08

## Appendix G: Friction/Wear results (B continued)

<b>Wear/Friction Measurements of High carbon steel against reinforced fluoroelastomer (Pin on Plate Contact)</b>					
<b>Tests</b>	<b>PV (Mpa *m/sec)</b>	<b>Roughness Ra (µm)</b>	<b>Roughness RMS (µm)</b>	<b>Friction Coefficient</b>	<b>Thermal Density Flow (W/m<sup>2</sup>)</b>
1	0.2	0.7	0.8	0.014	4375
2	0.4	0.5	0.65	0.008	1250
3	0.4	0.5	1	0.07	87500
4	0.8	0.55	0.65	0.025	15625
5	0.2	0.4	0.6	0.017	5312.5
6	0.4	0.2	0.225	0.012	1875
7	0.4	0.575	0.65	0.085	106250
8	0.8	0.6	0.85	0.035	21875
9	0.2	0.6	0.85	0.014	4375
10	0.4	0.4	0.5	0.015	2343.75
11	0.4	1.4	1.7	0.11	137500
12	0.8	1	1.3	0.04	25000
13	0.4	0.6	0.8	0.065	81250
14	0.4	0.45	0.4	0.085	106250
15	0.4	0.9	1.2	0.105	131250

## Appendix H: Oil Analysis/ISO Cleanliness Codes

ISO 4406:1999 Code Chart		
Particles per millilitre		
Range Code	More than	Up to/ Including
24	80000	160000
23	40000	80000
22	20000	40000
21	10000	20000
20	5000	10000
19	2500	5000
18	1300	2500
17	640	1300
16	320	640
15	160	320
14	80	160
13	40	80
12	20	40
11	10	20
10	5	10
9	2.5	5
8	1.3	2.5
7	0.64	1.3
6	0.32	0.64

Figure 163: The ISO 4406 standard. Classifies system cleanliness and determines particle counts in lubricants.

## Appendix I: Surface Tension Measurements for various liquids

**Process:** Measuring the surface lift of various liquids

**Test rig:** Optical microscope/Orifice tubes

**Tested Liquids:** Distilled water, Refrigerant, Lubricant 170, Lubricant 22

Surface Tension (N/m)					
In Various Liquids	Lift dh (m)	Density $\rho$ (kg/m <sup>3</sup> )	Gravitational Force g (m/sec <sup>2</sup> )	Diameter d (m)	Surface Tension $\sigma$ (mN/m)
Lubricant 22	0.00215	995	9.81	0.01	52.47
Pentane	0.0023	625	9.81	0.01	35.25
Water	0.0024	1000	9.81	0.01	58.86
Lubricant 170	0.00245	968	9.81	0.01	58.16

## Appendix J: Cavitation-Erosion Test results (A)

**Process:** Camera observations with the use of a high speed camera

**Test rig:** Ultrasonic cavitation apparatus integrated to a high speed camera

**Tested Liquids:** Distilled water, Refrigerant, Lubricant

Typical Cavitation Bubble Performance for Various Liquid Environments					
Bubble Performance in Distilled Water Environment					
Bubbles Radius ( $\mu\text{m}$ )	Time ( $\mu\text{sec}$ )	Bubbles Velocity (m/sec)	Boundary Distance ( $\mu\text{m}$ )	Normalised Distance ( $\gamma$ )	Average Jet Velocity (m/sec)
28	10	0.4	310	12.07	
24	20	0.6	302	13.58	
30	30	6	288	10.6	
90	40	7	220	3.44	18
20	50	0.5	240	13	18
25	60	2.5	180	8.2	
50	70	3.4	160	4.2	
84	80	2.4	160	2.9	16.8
60	90	2	140	3.33	16.8
40	100	1	110	3.75	
30	110	1.1	105	4.5	
19	120	2.1	95	6	
40	130	2	55	2.38	
60	140	3.1	40	1.67	
91	150	8.3	8	1.09	18.2
8	160				18.2

## Appendix J: Cavitation-Erosion Test results (A continued)

Typical Cavitation Bubble Performance for Various Liquid Environments					
Bubble Performance in Pentane Environment					
Bubbles Radius ( $\mu\text{m}$ )	Time ( $\mu\text{sec}$ )	Bubbles Velocity (m/sec)	Boundary Distance ( $\mu\text{m}$ )	Normalise Distance ( $\gamma$ )	Average Jet Velocity (m/sec)
50	10	1.2	196	4.92	
38	20	0.8	215	6.66	
30	30	1.4	214	8.13	
44	40	1.6	203	5.61	
60	50	0.5	171	3.85	
55	60	0.5	160	3.91	
50	70	0.5	159	4.18	
45	80	1	144	4.2	
55	90	0.3	128	3.33	
52	100	1.6	116	3.23	
36	110	1.1	115	4.19	
25	120	1.1	113	5.52	
36	130	1.9	99	3.75	
55	140	0.3	55	2	
58	150	3.7	8	1.14	11.6
21	160		0	1	11.6

## Appendix J: Cavitation-Erosion Test results (A continued)

Typical Cavitation Bubble Performance for Various Liquid Environments					
Bubble Performance in Lubricant Environment					
Bubbles Radius ( $\mu\text{m}$ )	Time ( $\mu\text{sec}$ )	Bubbles Velocity (m/sec)	Boundary Distance ( $\mu\text{m}$ )	Normalise Distance ( $\gamma$ )	Average Jet Velocity (m/sec)
50	10	3.5	99	2.98	
15	20	0.5	127	9.47	
20	30	2	120	7	
40	40	4	104	3.6	
80	50	2	60	1.75	
100	60	8.6	49	1.49	20
14	70	1.6	87	7.21	20
30	80	3	51	2.7	
60	90	2	28	1.47	
80	100	6.5	14	1.18	16
15	110	0.7	67	5.47	16
22	120	4.8	84	4.82	
70	130	2	45	1.64	
90	140	1.5	28	1.31	
105	150	1.5	20	1.19	
120	160	0.59375	15	1.13	24
25	170		0	1	24

## Appendix J: Cavitation-Erosion Test results (B)

Micro Jet Impact during the implosion of the bubble					
Liquid Environment	Time Step (µsec)	Normalise Distance (γ)	Velocity of the Micro-Jet (m/sec)	Impact Pressure (MPa)	Impact Pressure Regime
Water	40	3.75	1247.26	1840.96	Liquid-Liquid Impact
Water	150	1.11	109.28	161.30	Liquid-Solid Impact
Pentane	150	1.14	98.74	62.11	Liquid-Solid Impact
Lubricant	60	1.49	198.34	335.49	Liquid-Liquid Impact
Lubricant	100	1.18	124.40	210.41	Liquid-Liquid Impact
Lubricant	160	1.13	114.08	192.96	Liquid-Solid Impact

Microbubble Impact during the implosion of the bubble-Solid/Liquid Impact					
Liquid Environment	Time Step (µsec)	Microbubble Radius (µm)	Normalise Distance (γ)	Velocity of the Micro-Jet (m/sec)	Impact Pressure (MPa)
Water	150	9.1	1.88	313.19	462.27
Pentane	150	5.8	2.38	438.82	271.52
Lubricant	160	12.0	2.25	452.28	765.03
Microbubble Impact during the implosion of the bubble-Liquid/Liquid Impact					
Water	40	9.0	25.44	57422.38	84755.43
Pentane	50	No Collapse	No Collapse	No Collapse	No Collapse
Lubricant	60	10.0	5.90	3109.88	5260.36

Measurements of the maximum bubble energy of the bubble prior to collapse								
Liquids	Time step (sec)	Acoustic Power (Watt)	Impact Pressure (Mpa)	Viscosity (mPas)	Static Pressure (Pa)	Vapour Pressure (Pa) at 20°C	R <sub>max</sub> (m)	Bubble Energy (mJ)
Lubricant	150	9	236.81	30	100000	1300	0.00012	3.38E-04
Pentane	150	3	30.94	0.225	100000	53328	5.50E-05	6.81E-05
Water	160	6	132.84	1	100000	2230	0.000091	3.11E-04

## Appendix J: Cavitation-Erosion Test results (C)

**Process:** After test hardness measurements (3-hour, 5-hour and 8-hour)

**Test equipment:** Micro-hardness machine

**Materials:** Scroll: High carbon steel plate, Market steels: High carbon, Low carbon and Chromium

<b>Hardness Measurements</b>												
<b>3 Hours Experiments</b>												
<b>Steel Samples</b>	Point 1	Point 2	Point 3	Point 4	Point 5	Point 6	Point 7	Point 8	Point 9	Point 8	Point 7	Point 6
<b>Chromium</b>	876	876	839	839	876	876	891	805	686	805	891	876
<b>High Carbon</b>	805	757	686	686	713	772	805	660	636	660	805	772
<b>Low Carbon</b>	820	660	467	426	515	482	439	413	378	413	439	482
<b>Steel Plate</b>	533	533	533	571	551	551	545	482	467	482	545	551
<b>5 Hours Experiments</b>												
<b>Steel Samples</b>	Point 1	Point 2	Point 3	Point 4	Point 5	Point 6	Point 7	Point 8	Point 9	Point 8	Point 7	Point 6
<b>Chromium</b>	839	876	839	805	839	839	805	713	660	713	805	839
<b>High Carbon</b>	876	839	805	805	839	839	742	686	636	686	742	839
<b>Low Carbon</b>	839	686	551	660	551	533	533	498	439	498	533	533
<b>Steel Plate</b>	515	515	498	498	515	515	482	467	453	467	482	515
<b>8 Hours Experiments</b>												
<b>Steel Samples</b>	Point 1	Point 2	Point 3	Point 4	Point 5	Point 6	Point 7	Point 8	Point 9	Point 8	Point 7	Point 6
<b>Chromium</b>	876	805	742	958	876	742	742	713	636	713	742	742
<b>High Carbon</b>	821	805	378	591	805	713	742	571	378	571	742	713
<b>Low Carbon</b>	805	533	358	453	482	467	428	439	330	439	428	467
<b>Steel Plate</b>	571	561	571	482	515	515	453	439	416	439	453	515
<b>Steel Plate</b>	571	561	571	482	515	515	453	439	416	439	453	515

## Appendix J: Cavitation-Erosion Test results (D)

Process: Characterization of the ring areas (prolonged period of time)

Test equipment: Zygo interferometer microscope

Materials: Scroll expander: High carbon steel plate, Market steels: High carbon, Low carbon and Chromium

Ring Areas Characterization						
Chromium Sample	Time Steps (hours)	Roughness (Ra) ( $\mu\text{m}$ )	Roughness (rms) ( $\mu\text{m}$ )	Average Depth ( $\mu\text{m}$ )	Maximum Depth ( $\mu\text{m}$ )	Volume Remove ( $\text{mm}^3$ )
Pits	1	0.045	0.065	0.15-0.25	0.3	8.44E-05
Pits	2	1.9	2.8	7-12	14	6.00E-04
Crater	3	1	1.5	8.5	14	1.44E-03
Crater	5	8.8	10.5	36	50	2.04E-02
Crater	8	11.8	14.2	48	54	3.80E-02
High Carbon Sample	Time Steps (hours)	Roughness (Ra) ( $\mu\text{m}$ )	Roughness (rms) ( $\mu\text{m}$ )	Average Depth ( $\mu\text{m}$ )	Maximum Depth ( $\mu\text{m}$ )	Volume Remove ( $\text{mm}^3$ )
Pits	1	0.115	0.2	0.1-0.15	0.2	1.82E-04
Pits	2	1.7	2.4	3-7	12	1.26E-03
Crater	3	1.5	2.5	8	12	2.70E-03
Crater	5	5.6	6.3	15	21	2.20E-02
Crater	8	11	12.8	42	45	4.60E-02
Low Carbon Sample	Time Steps (hours)	Roughness (Ra) ( $\mu\text{m}$ )	Roughness (rms) ( $\mu\text{m}$ )	Average Depth ( $\mu\text{m}$ )	Maximum Depth ( $\mu\text{m}$ )	Volume Remove ( $\text{mm}^3$ )
Pits	1	0.275	0.4	0.12-0.25	0.3	2.21E-04
Crater	2	5.1	6	18	22	6.20E-03
Crater	3	4.8	6.1	23	35	1.62E-02
Crater	5	9.1	11.8	40	49	3.08E-02
Crater	8	21.3	29.2	115	182	7.80E-02
Steel Plate Sample	Time Steps (hours)	Roughness (Ra) ( $\mu\text{m}$ )	Roughness (rms) ( $\mu\text{m}$ )	Average Depth ( $\mu\text{m}$ )	Maximum Depth ( $\mu\text{m}$ )	Volume Remove ( $\text{mm}^3$ )
Pits	1	0.22	0.35	0.15-0.25	0.3	1.12E-04
Pits	2	0.4	0.65	3	5	6.60E-04
Crater	3	3.6	2.4	12	16	3.10E-03
Crater	5	3.8	5	18	23	9.60E-03
Crater	8	16.4	21.5	75	94	5.00E-02

## Appendix J: Cavitation-Erosion Test results (D continued)

<b>Chromium Sample</b>	<b>Ring Eroded Area (mm<sup>2</sup>)</b>	<b>Eroded Area (mm<sup>2</sup>)</b>	<b>MER (μm/h)</b>	<b>REC (h/μm)</b>	<b>MER on Crater (μm/h)</b>	<b>REC on Crater (h/μm)</b>	<b>MDE (μm)</b>	<b>Strain Energy (mJ)</b>
Pits	0.02	15	5.627E-03	177.73	2.11	0.47	0.006	0.84
Pits	0.2	15	2.000E-02	50.00	0.75	1.33	0.040	5.97
Crater	0.25	15	3.200E-02	31.25	0.96	1.04	0.096	14.33
Crater	0.9	15	2.720E-01	3.68	2.27	0.44	1.360	203.06
Crater	1.1	15	3.167E-01	3.16	2.16	0.46	2.533	378.25
<b>High Carbon Sample</b>	<b>Ring Eroded Area (mm<sup>2</sup>)</b>	<b>Eroded Area (mm<sup>2</sup>)</b>	<b>MER (μm/h)</b>	<b>REC (h/μm)</b>				
Pits	0.035	15	1.211E-02	82.60	2.59	0.39	0.012	0.21
Pits	0.4	15	4.200E-02	23.81	0.79	1.27	0.084	1.49
Crater	0.4	15	6.000E-02	16.67	1.13	0.89	0.180	3.20
Crater	0.785	15	2.933E-01	3.41	2.80	0.36	1.467	26.04
Crater	1.1	15	3.833E-01	2.61	2.61	0.38	3.067	54.44
<b>Low Carbon Sample</b>	<b>Ring Eroded Area (mm<sup>2</sup>)</b>	<b>Eroded Area (mm<sup>2</sup>)</b>	<b>MER (μm/h)</b>	<b>REC (h/μm)</b>				
Pits	0.4	15	1.472E-02	67.93	0.28	3.62	0.015	0.05
Crater	0.785	15	2.067E-01	4.84	1.97	0.51	0.413	1.37
Crater	0.785	15	3.600E-01	2.78	3.44	0.29	1.080	3.59
Crater	0.8	15	4.107E-01	2.44	3.85	0.26	2.053	6.83
Crater	0.7	15	6.500E-01	1.54	6.96	0.14	5.200	17.30
<b>Steel Plate Sample</b>	<b>Ring Eroded Area (mm<sup>2</sup>)</b>	<b>Eroded Area (mm<sup>2</sup>)</b>	<b>MER (μm/h)</b>	<b>REC (h/μm)</b>				
Pits	0.1	15	7.493E-03	133.45	0.56	1.78	0.007	0.18
Pits	0.2	15	2.200E-02	45.45	0.83	1.21	0.044	1.05
Crater	0.4	15	6.889E-02	14.52	1.29	0.77	0.207	4.91
Crater	0.65	15	1.280E-01	7.81	1.48	0.68	0.640	15.21
Crater	0.95	15	4.167E-01	2.40	3.29	0.30	3.333	79.24

## Appendix J: Cavitation-Erosion Test results (E)

**Process:** Characterization of the cavitation pits after 10 min test

**Test equipment:** SEM/Zygo interferometer microscope

**Materials:** Scroll expander: High carbon steel plate, Market steels: High carbon, Low carbon and Chromium

<b>Formation of Cavitation Pits after 10 min test</b>			
<b>Typical Depth of Pits (<math>\mu\text{m}</math>)</b>			
	<b>Lubricant</b>	<b>Pentane</b>	<b>Water</b>
High Carbon Steel	0.12	0.025	0.162
Low Carbon Steel	0.166	0.036	0.22
Chromium Steel	0.11	0.04	0.14
Scroll's Steel Plate	0.204	0.047	0.203
<b>Typical Area of Pits (<math>\mu\text{m}^2</math>)</b>			
	<b>Lubricant</b>	<b>Pentane</b>	<b>Water</b>
High Carbon Steel	79.4	56	88.57
Low Carbon Steel	76.5	65.63	116.25
Chromium Steel	65.45	44.17	97.05
Scroll's Steel Plate	70.67	54.35	82.6
<b>Typical Volume of Pits (<math>\mu\text{m}^3</math>)</b>			
	<b>Lubricant</b>	<b>Pentane</b>	<b>Water</b>
High Carbon Steel	7.15	2	11.33
Low Carbon Steel	10.26	2.75	22.19
Chromium Steel	6.04	2.22	9.41
Scroll's Steel Plate	10.02	2.87	15.28

<b>Cavitation Pits with maximum Depth</b>			
<b>Maximum Depth of Pits (<math>\mu\text{m}</math>)</b>			
	<b>Lubricant</b>	<b>Pentane</b>	<b>Water</b>
High Carbon Steel	0.21	0.038	0.29
Low Carbon Steel	0.32	0.096	0.44
Chromium Steel	0.2	0.075	0.28
Scroll's Steel Plate	0.27	0.09	0.4
<b>Diameter of Pits (<math>\mu\text{m}^2</math>)</b>			
	<b>Lubricant</b>	<b>Pentane</b>	<b>Water</b>
High Carbon Steel	95	30	95
Low Carbon Steel	85	50	50
Chromium Steel	75	50	50
Scroll's Steel Plate	38.5	60	80
<b>Volume of Pits (<math>\mu\text{m}^3</math>)</b>			
	<b>Lubricant</b>	<b>Pentane</b>	<b>Water</b>
High Carbon Steel	9.35	2.65	21.18
Low Carbon Steel	18.26	5.43	22.61
Chromium Steel	8.13	3.47	8.88
Scroll's Steel Plate	9.44	4.53	25.86

## Appendix J: Cavitation-Erosion Test results (E continued)

<b>Cavitation Pits with maximum Volume</b>			
<b>Maximum Volume of Pits (<math>\mu\text{m}^3</math>)</b>			
	<b>Lubricant</b>	<b>Pentane</b>	<b>Water</b>
High Carbon Steel	10.32	3.61	21.18
Low Carbon Steel	27.17	5.43	48.21
Chromium Steel	15.04	3.94	13.5
Scroll's Steel Plate	15.98	4.53	28.37
<b>Depth of Pits (<math>\mu\text{m}</math>)</b>			
	<b>Lubricant</b>	<b>Pentane</b>	<b>Water</b>
High Carbon Steel	0.1	0.028	0.29
Low Carbon Steel	0.24	0.096	0.35
Chromium Steel	0.18	0.062	0.15
Scroll's Steel Plate	0.25	0.09	0.27
<b>Diameter of Pits (<math>\mu\text{m}^2</math>)</b>			
	<b>Lubricant</b>	<b>Pentane</b>	<b>Water</b>
High Carbon Steel	150	120	95
Low Carbon Steel	155	50	180
Chromium Steel	130	75	130
Scroll's Steel Plate	95	60	145

<b>Cavitation Pits with a maximum Area</b>			
<b>Maximum Area of Pits (<math>\mu\text{m}^2</math>)</b>			
	<b>Lubricant</b>	<b>Pentane</b>	<b>Water</b>
High Carbon Steel	150	120	185
Low Carbon Steel	155	130	215
Chromium Steel	130	75	155
Scroll's Steel Plate	155	115	200
<b>Depth of Pits (<math>\mu\text{m}</math>)</b>			
	<b>Lubricant</b>	<b>Pentane</b>	<b>Water</b>
High Carbon Steel	0.1	0.028	0.1
Low Carbon Steel	0.24	0.033	0.09
Chromium Steel	0.18	0.062	0.095
Scroll's Steel Plate	0.15	0.025	0.17
<b>Volume of Pits (<math>\mu\text{m}^3</math>)</b>			
	<b>Lubricant</b>	<b>Pentane</b>	<b>Water</b>
High Carbon Steel	10.32	3.61	10.25
Low Carbon Steel	27.17	3.4	12.97
Chromium Steel	15.04	3.94	7.47
Scroll's Steel Plate	11.46	2.69	18.26

## Appendix K: Characteristic measurements of various cavities found across the steel plate of the SE<sub>1000</sub>

**Process:** Microscopic investigation of the critical/damaged areas of the SE<sub>1000</sub>

**Test equipment:** Optical and ZYGO interferometer microscopes

**Materials:** High carbon steel plate of the scroll expander

<b>Steel Plate Cavities Measurements</b>								
Craters	Roughness (Ra) (μm)	Roughness (rms) (μm)	Average Depth (μm)	Volume Remove (μm <sup>3</sup> )	Eroded Area (mm <sup>2</sup> )	Time Period (h)	MER ((μm/h)	REC (h/μm)
1	1	1.5	6.2	3320	3.85E-03	1000	8.62E-04	1.16E+03
2	0.4	0.9	5.2	5485	1.45E-02	1000	3.78E-04	2.64E+03
3	0.5	0.9	4.9	9200	2.52E-02	1000	3.65E-04	2.74E+03
4	1.2	1.7	6.3	7100	3.85E-03	1000	1.84E-03	5.42E+02
5	0.35	0.6	4.5	10300	2.52E-03	1000	4.09E-03	2.45E+02
6	1.2	1.5	6	14400	8.00E-03	1000	1.80E-03	5.56E+02
7	1	1.4	4.5	3975	3.85E-03	1000	1.03E-03	9.69E+02
:	:	:	:	:	:	:	:	:
:	:	:	:	:	:	:	:	:
94	0.5	0.9	5.7	24000	6.00E-03	1000	4.00E-03	2.50E+02
95	0.35	0.6	4	11100	2.52E-03	1000	4.40E-03	2.27E+02
96	0.4	0.9	4	2000	5.60E-03	1000	3.57E-04	2.80E+03
97	1.2	1.7	6.5	6500	3.85E-03	1000	1.69E-03	5.92E+02
98	1	1.3	3.8	3300	3.85E-03	1000	8.57E-04	1.17E+03
99	0.9	1.5	6	3800	3.85E-03	1000	9.87E-04	1.01E+03
<b>Average</b>			<b>5.16</b>	<b>7916.36</b>	<b>7.37E-03</b>		<b>1.52E-03</b>	<b>1.28E+03</b>

Unit	Representative area (mm <sup>2</sup> )	Num of pits	Ring Eroded Area (mm <sup>2</sup> )	Num of pits	Volume Loss (μm <sup>3</sup> )	Average Max Volume Loss (μm <sup>3</sup> )	MER (μm/h)	MER max(μm/h)
<b>SE<sub>1000</sub></b>	<b>8</b>	<b>200</b>	<b>200</b>	<b>8000</b>	<b>64000000</b>	<b>160000000</b>	<b>0.00032</b>	<b>0.0008</b>

## Appendix L: Project Time-Plan

Activity	Schedule												
	Year 1				Year 2				Year 3				Year 3+
Years													
Time Periods	I	II	III	IV	I	II	III	IV	I	II	III	IV	I
<b>Stage 1</b>													
Literature review/ Critique	■	■	■								■	■	
Scroll surface investigation/Analytical results			■	■	■	■				■	■		
Wear mechanism/Friction measurements				■	■	■	■	■					
Surface analysis/Friction wear results						■	■	■					
<b>Stage 2</b>													
Cavitation/ Photographic measurements										■	■		
Cavitation/ Experimental results Incubation stage							■	■	■				
Cavitation/ Experimental results final stage								■	■	■	■		
Surface analysis/ Cavitation results										■	■		
Comparison results/ Environmental assessment											■		
<b>Stage 3</b>													
Publications					■					■	■		■
Final report													■

## References

1. I. Tzanakis. 2006. *Combining solar and wind energy to meet demands in the built environment (Glasgow-Heraklion Crete analysis)*. MSc Dissertation Project, Strathclyde University
2. K. Alanne, A. Saari. 2004. *Sustainable small scale CHP technologies for buildings: the basis for multi-perspective decision-making*. Renewable and sustainable energy reviews, 8 ( 401- 431).
3. J. Godefroy, R. Boukhanouf, S. Riffat. 2007. *Design, testing and mathematical modelling of a small scale CHP and cooling system (small CHP-ejector trigeneration)*. Applied thermal engineering, 27 (68-78).
4. D.A Haralambopoulos, H. Polatidis. 2003. *Renewable energy projects: Structuring a multi criteria group decision making*. Renewable energy, 28 (962- 973).
5. Harrison, J. 2004. *Micro combined heat and Power*. EA Technology.
6. I. Tzanakis, M. Hadfield, Z. Khan. 2009. *Durability of domestic scroll compressor systems*. Surface effects and contact mechanics, 62 (229-240). ISBN: 978-1-84564-186-3
7. H.J. Kim, J.M. Ahn, S.O. Cho, K.R. Cho. 2008. *Numerical simulation on scroll expander-compressor unit for CO2 trans-critical cycles*. Applied Thermal Engineering, 28 (1654-1661).
8. V. Lemort, S. Quoilin, C. Cuevas, J. Lebrun. 2009. *Testing and modelling a scroll expander integrated into an Organic Rankine Cycle*. Applied Thermal Engineering, 29 (3094-3102).
9. S. Quoilin, V. Lemort, J. Lebrun. 2009. *Experimental study and modelling of an Organic Rankine Cycle using scroll expander*. Applied Energy.
10. M. Kane, D. Larrain, D. Favrat, Y. Allani. 2003. *Small hybrid solar power systems*. Energy, 28 (1427-1443).
11. T. Yanagisawa, M. Fukuta, Y. Ogi, T. Hikichi. 2001. *Performance of an oil-free scroll-type air expander*. Proceedings of the IMechE Conference on Compressors and their Systems, (167-174).
12. B. Aoun, D. Clodic. 2008. *Theoretical and experimental study of an oil-free scroll type vapour expander*. Proceedings of the Compressor Engineering Conference Purdue, (Paper 1188).
13. M. Cui. 2007. *Comparative study of the impact of the dummy port in scroll compressor*. International journal of refrigeration, 30 (912- 925).

14. B. Wang, X. Li, W. Shi, Q. 2007. *A general geometrical model of scroll compressors based on discretional initial angles of involute*. International journal of refrigeration, 28 (958- 966).
15. M. Duprez, E. Dumont, M. Frere. 2007. *Modelling of reciprocating and scroll compressors*. International journal of refrigeration, 30 (873-886).
16. C.H. Tseng, Y.C Chang. 2006. *Family design of scroll compressors with optimization*. Applied thermal engineering, 26 (1074-1086).
17. B. Wang, X. Li, W. Shi, Q. Yan. 2007. *Numerical research on the scroll compressor with refrigeration*. Applied Thermal engineering, 28 (440-449).
18. R. Radermacher, Y. Hwang. 2005. *Vapour Compression Heat Pumps with Refrigerant Mixtures*. USA: Taylor & Francis Group.
19. T. Mingley, A. Henne. 1930. *Organic fluorides as refrigerants*. Industrial and Engineering Chemistry, 22 (542-545).
20. T. Mingley. 1937. *From the periodic table to production*. Industrial and Engineering Chemistry, 29 (2), (239-244).
21. J. Calm. 2008. *The next generation of refrigerants- Historical review, considerations, and outlook*. International Journal of Refrigeration, 31 (1123-1133).
22. A.W. Adam. 1998. *Organic Rankine Engines*. Encyclopedia of Energy Technology and the Environment, 4 (2157- 2161).
23. Vanslambrouk, B. *New Technologies Workshop Cogean Europe. Brussels 2007. ORC different Applications*. Laboratory of Industrial Physics and Applied Mechanics: Hogeschool West Virginia, dept PIH.
24. Obernberger, I., Thonhofer, P. & Reisenhofer, E. 2002. *Description and evaluation of the new 1000kW<sub>el</sub> Organic Rankine Cycle process integrated in the biomass CHP plant in the Lienz*. Euroheat and Power, 10 (1-17).
25. P.J Mago, L.M Chamra, K. Srinivasam, C. Somajaji. 2007. *An examination of regenerative organic Rankine cycles using dry fluids*. Thermal engineering, 28 (998-1007).
26. T. Yamamoto, T. Furuata, N. Arai, K. Mori. 2007. *Design and testing of organic rankine cycle*. Energy, 26 (239-251).
27. B. Saleh, G. Koglbauer, M. Wendland, J.Fischer. 2007. *Working fluids for low – temperature organic Rankine Cycles*. Energy, 32 (1210-1221).
28. D. Wei, X. Lu, J. Gu. 2007 *Performance analysis and optimazation of organic Rankine cycle (ORC) for waste heat recovery*. Energy Conversion and Management, 48 (1113-1119).
29. S. Quoilin, 2007. *Experimental study and modeling of a low temperature rankine cycle for small scale cogeneration*. BSc Dissertation Project, University of Liege.

30. M. Sunami. 1999. *Physical and chemical properties of refrigeration lubrications*. Conference: ASHRAE Annual Meeting, Seattle, WA (US).
31. P.T Gibb, A.J. Whittaker, S. Corr, R. Yost, M. Shoji. 1999. *Determination of properties of highly optimized Polyolester lubricants*. Conference: ASHRAE Annual Meeting, Seattle, WA (US).
32. C. Ciantar. *Sustainable development of refrigerator systems using replacement environmentally acceptable refrigerants*. Ph. D thesis 2000.
33. K. Marsh, M. Kandil. 2002. *Review of thermodynamic properties of refrigerants + lubricants oils*. Fluid phase equilibria, 199 (319-334).
34. I.M. Huthings. 1992. *Tribology : Friction and wear of engineering materials*. London: Arnold.
35. G.W. Stachowiak, A.W. Batchelor, G.B. Stachowiak, 2004. *Experimental methods in tribology*. Sydney: Elsevier.
36. B.J. Hamrock, S.R. Schmid, B. O. Jacobson. 2004. *Fundamental of Fluid film Lubrication*. 2<sup>nd</sup> edition. New York: Basel.
37. D. Dowson, 1968. *Elastohydrodynamics*. Journal of mechanical engineering, 182 (151-167).
38. Magazine of machinery lubrication.
39. D. Dwonson, G.R. Higginson. 1959. *A numerical solution to the elastohydrodynamic problem*. Journal of Mechanical Engineering Science, 1 (6-15).
40. B.J. Hamrock, D. Dowson. 1981. *Ball bearing lubrication-the elastohydrodynamics of elliptical contacts*. Wiley-Interscience, New York.
41. J. Vizintin, M. Kalin,, K. Dohda, S. Jahanmir, 2004. *Tribology of mechanical systems: a guide to present and future technologies*. New York: Asme press.
42. I.M. Huthings. 1992. *Tribology: Friction and wear of engineering materials*. London: Arnold.
43. U. Jonson. 1998. *Elastohydrodynamic lubrication and lubricant rheology in refrigeration compressors*. Ph.D. Lulea University of Technology, Sweden.
44. P.F. Grando, M. Priest, A.T. Prata. 2005. *Lubrication in refrigeration systems. Performance of journal Bearings lubricated with oil and refrigerant mixture*. Tribology and Interface Engineering Series, 48 (481-491).
45. Yoon, H.K., Poppe, C.H. & Cusano, C. 1996. *Predicting lubricant performance in refrigerant compressors: A comparison between component testing and benchtesters*. Illinois.
46. N.E. Kotsovinos. 2007. *Book of Fluid Mechanics*. Democritus University of Thrace.
47. G.W. Stachowiak, A.W. Batchelor. 2001. *Engineering Tribology*. 2<sup>nd</sup> edition. USA: Butterworth Heinemann.

48. R.D. Arnell, P.B. Davies, J. Halling, T.L. Holmes. 1991 *Tribology Principles and Design Applications* 1<sup>st</sup> edition UK: MacMillan Education Ltd.
49. J. Bijwe. 2002 *Wear Failures of Reinforced Polymers*. ASM International 11 (1028-1043).
50. L. Chang, K. Friedrich. 2005. *Tribological Characteristics of Micro- and Nanoparticle Filled Polymer Composites*. Polymer Composites. 2005, (169-185).
51. A.E. Anderson, E. Arnold. 1992. *Friction Lubrication and Wear Technology*. New York: ASM International.
52. A.G. Evans, D.B. Marshall. 1981. *Fundamentals of friction and wear of materials*. Berkeley: California.
53. P. J. Blau. 2009. *Friction science and technology: from concepts to applications*. Taylor&Francis Group, CRC Press.
54. M. Mofidi, E. Kassfelt, B. Prakash. 2007. *Tribological behaviour of an elastomer aged in different oils*. Tribology international, 101 (129- 135).
55. B.J. Briscoe. 1980. *The sliding wear of polymers: A brief review in fundamentals of tribology*. MIT Press, (733-758).
56. P.W. Bridgman. 1935. *Effects of high shearing stress combined with high hydrostatic pressure*. Physical Review, 48 (825-847).
57. D.F. Moore. 1972. *The friction and lubrication of elastomers*. Pergamon, Oxford, UK.
58. B. Thomas, M. Hadfield, S. Austen. *Experimental wear modelling of lifeboat slipway launches*. Tribology International, 42 (1706-1714).
59. F. Deleau, D. Mazuyer, A. Koenen. 2009. *Sliding friction at elastomer/glass contact: Influence of the wetting conditions and instability analysis*. Tribology International, 42 (149-159).
60. H. Meng, G.X. Sui, G.Y. Xie, R. Yang. 2009. *Friction and wear behaviour of carbon nanotubes reinforced polyamide 6 composites under sliding and water lubricated condition*. Composites Science and Technology, 69 (606-611).
61. Z.Z. Zhang, Q.J. Xue, W.M. Liu, W.C. Shen. 1997. *Tribological properties of metal-plastic multilayer composites under oil lubricated conditions*. Wear, 210 (195-203).
62. S. Hashmi, U. Dwivedi, N.Chand. 2007. *Graphite modified cotton fibre reinforced polyester composites under sliding wear conditions*. Wear, 262 (1426-1432).
63. Stolarski, T.A. 2000. *Tribology in Machine Design*. USA: Butterworth Heinemann.
64. Van Der heide, E., Stam, E.D. Giraud, H. Lovato, G., Akdut, N. Clarysee, F. Caenen, P. & Heiklla, I. 2005. *Wear aluminium bronze in sliding contact with lubricated stainless steel sheet material*. Wear, 261 (68- 730).

65. M. Neale, M. Gee. 2001. *Guide to wear problems and testing for industry*. New York, USA: William Andrew Publishing.
66. X.Jia, R. Ling. 2007. *Two-body free-abrasive wear of polyethylene, nylon1010, epoxy and polyurethane coatings*. Tribology International, 40 (1276-1283).
67. A. Harsha, U. Tewari. 2003. *Two-body and three-body abrasive wear behaviour of polyaryletherketone composites*. 22 (403-418).
68. T. Ohtani, T.Yakou, S. Kitayama. 2004. *Two-body and three-body abrasive wear properties of katsura wood*. Journal of Wood Science. 47 (87-93).
69. F.P. Bowden, D. Tabor. 1964. *The friction and lubrication of solids, Part 2*. Clarendon Press, Oxford.
70. J. Takadoum. 2008. *Materials and surface engineering in tribology*. ISTE Ltd, UK.
71. K.H. Zum Gahr. 1998. *Wear by hard particles*. Tribology International, 31 (587-596).
72. G.M. Swallowe. 1999. *Mechanical properties and testing of polymers*. USA, Kluwer Academic Publishers.
73. K.C. Ludema, 1996. *Friction, Wear, Lubrication*. New York: CRC Press.
74. P. Samyn, P. De Baeyns, G. Schoukens, A.P. Van Peteghem. 2006. *Large-scale tests on friction and wear of engineering polymers for material selection in highly loaded sliding systems*. Materials and design, 27 (535- 555).
75. M. Chandrasekaran, A.W. Batchelor. 1997. *In situ observation of sliding wear tests of butyl rubber in the presence of lubricants in an X-ray microfocus instrument*. Wear, 211 (35-43).
76. J.F. Archard. 1961. *Single Contacts and Multiple Encounters*. Journal of Applied Physics, 32 (1420-1425).
77. J.K. Landcaster. 1967. *The influence of substrate hardness on the formation and endurance of molybdenum disulphide films*. Wear, 10 (103-107).
78. C. Lhymn. 1987. *The effect of normal load on the specific wear rate of fibrous composite*. Wear, 120 (1-27).
79. L. Chang, Z. Zhang, L. Ye, K. Friedrich. 2007 *Tribological properties of epoxy nanocomposites III. Characteristics of transfer films*. Wear, 262 (699-706).
80. J. M. Degrange, M. Thomine, P. Kapsa, J.M. Pelletier, L. Chazeau, G. Vigier, G. Dudrange, L. Guerbe. 2005. *Influence of viscoelasticity on the tribological behaviour of carbon black filled nitrile rubber (NRB) for tip seal application*. Wear, 259 (684-692).
81. N. Guermazi, K. Elleuch, H.F. Ayedi, V. Fridrici, Ph. Kapsa. 2009. *Tribological behaviour of pipe coating in dry sliding contact with steel*. Materials and Design, 30 (3094-3104).
82. N.S.M El-Tayeb, R. Md. Nasir. 2007. *Effect of soft carbon black on tribology of deproteinised and polyisoprene rubbers*. Wear, 262 (350-361).

83. H. Unal, A. Mimaroglou. 2003 *Friction and wear behaviour of unfilled engineering thermoplastics*. Materials and Design, 24 (183-187).
84. E. Santner, H. Czichos. 1989. *Tribology of polymers*. International Tribology, 22 (103-109).
85. H. Benabdallah. 2003. *Friction and wear of blended polyoxymethylene sliding against coated steel plates*. Wear, 254 (1239-1246).
86. H. Unal, U. Sen, A. Mimaroglu. 2004. *Dry sliding wear characteristics of some industrial polymers against steel counterface*. Tribology International, 37 (727-732).
87. J. P. Davim, R. Cardoso. 2009. *Effect of the reinforcement (carbon or glass fibres) on friction and wear behaviour of the PEEK against steel surface at long dry sliding*. Wear, 266 (795-799).
88. J.K Lancaster. 1972. *Lubrication of carbon fiber-reinforced polymers. Part 1. Water and aqueous solution*. Wear, 20 (315-333).
89. Y. Yamada, K. Tanaka, K. Friedrich. 1986. *Friction and wear of polymer composites*. Elsevier, (137-173).
90. M. Sumer, H. Unal, A. Mimaroglu. 2008. *Evaluation of tribological behaviour of PEEK and glass fibre reinforced PEEK composite under dry sliding and water lubricated conditions*. Wear, 265 (1061-1065).
91. J. Jia, J. Chen, H. Zhou, L. Hu, L. Chen. 2004. *Comparative investigation on the wear and transfer behaviours of carbon fiber reinforced polymer composites under dry sliding and water lubrication*. Composites science and technology, 65 (1139-1147).
92. J. Karger-Kocsis, D. Felhos, D. Xu, A.K. Schlarb. 2008. *Unlubricated sliding and rolling wear of thermoplastic dynamic vulcanizates (Santoprene) against steel*. Wear, 265 (292-300).
93. O. Jacobs, R. Jaskulka, F. Yang, W. Wu. 2004. *Sliding wear of epoxy compounds against different counterparts under dry and aqueous conditions*. Wear, 256 (9-15).
94. M. Modifi, E. Kassfelt, B. Prakash. 2007. *Tribological behaviour of an elastomer aged in different oils*. Tribology international, 101 (129- 135).
95. H. Benabdallah. 2008. *Friction wear and acoustic emissions of some plastics sliding against Si<sub>3</sub>N<sub>4</sub>*. Wear, 264 (152-156).
96. S.W. Zhang, H. Liu, R. He. 2004. *Mechanisms of wear of steel by natural rubber in water medium*. Wear, 256 (226-232).
97. J. Bijwe, J.J. Rajesh, A. Jeyakumar, A. Ghosh, U.S. Tewari. 2000. *Influence of solid lubricants and fibre reinforcement on wear behaviour of polyethersulphone*. Tribology International, 33 (697-706).

98. L. Chang, Z. Zhang, C. Breidt, K. Friedrich. 2005. *Tribological properties of epoxy nanocomposites I. Enhancement of the wear resistance by nano-TiO<sub>2</sub> particles*. *Wear*, 258 (141-148).
99. N.S.M. El-Tayeb, B.F. Yousif, T.C. Yap. 2006. *Tribological studies of polyester reinforced with CSM 450-R-glass fiber sliding against smooth stainless steel counterface*. *Wear*, 261 (443-452).
100. J. Bijwe, J. Indunathi, A.K. Ghosh, J. Reinf. 1999. *Evaluation of Engineering Polymeric Composites for Abrasive Wear Performance*. *Journal of Reinforced Plastics and Composites*, 18 (1573-1591).
101. L.Chang, Z. Zhang. 2006. *Tribological properties of epoxy nanocomposites PART II. A combinative effect of short carbon fibre with nano-TiO<sub>2</sub>*. *Wear*, 260 (869-878).
102. N.S.M El-Tayeb. 2009. *Two-body abrasive behaviour of untreated SC and R-G fibres polyester composites*. *Wear*, 266 (220-232).
103. L. Chang, Z. Zhang, H. Zhang, K. Friedrich. 2005. *Effect of nanoparticles on the tribological behaviour of short carbon fibre reinforced poly(etherimide) composites*. *Tribology International*, 38 (966-973).
104. S. Bahadur. 2000. *The development of transfer layers and their role in polymer tribology*. *Wear*, 245 (92-99).
105. L. Chang, Z. Zhang, H. Zhang, A.K. Schlarb. 2006 *On the sliding wear of nanoparticle filled polyamide 66 composites*. *Composites Science and Technology*, 66 (3188-3198).
106. A. Krella, A. Czyzniewski. 2007. *Influence of the substrate hardness on the cavitation erosion resistance of TiN coating*. *Wear*, 263 (395-401).
107. P.R. Williams, P.M. Williams, S.W.J. Brown. 1997. *A technique for studying liquid jets by cavitation bubble collapse under shockwaves, near a free surface*. *Journal of Non-Newtonian Fluid Mechanics*, 72 (101-110).
108. Flynn, H. G. 1964. *Physics of Acoustic Cavitation in Liquids*. *Physical Acoustics*, Vol IB, p. 157.
109. E.A Brujan, T. Ikeda, Y. Matsumoto. 2008. *On the pressure of cavitation bubbles*. *Experimental Thermal and Fluid Science*, 32 (1188-1191).
110. F. R. Young. 1999. *Cavitation*, Imperial College Press.
111. W. Lauterborn. 1980. *Cavitation and homogeneities in underwater acoustics*. Springer Verlag p. 3.
112. L. Sempsis. 2007. *Cavitation case study in a centrifugal pump*. MSc Dissertation Project, NTUA Athens.
113. B. E. Noltingk and E. A. Neppiras. *Cavitation produced by ultrasonics*. *Proc. Phys. Soc. (London)*, 63B, Pt. 9 (1950); 64B, Pt. 12 (1951).

114. Y. Lecoffre. 1999. *Cavitation Bubble Trackers*. English 1<sup>st</sup> edition. A.A. Balkema Publishers.
115. Lord Rayleigh. 1917. *On the pressure developed in a liquid during the collapse of a spherical cavity*. Phil Mag 34:94-8
116. R. Zhao, R.Xu, Z. Shen, J. Lu , X. Ni. 2007. *Experimental investigation of the collapse of laser-generated cavitation bubbles near a solid boundary*, Optics and laser technology, 39 (968-972).
117. A. Philipp, W. Lauterborn. 1998. *Cavitation erosion by single laser-produced bubbles*, Journal of fluid mechanics, 361 (75-116).
118. M. Plesset, R. Chapman. 1971. *Collapse of an initially spherical vapour cavity in the neighbourhood of a solid boundary*. Journal of Fluid Mechanics, 47:2:283-290.
119. C. Ohl, M. Arora, R. Ikink, N. Jong, M. Versluis, M. Delius, D. Lohse. 2006. *Sonoporation from Jetting Cavitation Bubbles*, Biophysical Journal, 91 (4285-4295).
120. R. Etienne, L. Jacques, F. Mohamed, M. Peter, A. François. 2007. *Cavitation bubble behaviour inside a liquid jet*, Physics of Fluids, 19 (067106).
121. X. Chen, R.Q. Xu, Z.H. Shen, J.Lu, X.W. Ni. 2004. *Optical investigation of cavitation erosion by laser-induced bubble collapse*. Optics and Laser Technology, 36 (197-203).
122. E.A. Brujan, A.F.H. Al-Hussany, R.L. Williams, P.R. Williams. 2008. *Cavitation erosion in polymer aqueous solutions*. Wear, 264 (1035–1042).
123. S. Popinet, S. Zaleski. 2002. *Bubble collapse near a solid boundary: A numerical study of the influence of viscosity*. Journal of Fluid Mechanics, 464 (137-163).
124. P.R Williams, P.M. Williams, S.W.J. Brown. 1998. *A study of liquid jets formed by bubble collapse under shock waves in elastic and Newtonian liquids*. Journal of Non-Newtonian Fluid Mechanics, 76 (307-325).
125. A. Berker, M.G. Bouldin, S.J. Kleis, W.E. Van Arsdale. 1995. *Effect of polymer on flow in journal bearings*. Journal of Non-Newtonian Fluid Mechanics, 53 (333-347).
126. B. Karunamurthy. *Erosion and rolling contact wear mechanisms in silicon nitride hybrid bearings*. PhD thesis 2009.
127. Y. Meged, C.H. Venner, W.E. ten Napel. 1995. *Classification of lubricants according to cavitation criteria*. Wear, 186 (443-453).
128. S. Behnia, A. Jafari, W. Soltanpoor, O. Jahanbakhsh. 2009. *Nonlinear transitions of a spherical bubble*. Chaos, Solitons and Fractals 41 (818-828).
129. Y. Iwai, S. Li. 2003. *Cavitation erosion in waters having different surface tensions*. Wear, 254 (1-9).

130. X.M. Liu, J. He, J. Lu, X.W. Ni. 2009. *Effects of surface tension on a liquid-jet produced by the collapse of a laser-induced bubble against a rigid boundary*. Optics and laser technology, 41 (21-24).
131. M. Utz, P. G. Debenedetti, F. H. Stillinger. 2001. *Isotropic tensile strength of molecular glasses*. 114 (10049-10057).
132. T. Obara, N.K. Bourne, J.E. Field. 1995. *Liquid-jet impact on liquid and solid surfaces*, Wear, 186-187 (338-394).
133. O. Lindau, W. Lauterborn. 2001. *Investigation of the counter-jet developed cavitation bubble that collapses near a rigid boundary*. CAV 2001: Fourth International Symposium on Cavitation.
134. A. Krella. 2005. *Influence of cavitation intensity on X6CrNiTi18-10 stainless steel performance in the incubation stage*. Wear, 258 (1723-1731).
135. M.D. Kass, J.H. Whealton, N.E. Clapp Jr., J.R. DiStefano, J.H. DeVan, J.R. Haines, M.A. Akerman and T.A. Gabriel. 1998. *Nonlinear cavitation erosion of stainless steel in mercury versus applied power*. Tribology Letters, 5 (231-234).
136. C.Z. Wu, Y.J. Chen, T.S. Shih. 2002. *Phase transformation in austempered ductile iron by micro-jet impact*. Materials characterization, 48 (43-54).
137. Yan-Ming Chen, Cavitation Erosion ASM Handbook. 11 (2002) 1002-1012.
138. A. Tezel, A. Sens, S. Mitragotri, 2002. *Investigations of the role of cavitation in low-frequency sonophoresis using acoustic spectroscopy*. J. Pharm. Sci. 91 (444-453).
139. B.S Mann. 2000. *High-energy particle impact wear resistance of hard coatings and their application in hydroturbines*. Wear, 237 (140-146).
140. M. Dular, B. Bachert, B. Stoffel, B.Sirok, 2004. *Relationship between cavitation structures and cavitation damage*. Wear, 257 (1176-1184).
141. A.Abouel-Kasem, K.M. Emar, S.M. Ahmed. 2009. *Characterizing cavitation erosion particles by analysis SEM images*. Tribology International, 42 (130-136).
142. E.A. Brujan, P.R Williams. 2006. *Cavitation phenomena in non-newtonian liquids*. Chemical Engineering Research and Design, 84 (293-299).
143. I. Tzanakis, M. Hadfield. 2010. *Observations of acoustically generated cavitation bubbles within typical fluids applied to a scroll expander lubrication system*. Journal of Hydrodynamics.
144. S. Hattori, R. Ishikura. 2009. *Revision of cavitation erosion database and analysis of stainless steel data*. Wear
145. C. Haoseng, L. Jiang, C. Darong, W. Jiadao. 2008. *Damages on steel surface at the incubation stage of the vibration cavitation erosion in water*. Wear, 265 (692-698).

146. X. Zhang, C. Liu, X. Liu, J. Dong, B. Yu. 2009. *Cavitation erosion behaviour of WC coatings on CrNiMo stainless steel by laser alloying*. Materials, 16 (203-207).
147. M. Dojcinovic, T. V. Husovic. 2008. *Cavitation damage of the medium carbon steel: Implementation of image analysis*. Materials Letters, 62 (953-956).
148. J. Steller. 1999. *International cavitation erosion test and quantitative assessment of material resistance to cavitation*. Wear, 233-235 (51-54).
149. K.Y. Chiu, F.T. Cheng, H.C. Man. 2007. *Hydrogen effect on the cavitation erosion resistance of AISI 316L stainless steel laser surface-modified with NiTi*. Materials Letters, 61 (239-243).
150. K.Y. Chiu, F.T. Cheng, H.C. Man. 2005. *Evolution of surface roughness of some metallic materials in cavitation erosion*. Ultrasonics, 43 (713-716).
151. S. Hattori, T. Ogiso, Y. Minami, I. Y. 2008. *Formation and progression of cavitation erosion surface for long exposure*. Wear, 265 (1619-1625).
152. A. Krella, A. Czyzniewski. 2007. *Influence of the substrate hardness on the cavitation erosion resistance of TiN coating*. Wear, 263 (395-401).
153. M. Futukawa, H. Kogawa, R. Hino, H. Date, H. Takeishi. 2000. *Erosion damage on solid boundaries in contact with liquid metals by impulsive pressure injection*. International Journal of Impact Engineering, 28 (123-135).
154. 142 A. Krella, A. Zielinski. 2000. *Characteristics of the incubation period of the cavitation erosion of aluminium-magnesium alloy*. Proceedings of the 9<sup>th</sup> International Scientific Conference "Achievements in Mechanical and Materials Engineering" (329-332).
155. J. Marian, J. Knap, M. Ortiz. 2004. *Nanovoid Cavitation by Dislocation Emission in Aluminum*. Physical Review Letters, 93(16):165503.
156. A. Krella, A. Zielinski. 2000. *Influence of cavitation intensity erosion of an Al-Mg alloy*. Proceedings of the Ninth International Scientific Conference AMME.
157. W. Liu, Y.G. Zheng, C.S. Liu, Z.M. Yao, W. Ke. 2003. *Cavitation erosion behaviour of Cr-Mn-N stainless steels in comparison with 0Cr13Ni5Mo stainless steel*. Wear, 254 (713-722).
158. A. Krella. 2005. *Influence of cavitation intensity on X6CrNiTi18-10 stainless steel performance in the incubation period*. Wear, 258 (1723-1731).
159. X.B. Zhang, C.S. Liu, X.D. Liu, J. Dong, B. Yu. 2009. *Cavitation erosion behaviour of WC coatings on CrNiMo stainless steel by laser alloying*. Materials, 16 (203-208).
160. K.Y. Chiu, F.T. Cheng, H.C. Man. 2005. *Cavitation erosion resistance of AISI 316L stainless steel laser surface-modified with NiTi*. Materials Science and Engineering, 392 (348-358).
161. F.T. Cheng, C.T. Kwok, H.C. Man. 2002. *Cavitation erosion resistance of stainless steel laser-clad with WC-reinforced MMC*. Materials Letters, 57 (969-974).

162. C.J. Heathcock, B.E. Protheroe. 1982. *Cavitation erosion of stainless steels*, Wear 81 (311–327).
163. Z. Wang, J. Zhu. 2004. *Correlation of martensitic transformation and surfacemechanical behaviour with cavitation erosion resistance for some iron-based alloys*, Wear, 256 (1208–1213).
164. A. Krella, A. Czyzniewski. 2007. *Influence of the substrate hardness on the cavitation erosion resistance of TiN coating*. Wear, 263 (395-401).
165. R.H. Richman and W.P. McNaughton. 1990. *Correlation of cavitation erosion behaviour with mechanical properties of metals*. Wear, 140 (63).
166. G. Wang, G. Ma, D. Sun, H. Yu, H. Meng. 2008. *Numerical study on fatigue damage properties of cavitation erosion for rigid metal materials*. Materials, 153 (261).
167. M. Dular, A. Osterman. 2008. *Pit clustering in cavitation erosion*. Wear, 265 (811-820).
168. Y. Chen, N.P Halm, E. Braun, E.A. Groll. 2002. *Mathematical modeling of scroll compressors – part I overall scroll compressor modeling*. International journal of refrigeration, 25 (751-764).
169. Y. Chen, N.P. Halm, E.A Groll, J.E. Braun. 2002. *Mathematical modeling of scroll compressor-part II overall scroll compressor modeling*. International journal of refrigeration, 25 (731-750).
170. Z. Jiang, D.K. Harrison, K. Cheng. 2003. *Computer- aided design manufacturing of scroll compressors*. Journal of materials processing technology, 138 (145- 151).
171. C. Cuevas, J. Lebrun. 2009. *Testing and modeling of a variable speed scroll compressor*. Applied thermal engineering, 29 (469-478).
172. L Paramonov. 2004. PhD Thesis: *Simulation-based evaluation of scroll compressors for refrigeration applications*. University of Southern Denmark.
173. P. Howell. 2004. *Fluid mechanical modeling of scroll compressor*. Mathematical institute, 131 (32-56).
174. N.P. Suh. 1973. *The Delamination Theory of Wear*. Wear, 25 (111-124).
175. N. Kotsovinos. 1978. *A note on the conservation of the axial momentum of a turbulent jet*. Journal of Fluid Mechanics, 87 (65-63).
176. G. Plint, *TE 57 Pressurised Lubricity Tester: Operating Instructions*. Phoenix Tribology Ltd
177. N. Garland. PhD Thesis 2004. *Sustainable design of hydrocarbon refrigerants applied to the hermetic compressor*. Bournemouth University.
178. B. L. Xin, X. W. Lin, T. Zhong, L.N. Wen. 2008. *A high-speed photographic study of ultrasonic cavitation near rigid boundary*. Journal of Hydrodynamics, 20 637-644.

179. M. Dunlap, J. E. Adaskaveg. 1997. *Introduction to the Scanning Electron Microscope*. Facility for Advance Instrumentation
180. ASTM International 2003 *Standard Test Method for Determination of Additive Elements, Wear Metals, and Contaminants in Used Lubricating Oils and Determination of Selected Elements in Base Oils by Inductively Coupled Plasma Atomic Emission Spectrometry (ICP-AES)*.
181. Z.P Lu, K. Friedrich. 1995. *On sliding friction and wear of PEEK and its composites*. *Wear*, 181-183 (624-631).
182. S.N. Kukureka, C.J. Hooke, M. Rao, P. Liao, Y.K. Chen. 1999. *The effect of fibre reinforcement on the friction and wear of polyamide 66 under dry rolling-sliding contact*. *Tribology International*, 32 (107-116).
183. R.I. Trezona, D.N. Allsopp, I.M. Hutchings, 1999. *Transitions between two-body and three-body abrasive wear: influence of test conditions in the microscale abrasive wear tests*, *Wear*, 225-229 (205-214).
184. J.D. Gates. 1998. *Two-body and three-body abrasion: a critical discussion*. *Wear*, 214 (139–146).
185. K. Adachi, I.M. Hutchings. 2003. *Wear-mode mapping for the micro-scale abrasion test*. *Wear*, 255 (23–29).
186. S. Qian-qian, C. Xian-hua. 2006. *On the friction and wear behaviour of PTFE composite filled with rare earths treated carbon fibers under oil-lubricated condition*. *Wear*, 260 (1243–1247).
187. S. Qian-qian, C. Xian-hua. 2007. *Friction and wear of rare earths modified carbon fibers filled PTFE composite under dry sliding condition*. *Applied Surface Science*, 253 (9000–9006).
188. M.S. Stark, J. Wilkinson, P. Lee, J. Lindsay Smith, M. Priest, R. Taylor, S. Chung. 2005. *The degradation of lubricants in gasoline engines: Lubricant flow and degradation in the piston assembly*. *Tribology and Interface Engineering Series*, 48 (779-786).
189. X.Chen, R.Q.Xu, Z.H. Shen, J.Lu, X.W.Ni. 2004. *Optical investigation of cavitation erosion by laser-induced bubble collapse*. *Optics and laser technology*, 36 (197-203).
190. Bai Li-Xin, Xu Wei-Lin, Tian Zhong, Li Nai-Wen. 2008. *A high-speed photographic study of ultrasonic cavitation near rigid boundary*. *Journal of Hydrodynamics*, 20 (637-644).
191. C. Ohl, T. Kurz, R. Geisler, O. Lindau, W. Lauterborn. 1999. *Bubble dynamics, shock waves and sonoluminescence*. *The Royal Society*, 357 (269-294).
192. R. Pecha, B. Gompf. 2000. *Microimplosions: Cavitation collapse and shock wave emission on a nanosecond time scale*. *Physics*, 84 (1328-1330).

193. R.P Tong, W.P Schiffers, J.S. Shaw, J.R. Blake, D.C Emmony. 1999. *The role of splashing in the collapse of the laser-generated cavity near a rigid boundary*. Journal of Fluid Mechanics, 380 (339-361).
194. I. Akhatov, R. Mettin, C. D. Ohl, U. Parlitz, W. Lauterborn. 1997. *Bjerknes force threshold for stable single bubble sonoluminescence*. Physics, 55 (3747-3750).
195. B. Schneider, A. Kosar, Y. Peles. 2007. *Hydrodynamic cavitation and boiling in refrigerant (R-123) flow inside microchannels*. Heat and Mass Transfer, 50 (2838-2854).
196. C. Mishra, Y. Pelesa. 2005. *Flow visualization of cavitating flows through a rectangular slot micro-orifice ingrained in a microchannel*. Physics of Fluids 17.
197. A. Gronroos, P. Pentti, K. Hanna. 2008. *Ultrasonic degradation of aqueous carboxymethylcellulose: Effect of viscosity, molecular mass and concentration*. Ultrasonics Sonochemistry, 15 (644-648).
198. C. Haosheng, L. Jiang. 2009. *A ring area formed around the erosion pit on 1Cr18Ni9Ti stainless steel surface in incipient cavitation erosion*. Wear, 266 (884-887).
199. Z.C. Wang, Y. Zhang, X.Q. Zhang. 2001. *Thermal effect of cavitation erosion*. Chin. J. Mater. Res, 15 (287-290).
200. P.J. Bowles, A. Geach. 1963. *Grain Boundary Cavitation in Molybdenum*. Nature, 200 (669).
201. A. Krella, A. Czyniewski. 2009. *Cavitation resistance of Cr-N coatings deposited on austenitic stainless steel at various temperatures*. Wear, 266 (800-809).
202. K.H. Loa, F.T. Chenga, H.C. Man. 2003. *Laser transformation hardening of AISI 440C martensitic stainless steel for higher cavitation erosion resistance*. Surface and Coatings Technology, 173 (96-104).
203. M. Szkodo. 2005. *Relationship between microstructure of laser alloyed C45 steel and its cavitation resistance*. Materials Processing Technology, 162-163 (410-415).
204. C. Haosheng, L. Shihan, W. Jiadao, C. Darong. 2008. *Spherical dendritic particles formed in cavitation erosion*. Material Letters, 62 (2707-2709).
205. Y.G. Zheng, S.Z. Luo, W. Ke. 2008. *Cavitation erosion- corrosion behaviour of CrMnB stainless overlay and 0Cr13Ni5Mo stainless steel in 0.5M NaCl and 0.5M HCL solutions*. Tribology International, 41 (1181-1189).
206. E. Mazancová, I. Schindler, K. Mazanec. *Stacking fault energy analysis from point of view of plastic deformation response of the twin and triplex alloys*. Conference of Metals 2009.
207. A. Erdemir, G.R. Fenske, R.A. Erck, F.A. Nichols, D.E Busch. 1991. *Tribological properties of boric acid and boric-acid-forming surfaces. Part II: Mechanisms of formation and self-lubrication of boric acid films on Coron-and Boric acid-containing surfaces*. Tribological Transactions, 47 (179-184).